UNIVERSITY OF CALIFORNIA

Los Angeles

Oligocene-Miocene Sedimentary and Volcanic Strata of the Vincent Gap Region, Eastern San Gabriel Mountains, Southern California, USA, and Their Tectonic Significance

A thesis submitted in partial satisfaction of the requirements for the degree

Master of Science in Geology

by

Kevin Thomas Coffey

2015

ABSTRACT OF THE THESIS

Oligocene-Miocene Sedimentary and Volcanic Strata of the Vincent Gap Region, Eastern San Gabriel Mountains, Southern California, USA, and Their Tectonic Significance

by

Kevin Thomas Coffey

Master of Science in Geology

University of California, Los Angeles, 2015

Professor Raymond V. Ingersoll, Chair

The Vincent Gap region of the eastern San Gabriel Mountains in southern California is a small but important piece of an originally continuous terrane separated into the Tejon, Soledad and Orocopia regions by the San Andreas fault system. The middle-upper Miocene Punchbowl Formation has been considered the oldest Neogene strata of the Vincent Gap region. The present study documents that strata southeast of the main exposure of the Punchbowl Formation, though aerially restricted, are temporally extensive; together with the Punchbowl Formation, they comprise a sedimentary record that spans from ~25 to ~6 Ma, includes equivalents of the Vasquez, Tick Canyon and Mint Canyon formations of the Soledad region, and relates to three sequential tectonic stages in southern California. Uppermost Oligocene-lower Miocene strata are closely correlative with the Plush Ranch, Vasquez and Diligencia formations of the Tejon, Soledad and Orocopia regions, respectively; they formed during extension induced by triple-junction instability. Interbedded 25 Ma volcanics near the base of these strata are chemically and chronologically similar to those of the Plush Ranch, Vasquez and Diligencia formations. Middle Miocene strata beneath the Punchbowl Formation are equivalent to the Tick Canyon Formation of the Soledad region, and document exhumation of the Pelona Schist. Sandstone petrofacies, conglomerate composition and detrital-zircon age data provide compatible but distinct provenance information; using all three in combination results in a more complete understanding of the provenance of each of these units. The results of this study imply that transrotation of the western Transverse Ranges and accompanying basement exhumation extended farther inboard than generally thought, adjacent to if not across the future trace of the San Andreas fault. Data from the Vincent Gap also reveal that the middle-upper Miocene Punchbowl Formation was likely part of a large drainage system, with the Mint Canyon Formation of the Soledad region representing a tributary of this system that joined downstream, and the Caliente Formation of the Tejon region representing the confluence of the two.

The thesis of Kevin Thomas Coffey is approved.

Raymond V. Ingersoll

Axel K. Schmitt

An Yin

University of California, Los Angeles

2015

TABLE OF CONTENTS:

LIST OF FIGURES Page:

LIST OF PLATES

Page:

(Plates can be found in the back of printed versions and as online supplements)

LIST OF TABLES

LIST OF APPENDICES

ACKNOWLEDGMENTS

I thank my advisor, Raymond V. Ingersoll, for guiding me through this research and providing crucial instruction, insight and feedback on countless occasions. I thank my other committee members, Axel K. Schmitt and An Yin, for their helpful comments. I thank Axel K. Schmitt for assistance in preparing and analyzing igneous-zircon samples and interpreting the results, for discussion of the study, and for valuable instruction and assistance during a prior research project. I thank Clinton Colasanti for conducting preliminary research and collecting sandstone samples used in this study. I thank Johanna Hoyt for collection of four Punchbowl Formation sandstone samples. I thank Dallon Stang for assistance preparing and analyzing one of the detrital-zircon samples and assistance during a reconnaissance field session. I thank Mark Pecha, Nicky Giesler and Chelsi White of the UA LaserChron Center for assistance analyzing detrital zircon and processing the resulting data. I thank Juliet Ryan-Davis, Jonathan Harris and Jade Star Lackey of Pomona College for assistance with mineral separation and for the use of their water shaking table. I thank Wan Ning Wu for assistance with igneous-zircon sample preparation and Matthew Wielicki for assistance with crushing of zircon samples.

Fieldwork, microscope thin sections and trace-element analyses were paid by a Graduate Student Research Grant from the Geological Society of America. Detrital-zircon analyses were paid by a UCLA Academic Senate research grant awarded to Raymond V. Ingersoll. The ion-microprobe facility at UCLA is partly supported by a grant from the Instrumentation and Facilities Program, Division of Earth Sciences, National Science Foundation. The Arizona LaserChron Center is partly supported by National Science Foundation grant NSF-EAR 1032156. Purchase of the XRF facility at Washington State University was supported by the Murdoch Foundation and the National Science Foundation.

INTRODUCTION

Purpose

Crowell (1962, 1975a) correlated a distinct suite of lithologies in the Soledad region with nearly identical suites in the Tejon and Orocopia regions, on opposite sides of the San Gabriel and San Andreas faults, respectively (Fig. 1). This same suite is present as a thin sliver between the Punchbowl and San Andreas faults in the Vincent Gap region (Fig. 1). The Tejon, Soledad and Orocopia regions and their correlations to one another have been studied in detail (e.g., Crowell, 1962, 1975a; Ehlig and Ehlert, 1972; Bohannon, 1975, 1976; Ehlert, 1982, 2003; Frizzell and Weigand, 1993; Ingersoll et al., 2014). Prior to this study, however, the role of the Vincent Gap region as part of this suite of correlated regions had not been properly investigated.

The purpose of this study was to determine the ages, source rocks and extent of uppermost Oligocene through upper Miocene strata of the Vincent Gap region, and their relations to one another, to offset equivalents in the Tejon, Soledad and Orocopia regions of southern California separated along the San Andreas fault system, and to the sequence of plate-tectonic stages in southern California since initiation of a transform margin approximately 30 Ma (e.g., Atwater, 1970, 1989; Nicholson et al., 1994). To accomplish this, geologic mapping was conducted, and sandstone and conglomerate compositional data, detrital- and igneous-zircon age data, trace-element data and paleocurrent data were collected and analyzed.

Location

This study was conducted in the Vincent Gap region of the eastern San Gabriel Mountains in southern California, USA, approximately 15 km west of the city of Wrightwood on California Highway 2 (Fig. 1). The study area is a narrow strip extending along the Punchbowl fault from Cabin Flat Campground in the southeast to Holcomb Canyon and Devil's Chair in the eastern part of Devil's Punchbowl County Park in the northwest (Plate 1).

REGIONAL GEOLOGY

Plate Interactions

Convergent Tectonics and Initiation of the Transform Margin

Oceanic crust began subducting beneath the western margin of North America following the Sonoma orogeny of the Permian and Triassic (e.g., Dickinson, 1981, 2004; Ingersoll, 1997, 2008a). Following the Nevadan orogeny, ~160-145 Ma (Ingersoll, 2008a), this subduction was of the Farallon plate. During Laramide time (~80-40 Ma), flat-slab subduction occurred in lieu of normal, steep-slab subduction (e.g., Dickinson and Snyder, 1978; Bird, 1984, 1988; Ingersoll, 2008a, b). Subduction continued uninterrupted until shortly after 30 Ma, when the Pacific-Farallon spreading ridge began to impinge on the North American-Farallon subduction zone, bringing the Pacific and North American plates into contact (Atwater, 1970, 1989). This created a new Pacific-North American plate boundary, along which seafloor spreading and subduction concurrently ceased and right-lateral transform motion began. As more of the Pacific-Farallon ridge has reached the trench and disappeared, this Pacific-North American plate boundary, which is modeled as having begun as a single point, has progressively lengthened. At either end of this transform plate boundary are triple junctions, at which the Pacific, Farallon and North American plates meet; as the transform has lengthened, these triple junctions have migrated apart (Atwater, 1970, 1989; Nicholson et al., 1994). At the northern end of the transform is the Mendocino triple junction (MTJ), presently offshore of Cape Mendocino, California, with the fragment of Farallon plate to its north termed the Juan de Fuca plate. At the southern end is the Rivera triple junction (RTJ), presently just south of the mouth of the Gulf of California, with the fragments of Farallon plate to its south termed the Rivera and Cocos plates. The MTJ has migrated northwestward steadily since its formation (Atwater, 1970). The RTJ, by contrast, has migrated largely by a series of discrete steps related to capture of microplate fragments of the Farallon plate by the Pacific plate (Atwater, 1970; Lonsdale, 1991; Nicholson et al., 1994). This southward stepping has had profound effects on southern California, sequentially imposing three distinct tectonic regimes over the past ~18 Ma (Ingersoll and Rumelhart, 1999; Ingersoll, 2008b).

Unstable Configuration of the Mendocino Triple Junction

The MTJ is a transform-transform-trench (FFT) triple junction and, as such, would be stable only if the trends of the trench and the Pacific-North American transform were parallel (Dickinson and Snyder, 1979). The current configuration, in which the trench trends ~north-south and the transform ~northwest-southeast, would form and continuously enlarge a triangular hole in the lithosphere if all plate boundaries and plate motions stayed fixed and all plates were undeformable (Dickinson and Snyder, 1979). The MTJ is interpreted to have had this unstable configuration since its initiation (Ingersoll, 1982); a lithospheric hole has been averted via extension and clockwise rotation of western North America and progressive inboard stepping of the Pacific-North American transform (Dickinson and Snyder, 1979; Ingersoll, 1982). MTJ instability may be a primary cause of Cenozoic extension of southwestern California, the Basin and Range province and the Rio Grande rift (Ingersoll, 1982; but see Tennyson, 1989).

Formation of Slab Window

Following contact between the Pacific-Farallon spreading ridge and the Farallon-North American trench, and conversion to a Pacific-North American transform, the formerly intervening Farallon plate, no longer present at the surface, continued to subduct (e.g., Nicholson et al., 1994). Because subduction had ceased at the trench, this subducting slab left in its wake a "slab window," a region in which the base of North American lithosphere was underlain directly by asthenosphere (e.g., Dickinson, 1997). Over time, the slab window has grown: inboard as the western edge of the slab has continued to subduct, and north and south as the Pacific-North American transform has lengthened (e.g., Dickinson and Snyder, 1979; Dickinson, 1997).

Microplate-Capture Event 1: Monterey and Arguello Plates

At ~24 Ma, the RTJ lay along the Farallon Fracture Zone (Nicholson et al., 1994). To the south, the Monterey and Arguello microplates, fragments of the Farallon plate, continued to subduct beneath southern California (Fig. 2). Around 22 Ma, segments of the spreading ridge along the western edge of the Monterey plate reached the subduction zone and shut down. The RTJ stepped south to the Morro Fracture Zone, which defined the border between the Monterey and Arguello microplates; the fragmented seafloor spreading and subduction that remained to the north of its new position slowed, shifting the Monterey microplate to a motion in between those of the Pacific and Farallon plates (Nicholson et al., 1994). By ~20 Ma, spreading and subduction ceased altogether, resulting in attachment of the Monterey microplate to the Pacific plate (Lonsdale, 1991; Nicholson et al., 1994). As the Monterey microplate was pulled northwest from beneath the North American plate, it dragged the overlying weak continental crust, the western Transverse Ranges (WTR) block, with it. This overlying crust, however, was prevented from translating northwest because of stable continental crust to its north, beyond the northern limit of the underlying Monterey microplate. As a result, the WTR block began to rotate clockwise, while undergoing extension at its northwestern and southeastern corners (Nicholson et al., 1994; Fig. 2).

At ~18-17 Ma, the RTJ stepped southward again, this time to the southern end of the Arguello microplate, which, like the Monterey, became attached to the Pacific plate, dragging the overlying continental crust with it (Lonsdale, 1991; Nicholson et al., 1994). Unlike the WTR, however, this overlying crust was not restricted at its northern end, as the WTR to its north was already moving northwest as well. As a result, this crust underwent oblique extension without a significant rotational component, opening up the inner borderland off the coast of southern California and the southern borderland off the coast of Baja California (Crouch and Suppe, 1993; Nicholson et al., 1994; Fig. 3B, C).

Prior to Pacific-North American transform motion, during normal, steep-slab subduction, four lithotectonic belts formed parallel to the former North American-Farallon convergent boundary: the Sierra Nevada-Salinia-Peninsula Ranges batholithic belt, the Foothill metamorphic complex, the Great Valley forearc strata, and the Franciscan subduction complex (Dickinson, 1981; Crouch and Suppe, 1993). Much of the subsequent disruption of these parallel belts is the result of extension and transrotation associated with capture of the Monterey and Arguello microplates.

Microplate-Capture Event 2: Guadalupe and Magdalena Plates

By ~12 Ma, the inner and southern borderlands were extensively extended (Nicholson et al., 1994). The narrow northern part of the Farallon plate had again fragmented into partially decoupled microplates, giving rise to the Guadalupe microplate immediately south of the RTJ and the Magdalena microplate south of that (Nicholson et al., 1994; Fig. 3C**)**. At ~12 Ma, these plates, like the Monterey and Arguello microplates, became coupled to the Pacific plate (Lonsdale, 1991; Nicholson et al., 1994). Seafloor spreading and subduction ceased along their western and eastern margins, respectively, and the San Gabriel-Chino Hills-Cristianitos-Tosco-Abreojos fault became the primary Pacific-North American transform (Spencer and Normark, 1979; Lonsdale, 1991; Nicholson et al., 1994; Ingersoll and Rumelhart, 1999; Fig. 3D).

Microplate-Capture Event 3: Baja California

The Peninsula Ranges batholith (PRB) is a region of relatively strong crust; as a result, the San Gabriel-Chino Hills-Cristianitos-Tosco-Abreojos fault formed to its west, deviating from a straight line in the process. About 6 or 5 Ma, the active transform jumped inland to the modern San Andreas fault, on the eastern side of the PRB (Lonsdale, 1991; Nicholson et al., 1994; Ingersoll and Rumelhart, 1999; Fig. 3E). This transferred Baja California to the Pacific plate, and highly oblique seafloor spreading began along the new, primarily transform boundary in the proto-Gulf of California (Lonsdale, 1991; Nicholson et al., 1994).

Tectonic Stages

Triple-Junction-Migration-Induced Extension and Volcanism (24-18 Ma)

As the MTJ migrated northward in the vicinity of southern California, resulting extension induced the formation of half-grabens in the Tejon, Soledad and Orocopia regions, which were filled by the syn-extensional Plush Ranch, Vasquez and Diligencia formations, respectively (Ingersoll, 2008b). The expanding slab window had recently grown to include the area beneath these regions (Dickinson, 1997), placing asthenosphere directly beneath thin, extending North American lithosphere. This resulted in eruption of the volcanics interbedded within the Plush Ranch, Vasquez and Diligencia formations (Ingersoll, 1982; Dickinson, 1997; Hendrix et al., 2010).

Transrotation (18-12 Ma)

The WTR have undergone ~110° of clockwise rotation since ~20-18 Ma (Dickinson, 1996; Ingersoll, 2008b), from their original ~N-S orientation west of the PRB to their current ~E-W orientation (the northern Channel Islands, and the Santa Monica, Santa Ynez and western San Gabriel Mountains; Crouch and Suppe, 1993; Ingersoll and Rumelhart, 1999). This rotation has been accommodated by extension along a low-angle detachment fault that formed in or near the former subduction channel (Ingersoll, 2008b), within or above the Pelona-Orocopia-Rand-Catalina (PORC) schists that were underplated to North America during Laramide flat-slab subduction (Crouch and Suppe, 1993; Jacobson et al., 2011). The hanging wall consists of PRB rocks overlain by Cretaceous and Paleogene strata, and syn-extensional Miocene sedimentary and volcanic strata (Crouch and Suppe, 1993); the detachment fault likely cuts up through these units along the Boney Mountain fault (Ingersoll, 2008b; Fig. 4). Isostatic compensation has uplifted and deformed this detachment, bringing it and the underlying Catalina Schist to the surface or near subsurface throughout the inner borderland (Crouch and Suppe, 1993).

In the Tejon region, the western Big Pine-Pine Mountain fault forms the northern edge of a zone of reverse faults that define the northern border of the WTR block (Onderdonk, 2005; Onderdonk et al., 2005). In contrast to rocks immediately south of this border, the block immediately to the north, which is the part of the Tejon region considered in this study, has not undergone any significant systematic vertical-axis rotation (e.g., Onderdonk, 2005).

Paleomagnetic data Paleomagnetic data record the substantial clockwise rotation that the WTR have undergone (Hornafius et al., 1986). Dickinson (1996) grouped these data into five "transrotational domains," with domains in the western part of the WTR recording greater rotation than those in the eastern part (Fig. 5). Dickinson (1996) attributed this trend to rotation of the WTR as a coherent lever, the rotational axis of which moved westward through time. An alternative possibility is that the rotational axis remained fixed, but the western WTR rotated more rapidly than the eastern WTR, causing the WTR to bend as it rotated. Standard deviations comparable in magnitude to the differences in amount of rotation of adjacent domains prevent confident interpretation of this trend. Terres and Luyendyk (1985) suggested that rotation of the

San Gabriel block (the easternmost domain of Dickinson, 1996; Fig. 5) occurred independently of WTR rotation as a result of its proximity to the eastern California shear zone; the almost identical magnitude of rotation experienced by the domain immediately to its west, however, makes this unlikely.

The total clockwise rotation of the WTR recorded by paleomagnetic data ranges from 53° ± 12° in the San Gabriel block to 85° ± 10°, and locally 95° ± 9°, in part of the western WTR (all uncertainties reported in text are 1σ; Hornafius et al., 1986; Dickinson, 1996; Fig. 5). All these values fall short of the ~110° of total clockwise rotation estimated to have occurred, based on geologic reasoning (Crouch and Suppe, 1993; Ingersoll, 2008b). Most of these data were collected from syn-rotational volcanics generated by crustal thinning associated with rotational extension, and thus clearly post-date some of the rotation. This may be the cause of the disparity, although comparison with paleomagnetic data from pre-rotational redbeds suggests that the WTR did not experience significant rotation prior to eruption of these volcanics (Hornafius et al., 1986; Dickinson, 1996). Paleomagnetic data from Santa Catalina Island indicate ~100° of clockwise rotation, which Hornafius et al. (1986) attributed to localized rotation of a small block containing part or all of Santa Catalina Island; it is also possible that these data merely record more of the ~110° of total rotation than the WTR samples. As with the WTR domains, the differences between the amounts of rotation recorded by Santa Catalina Island and the western domains of the WTR are comparable in magnitude to the standard deviations of these measurements (Hornafius et al., 1986; Dickinson, 1996).

Geologic data The ~110° clockwise rotation of the WTR is suggested by geologic and seismic data. Basement rocks and overlying pre-Miocene strata in the WTR have been correlated with equivalent rocks in the PRB (Crouch and Suppe, 1993; Ingersoll and Rumelhart, 1999).

Paleocurrent directions in Cretaceous and Paleogene marine strata are ~northward in the WTR and ~westward in the PRB; unrotating the WTR 110° restores these paleocurrent directions to ~westward, matching those in the PRB (Crouch and Suppe, 1993). Furthermore, in the PRB, these strata were deposited in shallow, proximal environments, with some of their source rocks nearby, whereas in the WTR, these strata were deposited in deeper, more distal environments, consistent with westward transport of material across the WTR prior to initiation of transrotation (Crouch and Suppe, 1993). Distinct rhyolitic "Poway" clasts found in the northern Channel Islands and along the California coast near San Diego also have ~northward paleocurrent directions in the WTR and ~westward paleocurrent directions in the PRB (Crouch and Suppe, 1993).

Seismic data Seismic data have also been interpreted as supporting transrotation. Using ~NE-SW seismic lines just offshore north of Oceanside, Crouch and Suppe (1993) mapped the detachment fault, isolated blocks of listrically rotated forearc strata and Miocene through Quaternary overlying strata. These interpretations are partly constrained by oil-well data.

Exhumation of the Pelona-Orocopia-Rand-Catalina schists After being underplated to North America in the Late Cretaceous and early Paleogene as a result of flat-slab subduction, the Pelona-Orocopia-Rand-Catalina (PORC) schists followed a complex thermotectonic path that brought them progressively nearer to Earth's surface during the Paleocene through Miocene, prior to onset of transrotation (Grove et al., 2003; Jacobson et al., 2007, 2011). During rotation of the WTR, extension caused final exhumation of these schists (Ingersoll, 2008b). The syn-rotational, middle Miocene San Onofre Breccia (Ellis, 1919; Woodford, 1925; Stuart, 1979), exposed in the Dana Point and Point Dume areas, contains distinctive clasts of Catalina blueschist (e.g., Woodford, 1925). The San Onofre Breccia is also found on Santa Rosa,Santa

Cruz and San Miguel Islands, where it is lower Miocene (e.g., McLean et al., 1976; Stuart, 1979; Crouch and Suppe, 1993), and Santa Catalina and Anacapa Islands, where it is middle Miocene (Scholl, 1959; Vedder et al., 1979). Near Dana Point and Point Dume, up to 50% of the clasts in the basal San Onofre Breccia are from the Coast Range ophiolite, which structurally overlies the Catalina Schist; upsection, clasts of Catalina Schist dominate (e.g., Crouch and Suppe, 1993). On Santa Rosa and Santa Cruz Islands, the Vaqueros Formation (and, on Santa Rosa Island, the coeval lower Rincon Formation) contains abundant clasts of forearc strata, Coast Range ophiolite and other units structurally above the Catalina Schist, whereas the overlying Rincon Formation and San Onofre Breccia are dominated by clasts of Catalina Schist (McLean et al., 1976; Crouch and Suppe, 1993). In both cases, this upsection shift toward Catalina Schist detritus represents an unroofing sequence.

Much nearer the rotational axis of the WTR, in the Soledad region, work by Ehlert (1982, 2003) and Hendrix (1993) on the middle Miocene Tick Canyon Formation suggests a similar unroofing trend, from cataclastic and mylonitic clasts to Pelona Schist clasts upsection. In the Vincent Gap region, Ingersoll and Colasanti (2004) and Colasanti and Ingersoll (2006) documented a similar unroofing sequence in conglomerate mapped by Dibblee (2002a) as a member of the Punchbowl Formation, but in this study referred to as the Vasquez Formation and the informally designated "Paradise Springs formation," with 100% sandstone clasts in the upper Vasquez Formation and >10% Pelona Schist clasts in the overlying Paradise Springs formation. Restoration of the ~40-50 km of post-middle Miocene slip that occurred on the Punchbowl fault (Dibblee, 1968; Ehlig, 1968, 1981) places the Paradise Springs formation adjacent to the Tick Canyon Formation and near the rotational axis of the WTR. The unroofing sequences in the Tick Canyon and Paradise Springs formations represent the first appearances of PORC schist clasts inboard of the inner borderland. During the second part of the middle Miocene transrotational phase, deposition of the middle to upper Miocene Mint Canyon and Punchbowl formations began atop the Tick Canyon and Paradise Springs formations, respectively (Ehlert, 1982, 2003; Hendrix and Ingersoll, 1987).

The San Francisquito fault and the multi-stranded Pelona detachment fault, which form the northwestern and southeastern boundaries, respectively, of Pelona Schist exposure at Sierra Pelona in the Soledad region, have been interpreted as the detachment fault along which triple-junction-induced extension occurred, and in the footwall of which the Pelona Schist was exhumed (Bishop and Ehlig, 1990; Hendrix et al., 2010; but see Weldon et al., 1993). In this interpretation, the two traces represent exposure of the fault in opposite limbs of the anticlinorium at the center of Sierra Pelona. As discussed by Hendrix et al. (2010), this detachment fault correlates with the Orocopia Mountains detachment fault of the Orocopia region (Robinson and Frost, 1996; but see Yin, 2002).

Because the Tejon region did not undergo significant vertical-axis rotation, it did not experience rapid uplift of the Pelona Schist: present exposures of Pelona Schist in the area are of its uppermost levels, overlain by the Sawmill Mountain thrust (equivalent to the Vincent-Chocolate Mountains thrust) and upper-plate mylonite and gneiss (e.g., Kellogg, 2003; Dibblee, 2006a); the San Francisquito/Pelona/Orocopia Mountains detachment fault and structurally lower levels of Pelona Schist exposed in the Soledad and Orocopia regions presumably remain beneath the surface in the Tejon region.

San Gabriel Transform (12-6 Ma)

When the San Gabriel-Chino Hills-Cristianitos-Tosco-Abreojos fault became the active Pacific-North American transform margin ~12 Ma, transtension began in the Los Angeles area as a result of the releasing bend in this fault at the northern end of the PRB (Ingersoll and Rumelhart, 1999). In the Los Angeles area, this formed the Puente basin, in which the upper Miocene Monterey Formation and related units were deposited atop the San Onofre Breccia and the middle Miocene Topanga Formation (Ingersoll and Rumelhart, 1999; Ingersoll, 2008b). A restraining bend farther north along the San Gabriel fault resulted in deposition in the transpressional Ridge basin (Crowell, 1982, 2003; Ingersoll and Rumelhart, 1999). In the Soledad region, deposition of the middle to upper Miocene Mint Canyon Formation continued, followed by deposition of the upper Miocene Castaic Formation (e.g., Dibblee, 1996a, b, 1997a, b). In the Vincent Gap region, deposition of the middle to upper Miocene Punchbowl Formation continued.

Transpression (6 or 5 Ma-present)

Transpression began in the WTR and Los Angeles basin area 6 or 5 Ma, when the active Pacific-North American transform stepped east to the southern San Andreas fault, forming a restraining bend (the proto-“Big Bend”; Ingersoll and Rumelhart, 1999). This caused contraction of the Fernando basin (the youngest phase of the Los Angeles basin), which was rapidly filled via deposition of the progressively shallower Capistrano Formation, Fernando Formation and younger deposits, collectively of Pliocene to Quaternary age, atop the Monterey Formation and related units (Ingersoll and Rumelhart, 1999). In the Soledad and Vincent Gap regions, deposition ceased. Uplift caused by transpression is responsible for exposures of Miocene strata deposited during previous stages.

The Punchbowl fault is a splay of the southern San Andreas fault (Fig. 1); it has accumulated ~45 km of slip (e.g., Ehlig, 1981) which resulted in separation of the Soledad and

Vincent Gap regions. This presumably occurred during the transpressional stage (e.g., Powell, 1993), as did slip on the southern San Andreas fault proper (e.g., Crowell, 1982; Powell, 1993).

Palinspastic Reconstructions

The Soledad and Orocopia regions were initially correlated based on similarities in both basement rocks (Crowell and Walker, 1962; Crowell, 1975a) and uppermost Oligocene to lower Miocene sedimentary and volcanic strata (Crowell, 1962, 1975a; but see Woodburne and Whistler, 1973; Spittler, 1974). Characteristics of basement and Miocene strata were also used to correlate the Tejon and Soledad regions (Crowell, 1962, 1975a; Carman, 1964). Original lateral proximity of the Tejon, Soledad and Orocopia regions has been supported and refined by source-rock/conglomerate-clast correlations and other sedimentologic data (e.g., Ehlig and Ehlert, 1972; Bohannon, 1975; Ehlert, 1982, 2003), and by chronological and geochemical similarities of volcanics (e.g., Weigand, 1982; Frizzell and Weigand, 1993). These correlations have been widely accepted, although reconstructions have been presented in which these regions do not correlate (e.g., Woodburne, 1975). A map-view palinspastic reconstruction at ~18 Ma, in which the various equivalent units of these three regions are re-aligned, is presented in Ingersoll et al. (2014).

Correlation of the Vincent Gap and Soledad regions was initially proposed by Dibblee (1967, 1968) and Ehlig (1968), based on similarities between the anticlinoria of Pelona Schist at Blue Ridge and Sierra Pelona, presence of the San Francisquito Formation in both regions, and similarities between the Fenner and San Francisquito faults. Ehlig (1981) based his 45-km slip estimate for the Punchbowl fault on correlation of the San Francisquito and Fenner faults; Dibblee (1967, 1968), Powell (1993) and Ehlig (1968) made comparable slip estimates of ~40 km, 44-45 km and ~50 km, respectively. Clasts of a distinct “polka-dot granite” within the

Punchbowl Formation have been used to suggest correlation of the Vincent Gap region with either the northwestern Orocopia region (Ehlert and Ehlig, 1977; Ehlig and Joseph, 1977) or the northern Little San Bernardino Mountains (Ehlig and Joseph, 1977; Matti and Morton, 1993). The Vincent Gap region has not been considered in many of the reconstructions discussed above, and its Oligocene-Miocene strata have received little attention.

Pre-Oligocene Offset Equivalents and Their Zircon Ages

Paleoproterozoic Gneiss

Paleoproterozoic gneiss outcrops in the Tejon, Soledad and Orocopia regions (Crowell, 1975a). It consists of layered gneiss and minor amphibolite and migmatite, intruded by slightly younger, variably metamorphosed granitic rock, including distinct augen gneiss (Ehlig, 1981). Zircon from layered gneiss in the Soledad region yielded an unspecified U-Pb age of 1715 ± 30 Ma (Ehlig, 1981), which Silver (1966) interpreted as the approximate age of the protolith. Zircon from augen gneiss in the Soledad and Tejon regions yielded unspecified U-Pb ages of 1660 ± 15 Ma (Silver, 1966) and 1690 ± 5 Ma (Stanley et al., 1998) respectively; zircon from foliated quartz monzonite in the southern San Gabriel Mountains yielded a ^{207}Pb-^{206}Pb age of 1670 ± 20 Ma (personal communication of Davis, 1978 in Ehlig, 1981). Metamorphism of the layered gneiss, amphibolite and migmatite protoliths likely occurred at this time as a result of intrusion of this granitic rock (Ehlig, 1981). Prior to offset by Cenozoic faulting, this gneiss formed a promontory of the North American craton, extending farther west than cratonal basement to both the north and south (e.g., Dickinson, 1981; Barth et al., 1995).

Mesoproterozoic Anorthosite-Gabbro-Syenite-Norite Complex

Although it is not presently exposed in the Vincent Gap region, outcrops of an intrusive complex of anorthosite, gabbro, syenite and norite are found in the Tejon, Soledad and Orocopia regions (Crowell, 1975a). In the Soledad region, it is present just southwest of the Nadeau-Punchbowl fault (e.g., Dibblee, 1997c), and thus would have been adjacent to the Vincent Gap region prior to Nadeau-Punchbowl fault slip. The anorthosite-gabbro-syenite-norite complex has been interpreted as an inverted-cone-shaped layered intrusion, with fractionation responsible for compositions from andesine anorthosite to syenite (Carter and Silver, 1971; Ehlig, 1981). It intruded the Paleoproterozoic gneiss at ~1180-1190 Ma, based on a syenite zircon model-concordia age of 1191 ± 4 Ma (Barth et al., 1995) and related pegmatite zircon ^{207}Pb-^{206}Pb ages of 1182 ± 8, 1175 ± 5 and 1172 ± 8 Ma (Silver et al., 1963; recalculated using the decay constants of Steiger and Jäger, 1977). The slightly younger U-Pb ages of the pegmatite samples have been attributed to recent lead loss by Barth et al. (1995).

Emplacement of the anorthosite-gabbro-syenite-norite complex likely created the Mendenhall Gneiss (Oakeshott, 1958) as a granulite-facies contact aureole within the Paleoproterozoic gneiss (Ehlig, 1981; Barth et al., 1995, 2001). Perturbation of the Paleoproterozoic gneiss by the intrusion of this complex also produced discordant zircon that yielded apparent ^{207}Pb-^{206}Pb ages of ~1400 Ma (Silver et al., 1963; Barth et al., 1995, 2001), responsible for the spurious inference of a major metamorphic event at ~1400 (e.g., Silver, 1971). Following emplacement of the anorthosite-gabbro-syenite-norite complex, no metamorphic or intrusive perturbation appears to have occurred within the Proterozoic basement until emplacement of Mesozoic plutons (Ehlig, 1981).

Late Triassic Lowe Granodiorite

The Lowe Granodiorite is a compositionally zoned pluton exposed within and east of the Soledad region (e.g., Ehlig, 1981). It ranges in composition from hornblende-rich diorite and quartz diorite to albite-rich granite and syenite (Ehlig, 1981). Feldspar content ranges from ~60 to 95%, and quartz content is typically ~10% (Ehlig, 1981). Zircon from the Lowe Granodiorite yielded U-Pb ages of 220 ± 10 Ma (unspecified age type; Carter and Silver, 1971; Silver, 1971) and 218.3 ± 0.3 Ma (^{206}Pb-^{238}U age; Barth et al., 1990), and a whole-rock Rb-Sr isochron age of 208 ± 7 Ma (Joseph et al., 1978), slightly younger than but overlapping in uncertainty with the zircon ages. These ages are significantly older than other Mesozoic plutons in southern California, and likely represent the initial stages of subduction beneath the North American plate (Ehlig, 1981).

Jurassic and Cretaceous Granitoids

Numerous overlapping plutons are present in much of the San Gabriel Mountains, and the Soledad, Vincent Gap, Tejon and Orocopia regions (e.g., Crowell, 1975a; Ehlig, 1981). These plutons are part of an originally continuous magmatic arc that included the granitoids of the Sierra Nevada, PRB, Salinia and Mojave block, formed by normal, steep-slab subduction along the margin of North America (Dickinson, 1981). In the San Gabriel Mountains, they are typically Late Cretaceous quartz diorite to quartz monzonite (Ehlig, 1981), though Silver (1971) recognized distinct episodes of plutonism at ~170-160 Ma and ~90-75 Ma. The largest exposed pluton in the San Gabriel Mountains, the Wilson Diorite (Miller, 1934), also referred to as the Mount Waterman pluton and the Mount Wilson pluton (Ehlig, 1981), is present in the study area southwest of the Punchbowl fault (Plate 1). Zircon from this pluton ~2.5 km southwest of the study area yielded an unspecified U-Pb zircon age of ~74 Ma (Silver and Nourse, 2001; Nourse, 2002); samples collected a few kilometers farther south yielded an unspecified U-Pb sphene age of 77 ± 2 Ma (unpublished data of Wooden in Grove and Lovera, 1996) and an inverse-isochron argon hornblende age of 71 ± 2 Ma (Grove and Lovera, 1996). Zircon from granodiorite intruded by this pluton just southwest of the study area on Pleasant View Ridge yielded a concordia lower intercept age of 164.3 ± 3.4 Ma (Barth et al., 1989).

In the Tejon region, unconformably underlying the Plush Ranch Formation along much of its northwestern edge (e.g., Kellogg, 2003) is the Mount Pinos granite (Carman, 1964; Pinos granite of Staatz, 1940), which ranges from biotite granite to biotite quartz diorite (Carman, 1964), with an unspecified U-Pb zircon age of 75.1 ± 1.6 Ma (written communication of Premo in Kellogg et al., 2008). An offset equivalent of this granite is present as a thin, fault-bounded strip along the northwestern edge of the Vasquez Formation just southeast of the Pelona Schist of Sierra Pelona (in the Texas Canyon subbasin, discussed below; Dibblee, 1997b); it is estimated as ranging in composition from biotite granite to quartz monzonite (Dibblee, 1997b). North of the Orocopia region are exposures of Late Jurassic plutons with interpreted crystallization ages of 151 ± 1 Ma, 155 ± 2 Ma and 157 ± 2 Ma (based on ^{206}Pb-^{238}U ages; Barth et al., 2008). In the Vincent Gap region northeast of the Punchbowl fault, underlying much of the San Francisquito and Vasquez formations, is a leucocratic granitoid of uncertain affinity (Plate 1).

Pelona-Orocopia-Rand-Catalina Schists

The Pelona-Orocopia-Rand schists are ≥90% meta-arkose, metamorphosed mostly to greenschist and albite-epidote amphibolite facies and locally to epidote-blueschist and upper amphibolite facies (Haxel and Dillon, 1978; Ehlig, 1981; Jacobson et al., 2011). The meta-arkose is inferred to have originated as turbidites deposited within the trench of the North American - Farallon convergent margin, with minor amounts of basalt, chert and carbonate from the subducting plate (Ehlig, 1981; Jacobson et al., 2011). The Catalina Schist is lithologically similar, but with a greater diversity of protoliths and metamorphic grades (Jacobson et al., 2011). The younger parts of the Catalina Schist overlap in age and have been correlated with the oldest parts of the Pelona-Orocopia-Rand schists; these PORC schists were underplated onto the base of North America via the Vincent-Chocolate Mountain thrust fault zone (Haxel and Dillon, 1978) during Laramide flat-slab subduction (e.g., Jacobson et al., 2011). The older parts of the Catalina Schist predate the other schists and flat-slab subduction, and correlate with the Franciscan subduction complex (Jacobson et al., 2011). Pelona Schist is exposed in the Tejon, Soledad and Vincent Gap regions; Orocopia Schist is exposed in the Orocopia region (e.g., Crowell, 1975a; Haxel and Dillon, 1978).

Detrital zircon within the PORC schists yielded U-Pb ages as young as ~60-70 Ma (Grove et al., 2003; Jacobson et al., 2000, 2011). Within the Pelona Schist, the vast majority of ages fall between ~70 and 110 Ma; some zircon yields older ages, including ~1200, ~1400, and ~1700 Ma, which correspond to the Proterozoic basement discussed above (Grove et al., 2003; Jacobson et al., 2000, 2011). Hornblende, muscovite and biotite $^{40}Ar/^{39}Ar$ cooling ages indicate progressive cooling of the PORC schists, and thus removal of overlying material, during Paleocene through Miocene time (Jacobson et al., 2007, 2011). This progressive shallowing of the PORC schists culminated in final exhumation during the middle Miocene, as discussed above. Subequal concentrations of U and Th in nearly all zircon from the PORC schists, together with the schists' typically low-grade metamorphism, indicates that the zircon is ultimately magmatic in origin (Hoskin and Schaltegger, 2003; Jacobson et al., 2011), and thus entirely detrital; no zircon appears to have formed during metamorphism.

Uppermost Cretaceous-Eocene San Francisquito and Maniobra Formations and Unnamed Strata

The type San Francisquito Formation (Dibblee, 1967) of the Soledad region consists of almost 4 km of deep-marine conglomerate, sandstone, mudstone and shale atop almost 100 m of shallow-marine limestone, sandstone, conglomerate, coquina and coal (Kooser, 1982). The deep-marine deposits are interpreted to have formed within the inner part of a nearshore submarine fan system (Kooser, 1982). Based on molluscan faunas, the type San Francisquito Formation is considered Upper Maastrichtian through middle Paleocene (Kooser, 1982).

The Vincent Gap region contains strata corresponding to the type San Francisquito Formation (Dibblee, 1967; Kooser, 1982); like the type section, they were initially considered (e.g., Arnold, 1906; Dickerson, 1914; Noble, 1954) part of the Martinez Formation (named by J.D. Whitney in Gabb, 1869), but have since been termed, and are here referred to as, the San Francisquito Formation (e.g., Dibblee, 1967). In the Vincent Gap region, ~1500 m of the San Francisquito Formation is exposed (Dibblee, 1987); molluscan fossils from the lower part indicate a Paleocene age (Arnold, 1906; Dickerson, 1914; Dibblee, 1987); the upper part is likely Eocene (Dibblee, 1967, 1987).

The Maniobra Formation of the Orocopia region (Crowell and Susuki, 1959) consists of two members: a lower member of nonmarine conglomerate and breccia with interbedded siltstone and sandstone, and an upper member of marine siltstone and sandstone deposited as turbidites in a submarine canyon (Crowell and Susuki, 1959; Advocate et al., 1988). The Maniobra Formation is Lower to Middle Eocene (Crowell and Susuki, 1959).

The Tejon region contains marine deposits of comparable age (e.g., Kellogg et al., 2008), presumably broadly correlated with the San Francisquito and Maniobra formations (e.g., Woodburne, 1975). Some of these deposits are unnamed; named deposits include the Coldwater Sandstone, Cozy Dell Shale, Matilija Sandstone, Juncal Formation, Sierra Blanca Limestone and Pattiway Formation (e.g., Kellogg et al., 2008).

Late Oligocene Telegraph Peak Granite and Associated Sills and Dikes

The Telegraph Peak granite (Nourse, 2002) is a pluton of either granitic (Nourse, 2002), granodioritic (Miller and Morton, 1977) or quartz monzonitic (Hsu et al., 1963) composition, exposed ~14 km southeast of the study area in the area around Telegraph Peak (e.g., Dibblee, 2003). The Telegraph Peak granite has yielded discordant zircon with a model-concordia age, interpreted as the emplacement age, of 25.6 ± 1 Ma (May and Walker, 1989) and an age of ~26 Ma from unspecified methods (oral communication of Weigand in Dibblee, 2003); all but the oldest previously reported K-Ar biotite ages, which range from 27 ± 3 Ma to 14.4 ± 0.4 Ma (Hsu et al., 1963; Miller and Morton, 1977; recalculated after Dalrymple, 1979), are incompatible with the zircon age, and have been interpreted as reflecting subsequent thermal disturbance during widespread emplacement of middle Miocene dikes (Nourse, 2002).

The hypabyssal intrusive of the study area (Plate 1) is part of a complex of rhyolite or rhyodacite sills and dikes associated with the Telegraph Peak granite (Dibblee, 2002d, 2003; Nourse, 2002). Correlation of the large body of hypabyssal intrusive in the southeastern part of the study area (Plate 1) with Vasquez Formation-and-equivalent volcanics was tentatively suggested by Weldon et al. (1993), although they mapped it as a fault-bounded sliver rather than as an intrusive within and adjacent to the Vincent thrust fault zone.

Oligocene-Miocene Sedimentary Strata

Uppermost Oligocene-Lower Miocene: Plush Ranch/Vasquez/Diligencia Formations

Plush Ranch Formation The Plush Ranch Formation of the Tejon region (Carman, 1954, 1964) consists of more than 1800 m of nonmarine conglomerate, sandstone, siltstone, shale, limestone and evaporites, with interbedded basalt and minor felsic tuff (Carman, 1964; Cole and Stanley, 1995; Hendrix et al., 2010). It is interpreted to have formed as alluvial and lacustrine deposits within a half-graben, bounded on the southeast by the northwest-dipping Lockwood Valley (or Big Pine) fault or its predecessor, interpreted as dip-slip during this time (Cole and Stanley, 1995; Onderdonk et al., 2005; Hendrix et al., 2010). The Plush Ranch basin was likely bounded on the northwest by antithetic faults (Cole and Stanley, 1995). Proterozoic gneiss and Mesozoic granitoid along the southeastern margin of the basin were the primary source-rocks for most of the basin; the Mount Pinos granite was the dominant source of deposits along the northwestern margin of the basin, which include lenticular megabreccia beds interpreted as seismically induced rockslides (Bohannon, 1975; Yarnold, 1993; Cole and Stanley, 1995; Kellogg and Miggins, 2002; Kellogg, 2003; Hendrix et al., 2010). The Plush Ranch Formation thickens westward (Hendrix et al., 2010).

Northwest of Plush Ranch basin, on the opposite side of Mount Pinos (including exposures of Pelona Schist) are Oligocene-Miocene strata generally mapped as Simmler Formation (e.g., Kellogg and Miggins, 2002; Dibblee, 2005a, b, 2006b; Fig. 1), but considered equivalent to the Plush Ranch Formation (personal communications of Hill and Dibblee in Carman, 1964). These Plush Ranch/Simmler strata are alluvial deposits, which coarsen upward, from mostly sandstone at the base to coarse conglomerate at the top (Dibblee, 2005a, b).

Basalt interbedded with lacustrine strata near the center of Plush Ranch basin (e.g., Hendrix et al., 2010) has yielded seven whole-rock K-Ar ages, ranging from 26.5 ± 0.5 Ma to 20.4 ± 0.9 Ma (Frizzell and Weigand, 1993), and plagioclase K-Ar ages of 17.9 ± 3.8 Ma and 20.1 ± 1.1 Ma (Crowell, 1973; recalculated after Dalrymple, 1979). These beds have a maximum thickness of ~200 m, and thin to the west (Carman, 1964; Hendrix et al., 2010). The basalt contains numerous fractures filled by calcite; in an especially prominent fracture, it is described as “very fine-grained tan calcite” (Carman, 1954, p. 70).

The Plush Ranch Formation, including Plush Ranch/Simmler strata, lie north of the northern boundary of the WTR block, and consequently have not undergone significant vertical-axis rotation (Onderdonk, 2005; Onderdonk et al., 2005).

Vasquez Formation The nonmarine Vasquez Formation of the Soledad region (Sharp, 1935; Jahns and Muehlberger, 1954; Muehlberger, 1958) consists primarily of alluvial sandstone and conglomerate (Hendrix and Ingersoll, 1987). Vasquez strata were deposited in three subparallel, ~northeast-southwest-trending (present orientations; vertical-axis rotation not restored) subbasins; from southeast to northwest, these are the Vasquez Rocks, Texas Canyon and Charlie Canyon subbasins (Jahns and Muehlberger, 1954; Muehlberger, 1958; Hendrix and Ingersoll, 1987; Fig. 1). The Vasquez Rocks and Texas Canyon subbasins are interpreted to have been physically and depositionally separate until integration of the two during deposition of the upper Vasquez Formation, but kinematically linked throughout their history (Bohannon, 1976; Hendrix and Ingersoll, 1987; Hendrix, 1993; Hendrix et al., 2010). These two subbasins constitute Soledad basin; the Charlie Canyon subbasin is included by some (e.g., Jahns and Muehlberger, 1954), but is sedimentologically distinct (Hendrix and Ingersoll, 1987). The Charlie Canyon subbasin lies immediately northwest of Sierra Pelona, and the Texas Canyon subbasin immediately southeast. The largest of the three, Vasquez Rocks subbasin, is the only one in which interbedded volcanics are preserved (Hendrix and Ingersoll, 1987).

The total stratigraphic thickness of the Vasquez Formation in the Vasquez Rocks and Texas Canyon subbasins is 5500 m and 4000 m, respectively (Hendrix and Ingersoll, 1987). The base of the Vasquez Formation in the Texas Canyon subbasin is truncated by the high-angle Pelona fault (e.g., Hendrix and Ingersoll, 1987; Hendrix, 1993). It is possible that the Texas

Canyon subbasin originally contained interbedded volcanics, but that they were part of the basal section removed by faulting (Hendrix, 1993; Hendrix et al., 2010).

The total stratigraphic thickness of the Vasquez Formation in the Charlie Canyon subbasin is 2300-2400 m (Sams, 1964; Hendrix and Ingersoll, 1987). Approximately 800 m of braided-fluvial deposits are overlain by ~1600 m of alluvial deposits that coarsen upward, from medium to coarse sandstone at the base to coarse conglomerate near the top (Sams, 1964; Hendrix and Ingersoll, 1987). At the top of the sequence is a granitoid rock-avalanche breccia (Sams, 1964; Weber, 1994; Dibblee, 1997a). Granitoid clasts in the upper part of the sequence, including in the rock-avalanche breccia, are dominantly "very coarse-grained quartz diorites" (Sams, 1964, p. 33), whereas basement granitoid immediately to the south (present direction; vertical-axis rotation not restored) is medium-grained, leucocratic quartz monzonite (Sams, 1964). Sams (1964) suggested that this quartz diorite was eroded from the ancestral Sierra Pelona, before the Pelona Schist had been exhumed (e.g., Hendrix and Ingersoll, 1987).

The interbedded volcanics of the Vasquez Rocks subbasin are primarily basaltic andesite, transitioning to dacite toward the eastern edge of the subbasin; some rhyodacitic to rhyolitic volcanics are also present (Hendrix and Ingersoll, 1987; Frizzell and Weigand, 1993). These volcanics have yielded nine whole-rock K-Ar ages, ranging from 37.5 ± 1.0 Ma to 14.7 ± 0.4 Ma, with preferred eruption ages between 25.6 and 23.1 Ma (Frizzell and Weigand, 1993) which are broadly supported by plagioclase K-Ar ages of 25.6 ± 2.2 Ma, 24.5 ± 0.8 Ma, 21.4 ± 0.8 Ma and 20.7 ± 0.8 Ma (Crowell, 1973; Spittler, 1974; Woodburne, 1975; recalculated after Dalrymple, 1979). Together with thin lenses of conglomerate, sandstone and mudstone, these volcanics comprise a volcanic-dominated interval near the base of the Vasquez Formation section (Hendrix and Ingersoll, 1987). This interval has a maximum thickness of ~1300 m near the Soledad fault, and thins uniformly to the northwest to a minimum thickness of ~400 m (Hendrix and Ingersoll, 1987). Immediately atop some of the volcanic horizons are deposits interpreted as lacustrine by Hendrix and Ingersoll (1987), including thin-bedded limestone. Volcanic-induced ponding of drainages may have created lacustrine environments (Hendrix and Ingersoll, 1987). Paleomagnetic data from Vasquez Formation volcanics indicate ~37° of net clockwise rotation; together with the ~16° of counterclockwise rotation recorded by the younger Mint Canyon Formation, this suggests a total clockwise rotation of ~53° in the Soledad region since deposition of the Vasquez Formation (Terres and Luyendyk, 1985; Hornafius, 1986; Dickinson, 1996; Fig. 5).

Weldon et al. (1993) speculated that some of the Vincent Gap region strata mapped as Vasquez Formation in this study might be equivalent to the type Vasquez Formation of the Soledad region. They suggested that these strata comprise one of several fault-bounded slivers of units juxtaposed by splays of the Punchbowl fault prior to deposition of the Punchbowl Formation. In contrast, Noble (1953, 1954), Dibblee (2002d) and the present study indicate that these strata and the Punchbowl Formation were both deposited northeast of the Punchbowl fault, and that movement along the Punchbowl fault postdates deposition of the Punchbowl Formation (e.g., Powell, 1993).

Diligencia Formation The Diligencia Formation of the Orocopia region (Crowell, 1975b) consists of ~1500-2000 m of nonmarine conglomerate, sandstone, siltstone and limestone of alluvial, fluvial and lacustrine origin, together with interbedded volcanics and shallow intrusives that have been classified as basalt and andesite, respectively (Spittler and Arthur, 1982; Frizzell and Weigand, 1993; Law et al., 2001; Ingersoll et al., 2014). Diligencia basin formed as a complex half-graben, controlled by both the Diligencia fault along its northeastern margin (northwestern margin prior to vertical-axis rotation) and the Orocopia detachment-fault system along its southwestern margin (southeastern margin prior to vertical-axis rotation; Robinson and Frost, 1996; Ingersoll et al., 2014). The Diligencia Formation was primarily derived from granitoid along its northern margin and Proterozoic basement along its southern margin (Spittler and Arthur, 1982; Ingersoll et al., 2014). Along part of its northern margin, the Diligencia Formation overlies the Maniobra Formation in angular unconformity (e.g., Crowell and Susuki, 1959; Advocate et al., 1988; Ingersoll et al., 2014). Basal strata are thickest along the northeastern fault-controlled margin of the basin (Ingersoll et al., 2014). A vertebrate fossil fragment from the Diligencia Formation most likely corresponds to the late Arikareean North American Land Mammal Ages (NALMA) stage (~23-20 Ma; Woodburne and Whistler, 1973).

Interbedded volcanics are basalt flows, cross-cut by younger, shallow-intrusive andesitic sills and dikes (Spittler and Arthur, 1982). The maximum thickness of the interbedded volcanics is 160 m, in the southeastern Diligencia basin (Spittler and Arthur, 1982). Spittler and Arthur (1982) suggested that these volcanics and shallow intrusives were fed by magma conduits in the southeastern and central parts of the basin. The volcanics have yielded six whole-rock K-Ar ages, ranging from 23.6 ± 0.5 Ma to 21.3 ± 0.6 Ma (Frizzell and Weigand, 1993), and plagioclase K-Ar ages of 23.0 ± 3.0 Ma, 20.6 ± 9.1 Ma and 19.1 ± 2.0 Ma (Crowell, 1973; Spittler, 1974; recalculated after Dalrymple, 1979). Nonmarine limestone and other lacustrine deposits are interbedded with, and overlie, the volcanics (Spittler, 1974; Spittler and Arthur, 1982). Paleomagnetic data from these volcanics indicate that the Diligencia Formation has undergone ~90-100° of clockwise vertical-axis rotation since deposition, ~41° of which likely occurred together with the surrounding eastern Transverse Ranges since the late Miocene (Carter et al., 1987).

Relationships of Oligocene-Miocene formations The Texas Canyon subbasin is interpreted to be the part of Soledad basin most closely correlated with Plush Ranch basin, as the spatial and structural relationships between the Oligocene-Miocene strata and surrounding units in the two areas match closely; they may even represent parts of originally connected basins (Bohannon, 1975; Hendrix et al., 2010; Ingersoll et al., 2014). Diligencia basin has been interpreted as most closely correlated with the Charlie Canyon subbasin of the Soledad region, as both lie northwest (original orientations prior to vertical-axis rotations) of anticlinoria of PORC schists (Bohannon, 1975; Hendrix et al., 2010; Ingersoll et al., 2014). The Charlie Canyon subbasin has similarly been correlated with the Simmler/Plush Ranch Formation strata north of Mount Pinos in the Tejon region (Bohannon, 1975).

Volcanic strata of the Tejon and Soledad regions are similar in age and major- and trace-element composition (Frizzell and Weigand, 1993; Cole and Basu, 1995). Approximately 20 km east of the Vasquez Rocks subbasin are exposures of rhyodacitic, dacitic and basaltic-andesitic flows, volcanic necks and domes, dikes and tuffaceous breccia (Buesch and Ehlig, 1982; Weigand, 1982; Hendrix et al., 2010). These flows lack interbedded sedimentary strata, and so were likely deposited on the margins of a topographically raised volcanic center (Hendrix et al., 2010). This volcanic source is likely the source of the interbedded volcanics of the Soledad region, and possibly the source of those of the Tejon region; this would explain the westward-thinning of the volcanics in these regions and the increasing average silica content eastward in the Soledad region.

Volcanic strata of the Orocopia region have the same distinct trace-element signatures as those of the Tejon and Soledad regions, and are broadly contemporaneous, indicating that they are from the same volcanic system (Frizzell and Weigand, 1993). Because the volcanics of the

Orocopia region are likely somewhat younger (Frizzell and Weigand, 1993), thin westward, and likely reached the surface via conduits in the central and southeastern parts of the basin (Spittler and Arthur, 1982), they are presumably derived from a volcanic center distinct from that east of the Soledad region, and less closely related to the volcanics of the Tejon and Soledad regions than those volcanics are to one another.

Middle Miocene: Tick Canyon/Paradise Springs Formations

Tick Canyon Formation The Tick Canyon Formation (Jahns, 1939, 1940) of the Soledad region consists of ~200-300 m of nonmarine conglomerate, sandstone, siltstone and claystone of alluvial, fluvial and lacustrine origin (Jahns, 1940; Woodburne, 1975). It is separated from the underlying Vasquez Formation by a low-angle angular unconformity (e.g., Jahns and Muehlberger, 1954). The Tick Canyon Formation thins significantly to the north-northwest (Muehlberger, 1958), and no equivalent unit has been identified in the Tejon or Orocopia regions (e.g., Carman, 1964; Woodburne, 1975; Ingersoll et al., 2014). Deposition was likely confined to an east-west-trending paleochannel incised into underlying Vasquez Formation (Hendrix et al., 2010). As discussed above, the Tick Canyon Formation contains an unroofing sequence, with clasts of Pelona Schist in upper strata (Ehlert, 1982, 2003; Hendrix, 1993). The Tick Canyon Formation also contains abundant volcanic clasts, most of which resemble volcanics of the Vasquez Formation (Hendrix, 1993; Hendrix et al., 2010). The Tick Canyon Formation contains vertebrate fossils originally interpreted as corresponding to the late Arikareean NALMA stage (~23-20 Ma; e.g., Woodburne, 1975), but subsequently determined to have a stratigraphic range that may extend into the early Hemingfordian NALMA stage (≥19 or 18 Ma; Lander, 1985).

The Tick Canyon Formation was originally considered part of the overlying Mint Canyon Formation (Kew, 1923, 1924) because there is no significant angular discordance between the two (e.g., Ehlert, 1982, 2003). The Tick Canyon Formation was distinguished by Jahns (1939, 1940) because of an apparent time gap between the fossils discussed above and those of the overlying Mint Canyon Formation, discussed below; the proposed disconformity has been mapped at different stratigraphic levels by different geologists (Ehlert, 2003). The revised stratigraphic range of the fossils within the Tick Canyon Formation permits a conformable relationship between the two formations, and Ehlert (1982, 2003) considers the Tick Canyon Formation to be basal Mint Canyon Formation based on apparent petrologic, lithologic and structural continuity across the two stratigraphic levels commonly cited as the disconformity. In this study, the strata in question are referred to as the Tick Canyon Formation because it is a convenient way to distinguish these aerially restricted, primarily locally derived strata from the more extensive and partly distantly derived overlying strata, and because it maintains consistency with maps and literature that consider the Tick Canyon Formation separately (e.g., Dibblee, 1996a, b; Hendrix et al., 2010). A disconformity between the Tick Canyon and Mint Canyon formations is not implied by this usage.

The Charlie Canyon subbasin of the Soledad region contains a Pelona Schist-bearing, poorly sorted alluvial breccia, stratigraphically above the Vasquez Formation but below the Mint Canyon Formation (e.g., Sams, 1964; Weber, 1994; Dibblee, 1997a). Dibblee (1997a) considered this breccia basal Mint Canyon Formation, but Sams (1964) and Weber (1994) referred to it as a separate formation, part of the San Francisquito Canyon breccia and the Powerhouse breccia-conglomerate, respectively. Sams (1964) noted the similarity in stratigraphic position with the Tick Canyon Formation of Soledad basin, but considered the two formations uncorrelated based on lithologic differences. Weber (1994) suspected that these strata were at least partly deposited in pre-existing canyons; such deposition would be comparable to that of the Tick Canyon Formation. In this study, these strata are referred to as part of the Tick Canyon Formation.

Paradise Springs formation Strata of the Vincent Gap region mapped in this study as the Paradise Springs and Vasquez formations (Plate 1) were described by Noble (1954) as a basal megabreccia of the Punchbowl Formation composed of clasts derived from the San Francisquito Formation. These strata contain fossils corresponding to the Clarendonian NALMA stage (~13.6-10.3 Ma; Tedford and Downs, 1965; Woodburne and Golz, 1972). Woodburne (1975) suggested that an unconformity might exist between these strata and the Punchbowl Formation proper. Dibblee (2002a, c, d) mapped these strata as Punchbowl Formation, grouping some of them together with the Punchbowl Formation proper (as map units "Tpc" and "Tps"), and others with the strata mapped in this study as Vasquez Formation (as map unit "Tprc"). Weldon et al. (1993), who interpreted the Punchbowl fault to have originated prior to deposition of the Punchbowl Formation, interpreted these strata as a coarse, fault-related breccia because of their present exposure as a thin sliver along the Punchbowl fault.

Unnamed shale of Peanut Hill The Tejon region contains areally restricted outcrops of shale with minor interbedded sandstone adjacent to outcrops of the Plush Ranch and Caliente formations (e.g., Kellogg, 2003; Dibblee, 2006a). Dibblee (2006a) interpreted these strata as lacustrine, Kellogg (2003) as marine. The age of these strata is poorly constrained, but Dibblee (2006a), who mapped them as "unnamed shale of 'Peanut Hill,'" tentatively suggested a stratigraphic position above the Plush Ranch Formation (mapped as Simmler Formation in Dibblee, 2006a) but below the Caliente Formation. If true, this would mean that these strata are approximately contemporaneous with the Tick Canyon and Paradise Springs formations. The lack of lithologic similarity of these strata to the Tick Canyon and Paradise Springs formations does not prevent their chronologic correlation; because rapid, transrotational uplift of the Pelona Schist did not occur in the Tejon region, proximal, coarse-grained schist-bearing deposits like those of the Tick Canyon Formation would not be expected to have formed there.

Middle-Upper Miocene: Caliente/Mint Canyon/Punchbowl Formations

Caliente Formation The Caliente Formation of the Tejon region (named by T. W. Dibblee, Jr. in Stock, 1947; Schwade, 1954) consists of nonmarine conglomerate, sandstone and mudstone, and minor tuffaceous and limestone beds, and is of fluvial and lacustrine origin (Ehlert, 2003). It overlies the Plush Ranch Formation in angular unconformity (e.g., Woodburne, 1975). The exposed thickness of the Caliente Formation is >610 m; its total thickness is unknown, though well data may suggest ~640 m (Carman, 1964; Ehlert, 2003). The Caliente Formation is aerially extensive, exposed over a distance of ~80 km (Ehlert, 2003). To the west, it grades into the marine Branch Canyon Formation (Hill et al., 1958). Based on fossil evidence from several prior studies, Woodburne (1975) assigned the Caliente Formation to the upper Arikareean through Hemphillian NALMA stages (~23-6 Ma). Caliente Formation sandstone exhibits moderate compositional variability (Hoyt, 2012).

Mint Canyon Formation The Mint Canyon Formation of the Soledad region (Kew, 1923, 1924) consists primarily of nonmarine conglomerate, sandstone and mudstone of fluvial, alluvial and lacustrine origin (Ehlert, 2003). It overlies the Vasquez Formation in angular unconformity (e.g., Jahns, 1940; Oakeshott, 1958; relation to the Tick Canyon Formation discussed above). Estimates of the maximum exposed thickness of the Mint Canyon Formation range from ~1230 m (Jahns, 1940) to ~1800 m (Ehlert, 2003), depending on the location measured and whether or not the Tick Canyon Formation is considered separately; when combined with well data reported by Winterer and Durham (1962), this suggests a total thickness >3800 m (Ehlert, 2003). Stirton

(1933) correlated vertebrate fossils in the Mint Canyon Formation with the Clarendonian NALMA stage (~14-10 Ma). Zircon from tuff beds in the upper Mint Canyon Formation yielded fission-track dates of 11.6 ± 1.2 Ma and 10.1 ± 0.8 Ma (Terres and Luyendyk, 1985). Mint Canyon Formation sandstone, in contrast with that of the Caliente Formation, exhibits substantial compositional variability (Hoyt, 2012).

Relationship of Caliente and Mint Canyon formations The Caliente and Mint Canyon formations have been correlated by Ehlig and Ehlert (1972), Ehlert (1982, 2003) and Hoyt (2012) using sandstone and conglomerate composition, paleocurrents, detrital-zircon ages and palinspastic reconstructions. Clasts of distinct rapakivi-textured quartz-latite porphyry, derived from a volcanic terrane in the northern Chocolate Mountains, are present in the Mint Canyon and Caliente formations (Ehlig and Ehlert, 1972; Joseph and Davis, 1977; Ehlert, 1982, 2003). Correlation of this Chocolate Mountains source with the Mint Canyon and Caliente formations has been used to refine the palinspastic reconstructions discussed above. Ehlert (2003) suggested that a Mint Canyon/Caliente drainage system flowed from the Chocolate Mountains in an alluvial wash consisting of the Salton Creek Trough northeast of the San Andreas fault and the Soledad basin southwest of the San Andreas fault. Prior to deposition of the Mint Canyon Formation, the ancestral Sierra Pelona was already a topographic high (Hendrix and Ingersoll, 1987), and would have bounded this drainage system to the northwest and supplied it with Pelona Schist detritus (Ehlert, 2003).

Punchbowl Formation The Punchbowl Formation (Noble, 1953, 1954) of the Vincent Gap region consists of ~1500 m of nonmarine conglomerate, sandstone and minor mudstone of dominantly fluvial origin (Dibblee, 1987). It contains fossils corresponding to the Hemphillian NALMA stage (~10-4 Ma), although no fossils have been dated from the uppermost beds of the

Punchbowl Formation (Woodburne, 1975). The basal Punchbowl Formation (map unit Npb in Plates 1, 2) yielded a horse fossil corresponding to the late Barstovian or early Clarendonian NALMA stages (~14-12 Ma; personal communications of Allen and Whistler in Liu, 1990). Using magnetostratigraphy, Liu (1990) constrained the age of the basal Punchbowl Formation to between 12.7 and 12.3 Ma, and dated the uppermost beds as ~8.5 Ma. Cross-bedding within the Punchbowl Formation implies a generally southwestward transport direction (present direction; vertical-axis rotation not restored; Dibblee, 1987), or a generally westward transport direction after correcting for the 27.5 ± 4.3° of counterclockwise rotation measured by Liu (1990).

Prior to work by Ingersoll and Colasanti (2004), Colasanti and Ingersoll (2006) and this study, the Punchbowl Formation was not known to overly older Miocene deposits. Consequently, the Punchbowl Formation has commonly been considered distinct from and largely younger than Miocene strata of the Soledad region (e.g., Woodburne, 1975). Correlation with the Mint Canyon Formation of the Soledad region has been proposed by various studies (e.g., Dibblee, 1967; Liu, 1990) and considered by others (e.g., Woodburne, 1975). Woodburne (1975) suggested that the drainage system represented by the Punchbowl Formation may be correlated with the marine Pico Formation to the west, and that Soledad basin southeast of Sierra Pelona was likely the route of this drainage system. Woodburne (1975) also mentioned the Caliente and Anaverde formations as possible correlatives of the Punchbowl Formation. Dibblee (1987) suggested that the Punchbowl Formation formed within what was originally part of Soledad basin. Dibblee (1987) noted that the Mint Canyon Formation contains similar fossils, but did not explicitly suggest a correlation between the two formations. Matti and Morton (1993) suggested that the Punchbowl Formation represents accumulation of relatively proximal deposits in an intermontane basin between the Soledad region and the Little San Bernardino Mountains, with its volcanic clasts derived from the Vasquez Formation volcanics of the Soledad region. Weldon et al. (1993) interpreted the Punchbowl Formation as representing infilling of a narrow, fault-controlled pull-apart basin formed along a hypothesized transpressional “San Gabriel transform system” that included the Punchbowl fault. This hypothesis is incompatible with the widely accepted tectonic history of southern California outlined above, and is not considered further.

The Cajon Valley formation, located northeast of the San Andreas fault near Cajon Pass, which separates the San Gabriel and San Bernardino Mountains, was originally referred to as the Punchbowl Formation based on spurious correlation with the type Punchbowl Formation of the Vincent Gap region (Noble, 1953, 1954). It has subsequently been shown to be distinct from the type Punchbowl Formation in age, lithology, and palinspastic position (Tedford and Downs, 1965; Woodburne and Golz, 1972; Liu, 1990; Stang, 2013), and consequently is not considered further. A detailed analysis of the provenance and possible offset equivalents of the Cajon Valley Formation is given by Stang (2013). A second spurious correlation with the Punchbowl Formation is that of the “western facies of the Punchbowl Formation” (Noble, 1953, 1954), lithologically similar strata found northeast of the San Andreas fault, northwest of the Punchbowl Formation between the San Andreas and Punchbowl faults, and southwest of the Punchbowl fault. These strata are substantially younger than and lithologically distinct from the type Punchbowl Formation (Woodburne, 1975). They have subsequently been renamed, and should not be confused or associated with the type Punchbowl Formation discussed in this study.

Upper Miocene Castaic Formation

The Castaic Formation of the Soledad region (Crowell, 1954) consists of ≥2100 m of shallow-marine shale, sandstone and minor conglomerate (Crowell, 1954; Ehlert, 1982). The

Castaic Formation is generally younger than the underlying Mint Canyon Formation, but fossils corresponding to the Mohnian Pacific Coast Benthonic Foraminiferal Age stage (13.5-7.5 Ma) in the Castaic Formation indicate that there is no significant age gap between the two (Woodburne, 1975). The two formations are in some places in angular unconformity and in others apparently conformable (Ehlert, 2003). The Castaic Formation is overlain by the marine, upper Miocene-lower Pliocene Pico Formation (e.g., Woodburne, 1975).

METHODS

Geologic Mapping

The geology of the study area, including faults and depositional contacts, bedding orientations and structural data, was mapped between 2012 August and 2014 July. Mapping was conducted on foot using USGS 7.5' quadrangles printed at 200% magnification and a Brunton Pocket Transit. A Garmin eTrex 20 handheld GPS was used to record locations of sampling, paleocurrent measurement and conglomerate-composition determination; locations outside the mapped study area and the location of sample JFH-11-28P were recorded using a Garmin eTrex Vista handheld GPS; all locations are given in Appendix A. Field maps were scanned, then digitized using Adobe Illustrator CS5, using a composite of four USGS US Topo digital topographic maps as the basemap. The resulting map includes only the southeastern part of Punchbowl Formation outcrop in the Devil's Punchbowl, as this area has already been mapped in detail (e.g., Noble, 1954; Dibblee, 2002a).

Paleocurrent Data

Paleocurrent directions were determined for several locations throughout the study area (Plate 2), at the same location as conglomerate-composition measurements. These determinations were made using imbricated cobbles within conglomeratic beds. At each location, orientations of planes of maximum cross-sectional area were measured for ten separate imbricated cobbles within a single conglomeratic bed. The bedding orientation was also measured, and used to restore imbrication measurements to their original horizontal-stratal orientations. The up-dip direction of each set of ten imbrications was averaged using circular-statistical methods (Prothero and Schwab, 2003) to give the approximate paleocurrent direction at each site. Bedding restoration was accomplished using STEREONET 9 (Allmendinger et al., 2012; Cardozo and Allmendinger, 2013).

Conglomerate Composition

Conglomerate composition was determined at locations across the study area (Plate 2). A flexible grid was affixed to conglomeratic beds and the lithology of the cobble at each crosshair determined until 100 counts were reached; grid spacing was varied between locations such that it always exceeded the average cobble size. Conglomerate composition was determined in the same manner in the Charlie Canyon subbasin of the Soledad region (Fig. 6). Cobble categories are given in Table 1.

Sandstone Composition

Collection and Preparation

Sandstone samples were collected throughout the study area in the Vincent Gap region (Plate 2); one sample was collected east of the Soledad region. Where possible, coarse sandstone was collected for ease of petrographic analysis. Most samples were taken directly from outcrop; some were gathered as loose clasts where true outcrops were not present. All samples were impregnated with epoxy, cut perpendicular to bedding where known, and mounted as standard 30-µm-thick, 27-mm-by-46-mm thin sections by Ram Alkaly of R.A. Petrographic Thin Sections. These thin sections, initially left without cover slides, were etched with concentrated hydrofluoric acid (HF) and stained with a saturated solution of sodium hexanitrocobaltate(III) ($Na_3Co(NO_2)_6$). Etching and staining distinguishes quartz (unetched; unstained), potassium feldspar (stained with yellow dots) and plagioclase feldspar (heavily etched; Gabriel and Cox, 1929; Reeder and McAllister, 1957; Ingersoll and Cavazza, 1991). The etched and stained thin sections were washed, dried and returned to Ram Alkaly for application of cover slips.

Petrography

Sandstone composition was determined by point counting thin sections using the Gazzi-Dickinson method (Gazzi, 1966; Dickinson, 1970; Ingersoll et al., 1984), in which each single crystal with a long axis greater than the silt/sand cutoff of 0.0625 mm is counted as that mineral, even if part of a larger, polycrystalline rock fragment. Point counts were performed using an Olympus BH-2 petrographic microscope fitted with a James Swift and Son Ltd. automatic point counter connected to a Prior model G electronic counter, with a grid spacing greater than the average grain size. Grain categories are defined in Table 2. Points counts were also performed on samples collected and prepared by others in the same manner; details are given in Table 3.

Table 4 contains unpublished point-count data from 13 thin sections from the Vasquez, Paradise Springs and basal Punchbowl formations of the Vincent Gap region collected and prepared in the same manner as in this study by Clinton Colasanti and Raymond V. Ingersoll in 2004 and point-counted by Raymond V. Ingersoll in 2004 using the same method and similar grain categories.

Detrital-Zircon Analysis (LA MC-ICPMS)

Collection and Preparation

Ten >1-kg sandstone samples were collected in the Vincent Gap region for detrital-zircon analysis, most of them at locations where sandstone was sampled and conglomerate composition determined. Three additional samples were collected east of the Soledad region, where conglomerate is not present; sandstone composition was only quantitatively determined for one of these samples because the other two were clearly first-order volcaniclastic (classification scheme of Ingersoll, 1990). Friable sandstone was preferentially sampled. Where such sandstone was absent, disaggregated sandstone was collected if clearly derived from immediately adjacent sandstone. Where possible, sandstone free of cobbles was sampled. Samples containing cobbles were disaggregated and sieved, and the >2-mm fraction was discarded prior to crushing.

Samples were sequentially crushed with a sledgehammer, a jaw-crusher, a disc-mill and a shatterbox (with some samples skipping the first one or two steps), then sieved with a sieve shaker, and the >250 μm and <63 μm fractions discarded. An initial density separation was then performed using a Mineral Technologies MD Gemini shaking table at Pomona College, eliminating >90% of material (part of sample KTC-14-dz1 was instead density separated using tetrabromoethane, $\rho = 2.97$ g/cm^3). Strongly and weakly magnetic minerals were removed from the remaining dense fractions using a neodymium hand magnet and a model L-1 Frantz Isodynamic magnetic separator, respectively (for sample KTC-12-Tps1, weakly magnetic minerals were removed by the Arizona LaserChron Center using a model LB-1 Frantz Magnetic Barrier laboratory separator). Remaining non-magnetic fractions underwent a final density separation in methylene iodide ($\rho = 3.32$ g/cm^3), with the exception of sample KTC-12-Tps1, which underwent this separation prior to removal of weak magnetic minerals. The resulting dense fractions were between 70% and 100% zircon, with the exception of sample KTC-12-Ttc2, which achieved this purity after being shaken in a Wig-L-Bug electric mixer with acrylic spheres to mechanically remove barite grains (this separation was performed by the Arizona LaserChron Center). These separates were sent to the Arizona LaserChron Center at the University of

Arizona, where large splits of them were mounted, together with grains of zircon references, on 2.54-cm-diameter epoxy plugs. These mounts were sanded down to a depth of ~20 μm to expose crystal interiors, polished, imaged using a scanning-electron-microscope backscattered-electron detector, cleaned in an ultrasonic bath with a solution of 2% HNO_3 and 1% HCl, rinsed with water, then isopropyl alcohol, and dried with Kimwipes.

Analysis

Detrital zircon was dated by U-Pb methods using laser-ablation multicollector inductively coupled plasma mass spectrometry (LA MC-ICPMS) at the Arizona LaserChron Center (Gehrels et al., 2006, 2008). Spots 30 μm in diameter and ~15 μm in depth were ablated using a Photon Machines Analyte G2 excimer laser. The ablated material was carried in helium into the plasma source of a Nu HR ICPMS, which is equipped with a flight tube that is sufficiently wide to permit measuring U, Th and Pb isotopes simultaneously. All measurements were made in static mode. ^{238}U, ^{232}Th, ^{208}Pb, ^{207}Pb and ^{206}Pb were measured using Faraday detectors with $3x10^{11}$-Ω resistors, and ^{204}Pb and ^{202}Hg were measured using discrete dynode ion counters. Ion yields were ~0.8 mV/ppm. Each analysis consisted of one 15-s integration on the peaks with the laser off (to determine background levels) and 15 1-s integrations with the laser firing, followed by a 30-s delay to purge the material from the previous analysis and prepare for the next.

Individual spot analyses have an ~0.5-1% measurement error as a result of errors in determining ^{206}Pb/^{238}U and ^{206}Pb/^{204}Pb. Errors in determining ^{207}Pb/^{206}Pb and ^{206}Pb/^{204}Pb cause a similar ~0.5-1% measurement error for zircon >1.0 Ga, and substantially more error in <1.0 Ga zircon because of the comparatively low radiogenic ^{207}Pb abundances. As a result, for most analyses, the ^{206}Pb/^{238}U age is more precise for ages younger than ~1.0 Ga, whereas the ^{207}Pb/^{206}Pb age is more precise for ages older than ~1.0 Ga.

To correct for interference that ^{204}Hg causes with the ^{204}Pb measurement, the intensity of ^{202}Hg was measured, divided by the natural $^{202}Hg/^{204}Hg$ ratio of 4.35, and subtracted from the measured intensity at mass 204 to give the ^{204}Pb intensity. This correction is generally insignificant, as most analyses have low Hg backgrounds (~150 counts/s at mass 204).

To correct for the common (i.e., non-radiogenic) Pb originally present in the zircon, the intensities of common ^{206}Pb and ^{207}Pb were calculated using the Hg-corrected ^{204}Pb intensity and the initial Pb composition from Stacey and Kramers (1975), then subtracted from the measured ^{206}Pb and ^{207}Pb intensities, respectively. Uncertainties of 1.5 and 0.3 (absolute) were applied to the $^{206}Pb/^{204}Pb$ and $^{207}Pb/^{204}Pb$ compositional values, respectively, to account for the variation in Pb isotopic composition of detrital zircon.

Fractionation of Pb/U (generally ~5%) and of the Pb isotopes (generally <0.2%) during analysis was rectified using the instrumental fractionation determined on large crystals of zircon reference Sri Lanka (563.5 ± 1.6 Ma; Gehrels et al., 2008), which were analyzed periodically during sample measurements under the same analytical conditions. The resulting uncertainty from this correction is generally ≤1% for both the $^{207}Pb/^{206}Pb$ and $^{206}Pb/^{238}U$ ages. Instrumental fractionation of U and Th was corrected using zircon standard Sri Lanka, which contains ~518 ppm U and ~68 ppm Th. The accuracy of final ages was verified using zircon reference R33 (419.3 ± 0.4 Ma; Black et al., 2004). Analytical data are reported in Appendix B.

Igneous-Zircon Analysis (SIMS)

Collection and Preparation

Four >1-kg igneous samples were collected in the Vincent Gap region: sample KTC-14-gr-big was a large, loose clast of granitoid collected immediately adjacent to outcrop; sample KTC-14-gd7 was collected directly from an outcrop of hypabyssal-intrusive rock; sample KTC-

13-and3 was a single, large, loose clast of rhyolite collected within a region of poorly exposed sandstone and conglomerate; sample KTC-14-and4 consisted of ~10 smaller clasts of rhyolite, clearly of a single lithology, chiseled out of an ~4 m-by-4 m region of a single conglomerate outcrop. These samples were crushed, partly by hand with a sledgehammer followed by a steel piston, and partly in the same manner as the sandstone samples described above. They were then sieved and separated by density and magnetic properties in the same manner as the sandstone samples. Zircon was hand-picked from the resulting separates under a binocular microscope at 45x magnification and mounted, together with grains of zircon reference AS3, in a 2.54-cm-diameter epoxy mount. This mount was polished, and cleaned in an ultrasonic bath with dilute hydrochloric acid, followed by distilled water, followed by methanol. The mount was dried and coated with ~20-30 nm of gold using a Hummer IV sputter coater.

Analysis

Igneous zircon was dated by U-Pb methods using the CAMECA ims1270 at UCLA, using the protocols described by Schmitt et al. (2003). An ~12-13-nA O^- primary ion beam was used, with the mass spectrometer tuned to a mass resolution of ~5000 (width at 10% peak height), and ~$2x10^{-3}$ Pa of O_2 pressure in the sample chamber to enhance Pb ionization. U/Pb and Th/U relative sensitivities were determined using grains of zircon reference AS3 (1099 Ma; Paces and Miller, 1993), which were analyzed intermittently throughout sample analysis, and applying a UO^+/U^+ vs. $^{206}Pb^+/U^+$ calibration similar to that of Compston et al. (1984). Concentrations of common (i.e., non-radiogenic) ^{206}Pb and ^{207}Pb were calculated by multiplying the measured intensity of ^{204}Pb by 18.86 and 15.62, respectively (anthropogenic common $^{206}Pb/^{204}Pb$ and $^{207}Pb/^{204}Pb$, respectively, for southern California; Sañudo-Wilhelmy and Flegal, 1994). These conrresponding counts were subtracted from measured ^{206}Pb and ^{207}Pb intensities, respectively, to give radiogenic ^{206}Pb and ^{207}Pb. U concentrations were estimated from $U^+/^{94}Zr_2O^+$ ratios by comparing unknowns to measured $U^+/^{94}Zr_2O^+$ in zircon reference 91500 (81.2 ppm U; Wiedenbeck et al., 1995). Details on the calibration data (number of standards, external reproducibility, and calibration parameters) are summarized in Appendix C.

Volcanic Trace-Element Analysis (XRF and ICPMS)

X-Ray Fluorescence (XRF)

Sample preparation Four samples of volcanic rock from the Vincent Gap region (the two rhyolite samples processed for igneous zircon and two volcanic samples of intermediate composition; Plate 2) and two samples of volcanic rock from the Orocopia region (one rhyolite, one intermediate) were analyzed via XRF. Sample preparation was performed by the Peter Hooper GeoAnalytical Lab at Washington State University (WSU). Fresh chips of each sample were hand-picked, and approximately 28 g of each sample was ground in a swing mill with tungsten-carbide surfaces for 120 s. Plastic mixing jars were each loaded with 3.5 g of sample powder and 7.0 g of Sprectromelt A-10 pure dilithium tetraborate ($Li_2B_4O_7$) flux. These materials were mixed for 600 s with the aid of a plastic ball added to each jar. The resulting mixtures were transferred into graphite crucibles with an internal diameter and depth of 34.9 mm and 31.8 mm, respectively, loaded into a silica tray, and heated in a 1000°C muffle furnace for 300 s, fusing them together. The resulting glass beads were reground in the swing mill for 35 s, then returned to the muffle furnace for an additional 300 s, refusing them. The glass beads recovered from this second fusion were labeled, polished with 600-grit silicon carbide, finished on a glass plate with alcohol to remove any metal from the grinding wheel, washed in an ultrasonic bath, rinsed with alcohol and wiped dry. These polished and cleaned beads were mounted, together with one bead each of internal standards BCR-P and GSP-1, for XRF analysis.

Analysis Concentrations of 10 major elements (Si, Ti, Al, Fe, Mn, Mg, Ca, Na, K and P) and 19 trace elements (Sc, V, Cr, Ni, Cu, Zn, Ga, Rb, Sr, Y, Zr, Nb, Ba, La, Ce, Nd, Pb, Th and U) were determined by the GeoAnalytical Lab at WSU using a Thermo ARL ADVANT'XP+ sequential XRF spectrometer. X-ray intensities were measured for each element using a rhodium target run at 50 kV and 50 mA at full vacuum and a 25-mm mask. Elemental concentrations were then determined by comparing these measurements with the measured intensities from two beads each of nine USGS standard samples (PCC-1, BCR-1, BIR-1, DNC-1, W-2, AGV-1, GSP-1, G-2, and STM-1), using the values recommended by Govindaraju (1994), as well as two beads of pure vein quartz to record background levels for all elements except Si. These USGS and vein-quartz standards are run on the WSU XRF instrument approximately once every three weeks or 300 samples. Internal standards BCR-P and GSP-1 were analyzed every 28 samples as a check on instrumental performance and precision. The intensities for all elements were automatically corrected for line interference and absorption effects due to other elements using the fundamental-parameter method. A thorough discussion of the methods used for XRF analysis at the GeoAnalytical Lab, including a discussion of the precision and accuracy of the XRF spectrometer and an element-by-element comparison with results from other laboratories, can be found in Johnson et al. (1999). Loss on ignition (LOI) determination of volatile content was performed at the same time.

ICPMS

Sample preparation The same four Vincent Gap region and two Orocopia region volcanic samples analyzed via XRF were analyzed via ICPMS. Sample preparation was performed by the GeoAnalytical Lab at WSU. Samples were powdered, and equal amounts (typically 2 g each) of powdered sample and Sprectromelt A-10 pure dilithium tetraborate

($Li_2B_4O_7$) flux were mixed and heated in graphite crucibles placed in a 1000°C muffle furnace for 1800 s, fusing the mixtures. The resulting glass beads were ground in a carbon-steel ring mill, and 250 mg of each re-powdered sample was weighed into 30 mL screw-top Teflon PFA vials. These samples were then dissolved, beginning with a first evaporation using 2 mL of HNO_3, 6 mL of HF, and 2 mL of $HClO_4$ per vial at 110°C. After the samples dried, they were rewetted and the sides of the containers were rinsed with >18-M deionized water. Then a second evaporation was performed, using 2 mL of $HClO_4$ per vial at 160°C. The remaining material was completely dissolved, forming clear solutions, by the addition to each vial of ~10 mL of >18-M deionized water, 3 mL of HNO_3, 5 drops H_2O_2 and 2 drops of HF, with a hot plate used to heat the samples. These solutions were then transferred to 60-mL HDPE bottles, and >18-M deionized water was added until each solution obtained a mass of 60 g.

Analysis Concentrations of 27 trace elements (14 rare-earth elements and Sc, Rb, Sr, Y, Zr, Nb, Cs, Ba, Hf, Ta, Pb, Th and U) were determined by the GeoAnalytical Lab at WSU using an Agilent 7700 ICP quadrupole mass spectrometer equipped with a Cetac ASX-510 auto-sampler housed in a HEPA-filtered enclosure, nickel sampling and skimmer cones, integrated peristaltic pumps and an all-Teflon PFA nebulizer with a Scott-type quartz spray chamber maintained at 2°C. The plasma is typically operated at 1250 W, and typical argon gas flow conditions are 0.25 L/s for the plasma gas, 0.017 L/s for the auxiliary gas, 0.013 L/s for the nebulization gas and 0.005 L/s for the make-up gas. Tuning parameters are software controlled. Each sample was diluted an additional 10x at the time of analysis using the Agilent’s Integrated Sample Introduction System (ISIS), yielding a final dilution factor of 1:4800. A positive-ion beam is extracted from the expanding jet of sample as it enters the vacuum region, focused, offset by 1 cm to remove photons and residual neutrally charged particles, and refocused into a quadrupole mass filter. The electron multiplier detects particles by pulse counting when the beam intensity is <3.0 MHz and by current integration when the beam intensity is >3.0 MHz.

Instrument drift was corrected using Ru, In and Re as internal standards. Internal standardization for rare-earth elements (REEs) was performed using a linear interpolation between In and Re after Doherty (1989) to compensate for mass-dependent differences in instrumental drift. Tuning was optimized to maintain a CeO/Ce ratio of less than 0.5% to minimize interference of light REE oxides with the signals of intermediate and heavy REEs. The remaining interferences were rectified using correction factors estimated using two mixed-element solutions, one containing Ba, Pr and Nd, the other containing Tb, Sm, Eu and Gd. Concentrations were standardized by comparison with analyses of duplicates of three in-house rock standards, which were interspersed within each set of 18 samples.

RESULTS

Geologic Mapping

The geologic map generated during this study is shown in Plate 1; Plate 2 shows sample locations and conglomerate composition data. The fault kinematics indicated are based primarily on geometric relationships of map units, constrained by limited fault orientation and slickenside data (Plate 1); the kinematics of the regionally significant Punchbowl fault and Vincent thrust fault zone have been well established by previous studies (e.g., Dibblee, 1967; Ehlig, 1981). The nature and exact location of many geologic units and their boundaries vary considerably from those shown on previous, less detailed maps (e.g., Dibblee 2002a, d). The boundary with Pelona Schist at the northeastern edge of Vasquez Formation exposure south of the Fenner fault, mapped as depositional by Dibblee (2002a, d), is a fault, with slickensides and a narrow zone of hydrothermal alteration; slickenlines indicate dip-slip. Interbedded volcanic strata, previously undescribed, are present within the Vasquez Formation. Immediately above the volcanic strata is thinly bedded tan limestone (too small to map). In the northwestern part of the map area, north of the Fenner fault, are previously undescribed lenses of very poorly sorted, very angular, matrix-poor megabreccias (map unit PεNvg in Plate 1) interbedded with Vasquez Formation conglomerate and sandstone. These deposits fit the definitions of "crackle breccia facies" and "jigsaw breccia facies" (Yarnold and Lombard, 1989, p. 12).

Paleocurrent Data

Calculated mean paleocurrent directions are shown in Plate 2 (raw and corrected data are given in Appendix D). They are highly variable, but tend to point obliquely away from the Fenner detachment fault, reactivated Fenner fault, and anticlinorium of Pelona Schist.

Conglomerate Composition

Conglomerate-composition data for the Vincent Gap region are shown in Plate 2 (raw count data are given in Appendix E). Clasts of Pelona Schist are only present in the upper part of the Miocene strata (the Paradise Springs and Punchbowl formations; Plate 2). Granitoid clasts dominate in the eastern part of the map area, whereas clasts of sandstone from the San Francisquito Formation dominate in much of the western map area. Trachyandesite and rhyolite make up a large percentage of clasts stratigraphically just above the interbedded trachyandesite flows; the more stable rhyolite clasts are found in low abundance throughout most of the section. The Punchbowl Formation, including its basal member, is dominated by granitoid and gneiss clasts; clasts of sandstone from the San Francisquito Formation are present, but much less abundant than in the underlying Paradise Springs and Vasquez formations.

Conglomerate-composition data for the Charlie Canyon subbasin of the Soledad region are shown in Fig. 6 (raw count data are given in Appendix E). The Vasquez Formation rock-avalanche breccia is composed entirely of granitoid clasts, as indicated by Sams (1964) and Dibblee (1997a). The breccia immediately above these rock-avalanche deposits is composed entirely of clasts of chloritic breccia. Upsection, clasts of chloritic breccia are less abundant, and clasts of Pelona Schist make up ~40% of the breccia.

Sandstone Composition

Sandstone composition is displayed on QFL, QmFkFp and LmLvLs ternaries in Figs. 7, 8 and 9 (recalculated parameters are given in Tables 3 and 4; raw point-count data are given in Appendix F). Most of the Vincent Gap Oligocene-Miocene sandstone samples show considerable compositional variation (Fig. 7); sandstone from the Punchbowl Formation, however, clusters very tightly on QFL and QmFkFp ternaries (the large spread on the LmLvLs ternary is presumably caused by the extremely low abundance of lithic grains). Sandstone from the basal Punchbowl Formation shows more variation than the overlying main member of the Punchbowl Formation, but less variation than the underlying Vasquez and Paradise Springs formations (Fig. 7). Where Vasquez Formation conglomerate is dominated by granitoid and volcanic clasts, the sandstone composition is dominated by feldspar, especially plagioclase. Where Vasquez Formation conglomerate is dominated by sandstone clasts from the San Francisquito Formation, the Vasquez Formation sandstone contains significantly more quartz and sedimentary lithics, and overlaps with the overlying Paradise Springs formation on all ternaries. This overlap is unsurprising given that clasts of Pelona Schist in the Paradise Springs formation, which was the criterion used to distinguish the formation from the underlying Vasquez Formation, have an abundance of only a few percent (Plate 2).

Sandstone from the Paradise Springs Formation of the Vincent Gap region is broadly similar to some samples from the Tick Canyon Formation of the Soledad region (Fig. 8). The

Punchbowl Formation sample from the opposite side of the Punchbowl fault and east of Soledad basin is indistinguishable from the other Punchbowl Formation samples (Fig. 9). Punchbowl Formation sandstone is similar to some Caliente Formation samples; other Caliente Formation samples resemble sandstone of the Mint Canyon Formation (Fig. 9).

Igneous-Zircon Analysis (SIMS)

Relative probability distributions of igneous-zircon ages are given in Fig. 10 (ages and raw data of individual analyses given in Appendix C; distributions generated using GenKS). Zircon from rhyolite clasts collected from Vasquez Formation conglomerate is dominantly xenocrystic (i.e., the majority of the zircon crystals are substantially older than the eruption age), and yields a signature similar to that of detrital zircon from Vasquez Formation sandstone (samples KTC-14-dz1 and dz3; Fig. 10). The youngest zircon in the granitoid is ~150 Ma; the youngest zircon in the hypabyssal intrusive is ~70 Ma. All igneous-zircon samples contain xenocrystic zircon of Proterozoic age.

Detrital-Zircon Analysis (LA MC-ICPMS)

Relative probability distributions of detrital-zircon ages are given in Fig. 10 (ages and raw data of individual analyses given in Appendix B; distributions generated using GenKS). Detrital-zircon ages for all samples from the Vincent Gap region south of the Fenner fault are predominantly ~1200 Ma and ~1700 Ma, and exhibit low, broad peaks at ~1400 Ma. All samples north of the Fenner fault lack ~1200 Ma zircon ages, and exhibit smaller peaks at ~1400 Ma and ~1700 Ma. Many samples contain peaks at ~150 Ma, and some samples contain peaks at ~220 Ma, ~75 Ma, and/or ~25 Ma.

Detrital-zircon ages from two volcaniclastic Tick Canyon Formation samples from the opposite side of the Punchbowl fault as the study area precisely date the Vasquez volcanics from which they are derived as 25.3 ± 0.1 Ma.

Volcanic Trace-Element Analysis (XRF and ICPMS)

For the XRF data, the sum of determined major- and trace-element abundances as oxides and the mass lost on ignition (LOI) is between 99.51% and 100.08% for all samples (Appendix G), and trace-element abundances determined by XRF and by ICPMS (Appendix H) are in close agreement, collectively suggesting that the results are reliable.

Major-element-oxide data classify two of the Vincent Gap region samples as rhyolite, one as trachyte and one as trachyandesite (Fig. 11), using the total-alkali-silica (TAS) classification scheme of Le Bas et al. (1986). The two Orocopia region samples were classified in the same manner as rhyolite and basaltic andesite, the latter near the border with basaltic trachyandesite. These samples likely correspond to the andesite and basalt, respectively, described by Spittler and Arthur (1982).

Two figures from Frizzell and Weigand (1993), which compare trace-element composition of volcanics from the Tejon, Soledad and Orocopia regions, were regenerated with the Orocopia- and Vincent-Gap-region data of this study and data of Cole and Basu (1995) included. In plots of Th, U and Hf vs. Ta (Fig. 12), the two intermediate Vincent Gap samples (the trachyte and trachyandesite) lie within the cluster of previous data, whereas the two rhyolite samples plot well away from the cluster in both the Th and U vs. Ta plots (Fig. 12A and B). Similarly, the basaltic-andesite sample from the Orocopia region plots within the cluster of previous data and adjacent to the other Orocopia region samples, whereas the rhyolite sample plots well away from the cluster in the Th and U vs. Ta plots, and within the cluster but away from the other Orocopia region samples in the Hf vs. Ta plot (Fig. 12C). In all three plots, the Orocopia region rhyolite plots adjacent to the Vincent Gap region rhyolites.

A similar separation of felsic and intermediate samples occurs in a chondrite-normalized plot of rare-earth-element abundances (Fig. 13). The Vincent-Gap- and Orocopia-region intermediate samples match previous data almost exactly (apparent lower levels of Dy, Ho and Er in this study's samples relative to previous data are not meaningful, as the previous data do not contain data points for these elements; apparent trends for the previous data in this region are straight lines connecting Tb and Tm abundances. Cole and Basu, 1995, did not present data points for these elements and for Gd and Tm). The Vincent Gap and Orocopia region rhyolite samples, though following a similar general trend as previous data, plot outside the cluster of previous data but adjacent to one another for nearly every element. Most noticeable in Fig. 13 are the large negative Eu anomalies exhibited by these three rhyolite samples. Interestingly, previous data show small negative Eu anomalies for Tejon and Soledad region samples, but not for Orocopia region samples.

DISCUSSION

Late Jurassic Granitoid

The granitoid, which is the main source rock for most of the Vasquez Formation in the Vincent Gap region, intruded ~150 Ma (Fig. 10), and is compositionally near the quadruple point of granite, quartz monzonite, granodiorite and quartz monzodiorite on a QAPF diagram (Streckeisen, 1974). Its zircon population is dominantly xenocrystic. The granitoid is similar to the granitoid bounding the Texas Canyon subbasin on the northwest in its relationship in outcrop with Pelona Schist and with the Vasquez Formation (Hendrix et al., 2010). The two granitoids are also similar in their abundance as clasts in the overlying Vasquez Formation in the two basins. Correlation of the Vincent Gap region granitoid with this Soledad region granitoid and, by extension, with the Mount Pinos granite (granite to quartz diorite) bounding the Plush Ranch Formation on the northwest, would seem likely, though the ~150 Ma age in the Vincent Gap region disagrees with the 75.1 ± 1.6 Ma age (Kellogg et al., 2008) of the Mount Pinos granite in the Tejon region. The Vincent Gap region granitoid is presumably broadly equivalent to the plutonics of similar age north of the Orocopia region.

Hypabyssal Intrusive

Because the Telegraph Peak granite, which is closely associated with the hypabyssal intrusive, has been reliably dated at ~26 Ma, the ~70 Ma zircon in the hypabyssal intrusive (Fig. 10) must be xenocrystic, likely from the Pelona Schist, into which it is intruded. The absence of analyzed ~26 Ma zircon is unsurprising given the small sample size (n = 15), and the low proportions of original (i.e., non-xenocrystic) zircon within the compositionally and chronologically similar rhyolite samples.

The reported age of the Telegraph Peak granite is within uncertainty of that of Vasquez/Plush Ranch/Diligencia formation volcanics; coupled with its similar composition and abundant xenocrystic zircon, this suggests that the Telegraph Peak granite and associated hypabyssal intrusives are an intrusive part of the same volcanic system as the Vasquez/Plush Ranch/Diligencia formation volcanics. Because these intrusives and volcanics predate motion on the Punchbowl fault, their present adjacent exposure on opposite sides of the Punchbowl fault (Plate 1) is coincidental. The intrusives are within the same structural block as the Soledad region, but ~45 km southeast. Noting that the Vasquez Formation of the Soledad region lies within the hanging wall of the regional detachment fault, whereas these intrusives lie within the footwall, R.V. Ingersoll (oral communication, 2015) suggested that the intrusives might represent the root of the Vasquez/Plush Ranch/Diligencia formation volcanics, because the former might restore to beneath the latter prior to slip on the detachment fault.

Detrital-Zircon Age Data

The abundant ~1200 Ma zircon in all Vincent-Gap-region samples south of the Fenner fault (Fig. 10) presumably has its ultimate source in the ~1200 Ma anorthosite-gabbro-syenite-norite complex, which is not exposed in the study area, but which outcrops in both the Soledad and Orocopia regions, the offset equivalent regions formerly adjacent to the southwest and northeast, respectively. The ultimate source of the ~1700 Ma zircon is ~1700 Ma gneiss, which is found on the south side of the Punchbowl fault in the study area and which is also present in both the Soledad and Orocopia regions. Low, broad peaks at ~1400 Ma are commonly found together with ~1700 and ~1200 Ma peaks in southern California (e.g., Jacobson et al., 2011; Hoyt, 2012); as discussed above, this age peak probably represents ~1700 Ma zircon perturbed during emplacement of the ~1200 Ma anorthosite-gabbro-syenite-norite complex, and now discordant (Barth et al., 1995). The ~150 Ma granitoid accounts for the ~150 Ma peaks, both directly and via sandstone from the San Francisquito Formation, which was partly derived from the granitoid. This granitoid, and/or its possible equivalents discussed above, are also likely the source of the enigmatic ~150 Ma zircon ages identified in the Mint Canyon and Caliente formations by Hoyt (2012). The nearby Lowe pluton is presumably the source of the ~220 Ma ages, the Pelona Schist of the ~75 Ma ages, and the rhyolite and related volcanics of the ~25 Ma ages. The ~245 Ma ages observed in the Punchbowl Formation samples are likely sourced from Middle Triassic plutons of the Mojave region, such as the ~242-243 Ma plutons of the Little San Bernardino Mountains and the Twentynine Palms region (e.g., Barth et al., 1997), which restore to near to Vincent Gap region prior to slip on the San Andreas fault (e.g., Ingersoll et al., 2014).

Near these plutons are younger ~212-213 Ma plutonics (e.g., Barth et al., 1997), which likely account for the few ~215 Ma ages in the Punchbowl Formation samples.

Ancestral Blue Ridge Drainage Divide

Zircon of ~1200 Ma is prominent in all Oligocene-Miocene deposits south of the Fenner fault, but entirely absent in those north of the Fenner fault (Fig. 10), indicating that strata north and south of the Fenner fault and the Pelona Schist anticlinorium formed in distinct basins. These results also agree with the weak trend of paleocurrents pointing away from the Fenner fault and schist anticlinorium (Plate 2). The existence of this drainage divide is unsurprising: the Fenner fault and anticlinorium of Pelona Schist are correlated with the San Francisquito fault and anticlinorium of Pelona Schist along Sierra Pelona, respectively, in the Soledad region, and the ancestral Sierra Pelona formed a topographic high and drainage divide throughout deposition of Oligocene-Miocene strata in that region (Hendrix et al., 2010). The topographic high of Sierra Pelona thus extended into the Vincent Gap region along the anticlinorium of Pelona Schist and the Fenner fault, as a paleotopographic high here termed the "ancestral Blue Ridge."

Uppermost Oligocene to Lower Miocene Vasquez Formation

Sedimentary Strata

Because granitoid conglomerate clasts dominate where the Vasquez Formation of the Vincent Gap region is nonconformably atop granitoid (or presumably was prior to faulting), whereas San Francisquito Formation sandstone clasts dominate where the Vasquez Formation overlies the San Francisquito Formation in angular unconformity (Plate 2), the different conglomerate compositions are presumably the result of spatial rather than temporal variation in available source rocks. Consistent with the range of conglomerate compositions is the high variability in Vasquez Formation sandstone composition (Fig. 7). These data, together with an inferred alluvial depositional environment, indicate that these strata were locally derived.

The Vasquez Formation of the Vincent Gap region generally resembles the Plush Ranch, Vasquez and Diligencia formations of the Tejon, Soledad and Orocopia regions, respectively, in terms of lithology, depositional mechanism, relationships with surrounding units, and composition. As in these equivalent regions, lacustrine deposits are rare, but occur immediately above volcanic strata. Basalt of the Vincent Gap region contains pervasive fractures filled with tan, fine-grained calcite, matching Carman's (1954) description of basalt of the Plush Ranch Formation. Lenses of granitoid crackle and jigsaw breccia in the Vasquez Formation of the Vincent Gap region are interpreted as rock-avalance deposits, using the criteria of Yarnold and Lombard (1989) and Yarnold (1993). These rock-avalanche deposits are similar to large, lenticular "granitic mega-breccia rockslide deposits" present in the Plush Ranch Formation along the northern margin of the basin (Hendrix et al., 2010, p. 111), and to rock-avalanche breccia at the top of the Vasquez Formation in the Charlie Canyon subbasin.

Despite the close original proximity of Paleoproterozoic gneiss and Mesoproterozoic anorthosite-gabbro-syenite-norite complex to the study area prior to slip on the San Andreas fault system, their dominance of zircon populations in sandstone samples from south of the Fenner fault is surprising given that no anorthosite-gabbro-syenite-norite clasts and only minimal gneiss clasts are present in the conglomerate (Plate 2). These zircon ages presumably indicate significant sediment contributions from these Proterozoic source rocks exclusively to the finer-grained fraction. If so, the original geometry of the basin south of the Fenner fault was likely comparable to that of Plush Ranch basin, with a major fault along the southern margin exposing Proterozoic basement and generating large alluvial-fan systems, the fine-grained, distal parts of which interfinger and mix with proximal, coarse-grained deposits shed from granitoid and the San Francisquito Formation along the northern margin of the basin (Cole and Stanley, 1995; Hendrix et al., 2010). Together with the similarity of the granitoids along the northern basin margins discussed above, paleocurrents compatible with similar transport radiating away from this northern margin, and fault contacts with Pelona Schist anticlinoria immediately north of these granitoids, this suggests that the basin in which the Vasquez Formation south of the Fenner fault formed is a close equivalent of the Texas Canyon and Vasquez Rocks subbasins of Soledad basin and the Plush Ranch basin of the Tejon region (Fig. 14A).

As discussed above, strata on opposite sides of the Fenner fault were separated during deposition by an ancestral Blue Ridge topographic high. The Vasquez Formation north of the Fenner fault and ancestral Blue Ridge presumably correlates with the Vasquez Formation of the Charlie Canyon subbasin of the Soledad region, which lies north of the San Francisquito fault and Sierra Pelona, offset equivalents of the Fenner fault and the ancestral Blue Ridge, respectively (Fig. 14A). Similar rockslide megabreccias near the tops of these sequences support this correlation. These strata presumably also correlate with the Plush Ranch/Simmler strata north of Pelona Schist exposures in the Tejon region. Consistent with this correlation is a general increase in clast size upsection in both the Charlie Canyon subbasin and these Plush Ranch/Simmler strata (Fig. 15B).

Volcanic Strata

Whereas intermediate volcanics are interbedded within the stratigraphically lowest exposures of the Vasquez Formation in the Vincent Gap region, rhyolite is present only as clasts within Vasquez Formation conglomerate. The abundance of both rhyolite and intermediate volcanic clasts in conglomerate immediately above the interbedded volcanic strata suggests that the two types of volcanics are closely related. Close agreement in trace-element composition of the intermediate volcanic samples from the Vincent Gap region (52.7 and 61.3 wt. % SiO_2, Appendix G) with previous data from intermediate volcanics of the Tejon, Soledad and Orocopia regions (51.5 to 59.0 wt. % SiO_2, Frizzell and Weigand, 1993; Figs. 12 and 13), and of the rhyolite samples from the Vincent Gap region (74.7 and 74.9 wt. % SiO_2, Appendix G) with the rhyolite sample from the Orocopia region (74.7 wt. % SiO_2, Appendix G), confirms correlation of the two types of volcanics with the Vasquez/Plush Ranch/Diligencia formation volcanics.

On the opposite (southwest) side of the Punchbowl fault (northeast of Soledad basin), zircon from volcaniclastic Tick Canyon Formation samples, for which the Vasquez volcanics were the source, yield an age of 25.3 ± 0.1 Ma. Close agreement of this precise age with the ~25 Ma zircon ages from the two Vincent Gap-region rhyolite samples and from Vincent Gap-region detrital-zircon samples (Fig. 10) allows its use as the age of the volcanic strata in the Vincent Gap region. Because these volcanic strata are very near the base of the Oligocene-Miocene sedimentary strata (Plate 1), the depositional age of these strata is well constrained. The volcanic strata of the Vincent Gap region exhibit closer correlation with those of the Tejon and Soledad regions (~26.5-23.1 Ma and ~25.6-23.6 Ma, respectively; Frizzell and Weigand, 1993), which were south of the ancestral-Sierra Pelona/ancestral-Blue Ridge drainage divide, than with those of the Orocopia region (~23.6-20.6; Frizzell and Weigand, 1993), which were north of this divide.

The trace-element data of Frizzell and Weigand (1993) and Cole and Basu (1995) are exclusively for samples with between 47.1 and 59.0 wt. % SiO_2. The trace-element data of this study, by contrast, are for samples of both comparable and significantly higher silica contents (Appendix G). These new data demonstrate a strong dependence of trace-element composition in this suite of volcanics on silica content. This is especially evident in the strong, closely overlapping negative Eu anomalies exhibited by the rhyolite samples from both the Vincent Gap and Orocopia regions, but not by the intermediate volcanic samples from either region (Fig. 9). Frizzell and Weigand (1993) noted that samples from the Soledad and Tejon regions, but not the Orocopia region, exhibit small negative Eu anomalies. Given the lower silica contents of their Orocopia-region samples (51.7-52.8 wt. % SiO_2) relative to their Tejon- and Soledad-region samples (51.5-55.1 and 57.5-59.0 wt. % SiO_2, respectively), and the presence of a strong Eu anomaly in Orocopia-region rhyolite, this observation was presumably the result of variable silica content.

Close agreement between age distributions of the dominantly xenocrystic zircon in the rhyolite and detrital zircon from stratigraphically just above the interbedded trachyandesite in the Vasquez Formation suggests that the rhyolite is composed dominantly of shallow crustal material melted by a more mafic magma. This supports the hypothesis of Frizzell and Weigand (1993) that the more felsic volcanics of this suite are the result of greater contributions of shallow crustal material than in the more mafic volcanics, rather than variable amounts of magma fractionation, as suggested by Spittler (1974) and Spittler and Arthur (1982).

The felsic volcanics of the Vincent Gap region contain zircon, allowing for dramatically more reliable and precise ages via U-Pb dating than previous ages for the Vasquez/Plush Ranch/Diligencia formation volcanic system, which were all acquired via K-Ar dating. Because the Orocopia region contains volcanics of comparable composition to the more felsic volcanics of the Vincent Gap region, it should be possible to acquire U-Pb zircon ages for these volcanics. Besides yielding a more precise age for the volcanics of the Orocopia region, this would test whether these volcanics are truly younger than those of the Plush Ranch, Vasquez and Vincent

Gap regions, as is currently hypothesized. They may instead be coeval, but overprinted by subsequent thermal perturbation, in much the same way that the Telegraph Peak granite (discussed above), with an age of ~26 Ma, yielded K-Ar ages of ~26-14 Ma. If the Orocopia region volcanics are ~25 Ma, they may be the source of the single ~25 Ma zircon in one Punchbowl Formation sample (JFH-11-25P).

Middle Miocene Paradise Springs Formation and Unroofing Sequence

Detailed geologic mapping of the Vincent Gap region (Plate 1), coupled with conglomerate composition data from throughout this mapped area (Plate 2), demonstrates that clasts of Pelona Schist are found in the Paradise Springs formation, but not in the underlying Vasquez Formation, verifying the unroofing sequence documented by Ingersoll and Colasanti (2004) and Colasanti and Ingersoll (2006). This finding is of regional significance, as it indicates that extension associated with WTR rotation must have included the Vincent Gap region. This requires the axis of WTR rotation to have been farther inboard than typically assumed, adjacent to, if not east of, the present San Andreas fault. An unroofing sequence is present both north and south of the Fenner fault and ancestral Blue Ridge.

Age distributions of detrital zircon from the schist breccia of the Paradise Springs formation (map unit Npss in Plate 1) and from one of the two other Paradise Springs formation samples show sharp peaks at ~75 Ma (Fig. 10); the Pelona Schist is presumably the source of this zircon (curiously, Paradise Springs formation sample KTC-14-dz4 does not show an ~75 Ma peak). Unexpectedly, smaller ~75 Ma age peaks are also seen in some samples from the Vasquez Formation. If this zircon population represents a direct contribution from exhumed Pelona Schist, then the timing of exhumation in the Vincent Gap region would be earlier than suggested by conglomerate composition data, and would no longer coincide with exhumation in the adjacent

Soledad region. More probable is that the ~75 Ma detrital-zircon population in Vasquez Formation samples was derived from a different source, possibly the same Late Cretaceous batholithic rocks from which the ~75 Ma zircon within the schist was derived. Because the Pelona Schist lacks primary zircon, its contribution to detrital-zircon populations is inherently ambiguous. The Pelona Schist may well contain primary monazite, however, in which case dating of detrital monazite (Hietpas et al., 2010) from the sandstone samples of this study could clarify the Pelona Schist's contributions to the fine-grained fractions of these samples.

Highly variable sandstone and conglomerate compositions within the Paradise Springs formation (Fig. 7; Plate 2), coupled with an inferred alluvial depositional environment and compositional and textural similarity to the underlying Vasquez Formation, indicate that this formation was locally derived. The Tick Canyon Formation of the Soledad region has highly variable sandstone composition that partly overlaps with that of the Paradise Springs formation (Fig. 8), and also represents primarily alluvial deposits. Both formations overlie sandstone, conglomerate and coeval volcanic strata of the Vasquez Formation, and both are overlain by middle-upper Miocene sandstone and conglomerate with no significant angular discordance. Additionally, both formations contain unroofing sequences documenting exhumation of the Pelona Schist. Collectively, this indicates that the two formations are equivalent. The type-section Tick Canyon Formation, located south of Sierra Pelona, correlates with the Paradise Springs formation south of the Fenner fault and the ancestral Blue Ridge; the Paradise Springs formation north of these features correlates with the Tick Canyon Formation of Charlie Canyon subbasin, discussed below (Fig. 14B).

Unroofing Sequence in the Charlie Canyon Subbasin of the Soledad Region

An unroofing sequence is exposed in the Charlie Canyon subbasin of the Soledad region, adjacent to the San Francisquito fault and the Pelona Schist of Sierra Pelona (Fig. 6). The upsection transition of breccia clasts from granitoid of the upper plate of the San Francisquito fault, to chloritic breccia indicative of detachment fault zones (e.g., Davis et al., 1986), to the Pelona Schist that makes up the lower plate represents a clear unroofing sequence similar to those observed in the type-section Tick Canyon Formation of Soledad basin, on the opposite side of the Sierra Pelona, and in the Paradise Springs formation of the Vincent Gap region. The breccia above the granitoid rock-avalanche deposits is better assigned to the Tick Canyon Formation, rather than to the Mint Canyon Formation or as its own unit as previously mapped (e.g., Sams, 1964; Weber, 1994; Dibblee, 1997a).

Fenner Fault as the Major Detachment Fault

Based on its straight trace, the Fenner fault dips steeply (Plate 1). Both within and outside the study area, the Fenner fault is north of a west-plunging anticlinorium of Pelona Schist; a similar distance south of this anticlinorium is a dip-slip fault that has been rotated to a high angle (mapped as “Fenner detachment fault” in Plate 1). These two faults converge approximately along the trace of the anticlinorium, suggesting that they are a single, originally low-angle detachment fault that has been folded along with the Pelona Schist. This interpretation is consistent with the interpretation that the Fenner fault is correlated with the San Francisquito detachment fault of the Soledad region. Poor exposure of the Fenner fault within the study area and a lack of access to Fenner Canyon, through which the trace of the Fenner fault continues, prevented direct measurement of its orientation. According to Dibblee (2002a, b), however, the Fenner fault dips steeply to the southeast; together with the orientation of the San Francisquito

Formation along the fault, this is inconsistent with interpretation of the Fenner fault as a low-angle detachment, and would instead suggest that the Fenner fault is a reverse fault. The solution is likely that, following rotation of an originally low-angle detachment to a high angle on the flank of the Pelona Schist anticlinorium, a reverse fault formed, reactivating the detachment in some places and offsetting it in others (cross section E-E' in Plate 3), and rupturing westward to link with the Punchbowl fault (Plate 1). Noble (1954) and this study (Plate 1) inferred continuation of the Fenner fault through the Paradise Springs formation, which would be consistent with this hypothesis, whereas other studies (e.g., Liu, 1990; Weldon et al., 1993; Dibblee, 2002a) interpreted the Fenner fault as predating, and being overlain by, the Paradise Springs formation; differing interpretations are possible because of poor, discontinuous exposure of the Fenner fault in this region.

Transpression may also have caused further folding of an originally broader anticlinorium to its present, tight geometry. This would mean that the Fenner and San Francisquito faults are equivalent, but that, because of reverse faulting on the Fenner fault and possible transpressional folding, the present traces of the two may not restore exactly in line with one-another. Proposed correlations of Dibblee (1968) and Ehlig (1968, 1981) would remain essentially unchanged, however, as the various lithologic units of the Vincent Gap region must still restore to near their equivalents in the Soledad region.

Correlation of the San Francisquito and Pelona detachment faults as exposures of a single, folded detachment fault on opposite limbs of the Sierra Pelona anticlinorium is incompatible with the hypothesis that the Clemens Well, Fenner and San Francisquito faults represent parts of a major transform fault, an idea that has been adopted in various palinspastic reconstructions (e.g., Powell, 1993; Weldon et al., 1993). Furthermore, according to

Goodmacher et al. (1989), the Clemens Well fault is part of the Orocopia Mountains detachment fault system, and could not have accommodated more than minor strike-slip motion. With the identification of the Fenner fault as a folded detachment fault exposed on both sides of an anticlinorium of Pelona Schist, all three segments of this fault system have been shown to be dominantly normal rather than transform, conclusively refuting the hypothesized Clemens Well-Fenner-San Francisquito transform fault.

Middle to Upper Miocene Punchbowl Formation and Drainage Integration

Sandstone samples from the basal Punchbowl Formation exhibit less compositional variation than the underlying Paradise Springs and Vasquez formations (Fig. 7), but are still somewhat variable. Sandstone samples from the main member of the Punchbowl Formation are compositionally nearly identical, clustering tightly together on QFL and QmFkFp ternaries (Fig. 7). Together with the transition to braided-stream deposits, this indicates that the Punchbowl Formation was deposited in a more integrated drainage system than the Paradise Springs and Vasquez formations, and that the basal member of the Punchbowl Formation represents the transition to this system. This argues against deposition of the Punchbowl Formation in an intermontane basin with sediment input from localized sources to the west and east as proposed by Matti and Morton (1993), as do the westward (original direction prior to vertical-axis rotation) paleocurrents within the Punchbowl Formation.

It is clear that the Punchbowl Formation overlies the middle Miocene Paradise Springs formation, equivalent to the Tick Canyon Formation of the Soledad region, which in turn overlies the uppermost Oligocene to lower Miocene Vasquez Formation, equivalent to the Vasquez Formation and Simmler/Plush Ranch Formation strata of the Soledad and Tejon regions, respectively. Given this new context, the middle to upper Miocene Punchbowl

Formation is presumably largely coeval with the middle to upper Miocene Mint Canyon and Caliente formations of the Soledad and Tejon regions, respectively.

The Punchbowl and Mint Canyon formations are compositionally distinct (Fig. 9), and their detrital-zircon age data do not match (Fig. 16). The Caliente Formation sandstone and detrital-zircon samples of Hoyt (2012) are readily divisible into northern, middle and southern subsets. Such a division reveals that detrital-zircon ages of the northern Caliente Formation are similar to those of the Punchbowl Formation, with prominent peaks at ~80, ~150 and ~245 Ma, and a complete absence of ~1200 Ma zircon; it is thus termed “Punchbowl-type” (Fig. 16). Detrital-zircon ages of the southern Caliente Formation, by contrast, match those of the Mint Canyon Formation, with prominent peaks at ~25, ~80, ~150, ~220, ~1200 and ~1700 Ma, and none at ~245 Ma; it is thus termed “Mint Canyon-type” (Fig. 16). Detrital-zircon ages of the geographically middle Caliente Formation exhibit peaks at every age that either the northern or the southern Caliente Formation has, suggesting that it represents a mixture of the two; it is thus termed “Punchbowl/Mint Canyon type” (Fig. 16). Sandstone compositions reveal a similar trend, with the northern (Punchbowl-type) Caliente Formation similar to the Punchbowl Formation, the southern (Mint Canyon-type) similar to the Mint Canyon Formation, and the middle (Punchbowl/Mint Canyon-type) between (Fig. 9).

Assuming that the Fenner fault of the Vincent Gap region correlates with the San Francisquito and Orocopia Mountains detachment faults of the Soledad and Orocopia regions, respectively (see above; Fig. 14B), the Punchbowl Formation must restore in line with the northwest side of the Sierra Pelona, rather than the southeast side where the Mint Canyon Formation is; it must also restore in line with the Orocopia Mountains, northwest of the Chocolate Mountains source area for the Mint Canyon Formation drainage. Because of both this paleogeographic separation and the differences in sandstone composition and detrital-zircon ages, the Punchbowl Formation cannot represent an up-drainage equivalent of the Mint Canyon Formation. Instead, the Punchbowl Formation and Punchbowl-type Caliente Formation likely represent a third-order (classification scheme of Ingersoll, 1990) river system that originated north or east of the Orocopia Mountains, and flowed west along the northwest side of the ancestral Blue Ridge and the ancestral Sierra Pelona; slightly higher relative abundances of quartz and potassium feldspar in Punchbowl-type Caliente Formation samples might be the result of either concentration of more stable grains during transport, mixing with sand enriched in quartz and potassium feldspar downstream from the Punchbowl Formation (perhaps due to an increased contribution from the San Francisquito Formation), or a combination of the two. The first- and second-order drainages (classification scheme of Ingersoll, 1990) represented by the Mint Canyon Formation and the Mint Canyon-type Caliente Formation would have comprised a tributary of this larger drainage, merging with it west of Sierra Pelona in the vicinity of the Punchbowl/Mint Canyon-type Caliente Formation, then continuing westward to the coast (Fig. 14C).

One observation difficult to reconcile with this proposed Punchbowl/Mint Canyon/Caliente Formation drainage system is the presence of strata mapped as Punchbowl Formation southeast of the Sierra Pelona, at the eastern edge of the Soledad region (e.g., Dibblee, 2001). The one sample from these strata analyzed in this study (KTC-12-Tps1) closely matches the Punchbowl Formation of the Vincent Gap region in sandstone composition (Fig. 9) and detrital-zircon ages (Fig. 10). This sample was collected from strata near the Nadeau fault; it is possible that it is northeast of the south branch of the Nadeau fault, which Dibblee (2001) mapped as nearby, but does not show the northwestern terminus of, and that strata mapped as

Punchbowl Formation by Dibblee (2001) farther southwest are actually Mint Canyon Formation-equivalent. Alternatively, these strata may be equivalent to the upper Punchbowl Formation, and post-date a rearrangement of drainage patterns in which the drainage represented by the Punchbowl Formation began to flow south of the Sierra Pelona. Additional sampling and study of these strata are required to understand their relation to the Punchbowl and Mint Canyon formations.

As mentioned by Ehlert (2003) and Hoyt (2012), the San Gabriel fault probably became active during deposition of the Caliente Formation. Consequently, by the time the upper part of the Caliente Formation was deposited, it had likely been separated from the Punchbowl Formation/Mint Canyon Formation drainage system. Following this separation, the confluence of this drainage system likely stepped inboard across the San Gabriel fault, to the western edge of the Sierra Pelona; this would explain the thin strip of upper Mint Canyon Formation that crosses and overlies the westernmost exposure of the Pelona Schist anticlinorium in the Charlie Canyon area of the Soledad region (Figs. 6, 15B). The uppermost Punchbowl Formation, which is younger than the Mint Canyon and Caliente formations, likely represents the continued existence of this drainage system into latest Miocene and possibly early Pliocene time, during which it was likely the source of the shallow-marine, upper Miocene Castaic and upper Miocene-lower Pliocene Pico formations of the Soledad region.

Post-Miocene Deformation

In the Vincent Gap region, no post-Miocene strata are present, save for unconsolidated Quaternary sediment (Plate 1). This is unsurprising, given that the regional tectonic regime shifted to transpressional near the end of the Miocene, and the Punchbowl and San Andreas faults became active. Faulting and folding subparallel to the Punchbowl fault in the Punchbowl

Formation in the western part of the study area (in the region of A-A' in Plate 1; Plate 3) are presumably transpressional features associated with slip and shortening on the Punchbowl fault. If so, these features all formed subsequent to initiation of the Punchbowl and San Andreas faults ~6 or 5 Ma, but prior to cessation of slip on the Punchbowl fault, which may have occurred during the Quaternary (Dibblee, 1968). Reverse motion on the Fenner fault would also have occurred during this interval of Punchbowl fault activity. The fault south of the Punchbowl syncline (near the middle of A-A' in Plate 3) does not terminate in the basal layers of the Punchbowl Formation, as indicated by previous studies (e.g., Dibblee, 2002a), and accordingly, is interpreted as a transpressional feature related to the Punchbowl fault, rather than as a middle Miocene extensional feature.

Faults and folds within the San Francisquito Formation and granitoid basement are subparallel to both the Punchbowl fault and the older detachment fault (Plate 1), and thus could be either high-angle reverse faults associated with latest Miocene to Quaternary transpression, possibly splaying off of the Punchbowl fault at depth as flower structures, or listric normal faults associated with upper Oligocene-lower Miocene extension, controlled by and likely merging at depth with the Fenner detachment fault. It is also possible that these faults began as normal faults and were subsequently reactivated as reverse faults because of their favorable orientation; this same process at a larger scale could explain why the trace of the Punchbowl fault follows that of the southern exposure of the Fenner detachment fault so closely.

Following cessation of slip on the Punchbowl fault, and continuing to the present, the Punchbowl block (between the Punchbowl and San Andreas faults) has experienced uplift relative to the block northeast of the San Andreas fault (the Mojave block; e.g., Dibblee, 1987). This is presumably responsible for the uplifted and dissected older alluvial deposits within the study area (map unit Qoa in Plate 1). As explained by Dibblee (1987), the block southwest of the Punchbowl fault (the San Gabriel Mountains block) has experienced not only this period of uplift, but also uplift relative to the Punchbowl block when the Punchbowl fault was active; as a result, elevations in the Punchbowl block are generally above those in the Mojave block, but below those in the San Gabriel Mountains block.

CONCLUSIONS

The Vincent Gap region of the eastern San Gabriel Mountains is an until-now underemphasized part of the Tejon-Soledad-Vincent Gap-Orocopia regions suite, which collectively comprised a single, continuous terrane prior to separation on the San Andreas fault system. It contains an Oligocene-Miocene sedimentary record spanning from ~25 Ma to ~6 Ma, with equivalents of the Vasquez, Tick Canyon and Mint Canyon formations of the Soledad region, rather than just the middle-upper Miocene Punchbowl Formation, as previously mapped.

Sedimentary and volcanic strata of the Vincent Gap region referred to in this study as the Vasquez Formation represent an offset equivalent of the uppermost Oligocene-lower Miocene Plush Ranch, Vasquez and Diligencia formations of the Tejon, Soledad and Orocopia regions, respectively. The basin in which these Vincent Gap strata south of the Fenner fault formed is equivalent to the Plush Ranch basin and the Texas Canyon and Vasquez Rocks subbasins of Soledad basin (Figs. 14A, 15A). All are bordered along much of their northern margins by compositionally similar granitoid rocks, though radiometric ages of these granitoids from the Tejon and Vincent Gap regions do not agree. The Vasquez Formation of Vincent Gap north of the Fenner fault formed in a basin equivalent to Diligencia basin, the Charlie Canyon subbasin of the Soledad region, and the basin in which the Plush Ranch/Simmler strata of the Tejon region were deposited (Figs. 14A, 15B). Interbedded lava flows are trachyandesitic to trachytic in composition. In addition, rhyolite clasts with no correlatives in outcrop exist. The dominance of xenocrystic zircon in the rhyolites implies magmatic contamination by shallow crustal material. U-Pb ages of volcanic zircon agree with previously published K-Ar ages from the Tejon and Soledad regions, but give a more precise and, because of zircon's resistance to alteration, robust result of 25.3 ± 0.1 Ma. Dating of volcanic zircon from the Tejon, Soledad and Orocopia regions by U-Pb methods could refine eruption ages and stratigraphic control in these regions, and determine whether the inferred younger age of the Diligencia Formation volcanics is real or the result of subsequent thermal perturbation.

Strata dubbed the Paradise Springs formation in this study are locally derived alluvial deposits equivalent to the middle Miocene Tick Canyon Formation of the Soledad region (Fig. 14B). Like the Tick Canyon Formation, these strata are the oldest deposits in the region that contain clasts of Pelona Schist, and thus document final exhumation of this schist in middle Miocene time. Presence of this unroofing sequence indicates that transrotational extension, and thus the rotational axis of the western Transverse Ranges, existed farther inboard than commonly assumed. The Fenner fault north of the anticlinorium of Pelona Schist, together with the previously unnamed fault on the opposite side of the anticlinorium of Pelona Schist, herein dubbed the "Fenner detachment fault" (Plate 1), represents the detachment fault along which Pelona Schist was exhumed. These faults are thus equivalent to the San Francisquito and Pelona detachment faults of the Soledad region and the Orocopia Mountains detachment fault of the Orocopia region (Fig. 14B). The Fenner fault north of the anticlinorium of Pelona Schist was probably reactivated as a high-angle reverse fault during transpression along the Punchbowl fault.

The middle-upper Miocene Punchbowl Formation represents a more integrated drainage system than those of the underlying Vasquez and Paradise Springs formations, with basal strata of the Punchbowl Formation representing the transition to this state. The Punchbowl Formation drainage system likely flowed along the northern (original orientation prior to vertical-axis rotation) edge of the ancestral Blue Ridge-Sierra Pelona to the Tejon region, where it was joined by a tributary from southeast of the ancestral Sierra Pelona, represented by the Mint Canyon Formation (Fig. 14C); the confluence of the two fluvial systems is represented by the Caliente Formation. The upper Punchbowl Formation likely represents the upstream equivalent of the marine Castaic and Pico formations, which overly the Mint Canyon Formation southwest of Sierra Pelona.

Detrital-zircon age data, sandstone petrofacies and conglomerate composition, though compatible, each reveal only some of a unit's source rocks. Using all three in combination allows for a more complete and robust characterization of provenance. This study illustrates the importance of integrating regional geology and plate tectonics with local structure, stratigraphy, sedimentology, geochemistry and geochronology when reconstructing the paleogeography and paleotectonic evolution of a complex region.

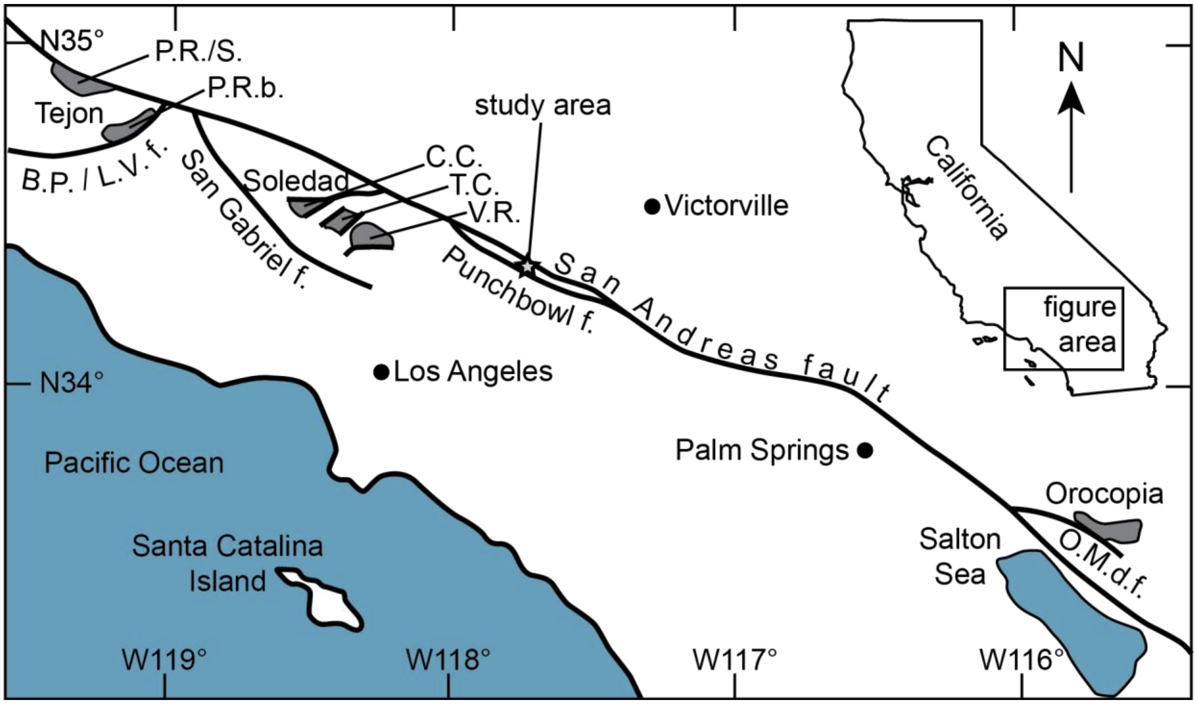

Figure 1: Regional map showing study area (Vincent Gap region), relevant faults, and Tejon, Soledad and Orocopia regions, with areal extent of Vasquez Formation and offset equivalents schematically shown in gray. f. = fault; B.P. / L.V. f. = Big Pine/Lockwood Valley fault; O.M.d.f. = Orocopia Mountains detachment fault. C.C. = Charlie Canyon subbasin; T.C. = Texas Canyon subbasin; V.R. = Vasquez Rocks subbasin; P.R.b. = Plush Ranch basin; P.R./S. = Plush Ranch/Simmler strata. Figure after Frizzell and Weigand (1993) and Law et al. (2001).

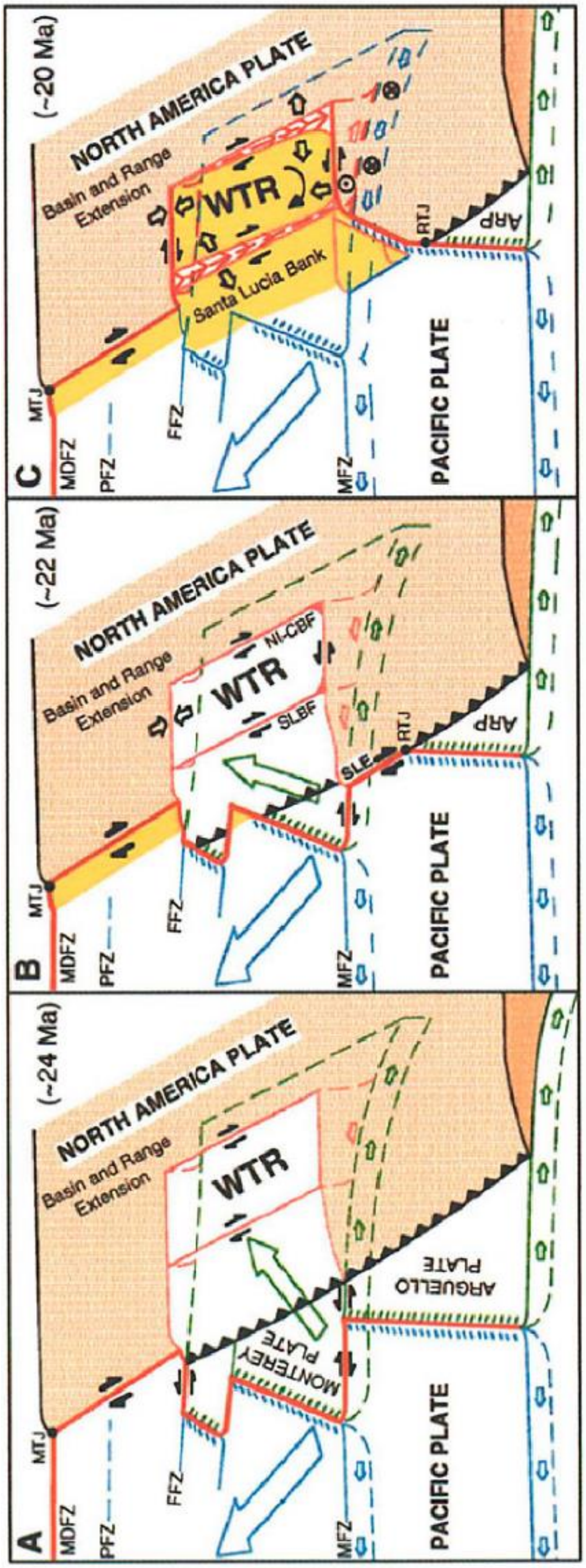
A
(~24 Ma)
NORTH AMERICA PLATE
Basin and Range
Extension
WTR
MONTEREY PLATE
ARGUELLO PLATE
PACIFIC PLATE
MDFZ
MTJ
PFZ
FFZ
MFZ
B
(~22 Ma)
NORTH AMERICA PLATE
Basin and Range
Extension
WTR
NI-CBF
SLBF
SLE
RTJ
ARP
PACIFIC PLATE
MDFZ
MTJ
PFZ
FFZ
MFZ
C
(~20 Ma)
NORTH AMERICA PLATE
Basin and Range
Extension
WTR
Santa Lucia Bank
RTJ
ARP
PACIFIC PLATE
MDFZ
MTJ
PFZ
FFZ
MFZ

Figure 2: Schematic block diagrams illustrating capture of Monterey microplate by Pacific plate. A: Monterey microplate is fully coupled to Farallon plate as it subducts beneath North America. B: As subduction and seafloor spreading slow, motion of Monterey microplate becomes intermediate to those of Pacific and Farallon plates. C: At ~20 Ma, seafloor spreading along western margin of Monterey microplate ceases entirely, coupling Monterey microplate to Pacific plate. Shear exerted on base of continental crust of North America initiates rotation of western Transverse Ranges. Yellow = North American crust captured by Pacific plate; red = edge of Pacific plate or areas of extension; FFZ, MFZ, MDFZ, PFZ = Farallon, Morro, Mendocino and Pioneer fracture zones, respectively; MTJ and RTJ = Mendocino and Rivera triple junctions, respectively; WTR = western Transverse Ranges block; NI-CBF = Newport-Inglewood-Coronado Bank fault; SLBF = Santa Lucia Bank fault; SLE = tectonically eroded Santa Lucia Escarpment; ARP = Arguello microplate. Figure from Nicholson et al. (1994).

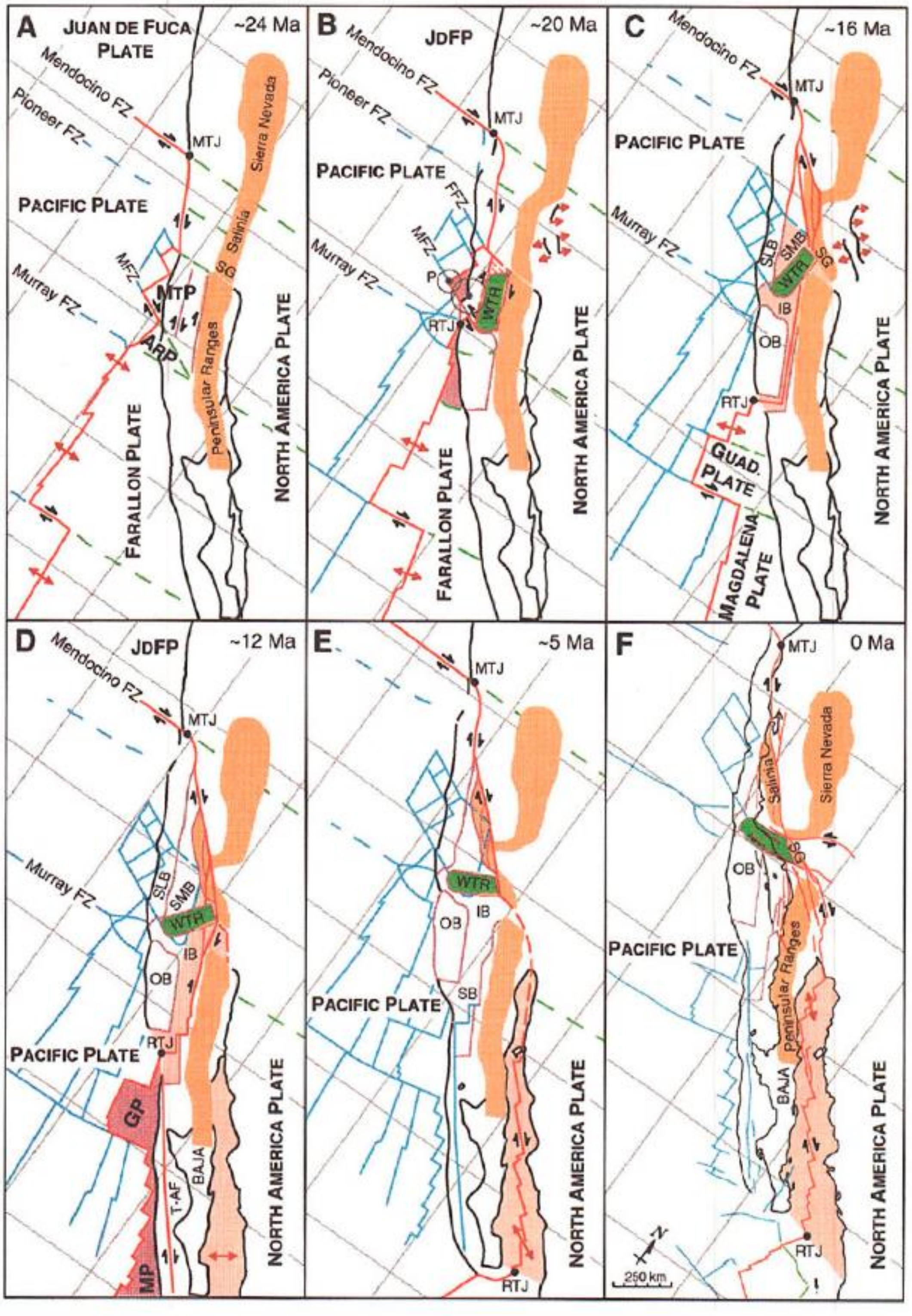

A
JUAN DE FUCA PLATE
~24 Ma
Mendocino FZ
Pioneer FZ
MTJ
Sierra Nevada
Salinia
PACIFIC PLATE
MFZ
SG
MTP
Murray FZ
ARP
Peninsular Ranges
FARALLON PLATE
NORTH AMERICA PLATE
B
Mendocino FZ
JDFP
~20 Ma
Pioneer FZ
MTJ
PACIFIC PLATE
FFZ
MFZ
Murray FZ
P
WTR
RTJ
FARALLON PLATE
NORTH AMERICA PLATE
C
Mendocino FZ
~16 Ma
MTJ
PACIFIC PLATE
Murray FZ
SLB
SMB
SG
WTR
IB
OB
RTJ
GUAD. PLATE
MAGDALENA PLATE
NORTH AMERICA PLATE
D
Mendocino FZ
JDFP
~12 Ma
MTJ
Murray FZ
SLB
SMB
WTR
IB
OB
RTJ
PACIFIC PLATE
GP
T-AF
BAJA
MP
NORTH AMERICA PLATE
E
~5 Ma
MTJ
WTR
IB
OB
SB
PACIFIC PLATE
RTJ
NORTH AMERICA PLATE
F
MTJ
0 Ma
Salinia
Sierra Nevada
SG
OB
PACIFIC PLATE
Peninsular Ranges
BAJA
RTJ
N
250 km
NORTH AMERICA PLATE

Figure 3: Interaction of the Pacific, North American and Farallon plates from 24 Ma to present. A: Monterey and Arguello microplates have formed. B: Monterey microplate is captured by Pacific plate, initiating rotation of WTR. C: Arguello microplate has been captured by Pacific plate, and inner borderland has begun to open. D: Guadalupe and Magdalena microplates are captured by Pacific plate, initiating transform motion on San Gabriel-Chino Hills-Cristianitos-Tosco-Abreojos fault. E: Baja California is captured by Pacific plate; transform jumps to San Andreas fault, and seafloor spreading begins in Gulf of California. F: Present. ARP = Arguello microplate; GP = Guadalupe microplate; MTP = Monterey microplate; SG = San Gabriel block; JDFP =Juan de Fuca plate (remnant of Farallon); SLB = Santa Lucia Bank; SMB = Santa Maria basin; IB, OB, SB = inner, outer and southern borderlands, respectively; T-AF = San Gabriel-Chino Hills-Cristianitos-Tosco-Abreojos fault; MP = Magdalena microplate; red areas = regions of transtension; purple areas = captured or soon-to-be captured microplates; orange areas = Mesozoic batholithic belt. See Figure 2 for other abbreviations. Figure from Nicholson et al. (1994).

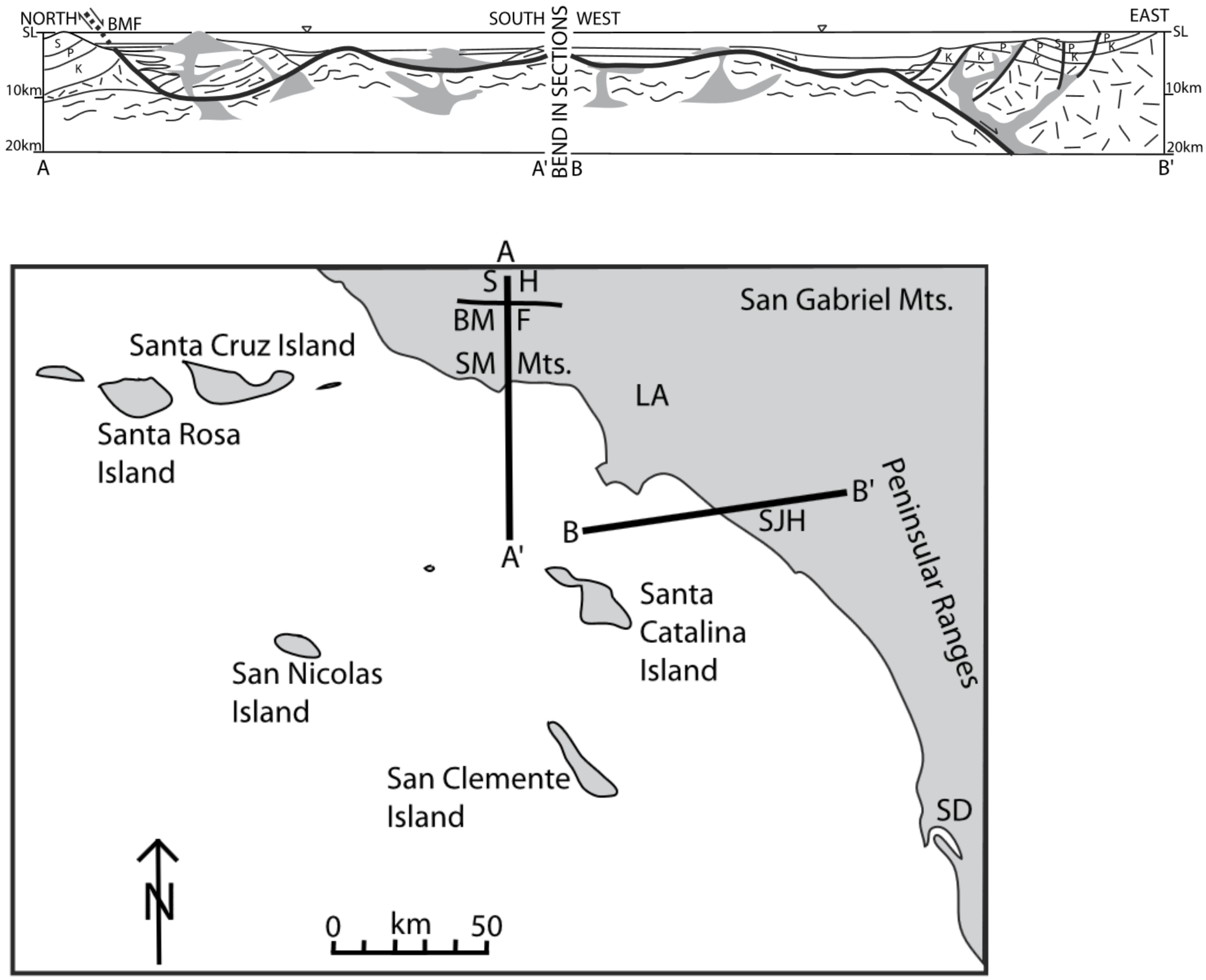

Figure 4: Cross sections through inner borderland between Western Transverse Ranges (A) and Peninsula Ranges (B'), showing exhumed detachment fault and Catalina Schist.

BMF = Boney Mountain fault; K = Cretaceous; LA = Los Angeles; P = Paleogene undifferentiated; S = Oligocene Sespe Formation; SD = San Diego; SH = Simi Hills; SJH = San Joaquin Hills; SM Mts. = Santa Monica Mountains. Unlabeled strata are middle Miocene and younger, interfingering with volcanic and hypabyssal rocks shown in gray. Squiggles represent Catalina Schist. Laths indicate Mesozoic plutonic and related metamorphic rocks. Thick black line is detachment fault; medium black lines are related faults; thin black lines are depositional contacts. Figure from Ingersoll (2008b).

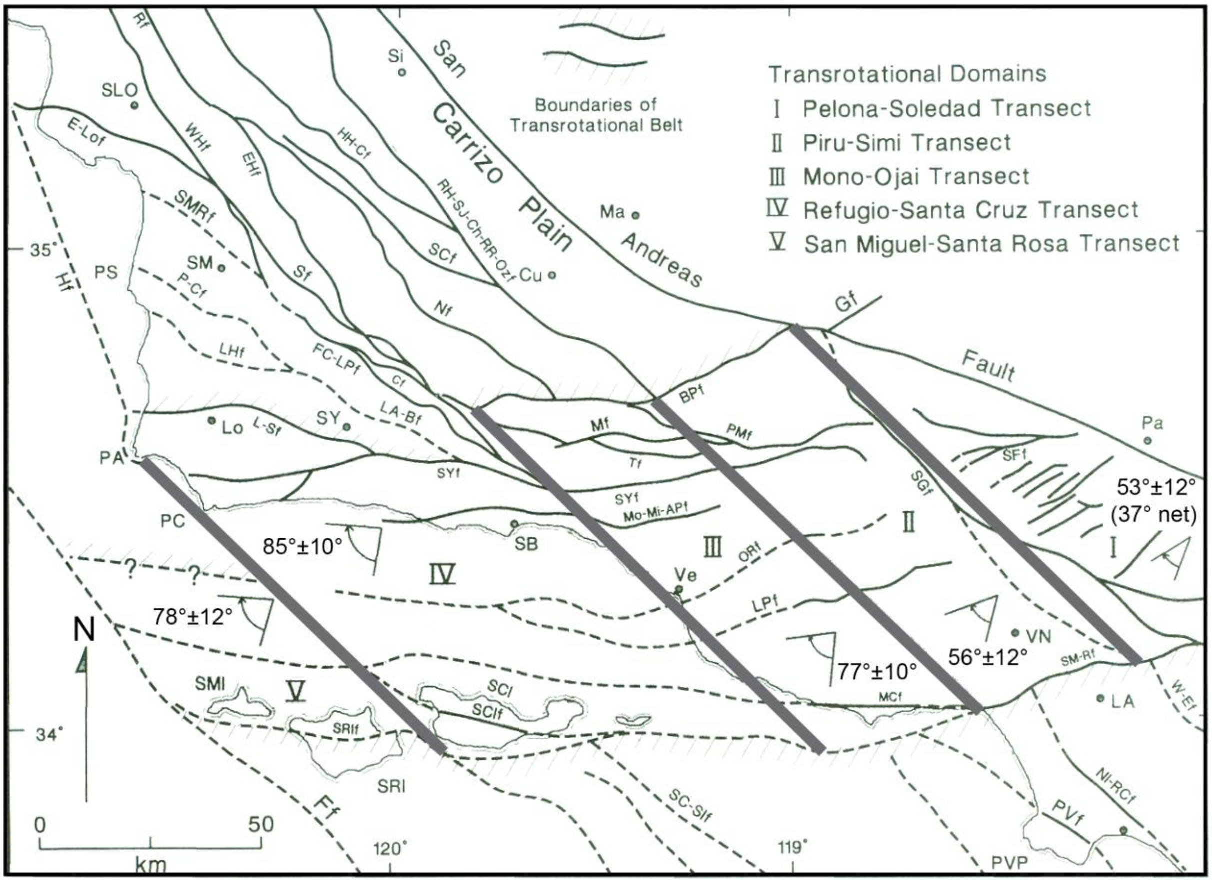

Figure 5: Transrotational domains of the western Transverse Ranges. Plotted value for domain I (37°) is net clockwise rotation measured, whereas listed value (53° ± 12°) is total clockwise rotation measured. Error values listed are 1σ. Not pictured is ~100° of clockwise rotation measured on Santa Catalina Island. Modified from Dickinson (1996), using data of Hornafius et al. (1986); see Dickinson (1996) for list of abbreviations. Vincent Gap region is just outside figure to the right.

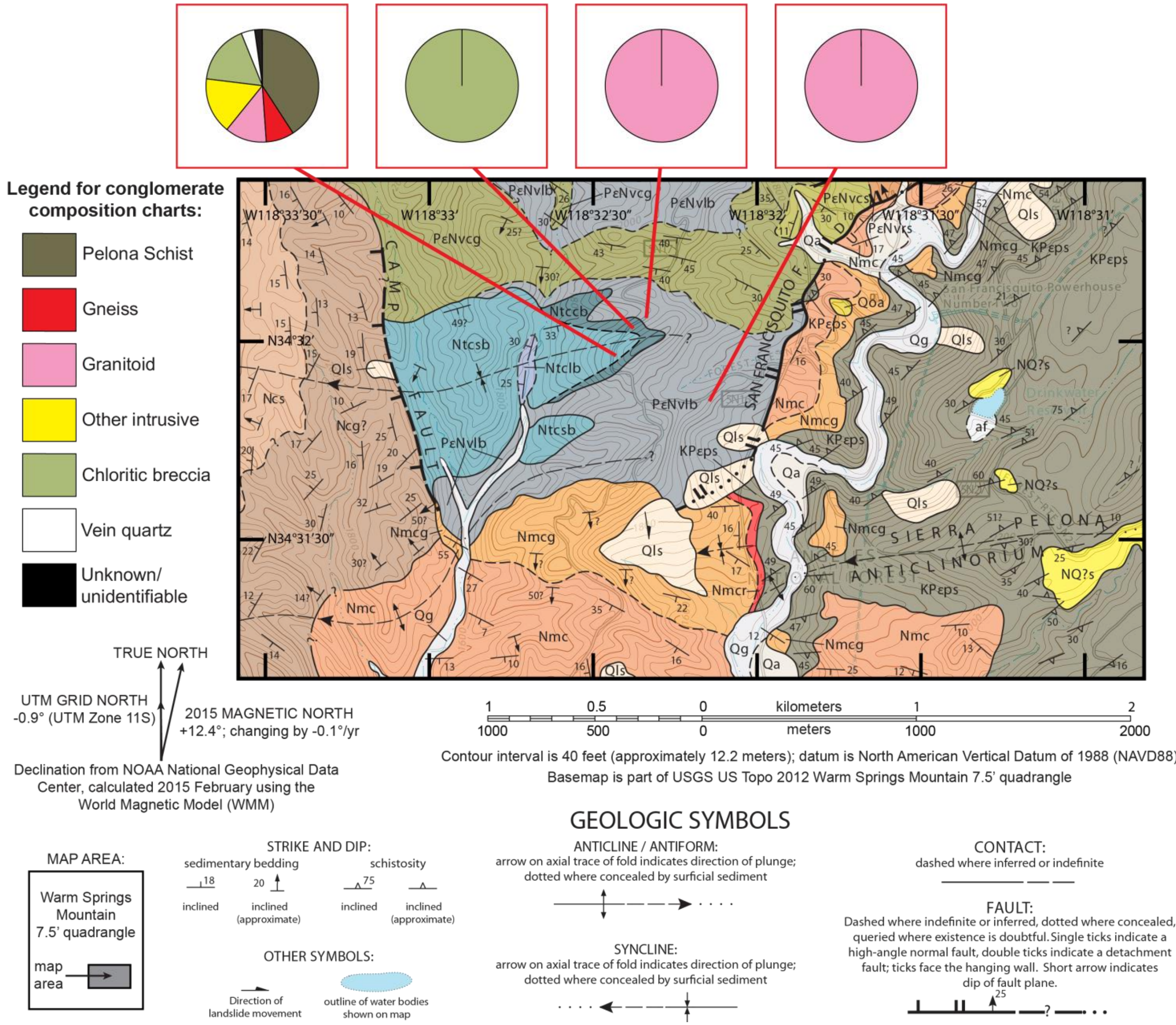
Legend for conglomerate composition charts:
Pelona Schist
Gneiss
Granitoid
Other intrusive
Chloritic breccia
Vein quartz
Unknown/ unidentifiable
TRUE NORTH
UTM GRID NORTH -0.9° (UTM Zone 11S)
2015 MAGNETIC NORTH +12.4°; changing by -0.1°/yr
Declination from NOAA National Geophysical Data Center, calculated 2015 February using the World Magnetic Model (WMM)
W118°33'30"
W118°33'
W118°32'30"
W118°32'
W118°31'30"
W118°31'
N34°32'
N34°31'30"
CAMP FAULT
SAN FRANCISQUITO F.
SIERRA PELONA ANTICLINORIUM
San Francisquito Powerhouse Number Two
kilometers
meters
1 0.5 0 1 2
1000 500 0 1000 2000
Contour interval is 40 feet (approximately 12.2 meters); datum is North American Vertical Datum of 1988 (NAVD88)
Basemap is part of USGS US Topo 2012 Warm Springs Mountain 7.5' quadrangle
GEOLOGIC SYMBOLS
MAP AREA:
Warm Springs Mountain 7.5' quadrangle
map area
STRIKE AND DIP:
sedimentary bedding
inclined
inclined (approximate)
schistosity
inclined
inclined (approximate)
OTHER SYMBOLS:
Direction of landslide movement
outline of water bodies shown on map
ANTICLINE / ANTIFORM:
arrow on axial trace of fold indicates direction of plunge; dotted where concealed by surficial sediment
SYNCLINE:
arrow on axial trace of fold indicates direction of plunge; dotted where concealed by surficial sediment
CONTACT:
dashed where inferred or indefinite
FAULT:
Dashed where indefinite or inferred, dotted where concealed, queried where existence is doubtful. Single ticks indicate a high-angle normal fault, double ticks indicate a detachment fault; ticks face the hanging wall. Short arrow indicates dip of fault plane.

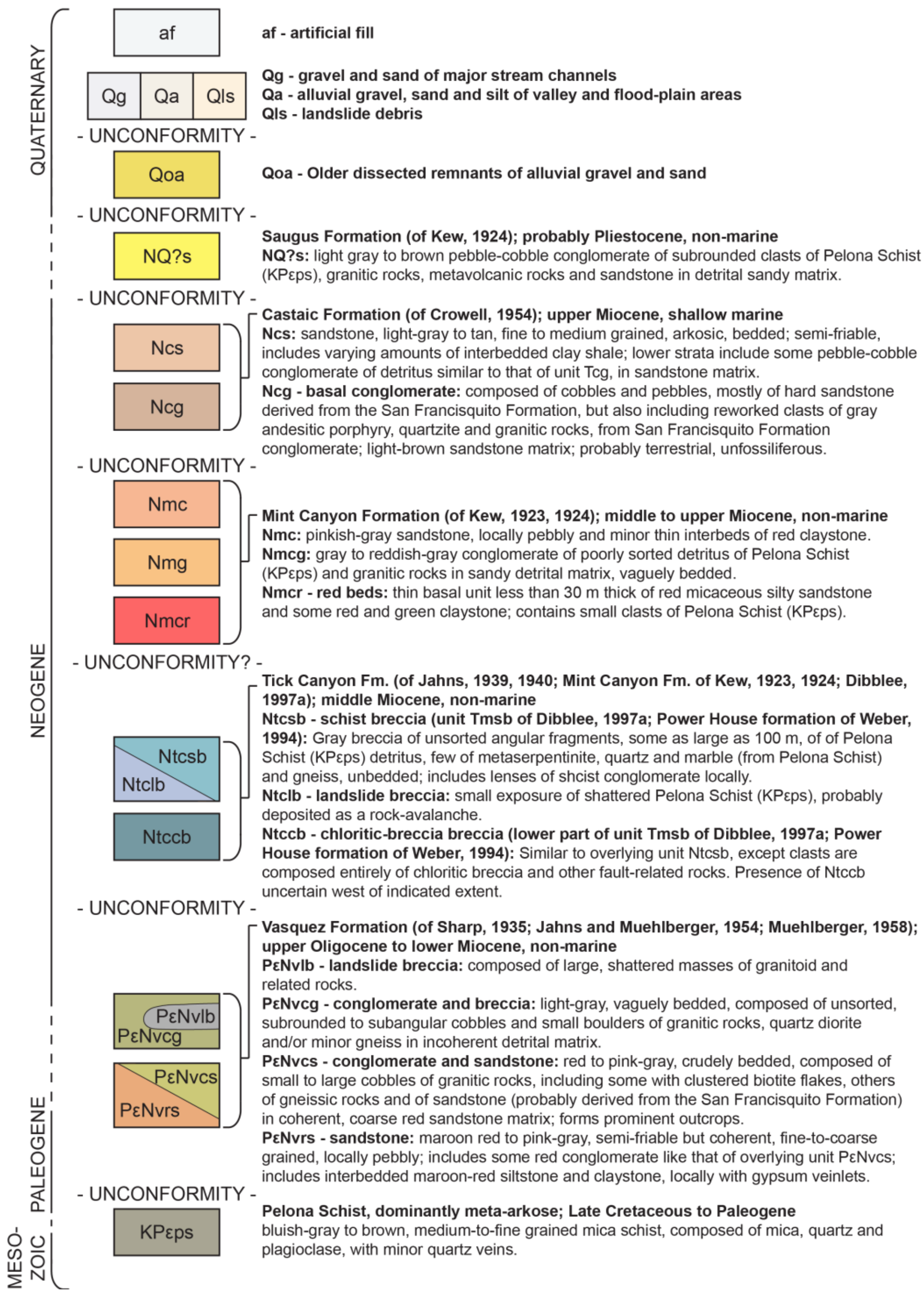

Figure 6: Geologic map of part of Charlie Canyon subbasin of Soledad region.

Conglomerate-composition data document an unroofing sequence similar to those found south of Sierra Pelona in Tick Canyon Formation of Soledad basin and in Paradise Springs formation of Vincent Gap region. Modified from Dibblee (1997a).

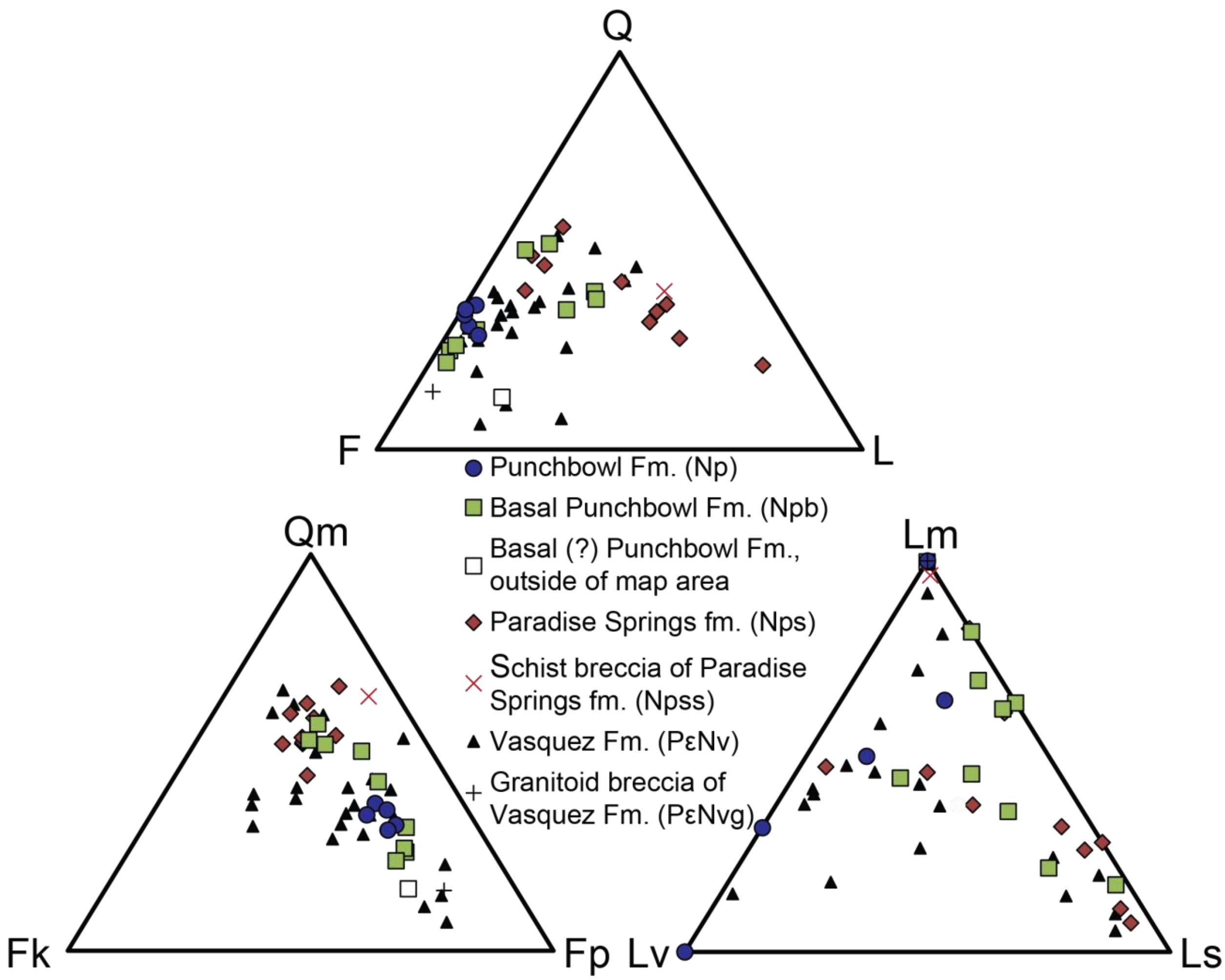

Figure 7: Sandstone composition of Oligocene-Miocene Vincent Gap strata. Composition determined using Gazzi-Dickinson point-count method and plotted on QFL, QmFkFp and LmLvLs ternary diagrams (grain categories defined in Table 2). Fm. = Formation; fm. = formation. Map unit symbols in parentheses (e.g., "Np") correspond to map units in Plates 1-3. One sample of basal(?) Punchbowl Formation is from well outside the map area of Plates 1, 2; it is plotted as a white-filled square, and corresponds to either map unit Npb or Np in Plates 1-3.

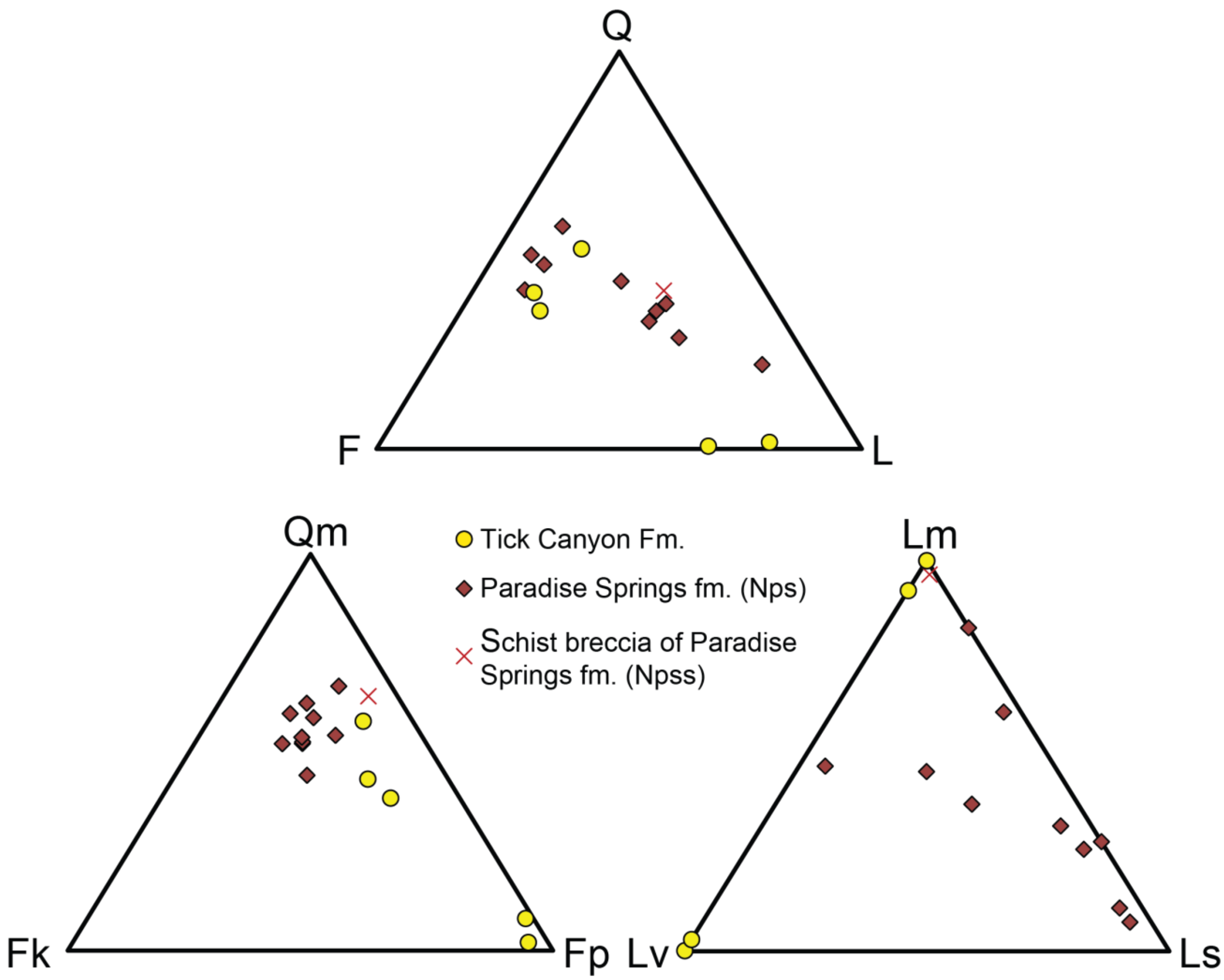

Figure 8: Comparison of sandstone composition of Paradise Springs and Tick Canyon formations. Details same as in Figure 6. Tick Canyon Formation is in Soledad region, outside of mapped area of Plates 1, 2.

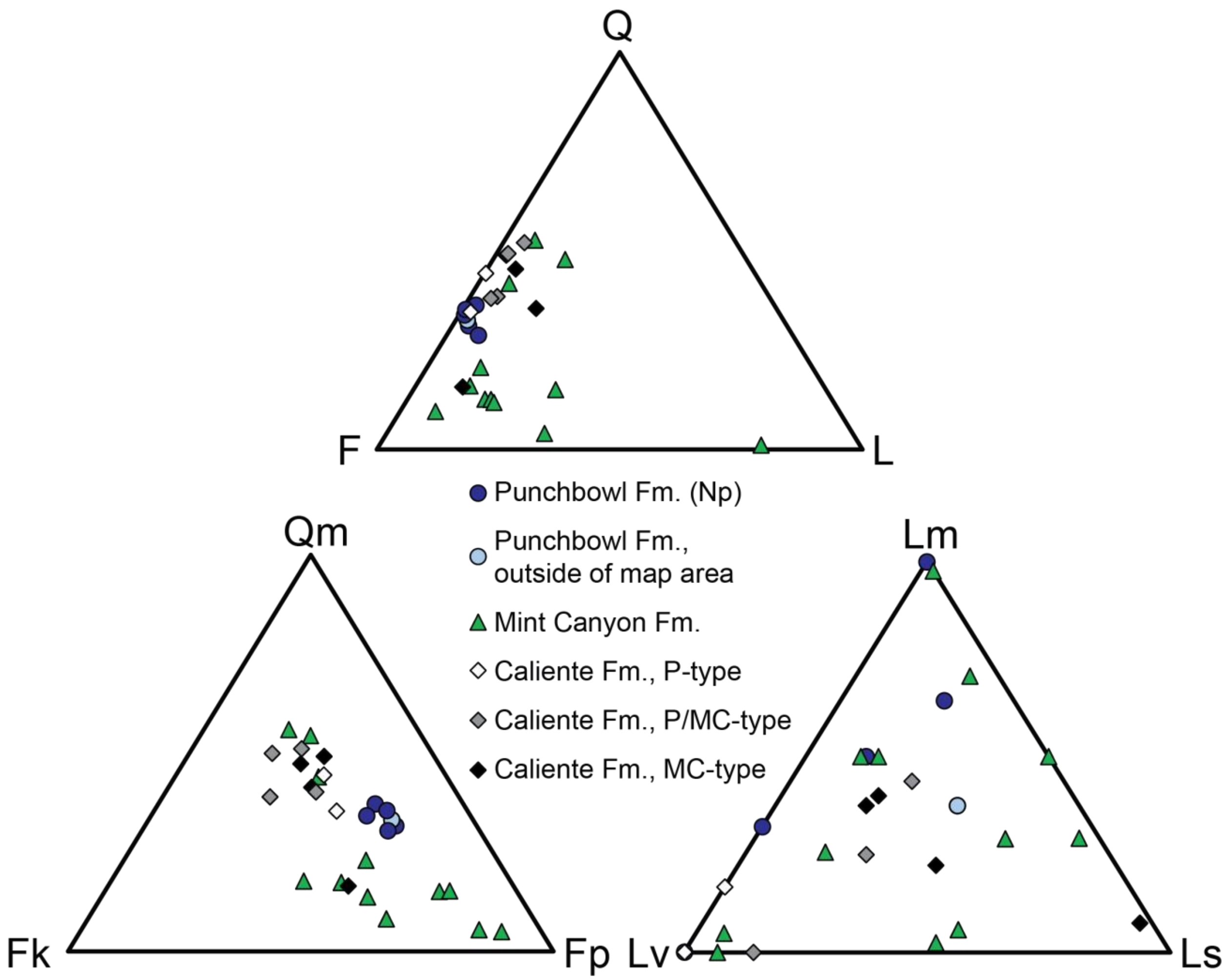

Figure 9: Comparison of sandstone composition of Punchbowl, Caliente and Mint Canyon formations. Details same as in Figure 6. Mint Canyon Formation is in Soledad region and Caliente Formation is in Tejon region; both are outside of mapped area of Plates 1, 2. One sample of Punchbowl Formation is from Soledad region; it is plotted with a lighter-blue fill than other Punchbowl Formation samples. “P-”, “P/MC-” and “MC-type” refer to Punchbowl-, Punchbowl/Mint Canyon-, and Mint Canyon-type, respectively; specific samples included in each category same as listed in Figure 16. Data for Mint Canyon and Caliente formations from Hoyt (2012).

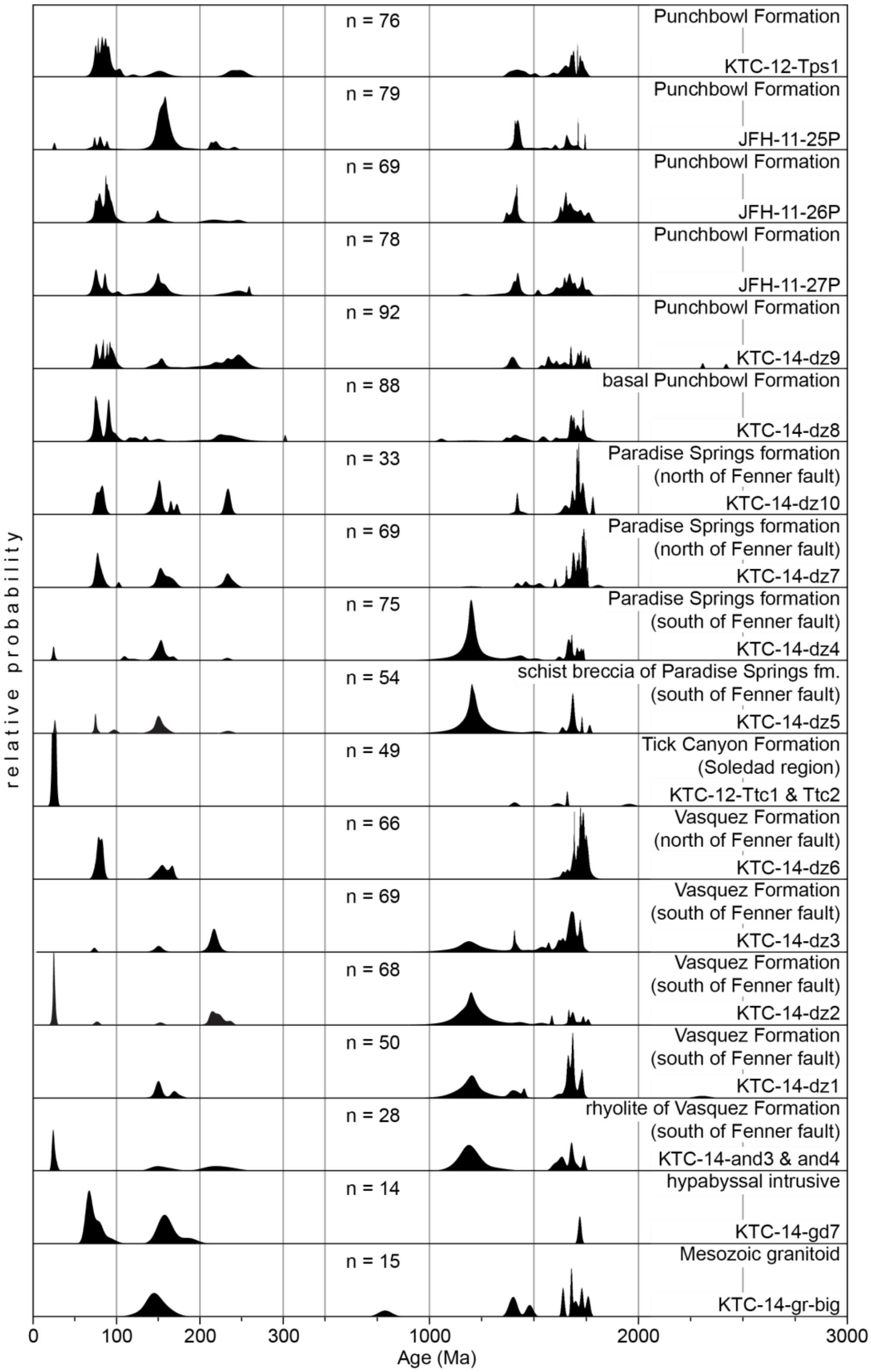
n = 76
Punchbowl Formation
KTC-12-Tps1
n = 79
Punchbowl Formation
JFH-11-25P
n = 69
Punchbowl Formation
JFH-11-26P
n = 78
Punchbowl Formation
JFH-11-27P
n = 92
Punchbowl Formation
KTC-14-dz9
n = 88
basal Punchbowl Formation
KTC-14-dz8
n = 33
Paradise Springs formation
(north of Fenner fault)
KTC-14-dz10
n = 69
Paradise Springs formation
(north of Fenner fault)
KTC-14-dz7
n = 75
Paradise Springs formation
(south of Fenner fault)
KTC-14-dz4
n = 54
schist breccia of Paradise Springs fm.
(south of Fenner fault)
KTC-14-dz5
n = 49
Tick Canyon Formation
(Soledad region)
KTC-12-Ttc1 & Ttc2
n = 66
Vasquez Formation
(north of Fenner fault)
KTC-14-dz6
n = 69
Vasquez Formation
(south of Fenner fault)
KTC-14-dz3
n = 68
Vasquez Formation
(south of Fenner fault)
KTC-14-dz2
n = 50
Vasquez Formation
(south of Fenner fault)
KTC-14-dz1
n = 28
rhyolite of Vasquez Formation
(south of Fenner fault)
KTC-14-and3 & and4
n = 14
hypabyssal intrusive
KTC-14-gd7
n = 15
Mesozoic granitoid
KTC-14-gr-big
relative probability
0
100
200
300
1000
2000
3000
Age (Ma)

Figure 10: Igneous- and detrital-zircon ages of all Vincent Gap samples. Relative-probability age distributions. Samples are arranged in approximate stratigraphic order, with youngest on top. Bottom three samples are igneous zircon; all others are detrital zircon. Note change of horizontal scale at 300 Ma; vertical scale also differs to left and right of this scale break, such that equal areas represent equal probability across graph. Labels indicate sample number and name of geologic unit. n = number of analyses. Three samples beginning “JFH-” are data of J.F. Hoyt, published in Ingersoll et al. (2013); all other data are of this study. Where peaks exceed height of plots, their upper parts are not shown.

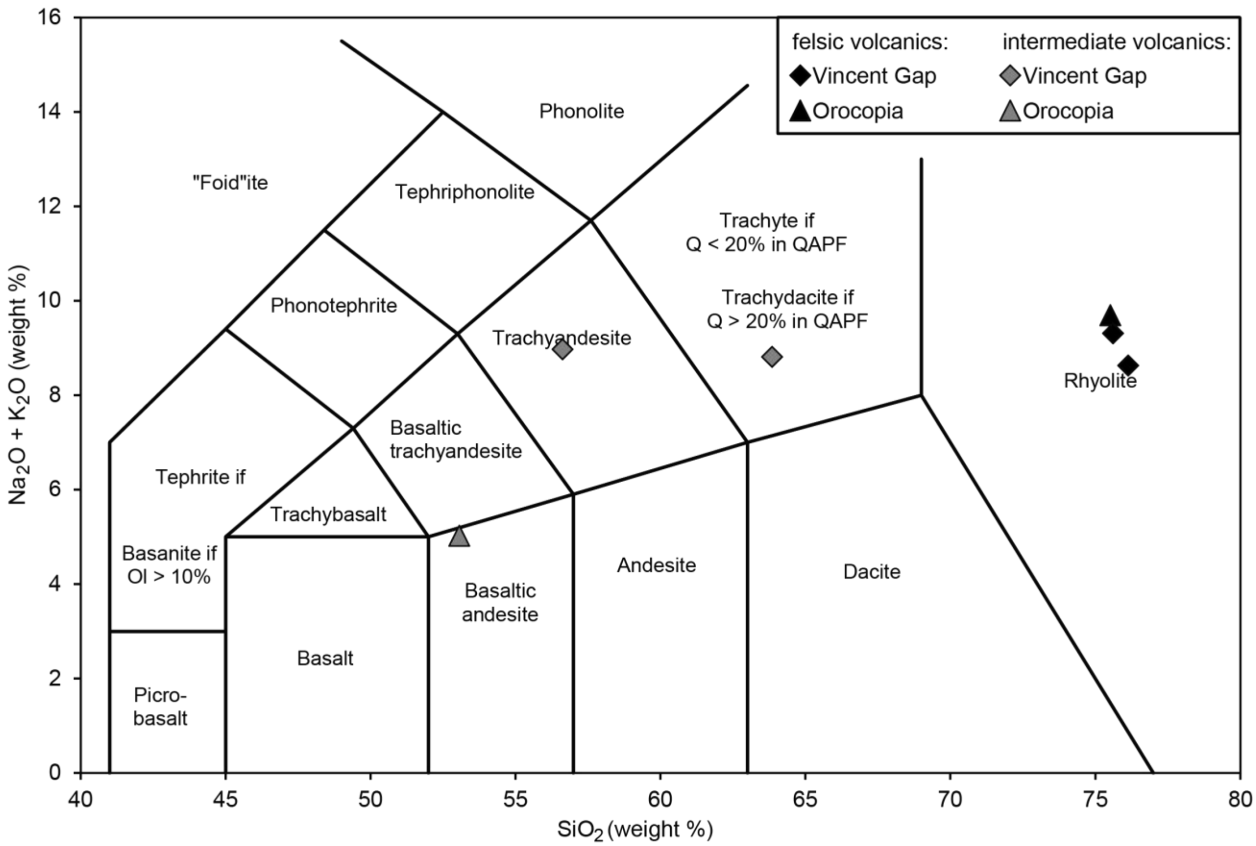

Figure 11: Classification of volcanic samples. Classification of volcanic samples according to classification of LeBas et al. (1986). “Vincent Gap” and “Orocopia” refer to samples from Vincent Gap and Orocopia regions, respectively. Vincent Gap region sample in trachyte/trachydacite field is trachyte.

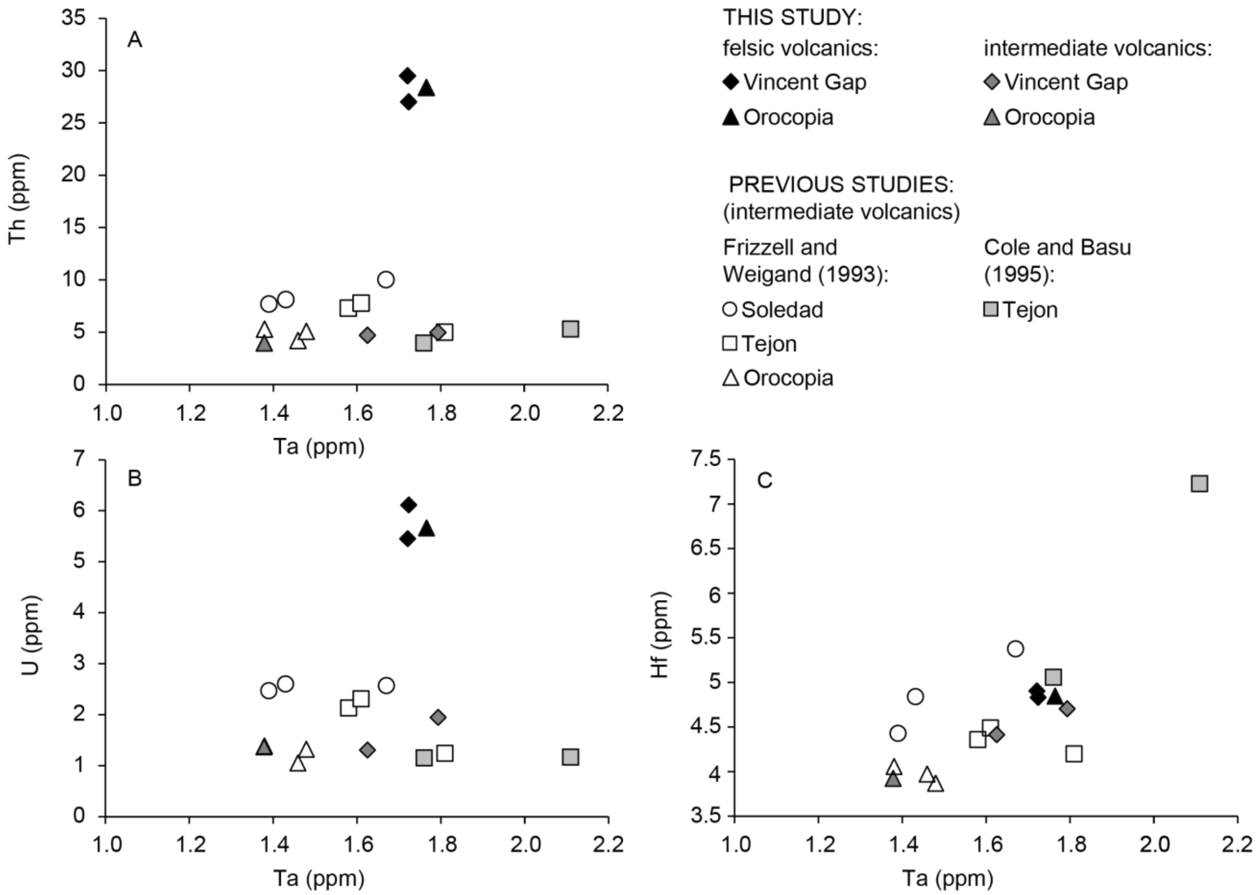

Figure 12: Plots of (A) Th, (B) U and (C) Hf vs. Ta for volcanic samples. "Vincent Gap" refers to samples from Vincent Gap region, etc. Scales of x-axes identical; scales of y-axes vary. Symbols with black and dark-gray interiors correspond to felsic and intermediate volcanics, respectively, analyzed in this study; symbols with white and light-gray interiors correspond to analyses of intermediate volcanics in Frizzell and Weigand (1993) and Cole and Basu (1995), respectively. Anomalous Soledad region sample of Cole and Basu (1995) with Ta > 2.6 ppm omitted. Figure after Frizzell and Weigand (1993).

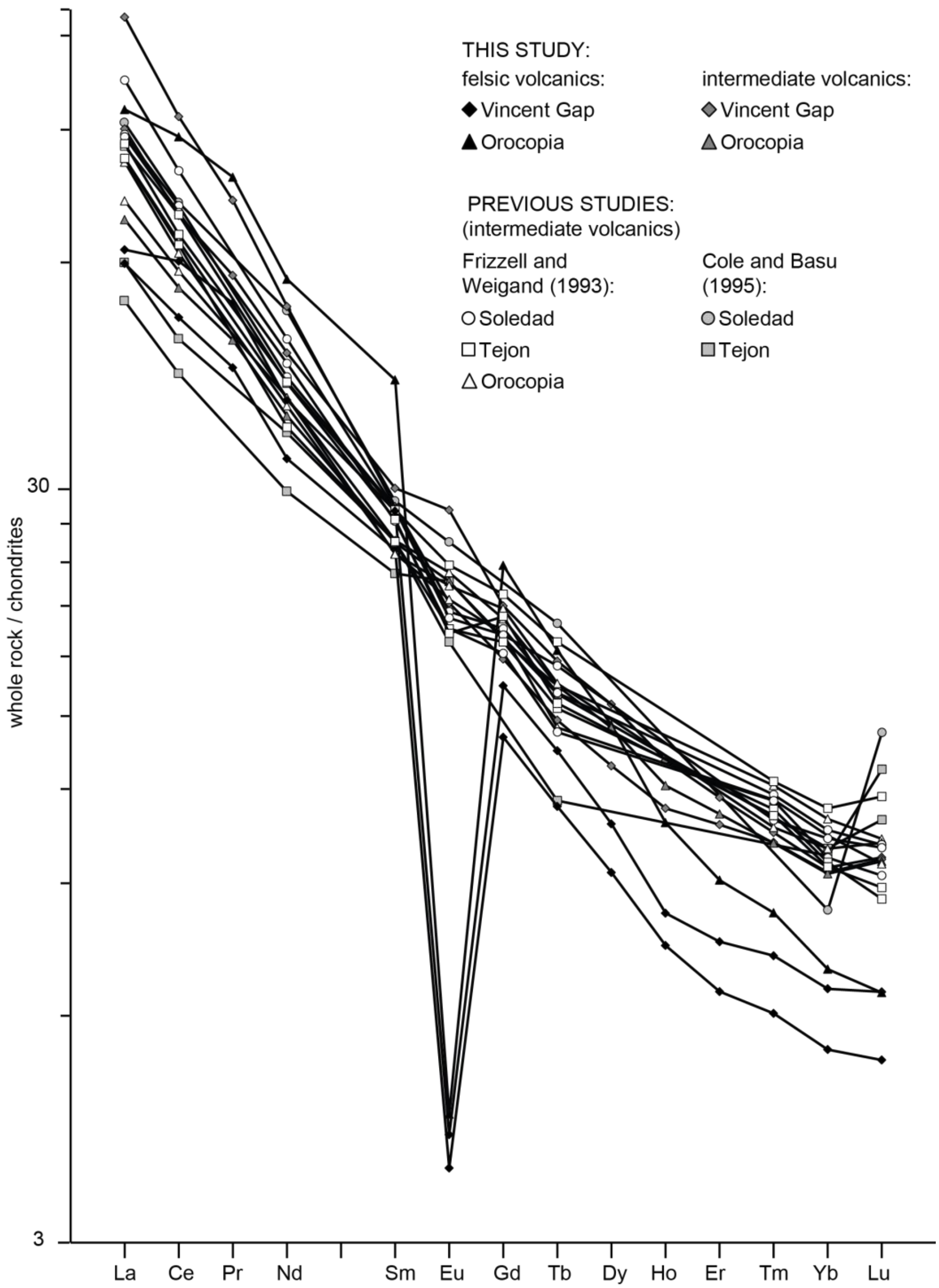

Figure 13: Chondrite-normalized rare-earth-element abundances of volcanic samples. Legend same as Figure 12. Chondrite values used are those of Anders and Grevesse (1989), multiplied by 1.3596 to maintain consistency with older literature, as in Korotev (1996). Scale of y-axis is logarithmic. Figure after Frizzell and Weigand (1993).

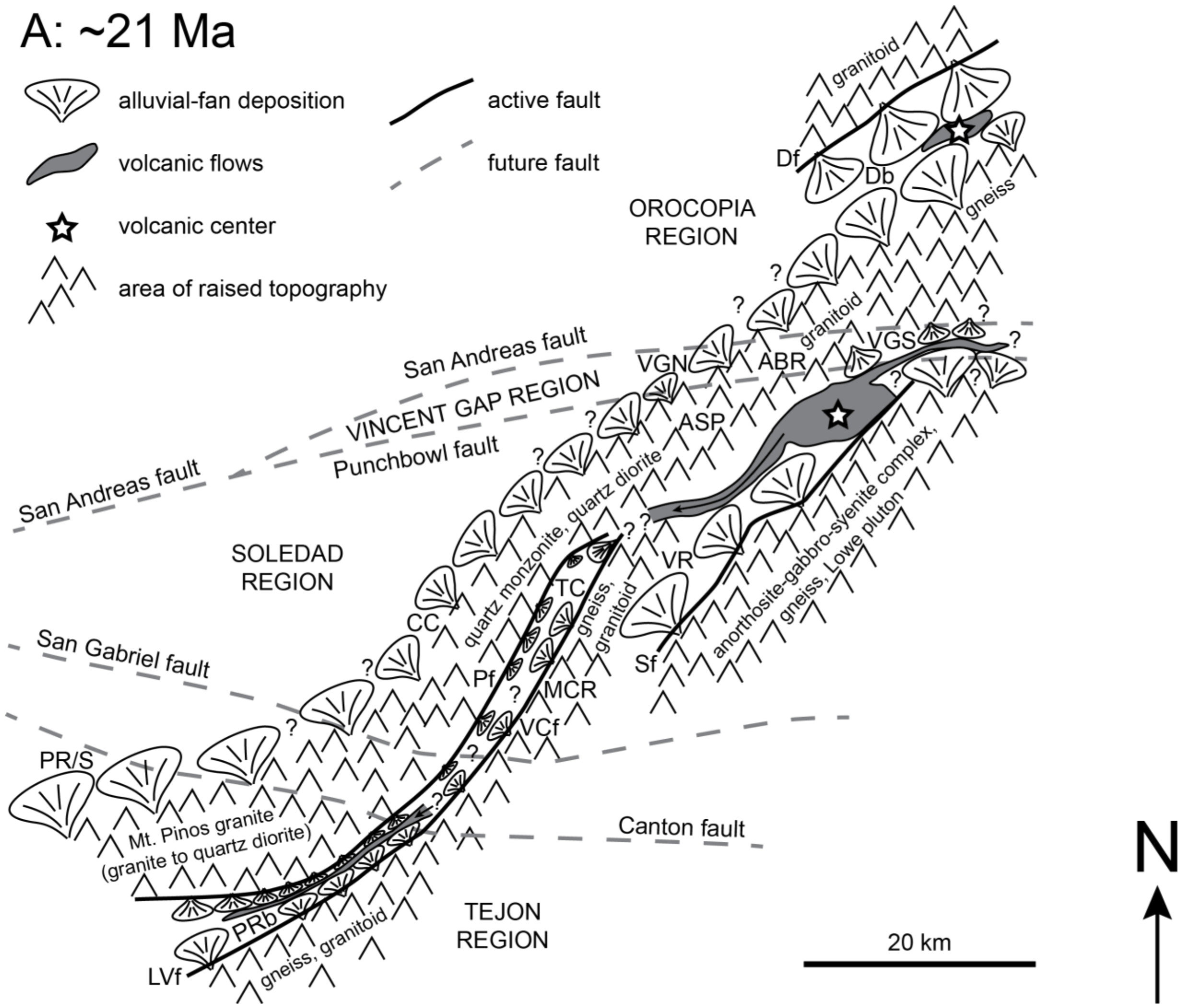

Figure 14: Schematic paleogeography, source rocks and depositional systems of Tejon-Soledad-Vincent Gap-Orocopia regions. A: Approximately 21 Ma, during deposition of Plush Ranch, Vasquez and Diligencia formations. ABR = ancestral Blue Ridge; ASP = ancestral Sierra Pelona; MCR = Mint Canyon Ridge; Df = Diligencia fault; LVf = Lockwood Valley (or Big Pine) fault; Pf = Pelona fault; Sf = Soledad fault; VCf = Vasquez Canyon fault; Db = Diligencia basin; PRb = Plush Ranch basin; PR/S = Plush Ranch/Simmler strata; CC = Charlie Canyon subbasin; TC = Texas Canyon subbasin; VR = Vasquez Rocks subbasin; VGN, VGS = Vasquez Formation of Vincent Gap region, north of and south of, respectively, the Fenner fault.

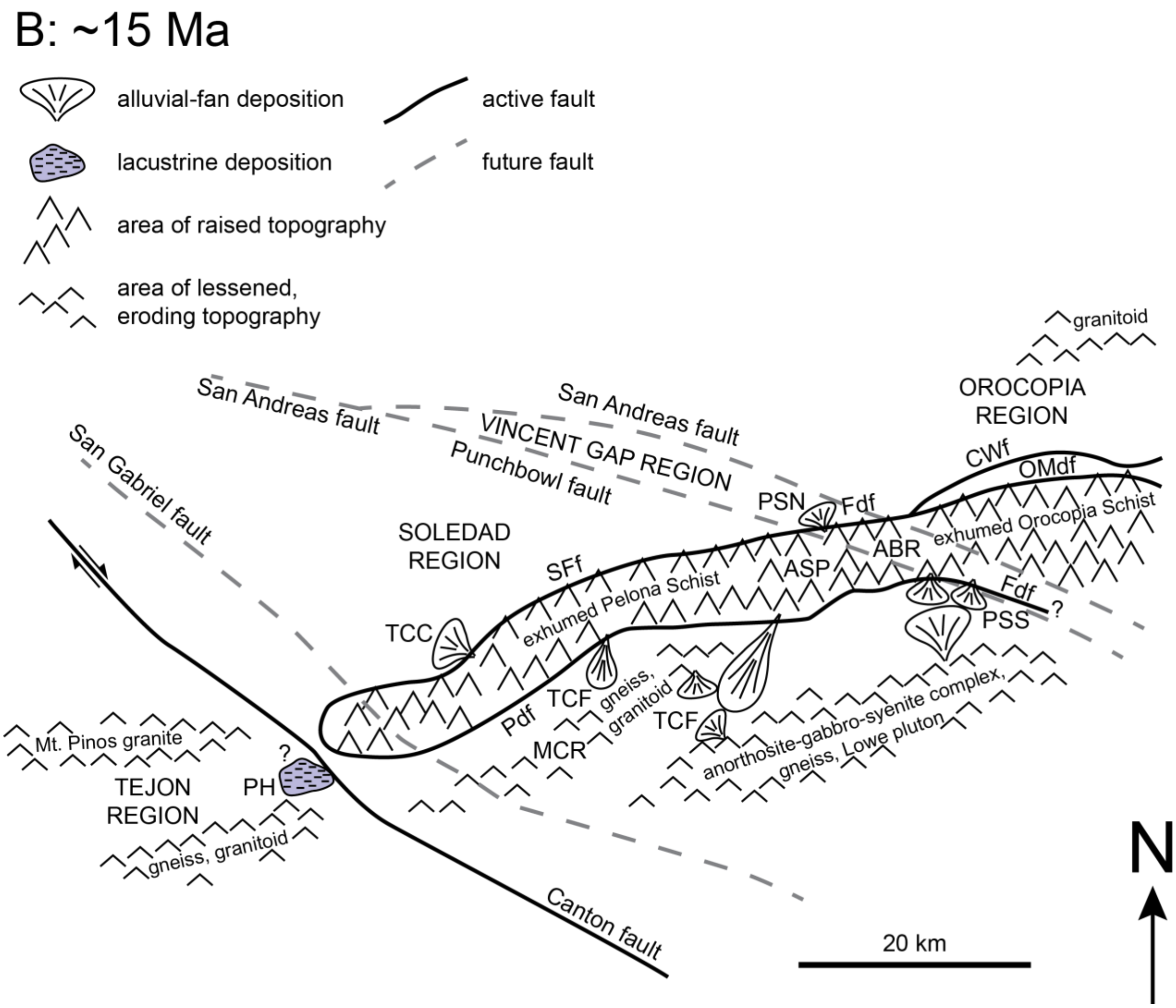

Figure 14: Schematic paleogeography, source rocks and depositional systems of Tejon-Soledad-Vincent Gap-Orocopia regions. B: Approximately 15 Ma, during deposition of Tick Canyon and Paradise Springs formations. ABR = ancestral Blue Ridge; ASP = ancestral Sierra Pelona; MCR = Mint Canyon Ridge; CWf = Clemens Well fault; Fdf = Fenner detachment fault; OMdf = Orocopia Mountains detachment fault; Pdf = Pelona detachment fault; SFf = San Francisquito fault; PH = “unnamed shale of Peanut Hill” of Dibblee (2006a); PSN, PSS = Paradise Springs formation, north of and south of, respectively, the Fenner fault; TCC = Tick Canyon Formation of Charlie Canyon; TCF = Tick Canyon Formation, type section. Note vertical-axis rotation of all regions except Tejon.

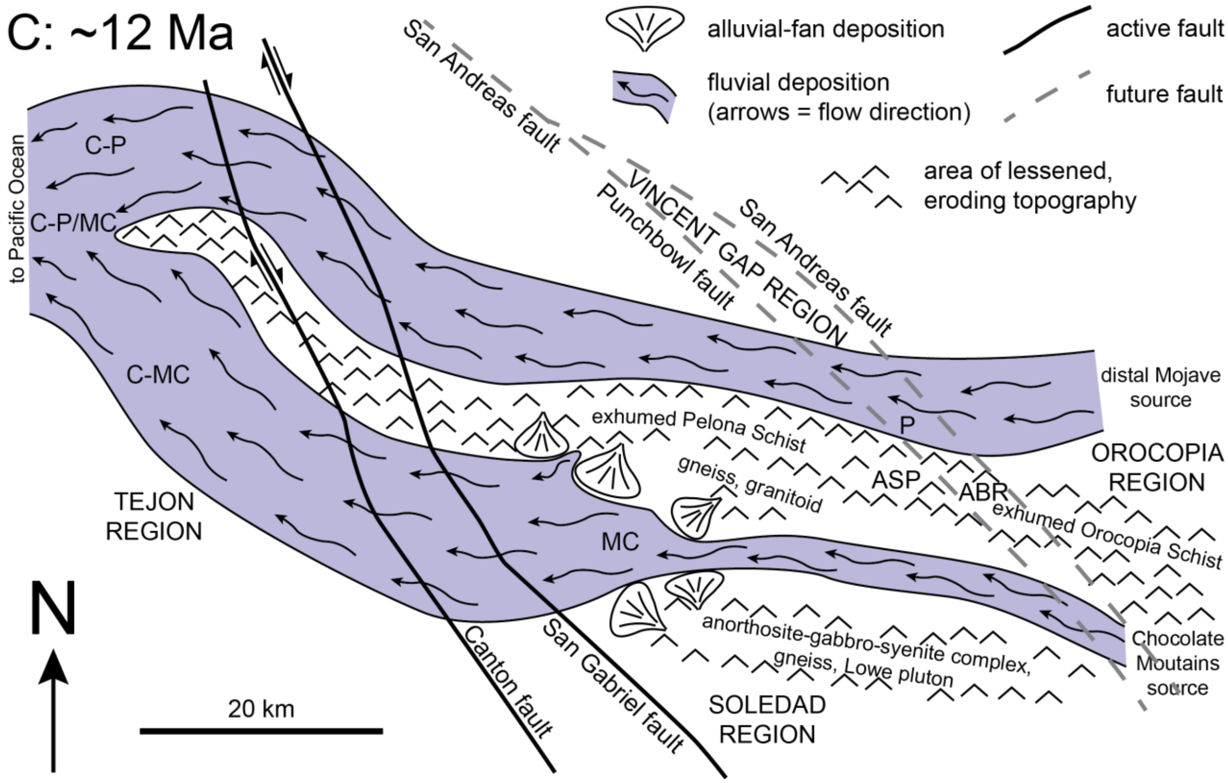

Figure 14: Schematic paleogeography, source rocks and depositional systems of Tejon-Soledad-Vincent Gap-Orocopia regions. C: Approximately 12 Ma, during deposition of Caliente, Mint Canyon and Punchbowl formations; slip is in the process of transferring from the dying Canton fault to the nascent San Gabriel fault. ABR = ancestral Blue Ridge; ASP = ancestral Sierra Pelona; C-MC, C-P, C-P/MC = Caliente Formation of Mint Canyon-, Punchbowl- and Punchbowl/Mint Canyon-type, respectively; MC = Mint Canyon Formation; P = Punchbowl Formation. See text and Figures 9, 16 for explanation of division of Caliente Formation into three types. Transrotational vertical-axis rotation of all regions except Tejon, already underway in B, is now complete (~53° clockwise), but subsequent rotations (Soledad region: ~16° counterclockwise; Vincent Gap region: ~28° counterclockwise; Orocopia region: ~41° clockwise), which bring these regions into their modern orientations, have yet to occur. Details of A, B and C after Ingersoll et al. (2014) and ideas and references presented in text.

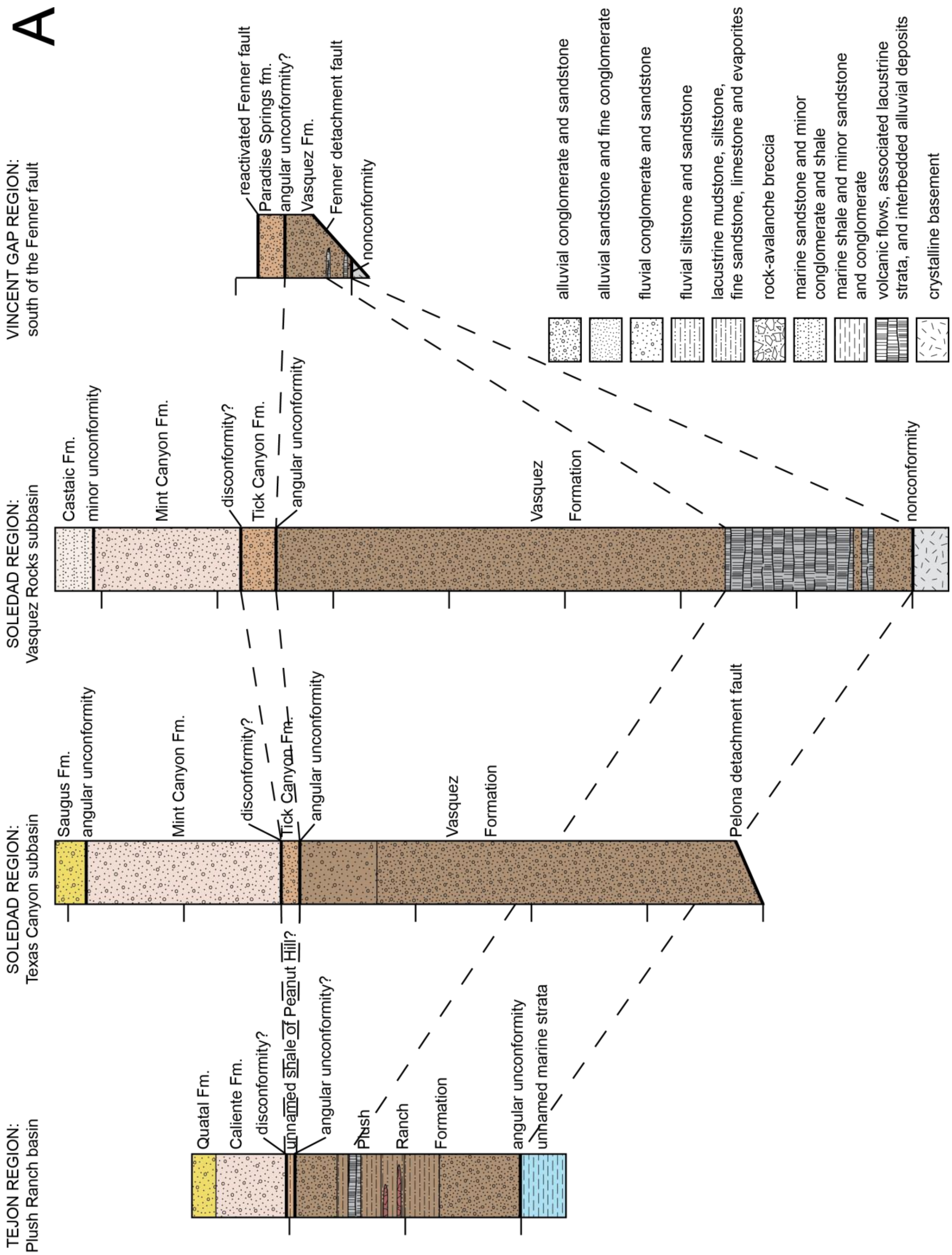
A
TEJON REGION:
Plush Ranch basin
Quatal Fm.
Caliente Fm.
disconformity?
unnamed shale of Peanut Hill?
angular unconformity?
Plush
Ranch
Formation
angular unconformity
unnamed marine strata
SOLEDAD REGION:
Texas Canyon subbasin
Saugus Fm.
angular unconformity
Mint Canyon Fm.
disconformity?
Tick Canyon Fm.
angular unconformity
Vasquez
Formation
Pelona detachment fault
SOLEDAD REGION:
Vasquez Rocks subbasin
Castaic Fm.
minor unconformity
Mint Canyon Fm.
disconformity?
Tick Canyon Fm.
angular unconformity
Vasquez
Formation
nonconformity
VINCENT GAP REGION:
south of the Fenner fault
reactivated Fenner fault
Paradise Springs fm.
angular unconformity?
Vasquez Fm.
Fenner detachment fault
nonconformity
alluvial conglomerate and sandstone
alluvial sandstone and fine conglomerate
fluvial conglomerate and sandstone
fluvial siltstone and sandstone
lacustrine mudstone, siltstone, fine sandstone, limestone and evaporites
rock-avalanche breccia
marine sandstone and minor conglomerate and shale
marine shale and minor sandstone and conglomerate
volcanic flows, associated lacustrine strata, and interbedded alluvial deposits
crystalline basement

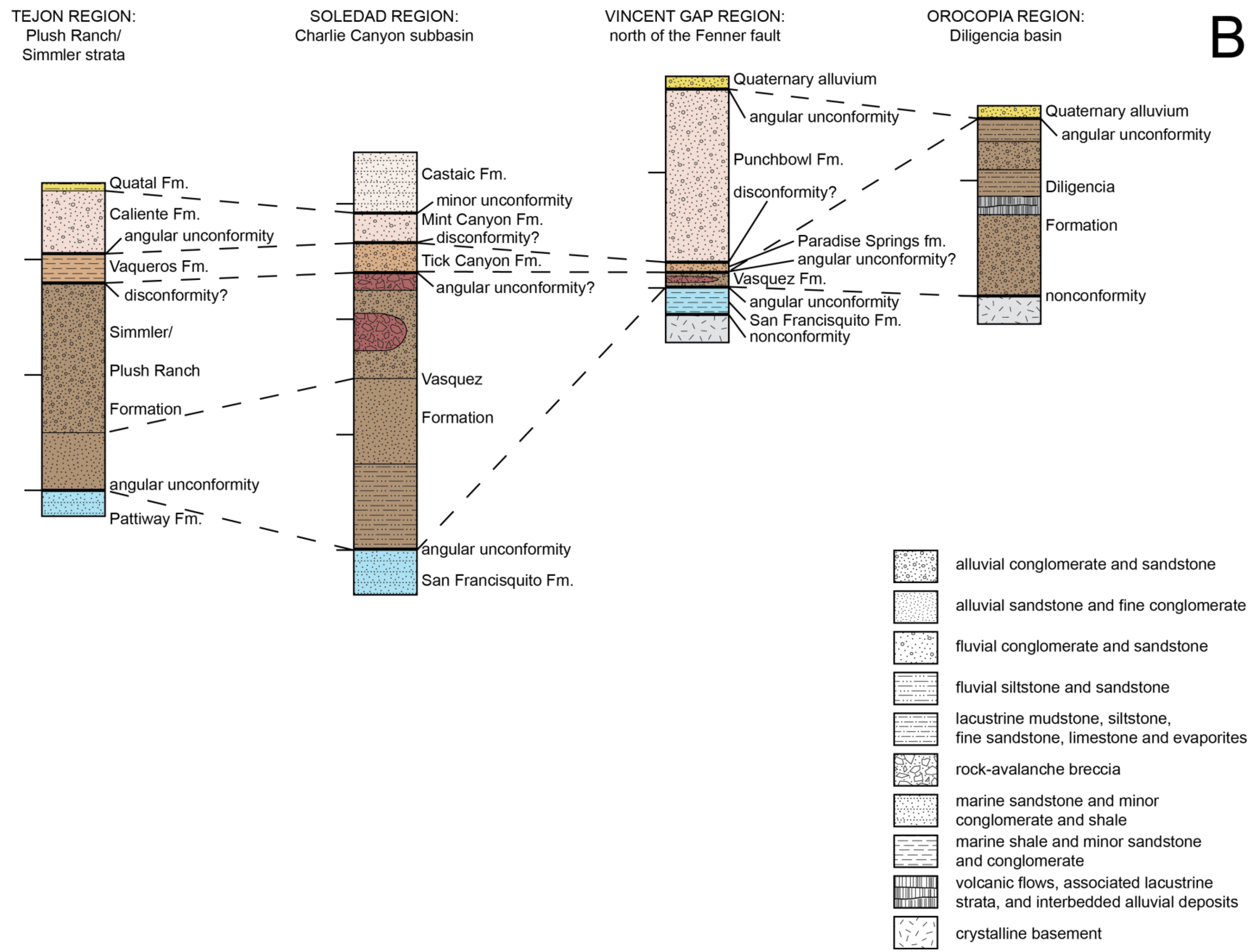
B
TEJON REGION:
Plush Ranch/
Simmler strata
SOLEDAD REGION:
Charlie Canyon subbasin
VINCENT GAP REGION:
north of the Fenner fault
OROCOPIA REGION:
Diligencia basin
Quatal Fm.
Caliente Fm.
angular unconformity
Vaqueros Fm.
disconformity?
Simmler/
Plush Ranch
Formation
angular unconformity
Pattiway Fm.
Castaic Fm.
minor unconformity
Mint Canyon Fm.
disconformity?
Tick Canyon Fm.
angular unconformity?
Vasquez
Formation
angular unconformity
San Francisquito Fm.
Quaternary alluvium
angular unconformity
Punchbowl Fm.
disconformity?
Paradise Springs fm.
angular unconformity?
Vasquez Fm.
angular unconformity
San Francisquito Fm.
nonconformity
Quaternary alluvium
angular unconformity
Diligencia
Formation
nonconformity
alluvial conglomerate and sandstone
alluvial sandstone and fine conglomerate
fluvial conglomerate and sandstone
fluvial siltstone and sandstone
lacustrine mudstone, siltstone,
fine sandstone, limestone and evaporites
rock-avalanche breccia
marine sandstone and minor
conglomerate and shale
marine shale and minor sandstone
and conglomerate
volcanic flows, associated lacustrine
strata, and interbedded alluvial deposits
crystalline basement

Figure 15: Schematic composite stratigraphic sections of the Vincent Gap region and offset equivalents. Sections are arranged from west (left) to east (right). Approximate present locations of these sections given in Figure 1; approximate paleogeographic locations given in Figure 14. Tick marks along left margins of columns are spaced every 1000 meters, and begin at base of Oligocene-Miocene strata. Units of matching color are equivalent. A: Basins south of the ancestral Sierra Pelona/ancestral Blue Ridge drainage divide of Figure 14. Sections are based on following sources: Tejon region: Carman (1964), Dibblee (2006a); Soledad region: Hendrix and Ingersoll (1987), Hendrix et al. (2010), Dibblee (1996a, b); Vincent Gap region: this study. B: Basins north of ancestral Sierra Pelona/ancestral Blue Ridge drainage divide of Figure 14. Sections are based on following sources: Tejon region: Dibblee (2005a, b); Soledad region: Sams (1964), Hendrix and Ingersoll (1987), Dibblee (1997a), this study; Vincent Gap region: Dibblee (1987), this study; Orocopia region: Spittler and Arthur (1982).

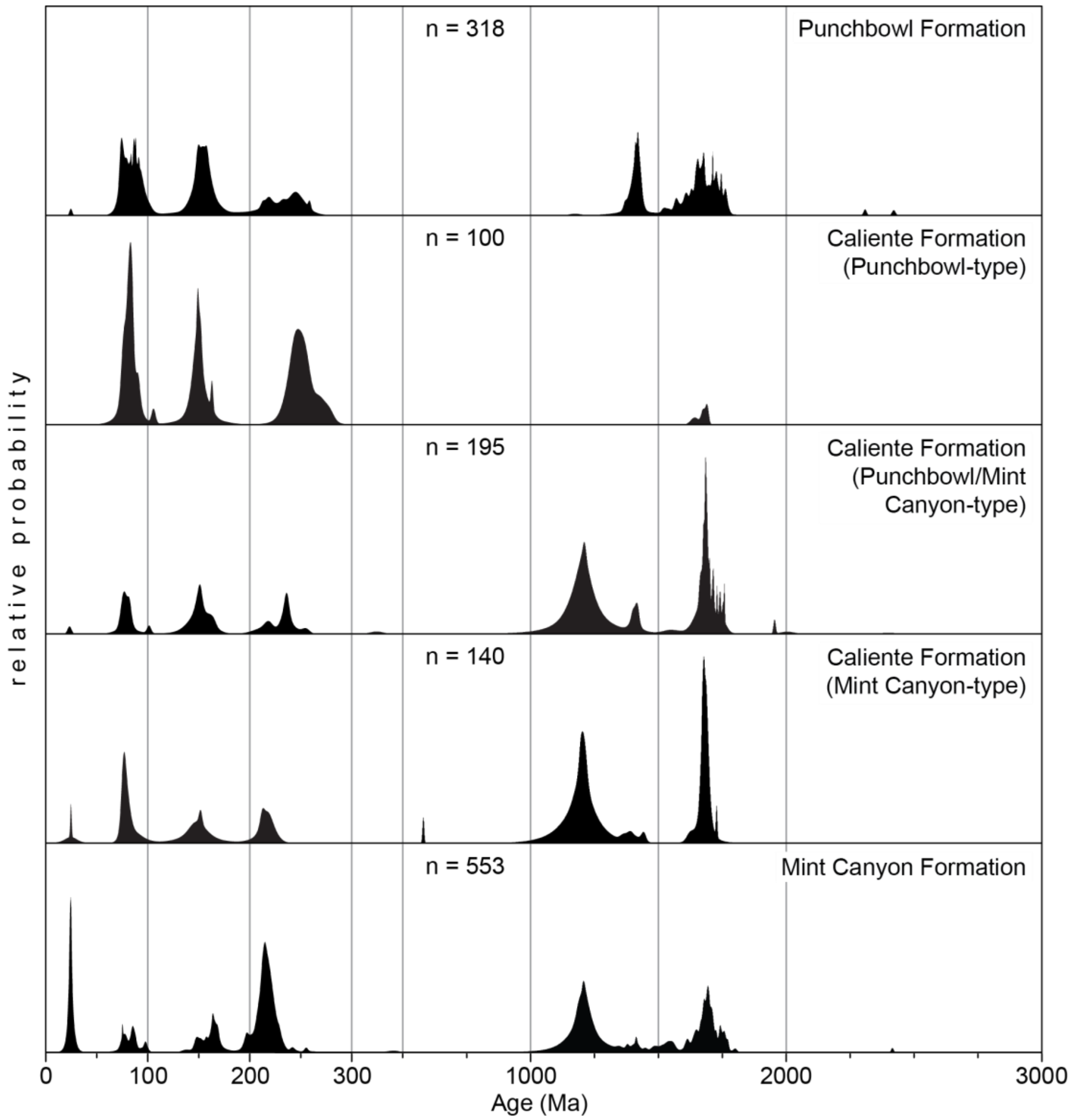

Punchbowl Formation
(total n = 318):
JFH-11-25P: n = 79
JFH-11-26P: n = 69
JFH-11-27P: n = 78
KTC-14-dz9: n = 92

Caliente Formation
(Punchbowl-type)
(total n = 100):
JFH-11-23C: n = 56
JFH-11-24C: n = 44

Caliente Formation
(Punchbowl/Mint Canyon-type)
(total n = 195):
JFH-11-19C: n = 42
JFH-11-20C: n = 32
JFH-11-21C: n = 74
JFH-11-22C: n = 47

Caliente Formation
(Mint Canyon-type)
(total n = 140):
JFH-11-15C: n = 31
JFH-11-16C: n = 36
JFH-11-17C: n = 39
JFH-11-18C: n = 34

Mint Canyon Formation
(total n = 553):
JFH-11-1M: n = 49
JFH-11-3M: n = 52
JFH-11-4M: n = 34
JFH-11-5M: n = 29
JFH-11-6M: n = 37
JFH-11-7M: n = 52
JFH-11-8M: n = 60
JFH-11-9M: n = 33
JFH-11-10M: n = 51
JFH-11-11M: n = 41
JFH-11-12M: n = 33
JFH-11-13M: n = 42
JFH-11-14M: n = 40

Figure 16: Comparison of detrital-zircon ages of Punchbowl, Caliente and Mint Canyon formations. Relative-probability age distributions. Breaks-in-scale as in Figure 10. n = total number of analyses. Each plot represents combination of multiple samples; name and number of analyses of each sample listed at bottom of figure. Samples JFH-11-25P, JFH-11-26P and JFH-11-27P are data of J.F. Hoyt, published in Ingersoll et al. (2013); samples JFH-11-21C and JFH-11-23C are data of Stang (2013); all other samples beginning “JFH-” are data of Hoyt (2012); sample KTC-14-dz9 is of this study. Data and locations of all Punchbowl Formation samples are presented in this study (Fig. 10; Appendices A, B). Locations of Caliente and Mint Canyon formation samples given in Appendix A; for data, see Hoyt (2012) and Stang (2013).

TABLE 1: DEFINITION OF CONGLOMERATE-CLAST CATEGORIES

Category	Symbol	Description
Pelona Schist	P.S.	Gray, coarse-grained mica schist
Gneiss	Gn.	Crystalline rock with gneissic compositional banding
Granitoid	Gr.	Felsic, phaneritic intrusive igneous rock
Other intrusive	O.I.	Intrusive igneous rock compositionally distinct from that of "granitoid" category
San Francisquito Formation sandstone and fine conglomerate	S.F.F.	Gray to tan sandstone and fine-grained conglomerate
Intermediate volcanics	I.V.	Dark gray to black volcanics of intermediate composition, containing abundant plagioclase laths
Felsic volcanics	F.V.	Gray, porphyritic volcanics of felsic composition
Reworked Vasquez Formation sandstone	R.V.F.	Maroon sandstone
Chloritic breccia and associated fault-related rock	C.B.	Chloritized and brecciated crystalline rock and other fractured and altered rock
Vein quartz, likely associated with Pelona Schist	V.Q.	Milky-white vein quartz
Unknown/unidentifiable	Unk.	Lithologies that do not fall within any of the above categories or could not be confidently identified

TABLE 2: DEFINITION OF ORIGINAL AND RECALCULATED SANDSTONE POINT-COUNT GRAIN CATEGORIES

Original Categories:

Category	**Symbol**	**Description**
quartz, monocrystalline	Qm	quartz crystal with a maximum diameter >0.0625 mm
quartz, polycrystalline	Qp	interlocking quartz crystals with maximum diameters <0.0625 mm; no other associated mineral phases
feldspar, plagioclase	Fp	plagioclase-feldspar crystal with a maximum diameter >0.0625 mm
feldspar, potassium	Fk	potassium-feldspar crystal with a maximum diameter >0.0625 mm
mica, monocrystalline	M	mica crystal with a maximum diameter >0.0625 mm
dense mineral, monocrystalline	D	crystal of any mineral phase not listed above with a maximum diameter >0.0625 mm
lithic fragment, metamorphic, aggregate	Lma	interlocking crystals with maximum diameters <0.0625 mm and little or no preferred orientation (typically quartz, feldspar and/or micas)
lithic fragment, metamorphic, tectonite	Lmt	interlocking crystals with maximum diameters <0.0625 mm and distinct preferred orientation (typically quartz, feldspar and/or micas)
lithic fragment, metamorphic, micaceous	Lmm	interlocking crystals of mica with maximum diameters <0.0625 mm; no other associated mineral phases
lithic fragment, metamorphic, metavolcanic	Lmv	interlocking crystals with maximum diameters <0.0625 mm recrystallized from a volcanic rock (commonly plagioclase and chlorite)
lithic fragment, volcanic, lathwork	Lvl	fragment of volcanic rock containing plagioclase laths
lithic fragment, volcanic, microlitic	Lvm	fragment of volcanic rock with groundmass containing plagioclase microlites
lithic fragment, volcanic, felsitic, seriate	Lvfs	fragment of volcanic rock with groundmass of variable crystal size
lithic fragment, volcanic, felsitic, granular	Lvfg	fragment of volcanic rock with equigranular, microcrystalline groundmass
lithic fragment, volcanic, vitric	Lvv	fragment of glassy volcanic rock
lithic fragment, sedimentary, siliciclastic	Lss	fragment of mudrock, i.e., grains have maximum diameters <0.0625 mm (siltstone, shale, mudstone)
lithic fragment, sedimentary, carbonate	Lsc	fragment of clastic or chemical sedimentary rock of dominantly carbonate composition and grain/crystal size <0.0625 mm
miscellaneous and unknown	M/U	any sand-sized grain which does not fall within one of the above categories or which could not be confidently identified
interstitial material	Int.	Interstitial material: cement, primary pore space, and detrital grains with maximum diameters <0.0625 mm

Recalculated Categories:

Category	**Symbol**	**Relationship to original categories**
total quartz	Q	Q = Qm + Qp
total feldspar	F	F = Fk + Fp
total lithics	L	L = Lma + Lmt + Lmm + Lmv + Lvm +Lvl +Lvfg +Lvfs + Lvv +Lss + Lsc
total metamorphic lithics	Lm	Lm = Lma + Lmt + Lmm + Lmv
total volcanic lithics	Lv	Lv = Lvm + Lvl + Lvfg + Lvfs + Lvv
total sedimentary lithics	Ls	Ls = Lss + Lsc
percent total quartz	QFL%Q	100% · Q / (Q + F + L)
percent total feldspar	QFL%F	100% · F / (Q + F + L)
percent total lithics	QFL%L	100% · L / (Q + F + L)
percent monocrystalline quartz	QmFkFp%Qm	100% · Qm / (Qm + Fk + Fp)
percent potassium feldspar	QmFkFp%Fk	100% · Fk / (Qm + Fk + Fp)
percent plagioclase feldspar	QmFkFp%Fp	100% · Fp / (Qm + Fk + Fp)
percent metamorphic lithics	LmLvLs%Lm	100% · Lm / (Lm + Lv + Ls)
percent volcanic lithics	LmLvLs%Lv	100% · Lv / (Lm + Lv + Ls)
percent sedimentary lithics	LmLvLs%Ls	100% · Ls / (Lm + Lv + Ls)

TABLE 3: RECALCULATED SANDSTONE POINT-COUNT DATA

Sample	QFL %Q	QFL %F	QFL %L	QmFkFp %Qm	QmFkFp %Fk	QmFkFp %Fp	LmLvLs %Lm	LmLvLs %Lv	LmLvLs %Ls	Fmk %M	Fmk %D	Qp/Q	Fp/F
Punchbowl Formation (map unit Np in Plates 1-3; some samples are from just outside of mapped area of Plates 1, 2):													
KTC-14-Np1	36.3	61.4	2.3	37.1	18.1	44.7	50.0	37.5	12.5	8.9	2.6	0.00	0.71
KTC-14-Np2	31.1	65.5	3.4	31.7	16.6	51.8	64.3	14.3	21.4	6.0	0.4	0.02	0.76
JFH-11-25P*	28.7	64.7	6.6	30.4	18.9	50.8	32.1	67.9	0.0	3.2	2.1	0.02	0.73
JFH-11-26P*	33.8	65.0	1.2	34.2	21.3	44.5	100.0	0.0	0.0	3.6	1.7	0.00	0.68
JFH-11-27P*	35.2	64.1	0.7	35.5	16.5	48.0	0.0	100.0	0.0	4.0	1.5	0.00	0.74
Punchbowl Formation (in the Soledad region, outside of mapped area; offset equivalent of map unit Np in Plates 1-3)													
KTC-12-Tps1	32.5	65.1	2.4	33.1	16.7	50.2	37.5	25.0	37.5	6.4	2.5	0.01	0.75
Basal Punchbowl Formation (map unit Npb in Plates 1-3):													
KTC-14-Nprc59	30.1	64.4	5.5	31.1	14.7	54.2	45.5	18.2	36.4	6.3	1.1	0.03	0.79
KTC-14-Nprc60	50.2	44.3	5.5	53.1	23.8	23.1	44.4	33.3	22.2	7.8	0.8	0.00	0.49
KTC-14-Np3	24.9	72.5	2.6	24.8	17.9	57.2	81.8	0.0	18.2	4.0	0.0	0.04	0.76
KTC-14-Npb1	26.1	70.6	3.2	25.8	17.8	56.4	21.4	14.3	64.3	2.3	0.4	0.06	0.76
KTC-14-Npb2	21.9	74.7	3.4	22.7	21.0	56.3	63.6	0.0	36.4	3.6	1.6	0.00	0.73
JFH-11-28P*	51.7	38.6	9.7	57.2	19.9	22.9	35.9	15.4	48.7	1.8	0.7	0.00	0.54
Basal (?) Punchbowl Formation (outside of mapped area; corresponds to map unit Npb or Np in Plates 1-3):													
P7-14-06-1**	13.1	67.7	19.2	15.8	22.0	62.2	100.0	0.0	0.0	20.0	12.3	0.03	0.74
Paradise Springs formation (map unit Nps in Plates 1-3):													
KTC-14-Nprc47	40.0	49.4	10.6	44.2	28.6	27.2	47.2	47.2	5.6	5.8	0.0	0.02	0.49
KTC-14-Nprc51	46.3	42.3	11.4	52.2	25.5	22.3	45.8	27.1	27.1	4.0	0.6	0.01	0.47
KTC-14-Nprc61	56.0	33.7	10.4	62.3	19.6	18.1	37.5	21.9	40.6	2.4	0.3	0.01	0.48
Schist breccia of Paradise Springs formation (map unit Npss in Plates 1, 2):													
KTC-14-dz5	39.8	20.9	39.3	64.1	6.0	29.9	96.2	1.3	2.5	21.9	4.5	0.06	0.83
Tick Canyon Formation (in the Soledad region, outside of mapped area of Plates 1, 2; an offset equivalent of the Paradise Springs formation):													
P4-08-06-2**	1.6	18.2	80.2	8.1	1.6	90.3	0.0	100.0	0.0	0.0	0.6	0.00	0.98
P2-11-06-3**	34.7	49.0	16.3	38.4	14.2	47.4	92.3	7.7	0.0	27.0	0.8	0.12	0.77
P2-11-06-5**	39.3	47.9	12.8	43.2	16.5	40.3	100.0	0.0	0.0	14.3	0.0	0.07	0.71
P4-08-06-6**	0.7	31.3	68.1	2.0	4.1	93.9	2.9	97.1	0.0	0.8	0.6	0.00	0.96
P2-11-06-7**	50.3	32.5	17.1	57.8	10.2	32.0	100.0	0.0	0.0	24.2	0.7	0.12	0.76
Vasquez Formation (map unit PɛNv in Plates 1-3):													
KTC-12-Tpc1	29.4	57.5	13.1	33.6	16.1	50.3	72.0	16.0	12.0	1.9	0.0	0.01	0.76
KTC-13-Tprc3	34.6	54.7	10.7	38.3	33.9	27.7	19.5	4.9	75.6	0.0	0.0	0.02	0.45
KTC-13-Tprc8	7.7	58.1	34.2	11.1	21.1	67.8	11.9	88.1	0.0	0.6	5.5	0.06	0.76
KTC-13-Tprc9	37.2	47.9	14.9	43.3	15.7	41.0	42.9	30.2	27.0	1.7	0.0	0.02	0.72
KTC-13-Tprc10	11.2	67.8	21.0	13.9	16.2	70.0	14.8	82.7	2.5	4.2	3.8	0.02	0.81
KTC-13-Tprc12	27.4	65.4	7.2	29.3	24.6	46.1	58.1	41.9	0.0	4.2	2.7	0.01	0.65
KTC-13-Tprc13	27.3	69.0	3.7	28.1	31.5	40.4	64.3	35.7	0.0	0.8	0.3	0.01	0.56
KTC-13-Tprc15	33.7	57.5	8.7	36.6	22.7	40.6	41.7	52.8	5.6	2.2	0.7	0.01	0.64
KTC-13-Tprc16	19.6	69.6	10.8	21.7	11.5	66.8	45.9	37.8	16.2	5.4	1.3	0.01	0.85
KTC-13-Tprc19	6.3	75.5	18.2	7.1	18.4	74.4	37.7	56.5	5.8	2.6	1.4	0.08	0.80
KTC-13-Tprc24	25.6	48.1	26.3	34.5	25.5	40.0	17.8	61.0	21.2	0.0	0.2	0.01	0.61
KTC-13-Tprc25f	38.2	56.0	5.8	40.5	13.3	46.2	47.6	42.9	9.5	0.5	0.0	0.00	0.78
KTC-13-Tprc29	53.7	35.9	10.4	59.5	17.7	22.8	53.8	46.2	0.0	2.0	0.3	0.02	0.56
KTC-13-Tprc36	39.6	56.1	4.3	41.1	32.3	26.6	81.3	6.3	12.5	2.2	0.2	0.01	0.45
KTC-14-Tprc40	50.0	43.3	6.7	53.5	4.2	42.3	91.7	4.2	4.2	1.8	0.0	0.01	0.91
KTC-14-Tprc44	31.4	59.5	9.1	34.1	20.8	45.1	26.5	38.2	35.3	4.1	0.7	0.02	0.68
KTC-14-Tprc45	35.8	49.6	14.6	41.1	21.8	37.2	40.3	53.2	6.5	2.2	0.2	0.03	0.63
KTC-14-Nprc48	40.5	40.2	19.3	50.0	24.0	26.0	37.3	28.8	33.9	1.5	0.3	0.01	0.52
KTC-14-Nprc50	36.1	54.4	9.5	39.4	42.1	18.5	58.3	30.6	11.1	3.1	0.5	0.02	0.31
KTC-14-Nprc56	36.3	62.5	1.3	36.7	43.8	19.5	100.0	0.0	0.0	1.5	0.0	0.00	0.31
KTC-14-Nprc57	29.8	63.8	6.4	31.8	27.9	40.3	14.3	14.3	71.4	3.0	0.3	0.00	0.59
KTC-14-Nprc58	30.5	65.9	3.6	31.3	46.3	22.4	80.0	20.0	0.0	2.6	0.0	0.01	0.33
Granitoid breccia unit of Vasquez Formation (map unit PɛNvg in Plates 1-3):													
KTC-14-Nprc49	14.5	81.2	4.3	15.2	14.9	69.9	100.0	0.0	0.0	0.2	0.0	0.00	0.82

*Collected and prepared in the same manner as in this study by Johanna Hoyt in 2011; independently determined point counts of these samples presented in Stang, 2013.

**Collected and prepared in the same manner as in this study by Clinton Colasanti in 2006.

TABLE 4: RECALCULATED SANDSTONE POINT-COUNT DATA OF RAYMOND V. INGERSOLL (UNPUBLISHED)

Sample	QFL %Q	QFL %F	QFL %L	QmFkFp %Qm	QmFkFp %Fk	QmFkFp %Fp	LmLvLs %Lm	LmLvLs %Lv	LmLvLs %Ls	Fmk %M	Fmk %D	Qp/Q	Fp/F
Basal Punchbowl Formation (map unit Npb in Plates 1-3):													
P13C	39.7	35.3	25.0	52.0	21.0	27.0	69.4	4.8	25.8	1.8	1.4	0.04	0.56
P17	37.8	35.9	26.3	50.3	14.4	35.4	62.1	3.4	34.5	5.1	0.4	0.04	0.71
P18	35.1	43.4	21.5	42.6	14.8	42.6	17.1	2.6	80.3	1.3	0.5	0.08	0.74
Paradise Springs formation (map unit Nps in Plates 1-3):													
P7a	32.0	27.8	40.2	52.6	25.3	22.2	10.9	4.7	84.4	1.2	0.3	0.04	0.47
P7b	27.9	23.7	48.4	53.8	24.8	21.4	7.3	4.4	88.3	0.0	0.0	0.01	0.46
P7c	34.7	25.0	40.3	54.3	17.7	28.0	61.1	3.5	35.4	3.6	0.6	0.14	0.61
P9	36.5	22.1	41.4	59.7	24.3	16.0	25.9	4.6	69.4	0.7	0.4	0.10	0.40
P11a	21.2	9.9	68.9	66.7	10.8	22.5	27.9	0.0	72.1	2.4	4.5	0.06	0.68
P11b	42.2	28.4	29.4	58.7	20.0	21.3	31.9	6.4	61.7	0.6	0.6	0.04	0.52
P12b	48.8	43.7	7.5	52.1	29.7	18.2	82.6	0.0	17.4	1.5	0.3	0.02	0.38
Vasquez Formation (map unit PεNv in Plates 1-3):													
P1	45.9	23.6	30.5	65.7	22.9	11.4	5.4	8.6	86.0	0.0	0.0	0.01	0.33
P2a	42.4	27.7	29.9	60.0	27.9	12.1	9.7	6.5	83.9	0.3	0.0	0.02	0.30
P2b	50.7	29.7	19.6	62.1	22.4	15.5	24.1	12.1	63.8	0.3	0.0	0.04	0.41

APPENDIX A: LATITUDE AND LONGITUDE OF SAMPLE AND MEASUREMENT LOCATIONS

Measurement #	(DMS)	(DMS)	(Plates 1, 2)	Ss.	Cgl.	Plct.	D.Z.	I.Z.	T.E.V.	Photo:
Field Observation Site #206	~N34°23'37.5"††	~W117°48'58.8"††	Np							B3
Field Observation Site #361	N34°24'49.1"	W117°50'12.8"	Pεsf							B20
Field Observation Site #366	N34°24'42.4"	W117°50'20.9"	Np							B22
Field Observation Site #379	N34°24'25.9"	W117°50'39.4"	Np							B24
Field Observation Site #394	N34°24'11.4"	W117°50'48.6"	Np/Mzqdc							B26
JFH-11-25P	N34°25'01.9"	W117°51'26.0"	Np§§	X			X			
JFH-11-26P	N34°25'0.03"	W117°51'13.5"	Np§§	X			X			
JFH-11-27P	N34°26'28.0"	W117°53'46.5"	Np§§	X			X			
JFH-11-28P	N34°24'35.5"	W117°50'14.7"	Npb	X						
KTC-12-Tpc1 / KTC-14-dz3	N34°22'26.8"	W117°45'07.8"	PεNv	X	X	X	X			B1
KTC-12-Tps1	N34°31'49.9 "	W118°05'24.9"	Np§§	X			X			
KTC-12-Ttc1	N34°31'22.3"	W118°06'36.4"	None§§§				X			
KTC-12-Ttc2	N34°31'20.7"	W118°05'52.9"	None§§§				X			
KTC-13-and3	~N34°22'49.8"*††	~W117°46'16.4"*††	Pεvv					X	X	
KTC-13-Ndva	*#	*#	None§§§§						X	
KTC-13-Ndvb	*#	*#	None§§§§						X	
KTC-13-Tprc3	N34°21'34.0"	W117°43'38.8"	PεNv	X						
KTC-13-Tprc8	N34°22'23.9"	W117°45'15.5"	PεNv	X						
KTC-13-Tprc9	N34°22'16.1"	W117°45'00.9"	PεNv	X	X	X				
KTC-13-Tprc10	N34°22'01.1"	W117°44'27.3"	PεNv	X						
KTC-13-Tprc12	N34°22'01.9"	W117°44'29.2"	PεNv	X						
KTC-13-Tprc13	N34°21'38.2"	W117°43'35.8"	PεNv	X	X	X				
KTC-13-Tprc15	N34°21'29.4"	W117°43'26.8"	PεNv	X						
KTC-13-Tprc16	N34°21'21.5"	W117°43'19.2"	PεNv	X						
KTC-13-Tprc17	N34°21'23.8"	W117°43'09.2"	PεNv		X					
KTC-13-Tprc19	N34°20'56.6"	W117°42'31.5"	PεNv	X						
KTC-13-Tprc23 / KTC-14-dz1	N34°21'22.1"	W117°43'04.5"	PεNv		X		X			
KTC-13-Tprc24	N34°21'23.3"	W117°42'56.6"	PεNv	X						
KTC-13-Tprc25f	N34°21'21.1"	W117°42'50.5"	PεNv	X						
KTC-13-Tprc26	N34°22'57.1"	W117°46'39.8"	PεNv		X	X				
KTC-13-Tprc29	N34°22'54.0"	W117°46'22.6"	PεNv	X						
KTC-13-Tprc32	N34°22'49.1"	W117°46'16.4"	PεNv		X					
KTC-13-Tprc36	N34°22'44.6"	W117°46'02.7"	PεNv	X						
KTC-14-and4	N34°21'22.1"	W117°43'04.5"	Pεvv§					X	X	
KTC-14-dz2	N34°21'21.4"	W117°43'18.7"	PεNv				X			
KTC-14-dz5	N34°23'21.8"	W117°47'48.3"	Npss	X	X		X			B7
KTC-14-gd7	~N34°21'11.4"†	~W117°43'36.2"†	Pε?gd					X		
KTC-14-gr-big	~N34°22'25.6"*††	~W117°45'06.9"*††	Mzgr					X		
KTC-14-Np1	N34°24'29.8"	W117°50'38.9"	Np	X						
KTC-14-Np2 / KTC-14-dz9	N34°23'38.0"	W117°48'59.8"	Np	X	X	X	X			B15
KTC-14-Np3	~N34°24'21.5"††	~W117°50'09.6"††	Npb	X						
KTC-14-Npb1	~N34°24'23.4"††	~W117°50'25.6"††	Npb	X						
KTC-14-Npb2	~N34°24'13.9"††	~W117°50'27.1"††	Npb	X						
KTC-14-Nprc47 / KTC-14-dz7	N34°23'33.4"	W117°48'30.9"	Nps	X	X	X	X			B9
KTC-14-Nprc48 / KTC-14-dz6	N34°23'36.2"	W117°48'31.5"	PεNv	X	X	X	X			B10
KTC-14-Nprc49	N34°23'29.0"	W117°47'43.3"	PεNvg	X	X					
KTC-14-Nprc50	N34°23'26.9"	W117°47'43.4"	PεNv	X						
KTC-14-Nprc51 / KTC-14-dz4	N34°23'17.3"	W117°47'43.5"	Nps	X	X	X	X			B5
KTC-14-Nprc56	N34°23'29.3"*	W117°47'52.0"*	PεNv	X						

KTC-14-Nprc57	N34°23'35.1"	W117°47'56.4"	PɛNv	X	X	X				B17
KTC-14-Nprc58	N34°23'28.2"	W117°47'57.5"	PɛNv	X						
KTC-14-Nprc59 / KTC-14-dz8	N34°23'25.9"	W117°48'25.8"	Npb	X	X	X	X			B19
KTC-14-Nprc60	N34°24'20.7"	W117°50'40.6"	Npb	X						
KTC-14-Nprc61 / KTC-14-dz10	N34°23'41.3"	W117°49'02.8"	Nps	X	X	X	X			
KTC-14-Nvg	N34°23'36.7"††	W117°48'08.6"††	PɛNvg		X					
KTC-14-Tprc40	N34°21'20.8"*	W117°42'53.5"*	PɛNv	X						
KTC-14-Tprc44	~N34°21'27.7"†	~W117°43'25.6"†	PɛNv	X						
KTC-14-Tprc45	~N34°21'28.8"†	~W117°43'22.8"†	PɛNv	X						
KTC-14-Tv6	N34°21'26.0"*	W117°42'50.6"*	Pɛvv						X	
KTC-14-vint	N34°21'26.3"	W117°43'00.1"	Pɛvv						X	
KTC-15-Ntccb1	N34°32'01.2"	W118°32'25.7"	None§§§§§		X					
KTC-15-Ntcsb1	N34°31'58.8"	W118°32'30.6"	None§§§§§		X					
KTC-15-PɛNvlb1	N34°32'04.1"	W118°32'20.3"	None§§§§§		X					
KTC-15-PɛNvlb2	N34°31'49.9"	W118°32'15.6"	None§§§§§		X					
P2-11-06-3	##	##	None§§§	X						
P2-11-06-5	##	##	None§§§	X						
P2-11-06-7	##	##	None§§§	X						
P4-08-06-2	###	###	None§§§	X						
P4-08-06-6	###	###	None§§§	X						
P7-14-06-1	N34°27'24.0"†	W117°57'04.9"†	Npb§§	X						

Sample locations for data of Hoyt (2012) included in Figs. 9, 16 (outside the mapped area of Plates 1, 2):

JFH-11-1M	N34°25'08.1"	W118°25'22.2"
JFH-11-3M	N34°22'36.5"	W118°25'59.1"
JFH-11-4M	N34°25'38.6"	W118°25'20.6"
JFH-11-5M	N34°26'55.6"	W118°23'34.8"
JFH-11-6M	N34°27'53.6"	W118°22'19.6"
JFH-11-7M	N34°28'51.3"	W118°22'42.3"
JFH-11-8M	N34°26'39.6"	W118°25'09.3"
JFH-11-9M	N34°28'17.8"	W118°26'06.4"
JFH-11-10M	N34°29'38.8"	W118°27'30.5"
JFH-11-11M	N34°28'46.3"	W118°27'56.6"
JFH-11-12M	N34°28'04.3"	W118°28'20.2"
JFH-11-13M	N34°27'41.7"	W118°29'01.8"
JFH-11-14M	N34°30'45.8"	W118°32'03.9"
JFH-11-15C	N34°47'25.8"	W119°02'34.6"
JFH-11-16C	N34°43'15.3"	W119°11'38.9"
JFH-11-17C	N34°45'18.0"	W119°13'45.9"
JFH-11-18C	N34°45'06.0"	W119°14'04.1"
JFH-11-19C	N34°44'05.3"	W119°23'48.6"
JFH-11-20C	N34°51'11.4"	W119°16'07.8"
JFH-11-22C	N34°50'18.4"	W119°21'25.4"
JFH-11-24C	N34°52'39.4"	W119°24'47.4"

Sample locations for data of Hoyt (2012) and Stang (2013) included in Figs. 9, 16 (outside the mapped area of Plates 1, 2):

JFH-11-21C	N34°50'28.9"	W119°20'03.6"
JFH-11-23C	N34°52'58.9"	W119°26'20.7"

DMS = degrees-minutes-seconds; Ss. = sandstone composition; Cgl. = conglomerate composition; Plct. = paleocurrent direction; D.Z. = detrital-zircon analyses; I.Z. = igneous-zircon analyses; T.E.V. = trace-element analysis of a volcanic sample; Photo = field photograph (Appendix I)

Accuracy of all latitude/longitude measurements is ~3-10 m, except where indicated by footnotes † and ††

*Sample was loose, but thought to be approximately in-place

†Location marked on map, but not recorded with GPS. Estimated location is accurate to within 50 m

††Location marked on map and well constrained, but not recorded with GPS. Estimated location is accurate to within 10 m

#Location neither recorded with GPS nor marked on a map, but within 0.5 km of N33°36'21.8", W115°46'25.7" (center of section 31 of T6S, R12E, San Bernardino Meridian, Riverside County, CA)

##Location neither recorded with GPS nor marked on a map, but within Vasquez Canyon, between N34°29'00" and N34°29'15" and W118°25'00" and W118°25'30"

###Location neither recorded with GPS nor marked on a map, but just south of Davenport Road, between N34°28'30" and N34°29'00" and W118°21'00" and W118°22'30"

§Pieces of volcanics interpreted as closely associated with Pεvv, but sampled from cobbles within PεNv at same site as KTC-13-Tprc23/KTC-14-dz1

§§Corresponds to the map unit listed, but lies outside of the mapped study area, and thus is not shown on Plate 2

§§§Samples are from the Tick Canyon Formation, which is entirely outside of the mapped study area shown in Plates 1, 2

§§§§Samples are from interbedded volcanics of the Diligencia Formation, which is entirely outside of the mapped study area shown in Plates 1, 2

§§§§§Samples are from the Tick Canyon and Vasquez Formations of the Soledad region, entirely outside of the mapped study area shown in Plates 1, 2, but corresponding to map units Ntccb/Ntcsb and PεNvlb, respectively, in Fig. 6

APPENDIX B: DETRITAL-ZIRCON DATA

Manually rejected ages are indicated by strikethrough; rejections are explained at bottom of tables.

Sample JFH-11-25P* n = 79

			(%)		(%)		(%)			Age (Ma)		Age (Ma)		Age (Ma)		Preferred	
U	^{206}Pb/	U/	^{206}Pb*/	±	^{207}Pb*/	±	^{206}Pb*/	±	error	^{206}Pb*/	±	^{207}Pb*/	±	^{207}Pb*/	±	age	±
(ppm)	^{204}Pb	Th	^{207}Pb*	(1σ)	^{235}U*	(1σ)	^{238}U*	(1σ)	corr.	^{238}U*	(1σ)	^{235}U*	(1σ)	^{206}Pb*	(1σ)	(Ma)	(1σ)
467	4796	1.6	21.4326	31.8	0.0255	32.2	0.0040	5.3	0.16	25.5	1.3	25.6	8.1	31.8	779.4	25.5	1.3
64	7227	2.7	9.3818	123.6	0.1655	123.9	0.0113	7.9	0.06	72.2	5.6	155.5	180.5	1741.9	41.3	72.2	5.6
356	36955	1.8	19.7920	9.2	0.0801	9.3	0.0115	1.4	0.15	73.7	1.0	78.3	7.0	219.2	212.2	73.7	1.0
70	4508	1.3	18.2470	112.6	0.0893	112.8	0.0118	7.8	0.07	75.7	5.9	86.8	94.2	404.2	825.6	75.7	5.9
523	21247	1.2	20.5390	5.3	0.0839	5.6	0.0125	1.8	0.32	80.0	1.4	81.8	4.4	132.8	125.5	80.0	1.4
531	3206	0.7	17.6574	22.9	0.0995	23.0	0.0127	2.3	0.10	81.6	1.9	96.3	21.1	477.3	512.3	81.6	1.9
142	7486	4.0	31.4724	44.6	0.0568	45.3	0.0130	7.7	0.17	83.0	6.4	56.1	24.7	b.d.	b.d.	83.0	6.4
268	16397	1.2	22.7863	15.6	0.0837	15.6	0.0138	1.5	0.10	88.6	1.3	81.7	12.3	b.d.	b.d.	88.6	1.3
87	15775	1.2	23.2750	40.9	0.0923	42.3	0.0156	10.7	0.25	99.7	10.6	89.7	36.3	b.d.	b.d.	99.7	10.6
121	5964	0.6	18.5541	11.4	0.1705	15.8	0.0229	10.9	0.69	146.2	15.8	159.8	23.4	366.7	258.7	146.2	15.8
423	20597	0.6	20.3795	5.4	0.1591	5.6	0.0235	1.5	0.27	149.9	2.3	149.9	7.8	151.1	126.7	149.9	2.3
69	6929	1.8	23.1704	25.9	0.1409	26.3	0.0237	4.1	0.16	150.9	6.1	133.8	32.9	b.d.	b.d.	150.9	6.1
87	9324	1.2	15.1662	11.4	0.2154	12.6	0.0237	5.5	0.43	151.0	8.1	198.1	22.7	804.3	238.5	151.0	8.1
47	5394	0.8	32.4388	69.0	0.1010	69.7	0.0238	9.5	0.14	151.4	14.3	97.7	65.0	b.d.	b.d.	151.4	14.3
243	19519	1.1	19.8879	8.1	0.1649	8.3	0.0238	1.8	0.22	151.5	2.8	155.0	11.9	208.0	187.0	151.5	2.8
95	11568	1.5	19.6699	18.9	0.1674	19.5	0.0239	4.7	0.24	152.1	7.1	157.2	28.3	233.6	438.9	152.1	7.1
53	7714	1.1	20.1008	52.2	0.1640	52.5	0.0239	5.9	0.11	152.3	8.8	154.2	75.3	b.d.	b.d.	152.3	8.8
144	25394	0.7	18.2990	11.2	0.1810	11.5	0.0240	2.5	0.22	153.0	3.8	168.9	17.9	397.8	251.8	153.0	3.8
90	7441	0.7	18.1647	15.6	0.1827	16.1	0.0241	3.9	0.24	153.3	5.9	170.4	25.3	414.3	351.4	153.3	5.9
93	12494	0.9	28.0657	34.5	0.1183	34.6	0.0241	2.8	0.08	153.4	4.3	113.5	37.2	b.d.	b.d.	153.4	4.3
480	177612	7.4	19.9999	3.9	0.1660	5.0	0.0241	3.1	0.62	153.4	4.7	156.0	7.2	195.0	90.9	153.4	4.7
139	22160	0.8	19.5563	17.4	0.1709	17.6	0.0242	2.8	0.16	154.4	4.3	160.2	26.1	246.9	403.7	154.4	4.3
168	34622	0.9	20.3491	14.0	0.1645	14.2	0.0243	2.8	0.20	154.6	4.3	154.6	20.4	154.6	328.4	154.6	4.3
67	6589	1.4	20.6289	84.8	0.1625	85.0	0.0243	5.1	0.06	154.8	7.8	152.9	121.2	b.d.	b.d.	154.8	7.8
99	8924	1.8	29.8009	31.8	0.1128	32.3	0.0244	5.9	0.18	155.2	9.0	108.5	33.3	b.d.	b.d.	155.2	9.0
110	12408	1.0	18.9410	16.1	0.1782	16.6	0.0245	3.9	0.23	155.9	6.0	166.5	25.5	320.0	369.0	155.9	6.0
169	17466	0.8	19.8209	8.1	0.1712	8.6	0.0246	2.9	0.34	156.7	4.5	160.4	12.8	215.9	188.2	156.7	4.5
79	17462	1.7	19.6879	26.2	0.1725	26.4	0.0246	3.2	0.12	156.8	5.0	161.6	39.4	231.4	613.3	156.8	5.0
104	35310	0.6	23.1994	28.6	0.1464	28.7	0.0246	3.2	0.11	156.9	5.0	138.8	37.3	b.d.	b.d.	156.9	5.0
115	20521	0.6	20.7571	12.6	0.1642	13.1	0.0247	3.7	0.28	157.4	5.7	154.4	18.8	107.9	298.3	157.4	5.7
95	11845	1.5	21.5654	28.8	0.1583	29.1	0.0248	4.1	0.14	157.7	6.3	149.2	40.4	16.9	705.2	157.7	6.3
75	8508	2.2	20.5763	19.7	0.1660	20.1	0.0248	4.2	0.21	157.8	6.6	156.0	29.1	128.6	466.9	157.8	6.6
371	61595	0.8	20.3704	6.9	0.1677	7.9	0.0248	4.0	0.50	157.8	6.2	157.4	11.6	152.2	161.5	157.8	6.2
189	21350	0.6	21.0282	11.6	0.1625	11.7	0.0248	1.9	0.16	157.8	2.9	152.9	16.7	77.2	275.8	157.8	2.9
82	6908	0.5	21.4970	20.2	0.1592	21.0	0.0248	5.7	0.27	158.0	8.8	150.0	29.3	24.5	489.6	158.0	8.8
160	22801	3.3	20.9777	8.3	0.1634	9.4	0.0249	4.5	0.48	158.3	7.1	153.7	13.4	82.9	196.5	158.3	7.1
92	21640	0.8	19.8320	22.0	0.1730	22.6	0.0249	5.0	0.22	158.4	7.8	162.0	33.8	214.6	515.0	158.4	7.8
1148	130708	1.3	20.0458	1.7	0.1714	1.9	0.0249	0.7	0.39	158.7	1.2	160.7	2.8	189.6	40.1	158.7	1.2
57	6907	1.6	16.2839	47.3	0.2112	47.4	0.0249	4.1	0.09	158.8	6.4	194.6	84.2	b.d.	b.d.	158.8	6.4
341	44007	0.9	20.8167	4.6	0.1654	4.8	0.0250	1.5	0.31	159.0	2.3	155.4	6.9	101.1	108.1	159.0	2.3

218	32413	1.0	21.7186	6.1	0.1596	6.6	0.0251	2.6	0.39	160.0	4.1	150.3	9.2	b.d.	b.d.	160.0	4.1
147	19904	1.6	23.8267	31.4	0.1458	32.1	0.0252	6.7	0.21	160.4	10.6	138.2	41.5	b.d.	b.d.	160.4	10.6
236	32538	1.1	20.6376	14.5	0.1683	15.2	0.0252	4.5	0.30	160.4	7.2	158.0	22.2	b.d.	b.d.	160.4	7.2
52	10386	1.6	23.0495	34.1	0.1522	35.1	0.0254	8.1	0.23	162.0	13.0	143.9	47.1	b.d.	b.d.	162.0	13.0
136	13901	0.8	23.5622	22.7	0.1493	23.2	0.0255	4.7	0.20	162.4	7.5	141.2	30.6	b.d.	b.d.	162.4	7.5
362	94451	1.3	19.5101	3.0	0.1806	3.7	0.0256	2.1	0.57	162.6	3.4	168.6	5.8	252.4	69.9	162.6	3.4
357	45960	0.4	19.6615	6.7	0.1798	7.1	0.0256	2.4	0.34	163.2	3.9	167.9	11.0	234.5	154.4	163.2	3.9
70	217	1.6	7.6832	6.4	0.4832	7.0	0.0269	2.7	0.38	171.3	4.5	400.2	23.1	2100.0	113.3	171.3	4.5
45	6610	1.1	22.6559	46.1	0.1712	47.5	0.0281	11.1	0.23	178.9	19.6	160.5	70.6	b.d.	b.d.	178.9	19.6
363	41282	2.1	19.9441	4.0	0.2023	6.9	0.0293	5.7	0.82	186.0	10.4	187.1	11.8	201.5	92.1	186.0	10.4
619	267120	1.4	19.9194	2.5	0.2326	2.6	0.0336	0.9	0.33	213.1	1.8	212.4	5.1	204.3	57.7	213.1	1.8
238	35992	2.3	20.1932	7.9	0.2353	8.0	0.0345	1.6	0.20	218.4	3.4	214.6	15.5	172.6	183.8	218.4	3.4
183	20516	1.9	20.8115	9.3	0.2290	9.4	0.0346	1.2	0.13	219.1	2.6	209.4	17.7	101.8	220.0	219.1	2.6
150	19030	2.0	20.1538	6.1	0.2395	7.2	0.0350	3.9	0.53	221.8	8.4	218.0	14.2	177.1	143.1	221.8	8.4
139	39261	2.4	19.3126	4.9	0.2504	5.7	0.0351	3.0	0.53	222.2	6.6	226.9	11.6	275.7	111.2	222.2	6.6
788	114198	8.9	19.3584	2.2	0.2718	2.7	0.0382	1.5	0.55	241.4	3.5	244.2	5.8	270.2	51.4	241.4	3.5
101	230376	1.6	11.2242	1.9	2.9489	2.2	0.2401	1.0	0.47	1387.0	12.7	1394.6	16.3	1406.2	36.3	1406.2	36.3
262	301577	3.8	11.2161	0.6	2.7212	1.6	0.2214	1.5	0.92	1289.0	17.0	1334.3	11.8	1407.5	12.3	1407.5	12.3
1281	696131	13.8	11.2020	0.1	2.8769	1.1	0.2337	1.1	0.99	1354.0	13.5	1375.9	8.4	1409.9	2.8	1409.9	2.8
282	436307	2.5	11.1851	0.4	3.0094	0.9	0.2441	0.8	0.88	1408.1	10.1	1410.0	6.9	1412.8	8.3	1412.8	8.3
194	393435	2.0	11.1681	1.0	2.9648	1.3	0.2401	0.9	0.66	1387.5	10.6	1398.7	9.8	1415.7	18.4	1415.7	18.4
367	490075	2.6	11.1499	0.3	2.9922	1.3	0.2420	1.2	0.96	1396.9	15.5	1405.6	9.8	1418.9	6.7	1418.9	6.7
306	654981	3.1	11.1206	0.5	2.7269	6.8	0.2199	6.8	1.00	1281.6	79.4	1335.8	50.9	1423.9	9.1	1423.9	9.1
430	493086	2.9	11.1147	0.5	3.0038	2.7	0.2421	2.7	0.99	1397.8	33.5	1408.6	20.6	1424.9	8.7	1424.9	8.7
401	456153	6.4	11.1130	0.4	2.7167	4.3	0.2190	4.3	1.00	1276.4	49.9	1333.0	32.1	1425.2	8.1	1425.2	8.1
613	531606	2.1	11.1087	0.4	3.0358	1.5	0.2446	1.4	0.97	1410.5	18.1	1416.7	11.2	1425.9	6.9	1425.9	6.9
367	490821	2.4	11.0604	0.4	3.0709	3.0	0.2463	2.9	0.99	1419.6	37.3	1425.5	22.6	1434.2	7.1	1434.2	7.1
120	89490	7.0	10.7634	1.4	3.3780	1.9	0.2637	1.3	0.68	1508.7	17.7	1499.3	15.1	1486.0	26.8	1486.0	26.8
316	247585	4.6	10.7550	5.3	2.4896	11.3	0.1942	9.9	0.88	1144.1	104.1	1269.0	81.7	1487.5	100.6	1487.5	100.6
141	195271	2.4	10.3729	1.1	3.3382	1.6	0.2511	1.2	0.75	1444.3	15.9	1490.0	12.8	1555.7	20.5	1555.7	20.5
471	797048	3.2	10.1148	0.4	3.6481	2.5	0.2676	2.4	0.98	1528.7	32.9	1560.1	19.6	1602.8	8.4	1602.8	8.4
109	84641	2.1	9.8574	1.0	4.0970	1.6	0.2929	1.2	0.77	1656.0	17.5	1653.7	12.7	1650.7	18.3	1650.7	18.3
676	525270	3.9	9.8318	0.3	3.4710	3.4	0.2475	3.4	1.00	1425.6	43.1	1520.6	26.7	1655.6	4.9	1655.6	4.9
839	828108	15.7	9.7911	0.4	3.9880	1.0	0.2832	0.9	0.92	1607.4	12.6	1631.7	7.8	1663.2	7.0	1663.2	7.0
380	3493282	3.6	9.7480	0.8	3.8910	2.4	0.2751	2.3	0.94	1566.6	31.6	1611.8	19.4	1671.4	14.7	1671.4	14.7
113	287554	2.0	9.6643	1.1	4.1478	1.6	0.2907	1.2	0.76	1645.2	18.0	1663.8	13.3	1687.3	19.5	1687.3	19.5
269	424038	2.3	9.5484	0.6	3.9973	4.8	0.2768	4.7	0.99	1575.3	66.0	1633.6	38.7	1709.6	11.7	1709.6	11.7
4650	1902527	19.1	9.5355	0.1	4.2000	1.9	0.2905	1.9	1.00	1643.9	28.3	1674.0	16.0	1712.0	1.3	1712.0	1.3
768	613479	1.6	9.3647	0.1	4.4668	1.2	0.3034	1.2	0.99	1708.1	17.8	1724.8	9.9	1745.2	2.3	1745.2	2.3

Sample JFH-11-26P* n = 69

U	^{206}Pb/	U/	(%) ^{206}Pb*/	±	(%) ^{207}Pb*/	±	(%) ^{206}Pb*/	±	error	Age (Ma) ^{206}Pb*/	±	Age (Ma) ^{207}Pb*/	±	Age (Ma) ^{207}Pb*/	±	Preferred age	±
(ppm)	^{204}Pb	Th	^{207}Pb*	(1σ)	^{235}U*	(1σ)	^{238}U*	(1σ)	corr.	^{238}U*	(1σ)	^{235}U*	(1σ)	^{206}Pb*	(1σ)	(Ma)	(1σ)
451	49170	15.7	22.8684	5.9	0.0704	6.1	0.0117	1.5	0.25	74.8	1.1	69.1	4.1	b.d.	b.d.	74.8	1.1
86	5356	0.8	18.7451	43.8	0.0865	44.8	0.0118	9.1	0.20	75.4	6.8	84.2	36.2	b.d.	b.d.	75.4	6.8
113	10250	1.5	30.3119	72.1	0.0542	72.6	0.0119	8.4	0.12	76.3	6.4	53.6	37.9	b.d.	b.d.	76.3	6.4
149	674	0.8	12.0146	22.3	0.1377	22.5	0.0120	3.5	0.16	76.9	2.7	131.0	27.7	1274.7	439.7	76.9	2.7
355	1018	1.2	12.2150	4.9	0.1355	7.1	0.0120	5.1	0.72	76.9	3.9	129.0	8.6	1242.3	96.8	76.9	3.9
540	108872	1.0	20.4121	7.9	0.0834	8.6	0.0124	3.4	0.40	79.1	2.7	81.4	6.8	147.4	186.1	79.1	2.7
111	7031	0.6	23.8572	65.9	0.0719	66.6	0.0124	10.1	0.15	79.7	8.0	70.5	45.4	b.d.	b.d.	79.7	8.0
167	364	0.6	7.1422	6.4	0.2402	7.7	0.0124	4.4	0.56	79.7	3.5	218.6	15.2	2227.4	110.5	79.7	3.5
389	63496	4.9	21.3985	16.0	0.0802	16.1	0.0124	1.9	0.12	79.7	1.5	78.3	12.2	35.5	385.4	79.7	1.5
288	581	4.3	9.5770	5.3	0.1818	6.0	0.0126	2.9	0.47	80.9	2.3	169.6	9.4	1704.1	97.7	80.9	2.3
228	30079	2.2	23.1660	16.0	0.0754	17.1	0.0127	6.0	0.35	81.1	4.8	73.8	12.2	b.d.	b.d.	81.1	4.8
970	83705	2.1	20.5641	4.4	0.0909	4.8	0.0136	1.7	0.36	86.8	1.5	88.3	4.0	129.9	104.6	86.8	1.5
157	15997	1.7	25.1277	26.2	0.0745	26.7	0.0136	5.6	0.21	87.0	4.8	73.0	18.8	b.d.	b.d.	87.0	4.8
1391	296606	8.8	20.9752	3.3	0.0894	3.3	0.0136	0.5	0.16	87.1	0.5	86.9	2.8	83.2	77.6	87.1	0.5
839	120480	12.6	17.8914	6.3	0.1064	6.9	0.0138	2.8	0.41	88.4	2.5	102.7	6.7	448.1	139.9	88.4	2.5
2513	385763	26.7	20.6662	0.9	0.0924	1.3	0.0138	0.9	0.69	88.7	0.8	89.7	1.1	118.3	22.2	88.7	0.8
452	46333	0.8	21.0198	10.2	0.0909	10.6	0.0139	2.5	0.24	88.7	2.2	88.3	8.9	78.1	243.9	88.7	2.2
1288	78146	0.5	20.7911	3.7	0.0941	3.9	0.0142	1.3	0.32	90.8	1.1	91.3	3.4	104.1	88.2	90.8	1.1
155	20350	2.6	26.8109	36.1	0.0742	36.3	0.0144	3.5	0.10	92.3	3.2	72.6	25.4	b.d.	b.d.	92.3	3.2
571	69817	1.4	22.1300	5.9	0.0901	6.3	0.0145	2.4	0.37	92.6	2.2	87.6	5.3	b.d.	b.d.	92.6	2.2
132	6091	0.8	21.6332	28.3	0.0926	28.8	0.0145	5.5	0.19	92.9	5.1	89.9	24.8	9.4	692.1	92.9	5.1
146	19495	1.2	22.8195	21.4	0.0881	22.5	0.0146	6.8	0.30	93.3	6.3	85.7	18.5	b.d.	b.d.	93.3	6.3
262	37571	1.3	21.0487	13.0	0.0968	13.2	0.0148	2.0	0.15	94.6	1.9	93.8	11.8	74.9	310.4	94.6	1.9
72	8205	1.4	20.6746	48.0	0.0989	48.5	0.0148	6.9	0.14	94.9	6.5	95.8	44.3	b.d.	b.d.	94.9	6.5
110	19397	1.1	22.8304	27.3	0.0899	28.3	0.0149	7.5	0.27	95.3	7.1	87.4	23.7	b.d.	b.d.	95.3	7.1
79	14111	1.3	18.5592	31.6	0.1146	33.6	0.0154	11.3	0.34	98.7	11.1	110.2	35.1	366.1	729.3	98.7	11.1
127	32518	5.5	19.8426	20.4	0.1601	20.7	0.0230	3.8	0.19	146.9	5.6	150.8	29.1	213.3	476.2	146.9	5.6
129	15314	1.0	21.9166	26.7	0.1469	27.0	0.0233	4.3	0.16	148.8	6.3	139.1	35.1	b.d.	b.d.	148.8	6.3
476	79022	0.7	21.0246	5.5	0.1536	5.6	0.0234	1.0	0.18	149.3	1.5	145.1	7.6	77.6	130.9	149.3	1.5
58	17535	2.2	25.5526	36.9	0.1305	37.9	0.0242	8.4	0.22	154.1	12.7	124.6	44.4	b.d.	b.d.	154.1	12.7
76	22949	0.6	23.7227	29.4	0.1408	29.8	0.0242	4.8	0.16	154.3	7.3	133.8	37.4	b.d.	b.d.	154.3	7.3
109	17043	1.1	20.6490	15.2	0.2233	15.8	0.0334	4.3	0.27	212.0	9.0	204.6	29.2	120.2	359.1	212.0	9.0
78	24944	1.2	19.1459	14.6	0.2436	15.5	0.0338	5.2	0.33	214.5	11.0	221.4	30.9	295.5	335.7	214.5	11.0
86	31514	1.1	19.0058	11.5	0.2582	12.5	0.0356	4.7	0.38	225.4	10.4	233.2	26.0	312.2	263.5	225.4	10.4
54	13625	1.3	21.3359	43.2	0.2435	43.8	0.0377	7.5	0.17	238.4	17.7	221.3	87.4	b.d.	b.d.	238.4	17.7
183	121861	0.9	19.5743	4.8	0.2746	5.3	0.0390	2.2	0.41	246.5	5.2	246.3	11.6	244.8	111.5	246.5	5.2
314	436159	9.0	11.4449	0.3	2.3997	1.7	0.1992	1.6	0.98	1170.9	17.6	1242.5	12.0	1368.8	6.1	1368.8	6.1
387	477063	6.5	11.3344	0.6	2.0536	1.6	0.1688	1.5	0.92	1005.6	14.0	1133.5	11.1	1387.4	12.0	1387.4	12.0
155	85467	4.3	11.2969	1.3	2.5085	2.3	0.2055	1.9	0.82	1204.9	20.4	1274.5	16.4	1393.8	24.5	1393.8	24.5
123	1145559	0.6	11.2295	1.0	2.9788	1.8	0.2426	1.5	0.83	1400.2	18.9	1402.2	13.7	1405.2	19.2	1405.2	19.2
366	1377191	0.9	11.2179	0.3	2.8393	1.1	0.2310	1.1	0.96	1339.8	12.8	1366.0	8.3	1407.2	6.2	1407.2	6.2
358	1136480	3.5	11.2041	0.4	2.8987	1.3	0.2355	1.2	0.94	1363.5	14.6	1381.6	9.5	1409.6	8.1	1409.6	8.1
69	81969	1.1	11.1792	1.8	2.9328	2.6	0.2378	1.8	0.71	1375.2	22.7	1390.4	19.5	1413.8	34.6	1413.8	34.6
584	1104996	83.8	11.1686	0.3	2.9548	1.0	0.2393	0.9	0.96	1383.3	11.7	1396.1	7.4	1415.7	5.0	1415.7	5.0

154	99903	0.8	11.1589	1.1	2.8439	2.1	0.2302	1.8	0.84	1335.3	21.4	1367.2	15.9	1417.3	21.8	1417.3	21.8
364	841878	3.4	11.1550	0.5	2.7465	0.9	0.2222	0.7	0.81	1293.5	8.8	1341.1	6.9	1418.0	10.3	1418.0	10.3
1779	3140230	13.7	11.1485	0.1	2.9965	1.0	0.2423	0.9	0.99	1398.6	11.9	1406.7	7.3	1419.1	2.4	1419.1	2.4
42	86088	1.6	10.0018	2.1	3.7530	3.2	0.2722	2.4	0.74	1552.2	32.6	1582.8	25.5	1623.7	39.5	1623.7	39.5
164	250639	2.2	9.9919	0.8	3.3929	1.2	0.2459	0.9	0.75	1417.2	11.8	1502.8	9.7	1625.6	15.1	1625.6	15.1
1092	7790875	5.0	9.9766	0.3	3.4319	2.7	0.2483	2.7	1.00	1429.8	35.0	1511.7	21.6	1628.4	4.9	1628.4	4.9
272	409280	3.5	9.9724	0.6	3.7248	1.8	0.2694	1.7	0.94	1537.8	22.8	1576.7	14.3	1629.2	11.6	1629.2	11.6
2035	2685559	3.9	9.8901	0.2	3.9278	0.7	0.2817	0.7	0.94	1600.1	9.5	1619.4	5.7	1644.6	4.4	1644.6	4.4
1530	2884254	5.2	9.8551	0.2	3.6878	1.8	0.2636	1.7	0.99	1508.2	23.5	1568.7	14.1	1651.2	3.9	1651.2	3.9
1008	3387533	20.4	9.8349	0.2	3.6265	0.7	0.2587	0.7	0.97	1483.1	9.3	1555.4	5.8	1655.0	3.5	1655.0	3.5
877	2068653	7.3	9.8241	0.6	3.4543	2.7	0.2461	2.7	0.98	1418.4	33.9	1516.8	21.4	1657.0	10.6	1657.0	10.6
218	601481	1.3	9.7857	0.6	3.8361	1.4	0.2723	1.2	0.91	1552.3	17.0	1600.4	10.9	1664.3	10.3	1664.3	10.3
309	840166	0.9	9.7425	0.5	3.5954	1.2	0.2540	1.1	0.92	1459.3	14.0	1548.5	9.3	1672.4	8.6	1672.4	8.6
134	836026	1.3	9.7229	0.7	4.3353	1.5	0.3057	1.3	0.89	1719.6	19.9	1700.1	12.3	1676.2	12.8	1676.2	12.8
158	305784	1.6	9.7216	0.6	4.1041	2.1	0.2894	2.0	0.96	1638.4	29.4	1655.1	17.3	1676.4	11.0	1676.4	11.0
125	322343	1.7	9.6775	0.6	4.3353	1.6	0.3043	1.5	0.92	1712.5	22.2	1700.1	13.3	1684.8	11.9	1684.8	11.9
126	101434	2.2	9.6104	1.0	4.2978	12.2	0.2996	12.1	1.00	1689.1	180.6	1692.9	100.7	1697.6	18.4	1697.6	18.4
287	757078	1.9	9.5938	0.5	3.8064	1.3	0.2649	1.1	0.91	1514.6	15.5	1594.1	10.1	1700.8	9.5	1700.8	9.5
688	505379	3.1	9.5300	0.7	3.6182	4.3	0.2501	4.2	0.99	1438.9	54.5	1553.5	34.1	1713.1	13.5	1713.1	13.5
339	768626	3.5	9.4801	0.5	4.2490	1.7	0.2921	1.7	0.96	1652.3	24.4	1683.6	14.3	1722.7	8.5	1722.7	8.5
216	437643	2.1	9.4468	0.6	4.3548	0.8	0.2984	0.6	0.73	1683.2	8.9	1703.8	6.8	1729.2	10.2	1729.2	10.2
268	262290	0.7	9.3472	0.6	4.8435	7.4	0.3284	7.4	1.00	1830.4	117.9	1792.5	62.6	1748.6	11.8	1748.6	11.8
209	449398	0.7	9.2894	0.5	4.5126	1.3	0.3040	1.2	0.93	1711.2	18.5	1733.3	11.1	1760.0	9.1	1760.0	9.1
102	7941	0.8	9.2580	3.8	3.8900	7.6	0.2612	6.6	0.87	1495.9	88.1	1611.6	61.6	1766.2	69.5	1766.2	69.5
145	356149	1.7	9.2435	0.5	4.5812	1.3	0.3071	1.2	0.91	1726.5	18.2	1745.9	11.0	1769.0	9.8	1769.0	9.8

Sample JFH-11-27P* **n = 78**

U (ppm)	^{206}Pb/ ^{204}Pb	U/ Th	(%) ^{206}Pb*/ ^{207}Pb*	± (1σ)	(%) ^{207}Pb*/ ^{235}U*	± (1σ)	(%) ^{206}Pb*/ ^{238}U*	± (1σ)	error corr.	Age (Ma) ^{206}Pb*/ ^{238}U*	± (1σ)	Age (Ma) ^{207}Pb*/ ^{235}U*	± (1σ)	Age (Ma) ^{207}Pb*/ ^{206}Pb*	± (1σ)	Preferred age (Ma)	± (1σ)
236	5630	1.2	18.6642	21.8	0.0824	22.8	0.0112	6.9	0.30	71.5	4.9	80.4	17.7	353.4	497.5	71.5	4.9
272	225	0.8	16.4575	8.6	0.0953	9.5	0.0114	3.9	0.42	72.9	2.9	92.5	8.4	630.9	185.7	72.9	2.9
191	7731	25.4	23.0110	73.6	0.0691	73.7	0.0115	3.9	0.05	73.9	2.8	67.9	48.4	b.d.	b.d.	73.9	2.8
1124	26912	3.6	21.9308	7.5	0.0730	8.1	0.0116	3.1	0.38	74.4	2.3	71.5	5.6	b.d.	b.d.	74.4	2.3
1402	55877	4.1	20.2491	3.8	0.0800	4.3	0.0117	2.0	0.47	75.3	1.5	78.1	3.2	166.1	88.3	75.3	1.5
402	5884	0.4	24.9594	13.9	0.0655	14.1	0.0119	2.2	0.16	76.0	1.7	64.4	8.8	b.d.	b.d.	76.0	1.7
282	4360	0.6	21.1555	20.4	0.0774	20.8	0.0119	3.8	0.18	76.1	2.9	75.7	15.2	62.8	490.7	76.1	2.9
283	5566	1.8	21.2623	17.7	0.0803	17.9	0.0124	2.5	0.14	79.4	2.0	78.5	13.5	50.8	425.0	79.4	2.0
534	14070	4.2	21.1471	12.9	0.0811	14.4	0.0124	6.4	0.44	79.7	5.0	79.1	11.0	63.8	308.5	79.7	5.0
270	1863	0.6	14.8285	26.9	0.1241	27.3	0.0133	4.4	0.16	85.4	3.8	118.7	30.6	851.3	568.7	85.4	3.8
964	33820	5.7	21.4217	6.6	0.0864	6.8	0.0134	1.7	0.25	86.0	1.4	84.2	5.5	33.0	157.3	86.0	1.4
781	22025	4.2	21.6289	4.9	0.0857	5.1	0.0134	1.4	0.28	86.1	1.2	83.5	4.1	9.9	117.0	86.1	1.2
490	12372	8.9	24.2842	12.2	0.0775	12.6	0.0136	3.0	0.24	87.4	2.6	75.8	9.2	b.d.	b.d.	87.4	2.6
177	12956	0.8	26.3801	44.1	0.0739	44.3	0.0141	4.9	0.11	90.5	4.4	72.4	31.0	b.d.	b.d.	90.5	4.4
122	4148	1.1	14.0985	67.5	0.1489	68.2	0.0152	9.7	0.14	97.4	9.4	141.0	90.1	b.d.	b.d.	97.4	9.4
277	12980	1.0	22.9074	19.4	0.0956	19.6	0.0159	2.9	0.15	101.6	3.0	92.7	17.4	b.d.	b.d.	101.6	3.0
99	3275	1.0	27.2429	56.5	0.0972	56.8	0.0192	6.2	0.11	122.7	7.5	94.2	51.2	b.d.	b.d.	122.7	7.5
32	2975	0.5	6.1228	371.2	0.4964	371.4	0.0220	10.6	0.03	140.6	14.7	409.3	-	2490.3	367.9	140.6	14.7
193	14453	0.8	20.0441	16.9	0.1570	17.2	0.0228	3.1	0.18	145.4	4.4	148.0	23.7	189.8	395.3	145.4	4.4
61	1862	1.1	28.8883	71.7	0.1104	72.2	0.0231	9.1	0.13	147.4	13.2	106.3	73.0	b.d.	b.d.	147.4	13.2
97	4044	0.8	28.6733	44.1	0.1121	44.4	0.0233	5.0	0.11	148.5	7.4	107.9	45.4	b.d.	b.d.	148.5	7.4
110	7153	0.6	19.1460	19.8	0.1681	20.3	0.0233	4.5	0.22	148.8	6.6	157.8	29.7	295.5	456.6	148.8	6.6
278	8047	0.6	19.9926	10.9	0.1611	11.0	0.0234	1.5	0.14	148.9	2.3	151.7	15.6	195.9	254.8	148.9	2.3
1158	52787	3.2	20.4260	2.0	0.1589	2.2	0.0235	0.9	0.40	150.0	1.3	149.8	3.1	145.8	47.1	150.0	1.3
44	1904	1.5	21.7324	35.1	0.1495	36.3	0.0236	9.2	0.25	150.2	13.7	141.5	48.0	b.d.	b.d.	150.2	13.7
26	1169	0.8	2.0125	800.1	1.6232	800.2	0.0237	14.6	0.02	150.9	21.7	979.2	-	b.d.	b.d.	150.9	21.7
141	15840	0.9	20.3078	13.3	0.1633	13.8	0.0240	3.6	0.26	153.2	5.4	153.6	19.6	159.4	311.9	153.2	5.4
81	7933	1.1	23.4361	35.9	0.1416	36.4	0.0241	5.8	0.16	153.3	8.8	134.5	45.8	b.d.	b.d.	153.3	8.8
144	7784	0.5	27.8948	31.4	0.1190	31.6	0.0241	3.4	0.11	153.4	5.2	114.2	34.1	b.d.	b.d.	153.4	5.2
29	1464	0.6	21.1774	57.8	0.1570	58.3	0.0241	7.4	0.13	153.6	11.3	148.1	80.5	b.d.	b.d.	153.6	11.3
243	5415	0.4	18.7729	13.3	0.1784	16.3	0.0243	9.3	0.57	154.7	14.2	166.7	25.0	340.3	303.4	154.7	14.2
292	9610	1.1	20.8052	13.7	0.1648	13.9	0.0249	2.0	0.14	158.4	3.2	154.9	20.0	102.5	326.2	158.4	3.2
44	2434	1.4	32.8131	107.3	0.1046	107.5	0.0249	7.4	0.07	158.5	11.6	101.0	103.8	b.d.	b.d.	158.5	11.6
364	21365	9.1	14.3000	3.4	0.3456	4.9	0.0358	3.6	0.73	227.0	7.9	301.4	12.8	926.3	69.2	227.0	7.9
79	13843	0.9	24.9389	22.2	0.2100	22.8	0.0380	5.2	0.23	240.3	12.2	193.5	40.1	b.d.	b.d.	240.3	12.2
66	7248	1.0	25.1201	28.0	0.2105	28.4	0.0384	4.3	0.15	242.6	10.2	194.0	50.1	b.d.	b.d.	242.6	10.2
86	14583	0.9	19.8792	20.1	0.2685	20.4	0.0387	3.4	0.17	244.8	8.1	241.5	43.9	209.1	470.5	244.8	8.1
119	7187	0.7	21.9023	12.4	0.2450	12.7	0.0389	2.8	0.22	246.1	6.7	222.5	25.4	b.d.	b.d.	246.1	6.7
73	11424	1.4	22.3545	18.6	0.2471	18.8	0.0401	2.9	0.16	253.2	7.3	224.2	37.9	b.d.	b.d.	253.2	7.3
390	41673	1.2	20.0549	5.4	0.2820	5.4	0.0410	0.5	0.08	259.1	1.2	252.2	12.1	188.6	125.5	259.1	1.2
331	131753	3.9	12.6532	1.1	1.6032	2.6	0.1471	2.3	0.90	884.8	19.4	971.5	16.2	1172.9	21.9	1172.9	21.9
50	24300	0.6	11.7110	3.0	2.6691	3.2	0.2267	1.2	0.39	1317.2	14.9	1319.9	23.7	1324.4	57.2	1324.4	57.2
60	23003	1.7	11.5393	2.7	2.8138	3.2	0.2355	1.8	0.57	1363.2	22.6	1359.2	24.3	1352.9	51.5	1352.9	51.5
105	71616	1.3	11.3490	1.8	2.7137	2.1	0.2234	1.1	0.50	1299.6	12.5	1332.2	15.7	1384.9	35.0	1384.9	35.0

203	120606	112.4	11.2664	0.8	2.5334	1.7	0.2070	1.5	0.90	1212.9	16.8	1281.7	12.3	1399.0	14.4	1399.0	14.4
418	261782	2.1	11.2303	0.4	2.7252	1.1	0.2220	1.0	0.93	1292.2	11.8	1335.3	8.0	1405.1	7.5	1405.1	7.5
147	64574	2.1	11.1712	0.8	2.8982	1.6	0.2348	1.3	0.85	1359.7	16.4	1381.4	11.9	1415.2	16.1	1415.2	16.1
137	84629	0.5	11.1411	0.9	2.9941	1.4	0.2419	1.1	0.78	1396.8	13.7	1406.1	10.7	1420.4	16.8	1420.4	16.8
754	299276	5.8	11.1341	0.2	2.9110	0.8	0.2351	0.7	0.96	1361.0	9.0	1384.8	5.8	1421.6	4.0	1421.6	4.0
98	151661	0.6	11.1150	0.8	2.9785	1.2	0.2401	0.9	0.72	1387.3	10.7	1402.2	9.1	1424.8	15.8	1424.8	15.8
197	147457	1.2	11.0994	1.2	3.1171	1.9	0.2509	1.6	0.80	1443.3	20.1	1436.9	14.9	1427.5	22.0	1427.5	22.0
474	192895	1.8	11.0952	0.3	2.9122	1.4	0.2343	1.4	0.98	1357.2	17.1	1385.1	10.7	1428.3	4.8	1428.3	4.8
393	245996	3.9	10.5697	0.4	3.1622	3.1	0.2424	3.0	0.99	1399.2	38.2	1448.0	23.7	1520.3	8.0	1520.3	8.0
85	136392	2.2	10.5693	2.3	2.6364	3.6	0.2021	2.8	0.77	1186.6	30.4	1310.9	26.6	1520.4	43.2	1520.4	43.2
173	56965	6.0	10.1463	1.0	3.7628	2.2	0.2769	2.0	0.90	1575.7	27.8	1584.9	17.8	1597.0	18.2	1597.0	18.2
5001	3261908	66.6	10.0817	0.5	3.5448	5.1	0.2592	5.1	1.00	1485.7	67.2	1537.3	40.3	1608.9	8.7	1608.9	8.7
99	57154	1.8	10.0069	1.5	3.6664	2.1	0.2661	1.5	0.69	1521.0	19.9	1564.1	16.9	1622.8	28.5	1622.8	28.5
172	138717	2.4	9.9453	0.7	3.6897	3.6	0.2661	3.6	0.98	1521.2	48.5	1569.1	29.2	1634.3	13.2	1634.3	13.2
22	6307	0.8	9.9277	5.0	3.9611	6.1	0.2852	3.6	0.58	1617.5	51.2	1626.3	49.8	1637.6	92.6	1637.6	92.6
209	144694	1.8	9.9230	0.7	3.6304	3.2	0.2613	3.1	0.97	1496.3	41.0	1556.2	25.1	1638.4	13.7	1638.4	13.7
574	680288	5.3	9.8771	0.2	3.6331	1.2	0.2603	1.2	0.98	1491.1	16.4	1556.8	9.9	1647.0	4.0	1647.0	4.0
759	266025	6.7	9.8293	0.8	3.6353	3.6	0.2592	3.5	0.98	1485.5	46.7	1557.3	28.7	1656.0	14.0	1656.0	14.0
551	776389	6.0	9.8084	0.4	3.9784	1.1	0.2830	1.1	0.94	1606.5	15.4	1629.8	9.3	1660.0	7.2	1660.0	7.2
458	380866	2.4	9.7674	0.3	4.0033	1.6	0.2836	1.5	0.98	1609.4	21.9	1634.9	12.8	1667.7	5.7	1667.7	5.7
401	278787	1.3	9.7417	0.3	4.2471	0.9	0.3001	0.9	0.95	1691.7	13.3	1683.2	7.7	1672.6	5.3	1672.6	5.3
312	199373	1.8	9.7035	0.4	3.9898	1.6	0.2808	1.6	0.97	1595.3	22.0	1632.1	13.1	1679.9	7.7	1679.9	7.7
170	148252	0.9	9.6914	0.6	4.0587	1.4	0.2853	1.2	0.89	1617.9	17.4	1646.1	11.1	1682.2	11.5	1682.2	11.5
82	63767	1.4	9.6818	1.6	3.7930	1.7	0.2663	0.7	0.43	1522.2	10.1	1591.3	13.8	1684.0	28.7	1684.0	28.7
618	430331	2.8	9.6156	0.3	4.3989	1.6	0.3068	1.6	0.98	1724.8	23.9	1712.1	13.3	1696.6	5.8	1696.6	5.8
686	189657	1.8	9.6014	0.9	3.7538	2.9	0.2614	2.8	0.95	1497.0	37.4	1582.9	23.5	1699.4	16.1	1699.4	16.1
210	106892	1.8	9.4949	0.5	4.3975	1.8	0.3028	1.7	0.97	1705.3	26.0	1711.9	14.8	1719.9	8.4	1719.9	8.4
471	457353	1.5	9.4315	0.2	4.5694	0.7	0.3126	0.6	0.93	1753.3	9.6	1743.7	5.6	1732.2	4.5	1732.2	4.5
384	242749	1.8	9.4225	0.4	4.3987	1.3	0.3006	1.2	0.95	1694.3	17.9	1712.1	10.5	1733.9	7.3	1733.9	7.3
297	198073	2.6	9.4197	1.5	4.5169	9.4	0.3086	9.3	0.99	1733.8	140.8	1734.1	78.2	1734.5	27.7	1734.5	27.7
261	117527	1.6	9.3746	0.6	4.5631	1.4	0.3102	1.2	0.88	1741.9	18.2	1742.5	11.2	1743.3	11.7	1743.3	11.7
160	144811	2.0	9.2707	0.5	4.8055	1.7	0.3231	1.7	0.96	1804.9	26.0	1785.9	14.5	1763.7	9.0	1763.7	9.0
446	222895	5.5	8.5631	4.8	4.8656	7.4	0.3022	5.7	0.77	1702.1	85.2	1796.3	62.6	1907.5	85.4	1907.5	85.4
1036	1302030	4.1	4.2528	1.8	13.3172	2.7	0.4108	1.9	0.73	2218.4	36.5	2702.4	25.2	3087.3	29.1	3087.3	29.1

Sample KTC-12-Tps1 n = 76

U (ppm)	$^{206}Pb/^{204}Pb$	U/Th	(%) $^{206}Pb^*/^{207}Pb^*$	± (1σ)	(%) $^{207}Pb^*/^{235}U^*$	± (1σ)	(%) $^{206}Pb^*/^{238}U^*$	± (1σ)	error corr.	Age (Ma) $^{206}Pb^*/^{238}U^*$	± (1σ)	Age (Ma) $^{207}Pb^*/^{235}U^*$	± (1σ)	Age (Ma) $^{207}Pb^*/^{206}Pb^*$	± (1σ)	Preferred age (Ma)	± (1σ)
122	5514	8.71	20.2	12.1	0.08	15.2	0.01	9.2	0.60	72.0	6.6	74.9	11.0	168	284.1	72	6.6
297	21415	3.58	22.1	14.0	0.07	14.5	0.01	4.0	0.27	72.7	2.9	69.4	9.7	b.d.	b.d.	73	2.9
203	7114	1.24	20.0	25.4	0.08	25.9	0.01	4.8	0.18	72.9	3.5	76.6	19.1	192	599.9	73	3.5
1123	2632	1.10	20.3	7.2	0.08	8.0	0.01	3.4	0.42	74.4	2.5	77.1	5.9	162	169.0	74	2.5
364	40891	3.27	21.4	13.9	0.08	14.0	0.01	1.9	0.14	74.7	1.4	73.5	9.9	35	333.1	75	1.4
391	17054	0.79	21.7	8.7	0.07	8.8	0.01	1.5	0.17	75.1	1.1	72.9	6.2	2	209.2	75	1.1
427	21707	4.35	21.8	8.8	0.07	9.3	0.01	2.8	0.30	75.7	2.1	73.1	6.5	b.d.	b.d.	76	2.1
1348	72992	8.55	21.1	2.7	0.08	2.8	0.01	0.6	0.23	78.0	0.5	77.9	2.1	73	64.3	78	0.5
163	6714	1.86	25.3	19.5	0.07	19.8	0.01	3.3	0.16	78.6	2.5	65.7	12.6	b.d.	b.d.	79	2.5
681	42494	4.84	20.6	4.1	0.08	4.3	0.01	1.4	0.32	79.2	1.1	80.6	3.3	125	96.1	79	1.1
177	7682	1.78	19.3	19.6	0.09	20.6	0.01	6.3	0.30	80.9	5.0	87.6	17.3	274	452.8	81	5.0
217	17170	2.20	20.8	13.0	0.08	13.2	0.01	2.1	0.16	81.8	1.7	82.5	10.5	103	309.0	82	1.7
390	19183	7.37	20.3	6.2	0.09	6.4	0.01	1.6	0.25	82.0	1.3	84.6	5.2	159	146.1	82	1.3
445	17522	1.41	21.9	7.2	0.08	7.4	0.01	1.9	0.25	82.2	1.5	78.9	5.6	b.d.	b.d.	82	1.5
749	42383	2.83	21.4	5.8	0.08	5.9	0.01	1.1	0.19	83.2	0.9	81.6	4.6	35	138.2	83	0.9
146	13978	1.48	24.0	59.1	0.08	59.3	0.01	4.6	0.08	84.5	3.9	74.1	42.4	b.d.	b.d.	85	3.9
445	16741	3.19	21.0	10.0	0.09	10.2	0.01	1.8	0.18	84.7	1.5	84.7	8.3	86	238.7	85	1.5
498	25917	2.20	22.0	11.3	0.08	11.4	0.01	1.5	0.13	86.0	1.3	82.2	9.0	b.d.	b.d.	86	1.3
85	3618	10.45	27.5	33.4	0.07	34.2	0.01	7.8	0.23	86.0	6.6	66.1	21.9	b.d.	b.d.	86	6.6
584	24286	3.43	21.4	5.7	0.09	5.8	0.01	1.2	0.20	87.1	1.0	85.2	4.7	34	135.7	87	1.0
222	12314	0.94	21.1	16.1	0.09	16.6	0.01	3.8	0.23	87.6	3.3	86.8	13.8	66	386.6	88	3.3
181	9245	1.33	23.7	17.7	0.08	18.2	0.01	4.3	0.24	87.8	3.8	77.9	13.6	b.d.	b.d.	88	3.8
158	6452	0.59	31.5	41.2	0.06	41.4	0.01	4.5	0.11	88.5	3.9	59.6	24.0	b.d.	b.d.	88	3.9
470	51917	6.17	21.1	3.9	0.09	4.4	0.01	2.0	0.46	89.0	1.8	88.2	3.7	66	93.4	89	1.8
787	73376	0.53	20.6	5.2	0.09	6.0	0.01	3.0	0.50	90.0	2.7	91.2	5.2	122	121.4	90	2.7
115	7383	2.32	28.8	31.1	0.07	31.6	0.01	5.7	0.18	90.4	5.1	66.4	20.3	b.d.	b.d.	90	5.1
203	8799	2.08	18.9	9.9	0.10	10.0	0.01	1.4	0.14	91.0	1.3	100.2	9.5	326	224.9	91	1.3
88	5739	0.82	24.6	44.4	0.08	44.6	0.01	3.9	0.09	91.8	3.5	78.5	33.7	b.d.	b.d.	92	3.5
206	6974	0.95	20.1	13.0	0.10	13.5	0.01	3.7	0.27	92.8	3.4	96.2	12.4	181	304.5	93	3.4
167	10228	2.50	25.8	32.1	0.08	33.3	0.01	8.9	0.27	95.7	8.4	78.1	25.1	b.d.	b.d.	96	8.4
157	8804	0.79	22.7	20.4	0.09	21.0	0.02	5.1	0.24	96.9	4.9	89.1	17.9	b.d.	b.d.	97	4.9
170	19487	0.89	20.0	12.5	0.11	12.7	0.02	2.7	0.21	102.2	2.7	106.3	12.9	200	290.1	102	2.7
238	34491	0.63	20.6	13.8	0.11	14.0	0.02	2.2	0.16	104.7	2.3	105.6	14.0	125	326.5	105	2.3
205	24591	0.78	18.8	10.7	0.14	11.4	0.02	3.7	0.33	120.1	4.4	131.3	14.0	338	243.6	120	4.4
50	4818	1.96	16.3	39.4	0.20	40.1	0.02	7.4	0.19	148.8	10.9	183.1	67.2	652	878.1	149	10.9
51	5831	0.59	30.0	59.7	0.11	60.1	0.02	6.8	0.11	149.1	10.0	103.8	59.4	b.d.	b.d.	149	10.0
30	1537	0.65	23.8	39.6	0.14	40.0	0.02	5.4	0.13	149.3	8.0	129.1	48.5	b.d.	b.d.	149	8.0
37	3308	0.93	19.7	39.2	0.17	39.7	0.02	6.0	0.15	151.7	9.0	156.7	57.7	232	938.5	152	9.0
116	6243	1.88	23.6	25.1	0.14	25.4	0.02	4.1	0.16	153.3	6.2	133.4	31.8	b.d.	b.d.	153	6.2
64	11222	0.82	23.4	15.0	0.15	17.5	0.03	9.1	0.52	165.8	14.9	144.9	23.7	b.d.	b.d.	166	14.9
330	55647	5.30	12.2	2.5	0.42	3.2	0.04	2.0	0.63	236.8	4.6	357.5	9.6	1241	48.9	237	4.6
56	7660	1.00	18.7	10.6	0.28	11.7	0.04	5.0	0.43	237.6	11.7	248.1	25.7	349	239.3	238	11.7
59	12191	0.77	20.3	23.8	0.26	24.2	0.04	3.9	0.16	241.6	9.2	234.5	50.6	164	564.4	242	9.2
57	7217	0.83	19.8	29.0	0.27	29.3	0.04	4.5	0.15	242.2	10.6	239.7	62.7	215	684.0	242	10.6

48	11390	1.01	18.3	15.5	0.29	16.0	0.04	4.0	0.25	245.9	9.7	261.2	36.8	401	348.6	246	9.7
49	7456	1.04	20.5	19.2	0.26	19.8	0.04	4.8	0.24	246.3	11.7	235.9	41.7	133	455.4	246	11.7
51	12518	0.86	17.3	16.3	0.31	16.8	0.04	3.8	0.22	249.8	9.2	277.7	40.8	520	360.8	250	9.2
124	33320	1.25	19.5	11.6	0.28	11.8	0.04	2.0	0.17	250.6	4.9	250.6	26.2	251	268.2	251	4.9
139	93480	53.34	11.4	0.7	2.63	1.9	0.22	1.8	0.92	1267.6	20.5	1310.1	14.2	1380	14.4	1380	14.4
102	96720	0.62	11.2	1.2	2.95	2.5	0.24	2.2	0.88	1388.1	27.6	1395.8	19.1	1408	23.1	1408	23.1
72	146559	0.87	11.2	1.2	2.72	3.3	0.22	3.1	0.94	1284.8	36.2	1333.2	24.7	1412	22.4	1412	22.4
82	86815	0.69	11.2	1.1	3.07	1.6	0.25	1.1	0.69	1432.3	14.2	1425.0	12.2	1414	21.9	1414	21.9
119	170389	0.54	11.1	0.9	2.96	1.2	0.24	0.7	0.60	1375.2	8.8	1398.0	9.0	1433	18.1	1433	18.1
76	14817	1.56	10.9	1.9	2.60	2.8	0.21	2.1	0.76	1207.9	23.7	1299.8	20.8	1455	35.2	1455	35.2
131	74568	8.60	10.9	0.7	3.02	4.3	0.24	4.3	0.99	1382.8	53.3	1412.9	33.1	1459	13.9	1459	13.9
646	330237	6.02	10.7	0.7	3.02	1.4	0.23	1.3	0.88	1354.0	15.4	1413.8	10.9	1505	12.6	1505	12.6
63	44777	1.68	10.2	1.6	3.43	2.5	0.26	2.0	0.78	1464.4	25.9	1512.3	19.9	1580	29.7	1580	29.7
270	200558	3.89	10.2	0.7	3.49	3.3	0.26	3.2	0.98	1475.9	42.4	1526.0	25.9	1596	12.8	1596	12.8
721	344291	4.81	10.0	0.5	3.63	2.0	0.26	1.9	0.96	1501.6	26.1	1555.1	16.1	1629	9.9	1629	9.9
213	221528	2.47	9.9	0.6	3.91	4.9	0.28	4.9	0.99	1595.2	69.3	1615.5	39.9	1642	10.6	1642	10.6
231	283030	5.24	9.8	0.5	3.61	2.9	0.26	2.9	0.98	1477.4	38.4	1550.9	23.5	1652	9.5	1652	9.5
242	307788	1.64	9.8	0.6	3.68	1.2	0.26	1.1	0.90	1499.3	14.9	1566.0	10.0	1657	10.3	1657	10.3
117	123683	0.99	9.7	0.9	4.24	2.4	0.30	2.3	0.93	1686.3	33.5	1681.2	19.9	1675	16.0	1675	16.0
314	381743	0.68	9.7	0.2	4.14	0.8	0.29	0.8	0.96	1651.7	11.6	1663.1	6.8	1678	4.5	1678	4.5
152	200218	1.13	9.7	0.8	3.34	4.6	0.24	4.5	0.99	1361.2	55.6	1490.6	35.9	1680	14.4	1680	14.4
397	631687	6.51	9.7	0.4	4.20	2.1	0.30	2.1	0.99	1669.7	30.7	1674.7	17.4	1681	6.6	1681	6.6
150	163112	1.69	9.7	0.8	4.05	3.4	0.28	3.3	0.97	1610.3	46.4	1644.0	27.3	1687	14.8	1687	14.8
396	598536	2.90	9.7	0.2	4.34	1.1	0.30	1.1	0.97	1712.3	16.0	1701.8	9.0	1689	4.5	1689	4.5
844	877993	7.47	9.6	0.2	4.32	0.8	0.30	0.8	0.97	1702.0	11.3	1697.7	6.4	1692	3.4	1692	3.4
1320	3498705	14.76	9.6	0.1	4.39	0.5	0.30	0.5	0.99	1712.7	7.4	1711.1	4.1	1709	1.2	1709	1.2
461	1042752	1.49	9.5	0.3	3.72	1.5	0.26	1.5	0.99	1471.8	19.9	1575.9	12.3	1718	4.7	1718	4.7
382	682518	2.65	9.5	0.2	4.30	1.6	0.30	1.6	0.99	1670.6	22.9	1693.3	12.9	1722	3.4	1722	3.4
378	344006	1.37	9.4	0.3	4.41	1.5	0.30	1.5	0.98	1699.8	21.8	1713.7	12.3	1731	5.7	1731	5.7
1412	243056	2.85	9.4	0.4	4.14	1.6	0.28	1.6	0.97	1605.6	22.7	1661.4	13.4	1733	6.7	1733	6.7
96	95259	1.63	9.4	0.7	4.60	3.0	0.31	2.9	0.97	1757.3	44.6	1750.1	24.9	1742	12.7	1742	12.7
157	192393	2.06	9.4	0.6	3.84	3.8	0.26	3.7	0.99	1492.5	49.8	1601.1	30.4	1747	10.3	1747	10.3

Sample KTC-12-Ttc1 n = 31

U	$^{206}Pb/$	U/	(%) $^{206}Pb^*/$	±	(%) $^{207}Pb^*/$	±	(%) $^{206}Pb^*/$	±	error	Age (Ma) $^{206}Pb^*/$	±	Age (Ma) $^{207}Pb^*/$	±	Age (Ma) $^{207}Pb^*/$	±	Preferred age	±
(ppm)	^{204}Pb	Th	$^{207}Pb^*$	(1σ)	$^{235}U^*$	(1σ)	$^{238}U^*$	(1σ)	corr.	$^{238}U^*$	(1σ)	$^{235}U^*$	(1σ)	$^{206}Pb^*$	(1σ)	(Ma)	(1σ)
342	3252	1.0	21.4705	33.8	0.0237	34.3	0.0037	5.9	0.17	23.8	1.4	23.8	8.1	27.5	830.7	23.8	1.4
207	2928	2.0	17.7471	34.6	0.0289	35.4	0.0037	7.4	0.21	23.9	1.8	28.9	10.1	466.1	787.9	23.9	1.8
301	4708	2.0	21.5246	45.4	0.0239	45.7	0.0037	5.5	0.12	24.0	1.3	24.0	10.8	b.d.	b.d.	24.0	1.3
141	2554	1.7	24.6544	46.7	0.0209	47.4	0.0037	7.8	0.16	24.1	1.9	21.0	9.9	b.d.	b.d.	24.1	1.9
168	2349	2.3	17.0782	51.2	0.0302	52.3	0.0037	10.9	0.21	24.1	2.6	30.2	15.6	b.d.	b.d.	24.1	2.6
376	4925	1.7	34.6142	56.1	0.0150	56.2	0.0038	4.0	0.07	24.2	1.0	15.1	8.4	b.d.	b.d.	24.2	1.0
161	1380	1.8	17.8099	86.9	0.0292	87.1	0.0038	6.7	0.08	24.2	1.6	29.2	25.1	b.d.	b.d.	24.2	1.6
190	1333	1.9	31.2727	40.5	0.0167	41.2	0.0038	7.6	0.18	24.4	1.8	16.8	6.9	b.d.	b.d.	24.4	1.8
~~207~~	~~3481~~	~~1.3~~	~~2.2638~~	-	~~0.2311~~	-	~~0.0038~~	~~8.8~~	~~0.00~~	~~24.4~~	~~2.2~~	~~211.1~~	-	~~b.d.~~	~~b.d.~~	~~24.4~~	~~2.2~~
208	2857	1.8	21.4304	31.2	0.0247	31.6	0.0038	5.1	0.16	24.7	1.2	24.7	7.7	32.0	763.8	24.7	1.2
287	2596	1.7	21.1338	28.2	0.0250	28.8	0.0038	5.7	0.20	24.7	1.4	25.1	7.1	65.3	683.9	24.7	1.4
227	4318	1.3	19.0926	29.9	0.0277	30.5	0.0038	6.0	0.20	24.7	1.5	27.8	8.3	301.9	694.8	24.7	1.5
343	825	1.0	20.3727	16.5	0.0261	17.2	0.0039	4.8	0.28	24.9	1.2	26.2	4.4	151.9	389.2	24.9	1.2
230	3745	2.0	21.3188	44.1	0.0250	44.6	0.0039	6.5	0.15	24.9	1.6	25.1	11.0	b.d.	b.d.	24.9	1.6
1630	38077	1.2	21.0454	3.8	0.0253	4.8	0.0039	3.0	0.62	24.9	0.8	25.4	1.2	75.2	90.0	24.9	0.8
223	4835	3.0	20.9171	49.6	0.0255	50.5	0.0039	9.6	0.19	24.9	2.4	25.6	12.8	b.d.	b.d.	24.9	2.4
950	13596	2.2	20.4789	10.5	0.0261	10.8	0.0039	2.4	0.22	24.9	0.6	26.2	2.8	139.7	247.7	24.9	0.6
1044	10441	1.9	22.4288	9.3	0.0239	9.4	0.0039	1.0	0.11	25.1	0.3	24.0	2.2	b.d.	b.d.	25.1	0.3
1297	21301	1.9	20.3733	5.8	0.0264	6.0	0.0039	1.6	0.27	25.1	0.4	26.4	1.6	151.8	135.2	25.1	0.4
875	9143	2.1	30.6659	20.8	0.0175	20.8	0.0039	1.3	0.06	25.1	0.3	17.6	3.6	b.d.	b.d.	25.1	0.3
202	3115	2.0	14.2173	39.8	0.0380	40.3	0.0039	6.7	0.17	25.2	1.7	37.9	15.0	938.2	848.9	25.2	1.7
234	2620	2.3	26.5602	20.8	0.0204	21.8	0.0039	6.8	0.31	25.2	1.7	20.5	4.4	b.d.	b.d.	25.2	1.7
1081	18171	1.1	21.9506	10.3	0.0246	10.7	0.0039	2.7	0.25	25.2	0.7	24.7	2.6	b.d.	b.d.	25.2	0.7
794	11206	2.1	20.7626	11.2	0.0261	11.4	0.0039	2.1	0.18	25.3	0.5	26.1	2.9	107.3	264.9	25.3	0.5
798	15485	1.5	21.4187	8.2	0.0253	8.5	0.0039	2.2	0.26	25.3	0.6	25.4	2.1	33.3	197.6	25.3	0.6
926	32106	2.2	22.4021	14.4	0.0243	14.8	0.0039	3.4	0.23	25.4	0.9	24.3	3.6	b.d.	b.d.	25.4	0.9
809	10611	1.2	21.9804	8.3	0.0247	8.6	0.0039	1.9	0.23	25.4	0.5	24.8	2.1	b.d.	b.d.	25.4	0.5
729	5435	1.7	21.4530	11.5	0.0253	11.6	0.0039	1.5	0.13	25.4	0.4	25.4	2.9	29.4	275.9	25.4	0.4
610	14643	1.5	22.3193	18.4	0.0244	18.5	0.0039	1.7	0.09	25.4	0.4	24.4	4.5	b.d.	b.d.	25.4	0.4
354	7286	1.2	22.2721	32.0	0.0244	32.2	0.0039	3.7	0.11	25.4	0.9	24.5	7.8	b.d.	b.d.	25.4	0.9
255	4378	1.8	39.5104	101.2	0.0139	101.4	0.0040	7.0	0.07	25.6	1.8	14.0	14.1	b.d.	b.d.	25.6	1.8
963	22722	2.3	20.7720	9.0	0.0264	9.5	0.0040	2.9	0.30	25.6	0.7	26.5	2.5	106.2	213.8	25.6	0.7

1 age manually rejected due to extremely high error in $^{207}Pb^*/^{235}U^*$ age.

Summary statistics for all 31 ages:

Final age: 25.1 ± 0.2 Ma 1σ
MSWD = 0.22
Probability = 1.00

Sample KTC-12-Ttc2 n = 18

U (ppm)	$^{206}Pb/^{204}Pb$	U/Th	$^{206}Pb^*/^{207}Pb^*$	± (%) (1σ)	$^{207}Pb^*/^{235}U^*$	± (%) (1σ)	$^{206}Pb^*/^{238}U^*$	± (%) (1σ)	error corr.	Age (Ma) $^{206}Pb^*/^{238}U^*$	± (1σ)	Age (Ma) $^{207}Pb^*/^{235}U^*$	± (1σ)	Age (Ma) $^{207}Pb^*/^{206}Pb^*$	± (1σ)	Preferred age (Ma)	± (1σ)
1658	8798	1.7	23.1375	6.2	0.0235	6.3	0.0039	1.4	0.22	25.4	0.4	23.6	1.5	b.d.	b.d.	25.4	0.4
476	3854	1.8	28.4503	42.3	0.0192	42.8	0.0040	6.3	0.15	25.4	1.6	19.3	8.2	b.d.	b.d.	25.4	1.6
282	5439	2.1	20.5821	25.7	0.0267	26.6	0.0040	7.0	0.26	25.6	1.8	26.7	7.0	127.9	613.4	25.6	1.8
601	10336	2.2	19.5043	17.1	0.0284	17.6	0.0040	4.1	0.23	25.8	1.1	28.4	4.9	253.0	395.8	25.8	1.1
1076	14473	1.2	22.1255	7.9	0.0250	9.1	0.0040	4.5	0.50	25.8	1.2	25.1	2.3	b.d.	b.d.	25.8	1.2
392	4544	1.6	20.4859	9.9	0.0272	10.4	0.0040	3.1	0.30	26.0	0.8	27.3	2.8	138.9	233.7	26.0	0.8
392	7255	1.9	23.3104	20.2	0.0240	20.6	0.0041	4.4	0.21	26.1	1.1	24.0	4.9	b.d.	b.d.	26.1	1.1
~~146~~	~~1803~~	~~1.8~~	~~18.0914~~	~~58.8~~	~~0.0311~~	~~60.7~~	~~0.0041~~	~~15.0~~	~~0.25~~	~~26.3~~	~~3.9~~	~~31.1~~	~~18.6~~	~~b.d.~~	~~b.d.~~	~~26.3~~	~~3.9~~
922	12060	1.9	21.2320	8.0	0.0266	8.2	0.0041	1.8	0.22	26.3	0.5	26.6	2.1	54.2	190.3	26.3	0.5
579	4680	1.4	23.2326	20.6	0.0243	20.9	0.0041	3.8	0.18	26.3	1.0	24.4	5.0	b.d.	b.d.	26.3	1.0
379	846	2.2	16.2634	27.6	0.0347	28.1	0.0041	5.3	0.19	26.4	1.4	34.7	9.6	656.3	601.8	26.4	1.4
953	19073	1.6	21.1239	12.0	0.0269	12.3	0.0041	2.8	0.23	26.5	0.7	26.9	3.3	66.4	285.6	26.5	0.7
~~212~~	~~7005~~	~~1.4~~	~~19.9815~~	~~49.5~~	~~0.0287~~	~~52.3~~	~~0.0042~~	~~16.8~~	~~0.32~~	~~26.7~~	~~4.5~~	~~28.7~~	~~14.8~~	~~b.d.~~	~~b.d.~~	~~26.7~~	~~4.5~~
643	9983	1.6	22.8741	37.2	0.0254	37.3	0.0042	3.2	0.09	27.1	0.9	25.4	9.4	b.d.	b.d.	27.1	0.9
433	15445	1.6	19.5990	27.4	0.0297	28.3	0.0042	7.2	0.26	27.2	2.0	29.7	8.3	241.9	640.9	27.2	2.0
~~160~~	~~1740~~	~~1.4~~	~~22.9758~~	~~72.7~~	~~0.0254~~	~~73.6~~	~~0.0042~~	~~11.7~~	~~0.16~~	~~27.2~~	~~3.2~~	~~25.5~~	~~18.5~~	~~b.d.~~	~~b.d.~~	~~27.2~~	~~3.2~~
908	18830	1.0	20.6953	11.3	0.0285	12.6	0.0043	5.6	0.45	27.5	1.5	28.5	3.5	115.0	267.0	27.5	1.5
~~169~~	~~3670~~	~~2.3~~	~~15.3526~~	~~39.9~~	~~0.0393~~	~~43.8~~	~~0.0044~~	~~18.0~~	~~0.41~~	~~28.1~~	~~5.1~~	~~39.1~~	~~16.8~~	~~778.7~~	~~872.4~~	~~28.1~~	~~5.1~~
~~219~~	~~1466~~	~~1.4~~	~~19.0980~~	~~27.3~~	~~0.0317~~	~~29.4~~	~~0.0044~~	~~10.8~~	~~0.37~~	~~28.2~~	~~3.0~~	~~31.7~~	~~9.2~~	~~301.3~~	~~633.5~~	~~28.2~~	~~3.0~~
~~147~~	~~2127~~	~~1.8~~	~~14.2149~~	~~36.0~~	~~0.0427~~	~~37.2~~	~~0.0044~~	~~9.5~~	~~0.26~~	~~28.3~~	~~2.7~~	~~42.4~~	~~15.5~~	~~938.5~~	~~761.4~~	~~28.3~~	~~2.7~~
~~602~~	~~10962~~	~~1.3~~	~~23.3774~~	~~28.8~~	~~0.0260~~	~~31.6~~	~~0.0044~~	~~13.1~~	~~0.42~~	~~28.3~~	~~3.7~~	~~26.0~~	~~8.1~~	~~b.d.~~	~~b.d.~~	~~28.3~~	~~3.7~~
~~438~~	~~2983~~	~~1.7~~	~~20.6988~~	~~25.2~~	~~0.0300~~	~~27.7~~	~~0.0045~~	~~11.4~~	~~0.41~~	~~28.9~~	~~3.3~~	~~30.0~~	~~8.2~~	~~114.6~~	~~603.9~~	~~28.9~~	~~3.3~~
~~119~~	~~1005~~	~~1.5~~	~~23.5555~~	~~80.0~~	~~0.0277~~	~~80.8~~	~~0.0047~~	~~11.5~~	~~0.14~~	~~30.4~~	~~3.5~~	~~27.7~~	~~22.1~~	~~b.d.~~	~~b.d.~~	~~30.4~~	~~3.5~~
131	70392	2.2	11.2119	0.8	2.6998	2.2	0.2195	2.1	0.93	1279.4	24.0	1328.4	16.4	1408.2	15.3	1408.2	15.3
290	271961	6.4	10.0560	1.1	3.5067	2.2	0.2558	1.9	0.86	1468.1	24.6	1528.7	17.2	1613.7	20.5	1613.7	20.5
396	409656	1.7	9.8072	0.2	4.1856	1.8	0.2977	1.8	0.99	1680.0	26.7	1671.2	14.9	1660.2	4.0	1660.2	4.0
43	43765	1.0	8.3300	1.4	5.2088	2.2	0.3147	1.6	0.76	1763.7	25.3	1854.1	18.3	1956.9	24.8	1956.9	24.8

9 ages manually rejected due to high relative error in $^{206}Pb^*/^{238}U^*$ and $^{207}Pb^*/^{235}U^*$ ages.

Summary statistics for 14 youngest ages:
Final age: 26.0 ± 0.2 Ma 1σ
MSWD = 0.54
Probability = 0.90

Summary statistics for the 45 youngest ages of KTC-12-Ttc1 and KTC-12-Ttc2 combined:
Final age: 25.3 ± 0.1 Ma 1σ
MSWD = 0.61
Probability = 0.98

Sample KTC-14-dz1 **n = 50**

			(%)		(%)		(%)			Age (Ma)		Age (Ma)		Age (Ma)		Preferred	
U	^{206}Pb/	U/	^{206}Pb*/	±	^{207}Pb*/	±	^{206}Pb*/	±	error	^{206}Pb*/	±	^{207}Pb*/	±	^{207}Pb*/	±	age	±
(ppm)	^{204}Pb	Th	^{207}Pb*	(1σ)	^{235}U*	(1σ)	^{238}U*	(1σ)	corr.	^{238}U*	(1σ)	^{235}U*	(1σ)	^{206}Pb*	(1σ)	(Ma)	(1σ)
340	21158	1.2	20.2893	4.4	0.1590	5.0	0.0234	2.3	0.46	149.1	3.4	149.8	7.0	161.5	104.0	149.1	3.4
79	4862	0.9	26.3258	26.9	0.1234	27.1	0.0236	3.3	0.12	150.1	4.9	118.1	30.2	b.d.	b.d.	150.1	4.9
145	8803	2.8	19.2818	12.9	0.1687	13.0	0.0236	2.0	0.15	150.3	3.0	158.3	19.1	279.4	296.0	150.3	3.0
200	11476	0.4	22.9905	5.6	0.1425	6.0	0.0238	2.1	0.36	151.4	3.2	135.3	7.6	b.d.	b.d.	151.4	3.2
28	5806	0.8	20.3386	93.2	0.1630	93.6	0.0240	8.3	0.09	153.1	12.6	153.3	133.9	155.8	848.3	153.1	12.6
253	31681	0.4	19.2741	5.6	0.1899	6.0	0.0266	1.9	0.32	168.9	3.1	176.6	9.7	280.3	129.4	168.9	3.1
170	4319	0.9	21.3682	9.4	0.1765	10.0	0.0274	3.2	0.32	174.0	5.5	165.1	15.2	38.9	226.2	174.0	5.5
26	15108	1.6	12.8763	5.5	2.1622	6.1	0.2019	2.6	0.42	1185.6	27.6	1169.0	42.0	1138.3	109.2	1138.3	109.2
23	11419	1.0	12.7643	3.2	2.2119	3.9	0.2048	2.3	0.58	1200.9	24.7	1184.8	27.2	1155.6	62.9	1155.6	62.9
40	21761	0.8	12.7056	2.6	2.1857	3.3	0.2014	2.0	0.61	1182.9	21.4	1176.5	22.6	1164.7	51.0	1164.7	51.0
37	39323	1.1	12.6706	3.0	2.2046	4.4	0.2026	3.2	0.73	1189.2	35.0	1182.5	30.9	1170.2	59.9	1170.2	59.9
66	35435	2.1	12.5798	2.1	2.1556	2.3	0.1967	1.0	0.43	1157.4	10.6	1166.9	16.0	1184.4	41.2	1184.4	41.2
166	171219	1.4	12.5419	1.0	2.2265	1.5	0.2025	1.1	0.74	1188.9	12.5	1189.4	10.9	1190.4	20.5	1190.4	20.5
31	13296	0.9	12.5032	3.2	2.2221	4.0	0.2015	2.3	0.59	1183.4	25.3	1188.0	28.0	1196.5	64.0	1196.5	64.0
17	14448	0.8	12.5025	4.4	2.2176	5.1	0.2011	2.7	0.53	1181.1	29.1	1186.6	35.9	1196.6	86.1	1196.6	86.1
105	90156	4.2	12.4804	1.3	2.2535	2.4	0.2040	2.0	0.84	1196.7	21.9	1197.9	16.8	1200.1	25.5	1200.1	25.5
169	107355	1.2	12.4721	0.7	2.1859	1.9	0.1977	1.7	0.92	1163.1	18.3	1176.6	13.0	1201.4	14.4	1201.4	14.4
34	49592	0.8	12.4655	3.3	2.2343	3.5	0.2020	1.2	0.34	1186.0	12.9	1191.9	24.7	1202.5	65.3	1202.5	65.3
31	20165	1.0	12.4575	3.7	2.2759	4.1	0.2056	1.9	0.45	1205.5	20.4	1204.8	28.9	1203.7	72.0	1203.7	72.0
26	20542	1.3	12.4517	4.5	2.2354	5.0	0.2019	2.2	0.44	1185.4	23.9	1192.2	35.1	1204.6	88.6	1204.6	88.6
40	30526	0.9	12.4365	2.1	2.2239	2.6	0.2006	1.5	0.57	1178.5	15.8	1188.6	18.0	1207.0	41.6	1207.0	41.6
16	18065	1.9	12.3901	3.5	2.2504	4.1	0.2022	2.2	0.53	1187.3	23.5	1196.9	28.8	1214.4	68.3	1214.4	68.3
58	42181	1.2	12.3833	3.0	2.3313	6.2	0.2094	5.4	0.87	1225.5	60.8	1221.9	44.3	1215.5	59.7	1215.5	59.7
83	78578	1.2	12.3733	0.8	2.2517	1.6	0.2021	1.4	0.88	1186.4	14.9	1197.3	11.1	1217.0	14.8	1217.0	14.8
24	12365	0.8	12.2119	8.4	2.3071	8.6	0.2043	1.5	0.17	1198.6	15.9	1214.5	60.7	1242.8	165.6	1242.8	165.6
15	6685	1.4	11.7422	8.2	2.3761	8.8	0.2024	3.2	0.36	1187.9	35.0	1235.4	63.2	1319.2	159.8	1319.2	159.8
99	67217	1.3	11.3029	0.7	2.8845	1.8	0.2365	1.7	0.92	1368.3	20.5	1377.9	13.7	1392.8	13.8	1392.8	13.8
61	132545	0.6	11.1704	1.6	2.9944	1.9	0.2426	1.0	0.54	1400.1	13.1	1406.2	14.6	1415.3	30.7	1415.3	30.7
94	63578	1.1	11.1472	0.8	2.9826	3.2	0.2411	3.1	0.97	1392.6	39.1	1403.2	24.6	1419.3	16.0	1419.3	16.0
129	90948	1.3	10.9475	0.4	3.0201	1.4	0.2398	1.3	0.96	1385.6	16.7	1412.7	10.6	1453.8	7.2	1453.8	7.2
131	57322	0.9	10.0304	0.9	3.8126	2.7	0.2774	2.6	0.95	1578.0	36.4	1595.4	22.1	1618.4	16.3	1618.4	16.3
198	195006	1.5	9.8447	0.5	4.2683	3.9	0.3048	3.8	0.99	1714.9	57.7	1687.3	31.8	1653.1	8.6	1653.1	8.6
263	370057	4.2	9.7992	0.2	4.0554	0.9	0.2882	0.9	0.96	1632.6	12.4	1645.4	7.3	1661.7	4.5	1661.7	4.5
379	539159	4.0	9.7808	0.3	4.2521	2.0	0.3016	1.9	0.99	1699.4	29.0	1684.2	16.2	1665.2	5.9	1665.2	5.9
338	537403	4.6	9.7713	0.3	4.1675	1.6	0.2953	1.5	0.99	1668.2	22.7	1667.7	12.8	1667.0	4.7	1667.0	4.7
95	146111	2.5	9.7666	1.3	4.1487	2.2	0.2939	1.7	0.80	1660.8	25.5	1663.9	17.8	1667.9	24.2	1667.9	24.2
61	129452	1.1	9.7405	1.2	4.2556	2.0	0.3006	1.5	0.78	1694.5	23.0	1684.8	16.3	1672.8	22.9	1672.8	22.9
167	142191	2.9	9.6915	0.4	4.4067	4.3	0.3097	4.2	0.99	1739.5	64.7	1713.6	35.3	1682.1	8.0	1682.1	8.0
85	95970	1.1	9.6885	0.8	4.2957	2.1	0.3018	1.9	0.93	1700.5	28.9	1692.5	17.2	1682.7	14.2	1682.7	14.2
251	244722	4.2	9.6842	0.4	4.2574	1.5	0.2990	1.4	0.96	1686.5	21.0	1685.2	12.1	1683.5	7.2	1683.5	7.2
221	355265	2.3	9.6778	0.4	4.2682	1.2	0.2996	1.2	0.95	1689.3	17.7	1687.3	10.3	1684.7	6.9	1684.7	6.9
380	159578	1.6	9.6741	0.2	4.2788	1.0	0.3002	1.0	0.98	1692.4	14.2	1689.3	8.0	1685.5	3.3	1685.5	3.3
110	107640	1.3	9.6616	0.8	4.2927	4.1	0.3008	4.1	0.98	1695.3	60.5	1692.0	34.0	1687.8	14.4	1687.8	14.4
501	502145	5.2	9.6559	0.2	4.2469	1.0	0.2974	1.0	0.98	1678.5	14.2	1683.1	8.1	1688.9	3.7	1688.9	3.7

74	121969	0.7	9.6279	0.9	4.3476	1.9	0.3036	1.7	0.89	1709.1	25.4	1702.4	15.8	1694.3	16.4	1694.3	16.4
316	313667	4.3	9.4915	0.3	4.4306	0.7	0.3050	0.7	0.90	1716.0	9.8	1718.1	6.0	1720.5	5.6	1720.5	5.6
365	408850	2.4	9.4362	0.4	4.3512	1.5	0.2978	1.5	0.97	1680.3	21.8	1703.1	12.5	1731.3	6.8	1731.3	6.8
271	635137	1.6	9.4355	0.2	4.5852	1.8	0.3138	1.8	0.99	1759.3	27.2	1746.6	14.9	1731.4	4.2	1731.4	4.2
98	137454	1.9	9.4307	0.7	4.4943	1.7	0.3074	1.5	0.91	1727.9	23.1	1729.9	13.9	1732.3	12.7	1732.3	12.7
633	432531	2.0	6.8229	2.1	8.5895	2.5	0.4250	1.3	0.53	2283.3	25.2	2295.4	22.6	2306.2	36.2	2306.2	36.2

Summary statistics for the 5 youngest ages:

Final age: 150. ± 2 Ma 1σ

MSWD = 0.078

Probability = 0.99

Sample KTC-14-dz2 n = 68

U (ppm)	^{206}Pb/ ^{204}Pb	U/ Th	(%) ^{206}Pb*/ ^{207}Pb*	± (1σ)	(%) ^{207}Pb*/ ^{235}U*	± (1σ)	(%) ^{206}Pb*/ ^{238}U*	± (1σ)	error corr.	Age (Ma) ^{206}Pb*/ ^{238}U*	± (1σ)	Age (Ma) ^{207}Pb*/ ^{235}U*	± (1σ)	Age (Ma) ^{207}Pb*/ ^{206}Pb*	± (1σ)	Preferred age (Ma)	± (1σ)
297	4110	1.2	21.1625	41.4	0.0245	42.3	0.0038	8.6	0.20	24.2	2.1	24.5	10.3	b.d.	b.d.	24.2	2.1
818	10315	0.9	22.9349	19.1	0.0228	19.6	0.0038	4.1	0.21	24.4	1.0	22.9	4.4	b.d.	b.d.	24.4	1.0
1286	25774	1.4	22.6325	8.7	0.0232	9.0	0.0038	2.2	0.25	24.5	0.5	23.3	2.1	b.d.	b.d.	24.5	0.5
222	1707	1.1	24.6792	40.4	0.0217	41.2	0.0039	8.0	0.20	25.0	2.0	21.8	8.9	b.d.	b.d.	25.0	2.0
596	5047	1.6	22.7393	25.4	0.0237	25.7	0.0039	3.8	0.15	25.1	1.0	23.7	6.0	b.d.	b.d.	25.1	1.0
1058	9081	1.6	19.9465	18.5	0.0270	18.7	0.0039	2.9	0.15	25.1	0.7	27.1	5.0	201.2	433.3	25.1	0.7
394	8900	1.9	22.8497	31.7	0.0240	32.4	0.0040	6.6	0.20	25.6	1.7	24.1	7.7	b.d.	b.d.	25.6	1.7
264	1923	1.2	39.9691	44.8	0.0137	45.0	0.0040	4.6	0.10	25.6	1.2	13.8	6.2	b.d.	b.d.	25.6	1.2
471	6543	1.2	21.9367	26.9	0.0252	27.6	0.0040	6.1	0.22	25.8	1.6	25.3	6.9	b.d.	b.d.	25.8	1.6
235	9577	2.6	22.2885	13.0	0.0741	13.5	0.0120	3.9	0.29	76.7	3.0	72.6	9.5	b.d.	b.d.	76.7	3.0
131	9545	1.1	21.4797	13.5	0.1538	13.8	0.0240	2.7	0.20	152.6	4.1	145.2	18.6	26.5	324.9	152.6	4.1
402	62040	1.2	19.9509	3.1	0.2316	3.3	0.0335	1.0	0.30	212.5	2.1	211.5	6.3	200.7	73.1	212.5	2.1
608	60083	3.0	19.3705	2.2	0.2421	2.5	0.0340	1.1	0.43	215.6	2.2	220.1	4.9	268.8	51.0	215.6	2.2
118	9345	1.1	19.0191	7.5	0.2499	8.5	0.0345	3.9	0.46	218.5	8.4	226.5	17.3	310.7	171.9	218.5	8.4
268	15842	1.5	19.7077	4.3	0.2417	5.1	0.0345	2.6	0.52	218.9	5.7	219.8	10.0	229.1	100.3	218.9	5.7
98	7937	2.1	19.6093	11.6	0.2449	12.1	0.0348	3.5	0.29	220.7	7.5	222.4	24.2	240.7	267.8	220.7	7.5
220	16342	1.2	18.7722	6.0	0.2568	7.0	0.0350	3.7	0.52	221.5	8.0	232.1	14.5	340.3	135.6	221.5	8.0
130	10224	1.7	21.3388	13.1	0.2261	13.4	0.0350	2.6	0.19	221.7	5.7	207.0	25.1	42.2	314.8	221.7	5.7
129	11381	1.6	21.7790	14.1	0.2227	14.2	0.0352	1.9	0.13	222.8	4.1	204.1	26.3	b.d.	b.d.	222.8	4.1
78	7999	1.3	18.9820	16.6	0.2556	16.9	0.0352	3.5	0.21	223.0	7.7	231.1	35.0	315.1	378.9	223.0	7.7
411	41189	0.9	19.3135	4.3	0.2670	4.5	0.0374	1.4	0.30	236.7	3.2	240.3	9.6	275.6	98.5	236.7	3.2
~~88~~	~~15300~~	~~2.0~~	~~12.9067~~	~~5.5~~	~~0.8281~~	~~7.3~~	~~0.0775~~	~~4.7~~	~~0.65~~	~~481.3~~	~~21.9~~	~~612.6~~	~~33.5~~	~~1133.5~~	~~110.5~~	~~481.3~~	~~21.9~~
11	7990	1.2	12.8823	9.7	2.1388	10.4	0.1998	3.6	0.35	1174.4	39.2	1161.4	71.8	1137.3	193.4	1137.3	193.4
27	12131	1.1	12.7635	5.3	2.1976	5.7	0.2034	2.0	0.35	1193.7	21.8	1180.3	39.7	1155.7	105.8	1155.7	105.8
74	10598	0.8	12.7213	1.7	2.1742	2.1	0.2006	1.1	0.54	1178.6	12.1	1172.8	14.4	1162.3	34.7	1162.3	34.7
134	73939	1.2	12.7169	1.3	2.1959	2.9	0.2025	2.6	0.90	1188.9	28.5	1179.8	20.3	1163.0	25.0	1163.0	25.0
16	6050	0.7	12.6182	8.5	2.2200	9.7	0.2032	4.7	0.48	1192.3	50.7	1187.4	68.2	1178.4	169.2	1178.4	169.2
47	6406	0.8	12.6159	3.6	2.2304	4.0	0.2041	1.8	0.45	1197.2	19.4	1190.6	27.9	1178.8	70.3	1178.8	70.3
54	27636	0.8	12.6017	2.4	2.2303	2.7	0.2038	1.3	0.47	1195.9	14.1	1190.6	19.2	1181.0	47.8	1181.0	47.8
34	30082	0.6	12.5893	3.0	2.2293	3.1	0.2035	1.0	0.32	1194.4	10.9	1190.3	22.0	1183.0	58.9	1183.0	58.9
29	21150	1.1	12.5733	3.8	2.2527	4.1	0.2054	1.6	0.38	1204.4	17.2	1197.6	28.9	1185.5	75.2	1185.5	75.2
62	25253	0.6	12.5556	3.0	2.2756	3.4	0.2072	1.6	0.47	1214.0	17.4	1204.7	23.9	1188.2	59.3	1188.2	59.3
31	9554	0.7	12.5406	3.9	2.2894	4.3	0.2082	1.7	0.40	1219.4	19.0	1209.0	30.2	1190.6	77.3	1190.6	77.3
244	29812	0.8	12.4943	0.7	2.1824	1.3	0.1978	1.1	0.86	1163.3	11.7	1175.4	8.9	1197.9	13.1	1197.9	13.1
18	6997	1.5	12.4901	8.9	2.2621	9.3	0.2049	2.5	0.26	1201.7	26.9	1200.6	65.3	1198.5	176.5	1198.5	176.5
334	188923	1.9	12.4889	0.4	2.1734	1.3	0.1969	1.2	0.94	1158.4	12.5	1172.6	8.7	1198.7	8.3	1198.7	8.3
37	14107	1.9	12.4787	3.9	2.3351	4.8	0.2113	2.8	0.59	1236.0	31.7	1223.0	34.1	1200.4	76.6	1200.4	76.6
39	19993	0.9	12.4756	3.7	2.2345	4.1	0.2022	1.8	0.45	1187.0	20.0	1191.9	29.0	1200.8	72.9	1200.8	72.9
71	29288	1.5	12.4698	2.1	2.2574	2.7	0.2042	1.6	0.61	1197.6	18.0	1199.1	18.9	1201.7	41.7	1201.7	41.7
47	28607	1.2	12.4682	2.3	2.2543	2.5	0.2039	1.2	0.45	1196.0	12.6	1198.1	17.9	1202.0	44.6	1202.0	44.6
94	36736	1.9	12.4634	1.1	2.2531	2.0	0.2037	1.6	0.83	1195.0	17.8	1197.8	13.8	1202.8	21.7	1202.8	21.7
74	14382	0.8	12.4602	2.1	2.2412	2.3	0.2025	0.9	0.39	1188.9	9.9	1194.0	16.3	1203.3	42.0	1203.3	42.0
12	6199	1.7	12.4529	6.8	2.2262	7.1	0.2011	2.0	0.29	1181.0	22.1	1189.3	49.8	1204.4	134.2	1204.4	134.2
210	140344	1.1	12.4476	0.8	2.3135	1.6	0.2089	1.4	0.86	1222.7	15.8	1216.4	11.7	1205.2	16.7	1205.2	16.7

132	87497	1.2	12.4386	0.8	2.2750	1.2	0.2052	0.8	0.71	1203.4	9.0	1204.6	8.2	1206.7	16.1	1206.7	16.1
43	51278	1.9	12.4362	2.9	2.2469	3.0	0.2027	1.0	0.34	1189.6	11.3	1195.8	21.4	1207.1	56.2	1207.1	56.2
32	10949	1.5	12.4228	3.0	2.2435	4.1	0.2021	2.7	0.67	1186.8	29.7	1194.7	28.7	1209.2	59.8	1209.2	59.8
45	34073	0.8	12.4145	4.3	2.2002	4.8	0.1981	2.0	0.41	1165.1	21.0	1181.1	33.3	1210.5	85.6	1210.5	85.6
46	37171	0.9	12.4141	4.0	2.2656	4.1	0.2040	1.0	0.25	1196.7	11.1	1201.7	29.1	1210.6	78.7	1210.6	78.7
38	8442	0.9	12.4139	3.3	2.2654	3.7	0.2040	1.6	0.43	1196.6	17.5	1201.6	26.0	1210.6	65.6	1210.6	65.6
37	33818	1.0	12.3878	4.3	2.2732	4.7	0.2042	1.9	0.40	1198.0	20.3	1204.0	33.1	1214.7	84.7	1214.7	84.7
65	15630	0.6	12.3409	1.3	2.2593	1.9	0.2022	1.3	0.70	1187.2	14.2	1199.7	13.1	1222.2	25.9	1222.2	25.9
80	21317	0.8	12.3333	1.9	2.2127	2.1	0.1979	0.8	0.41	1164.2	9.0	1185.1	14.6	1223.4	37.3	1223.4	37.3
26	6733	0.9	12.3242	6.0	2.2986	6.4	0.2055	2.2	0.34	1204.6	24.3	1211.9	45.4	1224.8	118.4	1224.8	118.4
20	5844	2.3	12.2283	6.1	2.3090	6.8	0.2048	3.0	0.43	1201.0	32.4	1215.1	48.3	1240.2	120.3	1240.2	120.3
29	8631	0.9	12.0423	6.5	2.2786	6.9	0.1990	2.1	0.31	1170.0	22.6	1205.7	48.6	1270.2	127.9	1270.2	127.9
29	20239	1.9	12.0378	5.1	2.3463	5.4	0.2048	1.8	0.33	1201.3	19.9	1226.4	38.8	1270.9	100.2	1270.9	100.2
19	9511	1.0	11.8202	7.6	2.3834	8.0	0.2043	2.4	0.30	1198.5	26.3	1237.6	56.9	1306.4	147.4	1306.4	147.4
20	17683	1.1	11.7581	8.0	2.3695	9.1	0.2021	4.3	0.47	1186.4	46.4	1233.4	64.9	1316.6	155.4	1316.6	155.4
86	66849	0.6	11.0463	1.3	3.0076	1.7	0.2410	1.1	0.64	1391.7	13.3	1409.5	12.8	1436.7	24.6	1436.7	24.6
68	36291	0.8	10.4756	1.3	3.3800	1.8	0.2568	1.3	0.72	1473.4	17.2	1499.8	14.2	1537.2	23.7	1537.2	23.7
456	201450	1.8	10.2053	0.2	3.6156	0.6	0.2676	0.6	0.92	1528.7	7.8	1553.0	5.0	1586.2	4.6	1586.2	4.6
565	775259	2.9	9.7703	0.2	4.1476	1.3	0.2939	1.2	0.99	1661.0	18.2	1663.7	10.3	1667.2	3.3	1667.2	3.3
61	33645	1.0	9.7401	1.0	4.3044	2.1	0.3041	1.8	0.88	1711.5	27.3	1694.2	16.9	1672.9	17.7	1672.9	17.7
356	163161	10.5	9.6945	0.3	4.1949	2.2	0.2949	2.2	0.99	1666.2	32.5	1673.0	18.3	1681.6	6.3	1681.6	6.3
340	219049	1.4	9.6497	0.3	4.2909	1.3	0.3003	1.2	0.97	1692.8	18.6	1691.6	10.6	1690.1	6.0	1690.1	6.0
186	125213	1.4	9.5161	0.8	4.3620	1.3	0.3010	1.1	0.80	1696.5	15.9	1705.2	11.0	1715.8	14.6	1715.8	14.6
530	385241	4.9	9.4069	0.3	4.4344	0.9	0.3025	0.9	0.95	1703.9	13.3	1718.8	7.7	1737.0	5.5	1737.0	5.5
178	106743	1.5	9.2908	0.4	4.7750	4.0	0.3218	4.0	1.00	1798.3	62.7	1780.5	33.7	1759.7	7.2	1759.7	7.2

1 age manually rejected due to discordance.

Summary statistics for the 9 youngest ages:
Final age: 24.9 ± 0.3 Ma 1σ
MSWD = 0.24
Probability = 0.98

Sample KTC-14-dz3 n = 69

			(%)		(%)		(%)			Age (Ma)		Age (Ma)		Age (Ma)		Preferred	
U	$^{206}Pb/$	U/	$^{206}Pb^*/$	±	$^{207}Pb^*/$	±	$^{206}Pb^*/$	±	error	$^{206}Pb^*/$	±	$^{207}Pb^*/$	±	$^{207}Pb^*/$	±	age	±
(ppm)	^{204}Pb	Th	$^{207}Pb^*$	(1σ)	$^{235}U^*$	(1σ)	$^{238}U^*$	(1σ)	corr.	$^{238}U^*$	(1σ)	$^{235}U^*$	(1σ)	$^{206}Pb^*$	(1σ)	(Ma)	(1σ)
443	9599	1.7	22.2147	9.6	0.0711	10.1	0.0115	3.4	0.33	73.4	2.4	69.7	6.8	b.d.	b.d.	73.4	2.4
350	12198	0.6	20.7965	5.6	0.1562	6.9	0.0236	3.9	0.57	150.1	5.8	147.4	9.4	103.5	133.2	150.1	5.8
319	21009	0.4	20.3284	5.2	0.1605	5.7	0.0237	2.2	0.39	150.7	3.3	151.1	8.0	157.0	122.3	150.7	3.3
60	6449	0.9	25.1539	32.9	0.1299	33.4	0.0237	5.6	0.17	151.0	8.3	124.0	39.0	b.d.	b.d.	151.0	8.3
208	15944	1.5	20.0157	6.3	0.2334	7.7	0.0339	4.5	0.58	214.8	9.5	213.0	14.8	193.2	146.2	214.8	9.5
104	13653	1.4	19.0512	9.9	0.2455	10.2	0.0339	2.6	0.26	215.1	5.6	222.9	20.5	306.8	225.9	215.1	5.6
154	19426	1.4	19.2284	7.1	0.2439	7.4	0.0340	1.8	0.25	215.6	3.9	221.6	14.7	285.7	163.2	215.6	3.9
116	13182	1.5	19.3918	12.9	0.2428	13.0	0.0341	1.5	0.11	216.4	3.2	220.7	25.9	266.3	298.2	216.4	3.2
859	89684	1.6	19.6402	1.5	0.2402	1.9	0.0342	1.2	0.60	216.8	2.5	218.5	3.8	237.0	35.5	216.8	2.5
187	10822	1.3	20.4714	6.7	0.2308	7.1	0.0343	2.5	0.35	217.2	5.3	210.8	13.6	140.6	157.1	217.2	5.3
190	10540	1.8	20.4774	8.2	0.2314	8.7	0.0344	2.9	0.33	217.8	6.2	211.3	16.6	139.9	192.7	217.8	6.2
76	5991	1.5	24.1725	22.1	0.1961	22.2	0.0344	1.9	0.09	217.9	4.2	181.9	37.0	b.d.	b.d.	217.9	4.2
159	22215	1.7	20.1111	4.4	0.2362	5.1	0.0345	2.6	0.51	218.4	5.6	215.3	9.9	182.1	102.1	218.4	5.6
355	41422	3.0	20.4157	2.7	0.2333	3.3	0.0346	1.8	0.55	219.0	3.9	213.0	6.3	147.0	63.6	219.0	3.9
43	7738	1.5	20.0712	31.9	0.2394	33.1	0.0349	8.8	0.26	220.8	19.0	217.9	65.0	186.7	760.1	220.8	19.0
28	24906	0.8	12.6995	5.9	2.2218	7.3	0.2046	4.3	0.59	1200.2	47.5	1187.9	51.3	1165.7	116.9	1165.7	116.9
21	22622	1.8	12.6828	5.5	2.2208	6.1	0.2043	2.6	0.42	1198.2	28.2	1187.6	42.6	1168.3	109.2	1168.3	109.2
12	7721	1.3	12.6723	7.2	2.1622	7.6	0.1987	2.4	0.32	1168.5	25.8	1169.0	52.8	1169.9	142.7	1169.9	142.7
52	21252	1.0	12.6666	3.3	2.1953	4.1	0.2017	2.5	0.60	1184.3	26.7	1179.6	28.5	1170.8	64.5	1170.8	64.5
89	110930	0.9	12.6312	1.3	2.1716	1.6	0.1989	1.0	0.60	1169.6	10.4	1172.0	11.3	1176.4	25.8	1176.4	25.8
22	26011	1.4	12.6278	6.2	2.2551	6.5	0.2065	1.8	0.28	1210.3	20.0	1198.4	45.7	1176.9	123.5	1176.9	123.5
22	20373	1.3	12.6044	5.6	2.1873	6.2	0.2000	2.7	0.43	1175.1	29.0	1177.0	43.4	1180.6	111.0	1180.6	111.0
63	76473	1.0	12.5926	2.1	2.1859	2.4	0.1996	1.0	0.45	1173.4	11.3	1176.6	16.4	1182.4	41.7	1182.4	41.7
70	49640	0.8	12.5716	1.4	2.2171	2.6	0.2022	2.1	0.84	1186.9	23.2	1186.5	17.9	1185.7	27.6	1185.7	27.6
36	23524	1.2	12.5562	4.1	2.2222	4.3	0.2024	1.2	0.28	1188.0	12.7	1188.1	29.8	1188.1	80.7	1188.1	80.7
83	75486	1.0	12.5483	3.1	2.2506	3.8	0.2048	2.1	0.56	1201.2	23.4	1197.0	26.7	1189.4	61.9	1189.4	61.9
84	37632	0.9	12.4729	1.4	2.2384	1.8	0.2025	1.1	0.63	1188.7	12.4	1193.2	12.7	1201.3	27.6	1201.3	27.6
18	16273	1.8	12.4623	9.7	2.2584	10.6	0.2041	4.4	0.41	1197.4	47.9	1199.4	75.0	1202.9	191.3	1202.9	191.3
60	15950	0.9	12.3607	2.2	2.2701	2.8	0.2035	1.7	0.61	1194.1	18.5	1203.0	19.5	1219.1	42.9	1219.1	42.9
12	8421	2.0	12.2657	8.1	2.2743	8.7	0.2023	3.2	0.36	1187.8	34.6	1204.4	61.7	1234.2	159.9	1234.2	159.9
44	25116	1.5	12.2524	3.4	2.2868	4.0	0.2032	2.1	0.53	1192.6	23.3	1208.2	28.4	1236.3	66.6	1236.3	66.6
29	10117	1.1	12.0536	5.5	2.3168	5.9	0.2025	2.1	0.35	1188.9	22.5	1217.4	42.0	1268.3	108.2	1268.3	108.2
509	137539	16.9	11.2189	0.2	2.9731	1.9	0.2419	1.9	1.00	1396.7	23.7	1400.8	14.4	1407.0	3.1	1407.0	3.1
255	324097	24.2	11.2188	0.5	3.0790	3.7	0.2505	3.7	0.99	1441.2	47.4	1427.5	28.4	1407.1	9.4	1407.1	9.4
74	30378	0.9	11.2162	1.8	2.9012	3.0	0.2360	2.4	0.79	1365.9	29.0	1382.2	22.6	1407.5	35.4	1407.5	35.4
310	21627	33.8	11.1559	0.6	2.9702	1.3	0.2403	1.2	0.91	1388.4	15.2	1400.0	10.2	1417.8	10.8	1417.8	10.8
69	75448	3.6	10.8148	1.4	3.2499	3.2	0.2549	2.8	0.89	1463.7	37.0	1469.1	24.6	1477.0	27.4	1477.0	27.4
162	221734	1.6	10.4744	0.8	3.6087	1.5	0.2741	1.3	0.84	1561.8	18.1	1551.4	12.3	1537.4	15.8	1537.4	15.8
89	73116	1.1	10.4342	1.6	3.4752	2.4	0.2630	1.9	0.76	1505.1	25.0	1521.6	19.3	1544.6	30.0	1544.6	30.0
605	1103729	4.6	10.3249	1.6	3.4154	2.5	0.2558	1.9	0.75	1468.1	24.4	1507.9	19.3	1564.4	30.3	1564.4	30.3
364	194114	5.9	10.2873	0.3	3.6717	2.5	0.2739	2.5	0.99	1560.8	34.9	1565.2	20.2	1571.2	6.0	1571.2	6.0
146	104309	1.5	10.0404	0.8	3.8748	5.4	0.2822	5.3	0.99	1602.2	75.4	1608.4	43.4	1616.6	14.9	1616.6	14.9
271	188184	3.8	10.0196	0.4	3.8670	1.3	0.2810	1.2	0.95	1596.5	17.5	1606.8	10.5	1620.4	7.9	1620.4	7.9
132	106020	0.7	10.0064	1.1	3.9430	1.5	0.2862	1.0	0.69	1622.3	14.7	1622.5	12.0	1622.9	19.8	1622.9	19.8

1410	514061	3.6	9.9179	0.3	3.9668	5.8	0.2853	5.8	1.00	1618.2	83.4	1627.4	47.4	1639.4	6.4	1639.4	6.4
67	48588	2.6	9.8531	1.2	4.0812	2.0	0.2917	1.6	0.79	1649.8	23.7	1650.6	16.7	1651.5	23.1	1651.5	23.1
45	44606	0.8	9.8229	1.6	4.1315	4.2	0.2943	3.9	0.92	1663.2	56.5	1660.6	34.1	1657.2	29.4	1657.2	29.4
62	237953	1.2	9.7895	1.0	3.9881	3.3	0.2832	3.2	0.95	1607.2	45.3	1631.8	27.2	1663.5	18.8	1663.5	18.8
213	146205	1.8	9.7885	0.4	4.2021	2.3	0.2983	2.3	0.99	1683.0	33.7	1674.4	18.9	1663.7	6.9	1663.7	6.9
547	249499	4.9	9.7437	0.4	4.1633	2.0	0.2942	2.0	0.98	1662.5	28.6	1666.8	16.3	1672.2	7.3	1672.2	7.3
136	133107	1.7	9.7403	0.4	4.1542	2.7	0.2935	2.7	0.99	1658.8	39.5	1665.0	22.4	1672.9	7.9	1672.9	7.9
81	112285	1.4	9.7178	1.4	4.1347	1.6	0.2914	0.7	0.45	1648.6	10.6	1661.2	13.2	1677.1	26.5	1677.1	26.5
436	504495	3.6	9.7014	0.3	4.1283	2.5	0.2905	2.4	0.99	1643.9	35.4	1659.9	20.1	1680.2	5.7	1680.2	5.7
278	244486	3.4	9.6909	0.4	4.2014	0.7	0.2953	0.5	0.78	1667.9	7.6	1674.3	5.4	1682.3	7.6	1682.3	7.6
148	173537	1.6	9.6801	0.9	4.2791	3.2	0.3004	3.0	0.96	1693.4	45.4	1689.4	26.2	1684.3	17.2	1684.3	17.2
116	26308	1.7	9.6600	1.1	4.2398	6.2	0.2970	6.1	0.98	1676.6	89.4	1681.8	50.6	1688.2	20.7	1688.2	20.7
136	131893	1.1	9.6522	0.9	4.1597	2.0	0.2912	1.8	0.88	1647.5	25.6	1666.1	16.3	1689.6	17.3	1689.6	17.3
53	41165	1.6	9.6519	1.0	4.2166	2.2	0.2952	2.0	0.90	1667.3	29.3	1677.3	18.2	1689.7	17.6	1689.7	17.6
715	240979	1.6	9.6497	0.7	4.1776	2.1	0.2924	2.0	0.94	1653.4	28.5	1669.6	17.1	1690.1	13.1	1690.1	13.1
86	74259	1.7	9.6486	0.9	4.3188	2.7	0.3022	2.5	0.95	1702.3	37.6	1697.0	21.9	1690.3	16.0	1690.3	16.0
410	201175	1.7	9.6443	0.3	4.2517	1.1	0.2974	1.1	0.96	1678.4	15.9	1684.1	9.2	1691.2	5.6	1691.2	5.6
116	27971	1.6	9.6407	1.1	4.1984	1.4	0.2936	1.0	0.66	1659.3	14.0	1673.7	11.9	1691.8	20.0	1691.8	20.0
209	102757	1.8	9.6346	0.3	4.2276	2.8	0.2954	2.8	0.99	1668.5	41.5	1679.4	23.3	1693.0	5.7	1693.0	5.7
221	313967	1.7	9.5237	0.4	4.4531	1.3	0.3076	1.3	0.96	1728.8	19.0	1722.3	10.9	1714.3	6.9	1714.3	6.9
629	390251	1.1	9.4876	0.3	4.4311	1.7	0.3049	1.6	0.99	1715.6	24.7	1718.2	13.8	1721.3	4.6	1721.3	4.6
425	262402	1.1	9.4812	0.2	4.4509	1.7	0.3061	1.7	0.99	1721.3	25.2	1721.9	13.9	1722.5	3.5	1722.5	3.5
122	209929	1.7	9.4594	0.6	4.5841	1.7	0.3145	1.6	0.93	1762.8	24.4	1746.4	14.1	1726.8	11.4	1726.8	11.4
418	148285	1.0	9.4350	0.2	4.4362	2.0	0.3036	2.0	0.99	1709.0	29.3	1719.1	16.3	1731.5	3.7	1731.5	3.7
119	83186	1.1	9.3953	0.8	4.5883	1.2	0.3127	0.9	0.77	1753.8	14.2	1747.2	10.1	1739.2	14.2	1739.2	14.2

Sample KTC-14-dz4 **n = 75**

U	^{206}Pb/	U/	(%) ^{206}Pb*/	±	(%) ^{207}Pb*/	±	(%) ^{206}Pb*/	±	error	Age (Ma) ^{206}Pb*/	±	Age (Ma) ^{207}Pb*/	±	Age (Ma) ^{207}Pb*/	±	Preferred age	±
(ppm)	^{204}Pb	Th	^{207}Pb*	(1σ)	^{235}U*	(1σ)	^{238}U*	(1σ)	corr.	^{238}U*	(1σ)	^{235}U*	(1σ)	^{206}Pb*	(1σ)	(Ma)	(1σ)
364	10028	1.2	23.9799	18.7	0.0219	19.2	0.0038	4.2	0.22	24.5	1.0	22.0	4.2	b.d.	b.d.	24.5	1.0
187	1745	1.2	21.3303	46.4	0.0249	47.2	0.0038	8.9	0.19	24.8	2.2	24.9	11.6	b.d.	b.d.	24.8	2.2
208	554	1.3	19.0064	13.6	0.1240	13.8	0.0171	2.4	0.18	109.3	2.6	118.7	15.5	312.2	310.5	109.3	2.6
104	6502	1.3	19.4575	13.9	0.1326	14.9	0.0187	5.4	0.36	119.5	6.4	126.4	17.8	258.5	321.5	119.5	6.4
136	7120	1.2	21.1790	12.8	0.1500	13.2	0.0230	3.2	0.24	146.8	4.7	141.9	17.5	60.2	306.8	146.8	4.7
142	14917	0.9	20.0173	11.3	0.1619	11.6	0.0235	2.6	0.22	149.8	3.8	152.4	16.4	193.0	262.7	149.8	3.8
122	10843	0.3	23.2096	9.6	0.1420	10.2	0.0239	3.5	0.34	152.3	5.3	134.9	12.9	b.d.	b.d.	152.3	5.3
177	14762	1.0	21.0101	3.0	0.1570	4.3	0.0239	3.1	0.71	152.4	4.6	148.1	5.9	79.2	71.1	152.4	4.6
66	5499	0.9	21.3745	24.6	0.1545	25.0	0.0239	3.9	0.16	152.6	6.0	145.9	33.9	38.2	597.6	152.6	6.0
199	10655	1.0	20.9020	7.1	0.1581	7.3	0.0240	1.6	0.22	152.7	2.4	149.0	10.1	91.5	168.5	152.7	2.4
198	20496	0.6	20.2306	8.8	0.1645	9.8	0.0241	4.3	0.44	153.8	6.5	154.7	14.1	168.3	206.2	153.8	6.5
268	48643	0.9	20.4026	4.8	0.1637	5.0	0.0242	1.3	0.27	154.3	2.0	153.9	7.1	148.5	111.9	154.3	2.0
103	20295	0.6	20.5447	11.2	0.1633	12.0	0.0243	4.2	0.35	155.0	6.4	153.6	17.1	132.2	264.5	155.0	6.4
111	9997	0.8	19.7164	9.9	0.1717	10.6	0.0245	3.8	0.35	156.3	5.8	160.9	15.8	228.1	229.9	156.3	5.8
568	116204	1.0	20.0585	2.3	0.1818	2.9	0.0264	1.7	0.60	168.2	2.9	169.6	4.5	188.2	53.9	168.2	2.9
152	19827	1.2	20.9797	7.2	0.2417	7.4	0.0368	1.8	0.24	232.8	4.0	219.8	14.6	82.7	169.9	232.8	4.0
19	32150	1.2	12.9278	3.8	2.1465	4.5	0.2013	2.4	0.53	1182.1	26.0	1163.9	31.3	1130.3	76.2	1130.3	76.2
24	9283	0.9	12.8295	6.5	2.1683	7.1	0.2018	2.9	0.41	1184.8	31.4	1170.9	49.5	1145.5	129.3	1145.5	129.3
12	8028	1.4	12.8278	6.3	2.1758	6.9	0.2024	2.9	0.42	1188.3	31.6	1173.3	48.3	1145.8	125.2	1145.8	125.2
36	21863	0.6	12.7389	4.3	2.1417	4.9	0.1979	2.4	0.49	1163.9	25.8	1162.4	34.0	1159.5	84.8	1159.5	84.8
13	17345	1.0	12.7084	7.4	2.1242	8.1	0.1958	3.4	0.41	1152.6	35.4	1156.7	56.2	1164.3	147.1	1164.3	147.1
48	29977	1.2	12.6250	1.8	2.2013	3.6	0.2016	3.1	0.86	1183.7	33.3	1181.5	25.1	1177.3	36.5	1177.3	36.5
16	6737	1.0	12.6039	7.3	2.2161	8.3	0.2026	3.9	0.47	1189.2	42.5	1186.2	58.2	1180.7	145.0	1180.7	145.0
99	86785	1.7	12.5990	0.8	2.2769	3.3	0.2081	3.2	0.97	1218.4	35.7	1205.1	23.4	1181.4	16.7	1181.4	16.7
65	32113	0.9	12.5961	2.3	2.1846	3.0	0.1996	2.0	0.65	1173.1	21.0	1176.2	21.0	1181.9	45.4	1181.9	45.4
45	25513	1.3	12.5753	1.8	2.2513	2.9	0.2053	2.2	0.78	1203.9	24.5	1197.2	20.3	1185.2	36.0	1185.2	36.0
58	54161	1.2	12.5750	1.5	2.1978	2.4	0.2004	1.9	0.80	1177.7	20.9	1180.4	17.0	1185.2	29.0	1185.2	29.0
47	47493	1.3	12.5667	2.8	2.2206	3.1	0.2024	1.4	0.44	1188.2	14.9	1187.6	21.9	1186.5	55.6	1186.5	55.6
73	62072	1.9	12.5595	1.1	2.2294	2.8	0.2031	2.5	0.91	1191.8	27.7	1190.3	19.6	1187.6	22.7	1187.6	22.7
56	25614	0.9	12.5549	2.4	2.2552	3.2	0.2054	2.1	0.66	1204.0	23.1	1198.4	22.4	1188.4	47.3	1188.4	47.3
114	83355	1.4	12.5291	0.6	2.2401	2.5	0.2036	2.4	0.97	1194.4	26.2	1193.7	17.4	1192.4	12.6	1192.4	12.6
371	198557	1.8	12.5106	0.3	2.2294	2.2	0.2023	2.1	0.99	1187.6	23.1	1190.3	15.1	1195.3	5.5	1195.3	5.5
27	10624	2.1	12.5064	3.6	2.2042	4.4	0.1999	2.6	0.59	1174.9	27.9	1182.4	31.0	1196.0	71.1	1196.0	71.1
166	97380	1.3	12.4986	0.8	2.2396	1.4	0.2030	1.1	0.81	1191.5	12.3	1193.5	9.8	1197.2	16.2	1197.2	16.2
154	22436	0.7	12.4925	0.9	2.2277	2.1	0.2018	1.9	0.90	1185.2	20.9	1189.8	15.0	1198.2	18.1	1198.2	18.1
289	127511	1.2	12.4902	0.5	2.2477	1.3	0.2036	1.3	0.94	1194.7	13.7	1196.1	9.4	1198.5	9.0	1198.5	9.0
65	20657	0.8	12.4779	2.1	2.1242	2.3	0.1922	1.0	0.44	1133.5	10.8	1156.7	16.1	1200.5	41.3	1200.5	41.3
225	58477	1.3	12.4776	0.4	2.2887	2.6	0.2071	2.6	0.99	1213.5	28.6	1208.8	18.5	1200.5	8.4	1200.5	8.4
139	255641	1.5	12.4744	1.3	2.2150	1.8	0.2004	1.3	0.73	1177.5	14.5	1185.8	12.9	1201.0	25.0	1201.0	25.0
219	161870	2.0	12.4679	0.5	2.3021	2.3	0.2082	2.3	0.98	1219.0	25.3	1212.9	16.5	1202.0	10.1	1202.0	10.1
126	93525	2.5	12.4630	0.8	2.3123	1.9	0.2090	1.8	0.91	1223.5	19.5	1216.1	13.7	1202.8	16.2	1202.8	16.2
178	107515	0.7	12.4546	0.5	2.2439	1.4	0.2027	1.3	0.92	1189.8	13.7	1194.9	9.6	1204.1	10.3	1204.1	10.3
74	47456	1.8	12.4513	1.1	2.2173	2.3	0.2002	2.0	0.88	1176.6	21.4	1186.5	15.9	1204.7	21.6	1204.7	21.6
35	25820	1.0	12.4365	2.4	2.2352	3.4	0.2016	2.4	0.72	1184.0	26.1	1192.1	23.7	1207.0	46.3	1207.0	46.3

142	63875	0.8	12.4290	0.8	2.2872	3.1	0.2062	3.0	0.97	1208.4	32.7	1208.4	21.7	1208.2	15.5	1208.2	15.5
196	129910	1.0	12.4246	0.5	2.2587	1.8	0.2035	1.8	0.96	1194.3	19.3	1199.5	13.0	1208.9	10.0	1208.9	10.0
124	99343	1.6	12.4217	0.8	2.2509	2.0	0.2028	1.8	0.91	1190.2	19.4	1197.1	13.8	1209.4	16.3	1209.4	16.3
167	83058	0.8	12.4210	0.5	2.2549	1.8	0.2031	1.7	0.96	1192.1	19.0	1198.3	12.8	1209.5	9.7	1209.5	9.7
100	166543	0.9	12.4042	1.2	2.2270	2.8	0.2003	2.5	0.90	1177.2	26.9	1189.6	19.4	1212.1	23.6	1212.1	23.6
46	21972	0.7	12.3899	1.9	2.2048	2.9	0.1981	2.2	0.76	1165.2	23.4	1182.6	20.2	1214.4	36.8	1214.4	36.8
50	28934	0.8	12.3707	2.1	2.2806	3.3	0.2046	2.5	0.75	1200.1	27.0	1206.3	23.1	1217.4	42.2	1217.4	42.2
15	11660	0.8	12.3440	8.9	2.2185	9.2	0.1986	2.4	0.26	1167.9	25.4	1186.9	64.8	1221.7	176.0	1221.7	176.0
117	107240	0.8	12.3341	0.9	2.2663	2.6	0.2027	2.5	0.94	1190.0	27.1	1201.9	18.6	1223.3	17.2	1223.3	17.2
14	10753	1.1	12.2841	7.3	2.2399	7.6	0.1996	2.3	0.30	1172.9	24.4	1193.6	53.4	1231.3	142.6	1231.3	142.6
43	55403	1.2	12.2497	2.4	2.3554	5.4	0.2093	4.8	0.89	1224.9	53.7	1229.2	38.5	1236.8	48.0	1236.8	48.0
10	8394	0.7	12.1922	5.9	2.3871	7.5	0.2111	4.7	0.62	1234.6	52.3	1238.7	53.7	1246.0	115.3	1246.0	115.3
60	16769	0.8	12.1558	4.7	2.2115	5.7	0.1950	3.2	0.56	1148.3	34.0	1184.7	40.1	1251.8	92.7	1251.8	92.7
65	10315	1.0	12.0266	5.9	2.2750	10.6	0.1984	8.8	0.83	1166.9	94.3	1204.6	75.1	1272.7	115.4	1272.7	115.4
52	40588	0.9	11.2254	1.6	2.9922	2.4	0.2436	1.9	0.77	1405.4	23.7	1405.6	18.6	1405.9	30.0	1405.9	30.0
49	85798	1.5	11.1220	1.5	3.0525	2.8	0.2462	2.4	0.85	1419.0	30.0	1420.9	21.2	1423.6	28.0	1423.6	28.0
116	12892	0.9	11.0151	0.9	3.0828	2.0	0.2463	1.8	0.91	1419.3	23.6	1428.4	15.6	1442.1	16.3	1442.1	16.3
120	61439	1.8	10.6386	1.2	3.4626	3.0	0.2672	2.8	0.92	1526.4	37.7	1518.7	23.8	1508.0	22.5	1508.0	22.5
168	313715	1.7	10.0122	0.6	3.8695	1.9	0.2810	1.8	0.96	1596.3	25.9	1607.3	15.5	1621.8	10.5	1621.8	10.5
152	358725	2.3	9.7994	0.3	4.1354	2.8	0.2939	2.8	0.99	1661.0	40.7	1661.3	22.9	1661.7	5.6	1661.7	5.6
81	117936	1.4	9.7853	0.8	4.1651	1.7	0.2956	1.5	0.88	1669.4	22.0	1667.2	13.8	1664.3	14.7	1664.3	14.7
786	617680	6.6	9.7562	0.4	4.2884	2.1	0.3034	2.1	0.99	1708.4	31.7	1691.1	17.6	1669.8	6.5	1669.8	6.5
116	147412	1.8	9.7504	0.5	4.1803	1.7	0.2956	1.7	0.95	1669.5	24.4	1670.2	14.3	1670.9	9.7	1670.9	9.7
105	109652	0.6	9.7396	0.7	4.0933	1.1	0.2891	0.9	0.79	1637.2	12.9	1653.0	9.2	1673.0	12.8	1673.0	12.8
57	43824	0.9	9.7149	0.7	4.2046	1.6	0.2962	1.5	0.91	1672.7	21.9	1674.9	13.5	1677.7	12.7	1677.7	12.7
207	438299	2.0	9.6922	0.1	4.2254	1.5	0.2970	1.5	1.00	1676.5	21.9	1679.0	12.2	1682.0	2.5	1682.0	2.5
76	57080	2.1	9.5811	0.9	4.4478	2.8	0.3091	2.7	0.94	1736.1	40.4	1721.3	23.3	1703.3	17.2	1703.3	17.2
487	24884	7.2	9.5634	0.2	4.3789	2.3	0.3037	2.3	1.00	1709.7	34.6	1708.4	19.1	1706.7	4.2	1706.7	4.2
196	129366	1.4	9.5059	0.3	4.3758	2.1	0.3017	2.0	0.99	1699.6	30.3	1707.8	17.0	1717.8	6.0	1717.8	6.0
304	63273	1.5	9.4518	0.2	4.5029	1.4	0.3087	1.4	0.99	1734.2	21.0	1731.5	11.6	1728.2	4.1	1728.2	4.1
113	79028	1.3	9.4009	0.2	4.4660	2.3	0.3045	2.3	1.00	1713.6	34.7	1724.7	19.2	1738.1	3.6	1738.1	3.6

Sample KTC-14-dz5 n = 54

U (ppm)	$^{206}Pb/^{204}Pb$	U/Th	(%) $^{206}Pb^*/^{207}Pb^*$	± (1σ)	(%) $^{207}Pb^*/^{235}U^*$	± (1σ)	(%) $^{206}Pb^*/^{238}U^*$	± (1σ)	error corr.	Age (Ma) $^{206}Pb^*/^{238}U^*$	± (1σ)	Age (Ma) $^{207}Pb^*/^{235}U^*$	± (1σ)	Age (Ma) $^{207}Pb^*/^{206}Pb^*$	± (1σ)	Preferred age (Ma)	± (1σ)
696	587	2.2	20.7297	17.4	0.0270	17.8	0.0041	3.8	0.21	26.1	1.0	27.0	4.7	111.0	412.8	26.1	1.0
524	24459	0.9	20.4826	6.2	0.0785	6.3	0.0117	1.2	0.19	74.7	0.9	76.7	4.7	139.3	146.5	74.7	0.9
292	4285	1.1	16.9919	12.0	0.0954	12.5	0.0118	3.5	0.28	75.4	2.6	92.6	11.1	561.6	263.4	75.4	2.6
114	5152	1.5	19.2833	16.7	0.1086	17.1	0.0152	3.9	0.23	97.2	3.7	104.7	17.0	279.2	384.0	97.2	3.7
60	3962	0.6	20.5520	19.6	0.1551	20.8	0.0231	6.7	0.32	147.3	9.8	146.4	28.3	131.4	465.7	147.3	9.8
298	44239	1.2	21.5879	5.7	0.1492	6.0	0.0234	1.6	0.26	148.9	2.3	141.2	7.8	14.4	138.1	148.9	2.3
75	5736	0.7	20.4207	18.9	0.1593	19.4	0.0236	4.5	0.23	150.3	6.7	150.1	27.1	146.4	445.9	150.3	6.7
56	3985	0.9	29.1644	32.8	0.1117	33.2	0.0236	4.9	0.15	150.5	7.4	107.5	33.9	b.d.	b.d.	150.5	7.4
230	20630	1.1	20.3526	5.0	0.1613	5.3	0.0238	1.7	0.32	151.7	2.5	151.8	7.4	154.2	116.5	151.7	2.5
101	12697	0.5	20.3493	15.7	0.1625	16.2	0.0240	3.9	0.24	152.8	5.9	152.9	23.0	154.6	369.6	152.8	5.9
122	13041	1.7	21.9482	17.1	0.1563	17.5	0.0249	3.8	0.22	158.4	6.0	147.4	24.0	b.d.	b.d.	158.4	6.0
142	26122	1.8	19.8525	9.4	0.2565	9.7	0.0369	2.4	0.25	233.8	5.5	231.8	20.1	212.1	218.5	233.8	5.5
39	30177	1.3	12.6793	2.6	2.1745	2.9	0.2000	1.4	0.48	1175.1	15.1	1172.9	20.4	1168.8	51.0	1168.8	51.0
15	7855	1.2	12.6475	9.2	2.2025	9.6	0.2020	2.9	0.30	1186.2	31.9	1181.8	67.5	1173.8	182.2	1173.8	182.2
65	29277	1.2	12.6331	1.4	2.2274	1.9	0.2041	1.3	0.69	1197.2	14.1	1189.7	13.2	1176.1	26.9	1176.1	26.9
22	15807	1.4	12.5922	6.4	2.2157	6.8	0.2024	2.2	0.33	1187.9	24.0	1186.0	47.6	1182.5	127.2	1182.5	127.2
43	29199	1.0	12.5872	2.5	2.2291	3.0	0.2035	1.7	0.57	1194.1	18.6	1190.2	21.1	1183.3	49.0	1183.3	49.0
23	24181	0.7	12.5856	5.2	2.2413	6.1	0.2046	3.2	0.52	1199.9	34.8	1194.1	42.8	1183.5	102.7	1183.5	102.7
47	47210	1.1	12.5365	3.2	2.2612	3.4	0.2056	1.4	0.39	1205.3	14.9	1200.3	24.3	1191.2	62.5	1191.2	62.5
22	28078	1.1	12.5261	3.7	2.2634	4.3	0.2056	2.1	0.50	1205.5	23.4	1201.0	30.1	1192.9	73.0	1192.9	73.0
20	13407	1.5	12.5260	5.4	2.2430	5.7	0.2038	1.8	0.31	1195.6	19.1	1194.6	40.1	1192.9	107.2	1192.9	107.2
252	191479	1.6	12.4905	0.6	2.2030	2.0	0.1996	1.9	0.96	1173.0	20.6	1182.0	14.0	1198.5	11.3	1198.5	11.3
94	41552	1.2	12.4883	1.1	2.2012	2.0	0.1994	1.8	0.86	1171.9	18.8	1181.4	14.3	1198.8	20.9	1198.8	20.9
42	43745	1.0	12.4724	2.4	2.2353	2.6	0.2022	1.1	0.43	1187.1	12.2	1192.2	18.4	1201.3	46.8	1201.3	46.8
352	319150	5.1	12.4675	0.3	2.2154	1.1	0.2003	1.0	0.97	1177.1	11.2	1185.9	7.5	1202.1	5.1	1202.1	5.1
113	30896	0.7	12.4546	2.0	2.2597	2.9	0.2041	2.1	0.72	1197.4	22.8	1199.8	20.4	1204.1	39.5	1204.1	39.5
157	133879	1.2	12.4352	0.7	2.2979	1.8	0.2072	1.6	0.92	1214.1	17.7	1211.6	12.4	1207.2	13.8	1207.2	13.8
149	96612	1.1	12.4296	0.8	2.2656	1.5	0.2042	1.3	0.86	1198.1	14.5	1201.7	10.9	1208.1	15.7	1208.1	15.7
301	146919	1.1	12.4123	0.7	2.2509	2.4	0.2026	2.3	0.95	1189.4	25.0	1197.1	17.0	1210.9	14.3	1210.9	14.3
64	69947	0.9	12.3915	1.8	2.2855	3.4	0.2054	2.9	0.85	1204.3	31.8	1207.8	24.2	1214.1	36.0	1214.1	36.0
316	102694	1.2	12.3847	0.4	2.3249	2.6	0.2088	2.6	0.99	1222.6	28.4	1219.9	18.4	1215.3	8.6	1215.3	8.6
68	62810	0.8	12.3682	1.6	2.2771	1.9	0.2043	0.9	0.50	1198.2	10.3	1205.2	13.3	1217.9	32.1	1217.9	32.1
27	29894	1.0	12.3643	6.2	2.3368	6.7	0.2095	2.6	0.39	1226.4	29.1	1223.5	47.8	1218.5	121.9	1218.5	121.9
61	89446	1.2	12.3559	2.2	2.2930	2.6	0.2055	1.4	0.54	1204.7	15.4	1210.1	18.2	1219.8	42.5	1219.8	42.5
8	6680	1.5	12.3497	7.6	2.2357	8.6	0.2002	4.0	0.47	1176.6	43.1	1192.3	60.1	1220.8	148.7	1220.8	148.7
42	85549	1.0	12.3275	2.0	2.2826	3.6	0.2041	3.0	0.83	1197.2	32.5	1206.9	25.3	1224.3	39.1	1224.3	39.1
203	166440	0.9	12.3265	1.0	2.2613	1.7	0.2022	1.4	0.82	1186.9	14.8	1200.3	11.7	1224.5	18.8	1224.5	18.8
56	35504	1.2	12.3159	2.1	2.2878	4.6	0.2044	4.1	0.89	1198.7	44.5	1208.5	32.5	1226.2	41.9	1226.2	41.9
63	64398	1.4	12.1796	2.2	2.3593	3.9	0.2084	3.2	0.83	1220.3	35.5	1230.4	27.6	1248.0	42.7	1248.0	42.7
19	11960	1.0	12.1732	5.4	2.3165	6.8	0.2045	4.1	0.60	1199.5	44.7	1217.3	48.0	1249.0	105.5	1249.0	105.5
33	29432	1.0	12.0999	2.6	2.3105	3.1	0.2028	1.6	0.52	1190.1	17.4	1215.5	21.7	1260.9	51.2	1260.9	51.2
29	5889	1.3	11.9582	4.3	2.3827	4.9	0.2066	2.2	0.46	1210.9	24.5	1237.4	34.9	1283.8	84.6	1283.8	84.6
14	10053	1.6	11.7750	7.0	2.4079	7.5	0.2056	2.7	0.36	1205.5	29.8	1244.9	53.9	1313.8	136.0	1313.8	136.0
55	74205	1.4	10.5991	1.9	3.3455	3.5	0.2572	3.0	0.85	1475.3	39.9	1491.7	27.8	1515.1	35.1	1515.1	35.1

608	441493	4.8	9.9278	0.5	3.6338	2.3	0.2616	2.2	0.98	1498.2	29.9	1557.0	18.2	1637.5	9.0	1637.5	9.0
144	102070	1.1	9.7359	0.5	4.1543	2.8	0.2933	2.7	0.98	1658.2	39.6	1665.0	22.5	1673.7	9.0	1673.7	9.0
261	208967	5.6	9.6846	0.5	4.2103	1.7	0.2957	1.7	0.96	1670.1	24.7	1676.0	14.3	1683.5	9.0	1683.5	9.0
298	353822	1.5	9.6745	0.3	4.3248	2.6	0.3035	2.6	0.99	1708.4	38.6	1698.1	21.3	1685.4	5.4	1685.4	5.4
265	247076	2.0	9.6740	0.3	4.2812	1.4	0.3004	1.3	0.98	1693.2	19.9	1689.8	11.3	1685.5	5.4	1685.5	5.4
146	126163	1.3	9.6459	0.3	4.3494	2.2	0.3043	2.1	0.99	1712.5	32.0	1702.8	17.8	1690.8	5.9	1690.8	5.9
74	27025	1.5	9.6316	1.3	4.2826	2.3	0.2992	1.9	0.83	1687.1	28.3	1690.0	19.0	1693.6	24.0	1693.6	24.0
244	29257	4.1	9.6272	0.5	4.2213	1.1	0.2947	1.0	0.89	1665.2	14.8	1678.2	9.3	1694.4	9.5	1694.4	9.5
252	211860	5.3	9.4403	0.2	4.4971	1.4	0.3079	1.4	0.99	1730.4	20.9	1730.4	11.5	1730.5	3.3	1730.5	3.3
239	157062	6.0	9.2512	0.4	4.7643	2.8	0.3197	2.8	0.99	1788.1	44.0	1778.6	23.8	1767.5	6.4	1767.5	6.4

Sample KTC-14-dz6 n = 66

U (ppm)	^{206}Pb/^{204}Pb	U/Th	(%) ^{206}Pb*/^{207}Pb*	± (1σ)	(%) ^{207}Pb*/^{235}U*	± (1σ)	(%) ^{206}Pb*/^{238}U*	± (1σ)	error corr.	Age (Ma) ^{206}Pb*/^{238}U*	± (1σ)	Age (Ma) ^{207}Pb*/^{235}U*	± (1σ)	Age (Ma) ^{207}Pb*/^{206}Pb*	± (1σ)	Preferred age (Ma)	± (1σ)
231	7909	0.7	22.4932	20.0	0.0709	20.3	0.0116	3.4	0.17	74.1	2.5	69.6	13.6	b.d.	b.d.	74.1	2.5
205	9323	0.7	22.8052	24.7	0.0724	25.2	0.0120	5.3	0.21	76.7	4.0	71.0	17.3	b.d.	b.d.	76.7	4.0
426	10541	0.9	21.5971	11.3	0.0775	11.4	0.0121	1.7	0.15	77.8	1.3	75.8	8.4	13.4	272.8	77.8	1.3
154	8109	0.6	25.2922	28.7	0.0665	29.1	0.0122	4.5	0.16	78.2	3.5	65.4	18.4	b.d.	b.d.	78.2	3.5
306	6289	0.7	19.7224	8.7	0.0854	9.5	0.0122	3.7	0.39	78.2	2.9	83.2	7.6	227.4	202.0	78.2	2.9
229	7520	0.9	21.3821	15.5	0.0789	15.8	0.0122	3.0	0.19	78.4	2.4	77.1	11.7	37.4	373.2	78.4	2.4
433	13633	1.2	20.8126	9.5	0.0816	9.8	0.0123	2.2	0.22	78.9	1.7	79.6	7.5	101.7	225.4	78.9	1.7
276	8151	1.0	23.8827	20.1	0.0717	20.8	0.0124	5.3	0.25	79.5	4.2	70.3	14.1	b.d.	b.d.	79.5	4.2
109	17027	1.0	22.0938	41.6	0.0775	41.8	0.0124	4.6	0.11	79.6	3.6	75.8	30.6	b.d.	b.d.	79.6	3.6
247	17577	0.9	21.4366	14.5	0.0811	15.4	0.0126	5.0	0.33	80.8	4.0	79.2	11.7	31.3	349.7	80.8	4.0
185	10031	0.6	22.0972	22.6	0.0789	22.8	0.0126	3.4	0.15	81.0	2.8	77.1	17.0	b.d.	b.d.	81.0	2.8
146	7077	0.9	21.6124	29.1	0.0813	29.4	0.0127	4.2	0.14	81.6	3.4	79.3	22.5	11.7	713.6	81.6	3.4
351	14366	0.9	21.0883	8.2	0.0840	8.7	0.0129	2.6	0.31	82.3	2.2	81.9	6.8	70.4	196.5	82.3	2.2
343	7202	0.5	20.8967	10.4	0.0852	10.6	0.0129	1.8	0.17	82.7	1.5	83.0	8.4	92.1	247.0	82.7	1.5
428	47904	0.6	20.5269	9.1	0.0876	9.2	0.0130	1.6	0.17	83.5	1.3	85.3	7.5	134.2	213.2	83.5	1.3
260	12864	1.2	19.8915	15.9	0.0905	16.2	0.0131	3.1	0.19	83.7	2.6	88.0	13.7	207.6	371.6	83.7	2.6
185	8564	0.4	21.0286	10.4	0.1508	10.7	0.0230	2.2	0.21	146.6	3.3	142.6	14.2	77.1	248.6	146.6	3.3
86	4463	0.8	26.2484	24.4	0.1242	25.2	0.0236	6.4	0.26	150.6	9.6	118.9	28.3	b.d.	b.d.	150.6	9.6
181	9495	1.7	19.6365	8.5	0.1680	8.9	0.0239	2.5	0.28	152.4	3.8	157.7	13.0	237.5	197.4	152.4	3.8
92	7120	0.7	19.7499	32.1	0.1676	32.7	0.0240	6.3	0.19	152.9	9.5	157.3	47.8	224.2	760.5	152.9	9.5
114	17951	0.6	17.5271	14.2	0.1908	14.4	0.0243	2.5	0.17	154.5	3.8	177.3	23.4	493.7	313.6	154.5	3.8
122	7539	0.7	21.6428	20.6	0.1549	20.7	0.0243	2.4	0.12	154.9	3.7	146.3	28.2	8.3	499.2	154.9	3.7
243	13118	0.9	20.9065	11.3	0.1614	11.5	0.0245	2.0	0.18	155.9	3.1	152.0	16.2	90.9	268.3	155.9	3.1
171	19190	0.8	21.7533	17.2	0.1627	17.3	0.0257	1.8	0.11	163.4	3.0	153.1	24.6	b.d.	b.d.	163.4	3.0
136	10332	0.8	24.4567	16.1	0.1451	16.4	0.0257	3.0	0.19	163.8	4.9	137.5	21.1	b.d.	b.d.	163.8	4.9
348	43234	1.1	19.6453	4.7	0.1841	5.0	0.0262	1.8	0.36	166.9	3.0	171.6	7.9	236.4	108.5	166.9	3.0
371	22616	1.1	20.2627	5.5	0.1790	5.6	0.0263	1.1	0.20	167.4	1.9	167.2	8.6	164.6	128.5	167.4	1.9
362	216242	1.0	11.2197	0.5	2.9022	1.5	0.2362	1.5	0.95	1366.7	17.9	1382.5	11.5	1406.9	8.8	1406.9	8.8
548	306698	100.0	10.0176	1.7	4.0998	2.1	0.2979	1.3	0.62	1680.7	19.8	1654.3	17.5	1620.8	31.3	1620.8	31.3
483	371727	5.0	9.9102	0.4	3.5647	1.1	0.2562	1.0	0.91	1470.5	12.8	1541.7	8.5	1640.8	8.2	1640.8	8.2
899	109182	2.7	9.8014	0.4	3.8720	2.1	0.2752	2.1	0.98	1567.4	28.5	1607.9	16.8	1661.3	6.7	1661.3	6.7
106	32470	1.9	9.6783	0.6	3.9365	3.2	0.2763	3.2	0.98	1572.8	44.1	1621.2	26.1	1684.6	11.4	1684.6	11.4
225	188903	4.4	9.6669	0.4	4.3152	2.5	0.3025	2.4	0.99	1703.9	36.5	1696.3	20.4	1686.8	7.3	1686.8	7.3
170	232090	1.0	9.6565	0.4	4.2067	1.2	0.2946	1.2	0.95	1664.6	17.2	1675.3	10.1	1688.8	6.9	1688.8	6.9
31	14788	0.7	9.6564	3.0	4.2441	3.3	0.2972	1.4	0.43	1677.6	21.0	1682.6	27.4	1688.8	55.5	1688.8	55.5
51	35740	1.6	9.6407	1.6	4.3762	2.2	0.3060	1.6	0.71	1720.9	24.0	1707.9	18.5	1691.8	29.0	1691.8	29.0
1047	1092696	4.5	9.6321	0.1	4.3472	0.5	0.3037	0.5	0.99	1709.6	7.8	1702.4	4.3	1693.5	1.1	1693.5	1.1
862	492708	13.8	9.6272	0.2	3.8245	1.3	0.2670	1.3	0.98	1525.8	17.1	1597.9	10.3	1694.4	4.6	1694.4	4.6
134	194823	1.9	9.5821	0.6	4.4388	1.0	0.3085	0.8	0.78	1733.2	12.2	1719.6	8.5	1703.1	11.8	1703.1	11.8
372	348894	1.7	9.5521	0.2	4.2641	0.5	0.2954	0.5	0.94	1668.5	7.3	1686.5	4.3	1708.8	3.2	1708.8	3.2
214	150552	2.1	9.5244	0.8	4.4408	1.2	0.3068	0.8	0.73	1724.7	12.8	1720.0	9.6	1714.2	14.5	1714.2	14.5
352	378157	1.9	9.5072	0.5	4.4109	1.2	0.3041	1.1	0.92	1711.8	16.6	1714.4	9.9	1717.5	8.5	1717.5	8.5
217	39306	0.9	9.5070	5.3	4.0649	7.9	0.2803	5.9	0.74	1592.8	83.5	1647.3	64.9	1717.5	97.6	1717.5	97.6
176	199746	1.9	9.5011	0.5	4.5460	2.7	0.3133	2.7	0.98	1756.7	41.1	1739.4	22.7	1718.7	10.0	1718.7	10.0

1642	208855	2.1	9.4902	0.1	3.9825	3.6	0.2741	3.6	1.00	1561.7	49.5	1630.6	29.0	1720.8	2.5	1720.8	2.5
842	567888	19.2	9.4743	0.1	4.4580	0.7	0.3063	0.7	0.99	1722.6	11.1	1723.2	6.2	1723.9	2.1	1723.9	2.1
164	127269	1.6	9.4740	0.9	4.4289	1.8	0.3043	1.6	0.87	1712.7	23.6	1717.8	15.0	1723.9	16.7	1723.9	16.7
238	28233	2.4	9.4719	0.4	3.9740	0.9	0.2730	0.8	0.89	1556.0	11.5	1628.9	7.6	1724.3	8.0	1724.3	8.0
202	119929	2.8	9.4627	0.6	4.3082	2.7	0.2957	2.6	0.97	1669.8	38.0	1694.9	21.9	1726.1	11.1	1726.1	11.1
346	363204	14.3	9.4623	0.3	4.6012	0.9	0.3158	0.9	0.95	1769.0	13.7	1749.5	7.8	1726.2	5.4	1726.2	5.4
205	82360	6.1	9.4473	0.6	4.6230	1.7	0.3168	1.6	0.94	1773.9	25.1	1753.4	14.5	1729.1	11.1	1729.1	11.1
334	355329	1.6	9.4164	0.4	4.6033	0.9	0.3144	0.8	0.92	1762.2	13.0	1749.9	7.6	1735.1	6.5	1735.1	6.5
396	423571	3.1	9.4149	0.2	4.4910	1.9	0.3067	1.9	0.99	1724.3	28.3	1729.3	15.6	1735.4	4.2	1735.4	4.2
170	130744	1.5	9.4139	0.4	4.5764	0.9	0.3125	0.8	0.88	1752.8	12.1	1745.0	7.5	1735.6	7.9	1735.6	7.9
221	125755	1.7	9.4112	0.4	4.5731	1.0	0.3121	0.9	0.91	1751.2	13.5	1744.4	8.0	1736.1	7.2	1736.1	7.2
364	498389	6.6	9.4088	0.2	4.4792	0.9	0.3057	0.9	0.96	1719.3	12.9	1727.1	7.4	1736.6	4.5	1736.6	4.5
320	222849	2.1	9.3931	0.2	4.5687	1.6	0.3112	1.6	0.99	1746.8	24.0	1743.6	13.1	1739.7	3.4	1739.7	3.4
103	67748	1.9	9.3851	1.0	4.5734	1.3	0.3113	0.8	0.63	1747.1	12.4	1744.4	10.8	1741.2	18.4	1741.2	18.4
670	977610	1.4	9.3386	0.3	4.5794	1.2	0.3102	1.2	0.98	1741.5	17.7	1745.5	9.9	1750.3	4.8	1750.3	4.8
385	212249	1.8	9.3343	0.2	4.6977	1.2	0.3180	1.2	0.99	1780.1	18.2	1766.8	9.9	1751.2	3.6	1751.2	3.6
128	61786	1.5	9.3269	0.8	4.6549	1.0	0.3149	0.5	0.56	1764.7	8.4	1759.2	8.2	1752.6	14.8	1752.6	14.8
360	455112	7.2	9.3258	0.4	4.6751	1.3	0.3162	1.2	0.94	1771.2	18.5	1762.8	10.6	1752.8	7.7	1752.8	7.7
113	66966	1.9	9.3104	0.9	4.5953	2.1	0.3103	1.9	0.90	1742.2	28.5	1748.4	17.2	1755.9	16.1	1755.9	16.1
115	94999	1.7	9.2991	0.6	4.7798	2.1	0.3224	2.0	0.96	1801.3	31.1	1781.4	17.4	1758.1	10.9	1758.1	10.9
319	186967	1.5	9.2895	0.2	4.6300	0.6	0.3119	0.6	0.93	1750.2	8.6	1754.7	5.0	1760.0	4.0	1760.0	4.0
97	251972	1.4	9.2220	1.0	4.7821	1.6	0.3198	1.2	0.75	1789.0	18.8	1781.8	13.4	1773.3	19.1	1773.3	19.1

Sample KTC-14-dz7 n = 69

			(%)		(%)		(%)			Age (Ma)		Age (Ma)		Age (Ma)		Preferred	
U	$^{206}Pb/$	U/	$^{206}Pb^*/$	±	$^{207}Pb^*/$	±	$^{206}Pb^*/$	±	error	$^{206}Pb^*/$	±	$^{207}Pb^*/$	±	$^{207}Pb^*/$	±	age	±
(ppm)	^{204}Pb	Th	$^{207}Pb^*$	(1σ)	$^{235}U^*$	(1σ)	$^{238}U^*$	(1σ)	corr.	$^{238}U^*$	(1σ)	$^{235}U^*$	(1σ)	$^{206}Pb^*$	(1σ)	(Ma)	(1σ)
178	9367	0.5	22.4181	11.3	0.0725	11.6	0.0118	2.4	0.20	75.5	1.8	71.0	7.9	b.d.	b.d.	75.5	1.8
103	5906	0.7	30.5078	47.1	0.0536	48.0	0.0119	9.2	0.19	76.0	7.0	53.0	24.8	b.d.	b.d.	76.0	7.0
113	10036	0.4	17.8419	23.4	0.0925	23.7	0.0120	3.9	0.16	76.7	2.9	89.8	20.4	454.3	524.7	76.7	2.9
506	37638	1.0	21.2333	4.5	0.0780	5.5	0.0120	3.3	0.59	77.0	2.5	76.2	4.1	54.1	106.5	77.0	2.5
290	5537	1.0	19.6518	9.7	0.0846	9.8	0.0121	1.5	0.16	77.3	1.2	82.5	7.8	235.7	223.8	77.3	1.2
207	11121	0.9	20.4219	9.3	0.0822	10.2	0.0122	4.0	0.39	78.0	3.1	80.2	7.8	146.3	219.4	78.0	3.1
134	8189	0.6	25.0083	25.0	0.0680	25.6	0.0123	5.5	0.22	79.0	4.4	66.8	16.5	b.d.	b.d.	79.0	4.4
186	19837	1.2	20.9863	13.7	0.0813	14.6	0.0124	5.1	0.35	79.3	4.0	79.4	11.1	81.9	326.1	79.3	4.0
99	6930	0.9	27.1018	35.7	0.0632	35.8	0.0124	3.6	0.10	79.5	2.8	62.2	21.6	b.d.	b.d.	79.5	2.8
206	5361	1.0	21.7799	18.7	0.0807	19.1	0.0127	4.1	0.21	81.6	3.3	78.8	14.5	b.d.	b.d.	81.6	3.3
64	4505	0.9	33.3084	41.4	0.0531	41.8	0.0128	5.7	0.14	82.1	4.7	52.5	21.4	b.d.	b.d.	82.1	4.7
164	9077	0.5	23.6654	15.6	0.0770	16.4	0.0132	5.0	0.31	84.6	4.2	75.3	11.9	b.d.	b.d.	84.6	4.2
706	39858	1.6	21.0660	3.0	0.1050	3.6	0.0160	2.0	0.55	102.6	2.0	101.4	3.5	72.9	72.1	102.6	2.0
764	103548	0.8	20.6404	2.9	0.1583	4.3	0.0237	3.1	0.73	150.9	4.7	149.2	5.9	121.3	69.2	150.9	4.7
417	12453	0.5	20.5484	4.0	0.1596	4.4	0.0238	1.9	0.42	151.5	2.8	150.3	6.2	131.7	94.3	151.5	2.8
203	21828	1.3	20.2412	7.9	0.1627	8.2	0.0239	2.1	0.26	152.2	3.2	153.1	11.6	167.0	184.5	152.2	3.2
40	3815	0.5	19.8526	23.6	0.1666	24.2	0.0240	5.5	0.23	152.8	8.3	156.4	35.1	212.1	552.8	152.8	8.3
196	13450	1.0	19.7986	6.7	0.1676	7.0	0.0241	1.9	0.27	153.3	2.9	157.3	10.2	218.5	156.2	153.3	2.9
281	32541	1.2	20.1799	3.1	0.1649	4.3	0.0241	3.0	0.69	153.7	4.5	155.0	6.2	174.1	72.5	153.7	4.5
36	3116	0.3	19.4016	22.0	0.1762	22.4	0.0248	4.4	0.20	157.9	6.9	164.8	34.2	265.2	510.4	157.9	6.9
134	2956	1.3	18.7065	8.6	0.1832	9.2	0.0249	3.5	0.38	158.3	5.5	170.8	14.5	348.2	193.7	158.3	5.5
55	2824	0.5	26.9262	53.7	0.1291	54.4	0.0252	8.5	0.16	160.5	13.6	123.3	63.3	b.d.	b.d.	160.5	13.6
65	2991	1.1	20.4368	13.3	0.1723	14.1	0.0255	4.8	0.34	162.6	7.7	161.4	21.1	144.5	312.7	162.6	7.7
243	20016	0.7	21.2366	4.4	0.1666	5.4	0.0257	3.1	0.57	163.3	5.0	156.4	7.8	53.7	105.9	163.3	5.0
151	26833	0.8	21.9736	7.8	0.1611	8.1	0.0257	2.4	0.30	163.4	3.9	151.6	11.4	b.d.	b.d.	163.4	3.9
538	58010	0.7	20.3238	2.1	0.1809	3.0	0.0267	2.0	0.69	169.7	3.4	168.8	4.6	157.5	49.9	169.7	3.4
199	6779	2.0	19.9413	5.6	0.2474	6.1	0.0358	2.3	0.39	226.6	5.2	224.5	12.3	201.8	130.4	226.6	5.2
181	27809	1.1	19.6172	4.1	0.2584	4.2	0.0368	1.1	0.26	232.7	2.5	233.4	8.8	239.7	93.6	232.7	2.5
368	113628	4.5	19.4454	2.2	0.2611	2.6	0.0368	1.3	0.51	233.1	3.1	235.5	5.5	259.9	51.6	233.1	3.1
832	171211	4.4	19.7616	1.3	0.2595	2.8	0.0372	2.5	0.88	235.4	5.8	234.2	5.9	222.8	30.5	235.4	5.8
401	16806	1.3	19.4816	2.6	0.2653	3.8	0.0375	2.8	0.73	237.3	6.4	239.0	8.1	255.7	60.0	237.3	6.4
249	29118	3.6	19.2440	5.3	0.2693	5.8	0.0376	2.4	0.41	237.8	5.5	242.1	12.5	283.9	121.8	237.8	5.5
165	15382	1.3	18.8164	5.1	0.2755	5.7	0.0376	2.5	0.44	237.9	5.9	247.1	12.6	335.0	116.5	237.9	5.9
43	21333	1.6	12.4781	2.0	2.2574	2.1	0.2043	0.7	0.33	1198.3	7.6	1199.1	14.8	1200.5	39.2	1200.5	39.2
174	202152	2.5	11.1341	0.5	3.0949	2.3	0.2499	2.2	0.97	1438.1	28.3	1431.4	17.3	1421.6	10.1	1421.6	10.1
206	358921	2.6	10.9068	0.5	3.3934	2.8	0.2684	2.8	0.98	1532.8	37.8	1502.9	22.0	1460.9	9.4	1460.9	9.4
1109	63096	11.3	10.7719	1.3	2.8497	3.3	0.2226	3.0	0.92	1295.8	35.4	1368.7	24.6	1484.5	24.4	1484.5	24.4
463	204775	5.7	10.5290	0.7	3.5076	1.3	0.2679	1.1	0.86	1529.9	15.6	1528.9	10.5	1527.6	12.8	1527.6	12.8
44	33939	2.2	10.5155	4.6	3.1110	8.3	0.2373	6.8	0.83	1372.5	84.4	1435.4	63.5	1530.0	87.5	1530.0	87.5
783	732561	19.7	10.1155	0.3	3.5120	1.9	0.2577	1.9	0.99	1477.8	24.8	1529.9	15.0	1602.7	4.9	1602.7	4.9
424	823472	3.4	9.8293	0.1	3.7909	1.1	0.2702	1.1	0.99	1542.1	14.4	1590.8	8.5	1656.0	2.7	1656.0	2.7
38	61243	0.8	9.7949	1.0	4.2735	2.6	0.3036	2.4	0.92	1709.1	36.1	1688.3	21.6	1662.5	19.2	1662.5	19.2
206	161618	1.9	9.7673	0.8	4.0866	1.3	0.2895	1.0	0.78	1639.0	15.0	1651.6	10.8	1667.7	15.3	1667.7	15.3
434	388005	1.4	9.7194	1.4	4.1430	2.3	0.2920	1.8	0.79	1651.8	26.0	1662.8	18.4	1676.8	25.3	1676.8	25.3

232	131464	3.0	9.7108	1.0	4.0356	3.4	0.2842	3.3	0.96	1612.6	46.7	1641.4	27.8	1678.5	18.0	1678.5	18.0
423	456123	5.9	9.6705	0.2	4.1775	1.3	0.2930	1.3	0.98	1656.5	19.4	1669.6	11.0	1686.1	4.5	1686.1	4.5
440	300824	3.4	9.6616	0.2	4.0854	1.9	0.2863	1.9	0.99	1622.9	26.9	1651.4	15.4	1687.8	3.7	1687.8	3.7
153	47495	1.4	9.6450	0.4	4.0893	2.7	0.2861	2.7	0.99	1621.8	38.3	1652.2	22.0	1691.0	7.1	1691.0	7.1
667	310749	3.9	9.6291	0.2	3.8244	1.5	0.2671	1.5	0.99	1526.0	19.8	1597.9	11.8	1694.1	3.6	1694.1	3.6
339	431468	1.8	9.6012	0.3	4.3950	1.4	0.3060	1.3	0.97	1721.2	19.9	1711.4	11.3	1699.4	6.3	1699.4	6.3
1145	407528	10.1	9.5594	0.2	4.3201	0.8	0.2995	0.8	0.98	1688.9	12.1	1697.2	6.8	1707.4	3.0	1707.4	3.0
646	504678	9.6	9.5276	0.3	4.0446	3.9	0.2795	3.9	1.00	1588.8	54.5	1643.2	31.6	1713.6	4.8	1713.6	4.8
885	746172	10.5	9.5219	0.4	4.3066	1.6	0.2974	1.5	0.97	1678.5	22.5	1694.6	12.9	1714.7	7.0	1714.7	7.0
821	1320693	10.8	9.5111	0.1	4.4872	1.7	0.3095	1.7	1.00	1738.4	26.5	1728.6	14.5	1716.7	2.7	1716.7	2.7
180	276407	3.0	9.4412	0.7	4.6339	5.5	0.3173	5.4	0.99	1776.5	84.4	1755.4	45.7	1730.3	12.1	1730.3	12.1
239	100378	2.8	9.4400	0.5	4.6315	8.8	0.3171	8.8	1.00	1775.5	136.1	1755.0	73.5	1730.5	9.3	1730.5	9.3
346	338662	1.8	9.4370	0.1	4.3727	2.1	0.2993	2.1	1.00	1687.8	31.1	1707.2	17.4	1731.1	2.3	1731.1	2.3
136	88840	3.6	9.4229	0.5	4.4222	2.7	0.3022	2.6	0.98	1702.3	39.4	1716.5	22.2	1733.9	8.7	1733.9	8.7
110	159898	1.6	9.4229	0.5	4.4973	2.2	0.3074	2.2	0.97	1727.7	33.0	1730.5	18.6	1733.9	10.0	1733.9	10.0
545	595160	2.7	9.4201	0.2	4.6723	1.3	0.3192	1.3	0.99	1785.9	20.7	1762.3	11.2	1734.4	3.5	1734.4	3.5
147	202247	2.8	9.4103	0.6	4.7518	2.4	0.3243	2.3	0.96	1810.7	35.9	1776.4	19.8	1736.3	11.6	1736.3	11.6
696	798455	1.6	9.3965	0.2	4.6085	1.8	0.3141	1.8	1.00	1760.7	27.8	1750.8	15.1	1739.0	2.9	1739.0	2.9
180	124560	2.2	9.3776	0.3	4.6184	1.7	0.3141	1.7	0.98	1760.9	26.3	1752.6	14.5	1742.7	6.3	1742.7	6.3
604	1208583	2.4	9.3759	0.2	4.5497	3.9	0.3094	3.9	1.00	1737.7	58.9	1740.1	32.3	1743.0	3.8	1743.0	3.8
155	137718	1.9	9.3755	0.3	4.5304	1.6	0.3081	1.5	0.98	1731.1	23.2	1736.6	13.0	1743.1	5.9	1743.1	5.9
240	98933	1.5	9.3724	0.3	4.4048	1.6	0.2994	1.6	0.98	1688.4	23.4	1713.2	13.3	1743.7	6.0	1743.7	6.0
1004	670318	1.6	9.3410	0.1	4.5631	1.9	0.3091	1.9	1.00	1736.5	29.1	1742.6	15.9	1749.9	1.5	1749.9	1.5
685	991908	1.5	9.3035	0.1	4.5629	1.4	0.3079	1.4	1.00	1730.3	20.6	1742.5	11.3	1757.2	2.4	1757.2	2.4
91	89709	2.1	9.0479	1.0	4.9377	3.5	0.3240	3.4	0.96	1809.3	52.9	1808.7	29.5	1808.0	17.7	1808.0	17.7

Sample KTC-14-dz8 n = 88

U (ppm)	^{206}Pb/ ^{204}Pb	U/ Th	(%) ^{206}Pb*/ ^{207}Pb*	± (1σ)	(%) ^{207}Pb*/ ^{235}U*	± (1σ)	(%) ^{206}Pb*/ ^{238}U*	± (1σ)	error corr.	Age (Ma) ^{206}Pb*/ ^{238}U*	± (1σ)	Age (Ma) ^{207}Pb*/ ^{235}U*	± (1σ)	Age (Ma) ^{207}Pb*/ ^{206}Pb*	± (1σ)	Preferred age (Ma)	± (1σ)
55	5417	0.6	19.3808	78.9	0.0808	79.4	0.0114	8.3	0.10	72.8	6.0	78.9	60.3	b.d.	b.d.	72.8	6.0
166	5353	1.9	24.2787	11.9	0.0651	12.6	0.0115	4.1	0.33	73.5	3.0	64.1	7.8	b.d.	b.d.	73.5	3.0
313	10820	2.9	22.8402	18.8	0.0698	18.9	0.0116	1.8	0.10	74.1	1.3	68.5	12.5	b.d.	b.d.	74.1	1.3
463	22126	1.8	20.9511	11.9	0.0766	11.9	0.0116	1.1	0.09	74.6	0.8	74.9	8.6	85.9	281.9	74.6	0.8
308	2818	1.5	19.1546	11.7	0.0838	12.6	0.0116	4.8	0.38	74.7	3.5	81.8	9.9	294.5	267.4	74.7	3.5
62	2529	0.5	21.9953	52.1	0.0730	52.9	0.0116	9.3	0.18	74.7	6.9	71.6	36.6	b.d.	b.d.	74.7	6.9
161	6389	1.5	28.3447	43.0	0.0567	43.1	0.0117	2.4	0.06	74.8	1.8	56.0	23.5	b.d.	b.d.	74.8	1.8
84	2712	0.8	20.5010	33.3	0.0786	33.7	0.0117	5.6	0.16	74.9	4.1	76.9	25.0	137.2	801.7	74.9	4.1
364	20645	1.6	20.9500	7.2	0.0771	7.5	0.0117	2.3	0.31	75.1	1.7	75.4	5.5	86.1	170.3	75.1	1.7
698	53980	2.5	20.8628	3.4	0.0775	4.0	0.0117	2.1	0.53	75.1	1.6	75.8	2.9	95.9	80.6	75.1	1.6
343	7361	1.1	21.5190	9.9	0.0766	10.0	0.0119	1.5	0.15	76.6	1.1	74.9	7.3	22.1	238.9	76.6	1.1
281	17450	1.1	25.1617	9.9	0.0661	10.1	0.0121	1.8	0.18	77.3	1.4	65.0	6.4	b.d.	b.d.	77.3	1.4
260	13038	1.2	23.8427	11.5	0.0704	11.8	0.0122	2.5	0.21	78.0	2.0	69.1	7.9	b.d.	b.d.	78.0	2.0
336	15772	1.9	23.6993	11.7	0.0711	12.0	0.0122	2.6	0.21	78.3	2.0	69.7	8.1	b.d.	b.d.	78.3	2.0
168	9415	1.0	19.8512	15.2	0.0852	15.9	0.0123	4.6	0.29	78.6	3.6	83.0	12.7	212.3	354.2	78.6	3.6
155	10050	1.2	21.1397	13.7	0.0813	14.0	0.0125	2.6	0.18	79.9	2.0	79.4	10.7	64.6	328.2	79.9	2.0
298	22614	0.6	20.6412	8.2	0.0841	8.4	0.0126	1.9	0.23	80.7	1.5	82.0	6.6	121.1	193.8	80.7	1.5
322	15011	4.0	20.5839	9.1	0.0922	9.4	0.0138	2.4	0.26	88.1	2.1	89.5	8.0	127.7	213.8	88.1	2.1
195	12368	1.6	20.8881	17.3	0.0922	17.5	0.0140	2.5	0.14	89.4	2.2	89.6	15.0	93.0	413.3	89.4	2.2
954	34498	1.0	20.8790	1.5	0.0926	2.2	0.0140	1.6	0.73	89.7	1.4	89.9	1.9	94.1	36.5	89.7	1.4
410	32735	1.4	20.5594	6.8	0.0945	7.0	0.0141	1.4	0.20	90.2	1.3	91.6	6.1	130.5	160.7	90.2	1.3
502	47417	0.4	21.3614	4.9	0.0911	5.3	0.0141	2.1	0.39	90.4	1.9	88.6	4.5	39.7	117.8	90.4	1.9
303	19578	1.4	19.6863	9.6	0.0990	11.0	0.0141	5.5	0.49	90.5	4.9	95.9	10.1	231.6	221.8	90.5	4.9
283	15177	2.5	20.1776	12.4	0.0971	12.7	0.0142	2.6	0.20	90.9	2.3	94.1	11.4	174.4	291.4	90.9	2.3
260	17183	1.1	22.0972	9.0	0.0887	9.3	0.0142	2.4	0.26	91.0	2.2	86.3	7.7	b.d.	b.d.	91.0	2.2
910	7883	0.8	20.7255	2.3	0.0946	2.6	0.0142	1.2	0.47	91.0	1.1	91.8	2.3	111.5	54.0	91.0	1.1
446	42752	0.6	20.3311	6.1	0.0978	6.3	0.0144	1.6	0.26	92.3	1.5	94.7	5.7	156.7	141.9	92.3	1.5
281	4730	0.4	15.8759	21.0	0.1257	21.8	0.0145	6.0	0.27	92.7	5.5	120.3	24.7	707.8	450.6	92.7	5.5
73	7797	1.0	30.1801	51.7	0.0681	52.0	0.0149	6.0	0.12	95.5	5.7	66.9	33.7	b.d.	b.d.	95.5	5.7
85	7298	0.8	25.1369	58.1	0.0835	58.4	0.0152	5.1	0.09	97.4	4.9	81.4	45.7	b.d.	b.d.	97.4	4.9
78	3458	1.0	25.1721	39.3	0.0834	39.4	0.0152	3.0	0.08	97.4	2.9	81.4	30.8	b.d.	b.d.	97.4	2.9
290	24155	1.3	21.7739	9.8	0.1005	10.9	0.0159	4.8	0.44	101.5	4.9	97.3	10.1	b.d.	b.d.	101.5	4.9
243	14910	1.6	21.3294	7.2	0.1169	7.5	0.0181	2.3	0.31	115.5	2.7	112.2	8.0	43.3	171.3	115.5	2.7
87	2054	0.7	20.0665	15.3	0.1312	15.6	0.0191	2.9	0.19	121.9	3.5	125.2	18.3	187.2	357.6	121.9	3.5
104	9120	0.5	25.5148	29.4	0.1062	29.7	0.0197	4.6	0.15	125.5	5.7	102.5	29.0	b.d.	b.d.	125.5	5.7
516	35565	1.4	20.1278	3.3	0.1447	3.7	0.0211	1.5	0.42	134.7	2.0	137.2	4.7	180.1	77.7	134.7	2.0
25	2019	0.5	18.2731	58.6	0.1685	59.0	0.0223	6.8	0.11	142.3	9.5	158.1	86.6	b.d.	b.d.	142.3	9.5
77	4600	0.6	19.9871	16.5	0.1636	16.7	0.0237	3.1	0.18	151.1	4.6	153.9	23.9	196.5	384.7	151.1	4.6
54	1021	0.5	16.3454	18.4	0.2286	20.9	0.0271	9.9	0.47	172.3	16.9	209.0	39.6	645.6	399.3	172.3	16.9
49	9244	0.8	20.9102	19.7	0.2045	20.3	0.0310	5.0	0.24	196.9	9.6	188.9	35.1	90.6	471.3	196.9	9.6
63	16602	0.8	21.0062	9.9	0.2179	11.1	0.0332	5.0	0.45	210.5	10.3	200.2	20.2	79.7	236.1	210.5	10.3
108	18202	1.5	21.0466	13.4	0.2305	13.5	0.0352	1.9	0.14	222.9	4.1	210.6	25.7	75.1	319.6	222.9	4.1
87	8606	1.2	20.1595	8.2	0.2407	8.5	0.0352	2.2	0.26	223.0	4.9	219.0	16.7	176.5	190.9	223.0	4.9
47	4016	0.7	26.0446	34.3	0.1899	34.6	0.0359	4.2	0.12	227.1	9.3	176.5	56.1	b.d.	b.d.	227.1	9.3

120	11403	1.1	19.3629	9.2	0.2564	9.6	0.0360	2.9	0.30	228.0	6.5	231.8	19.9	269.7	210.9	228.0	6.5
79	24910	1.4	20.3042	13.3	0.2502	13.8	0.0368	3.5	0.26	233.2	8.1	226.7	27.9	159.8	312.0	233.2	8.1
74	11837	1.0	20.5757	8.5	0.2472	9.0	0.0369	2.7	0.30	233.5	6.2	224.3	18.0	128.6	201.4	233.5	6.2
95	5066	1.2	19.0587	8.1	0.2739	8.6	0.0379	2.9	0.34	239.6	6.8	245.8	18.8	305.9	184.7	239.6	6.8
52	12947	1.0	20.3814	10.5	0.2606	11.2	0.0385	4.0	0.36	243.7	9.5	235.2	23.6	150.9	246.5	243.7	9.5
111	23295	1.0	18.7905	7.0	0.2836	7.8	0.0387	3.5	0.44	244.5	8.3	253.5	17.6	338.1	159.3	244.5	8.3
36	5801	0.7	21.0708	14.0	0.2654	15.0	0.0406	5.2	0.35	256.3	13.0	239.0	31.9	72.4	335.2	256.3	13.0
32	4365	0.8	24.0339	39.5	0.2333	40.3	0.0407	8.1	0.20	256.9	20.3	212.9	77.5	b.d.	b.d.	256.9	20.3
306	67361	3.8	15.7890	2.0	0.4297	2.6	0.0492	1.7	0.64	309.6	5.1	363.0	8.1	719.5	43.0	309.6	5.1
181	100729	1.0	13.4089	0.7	1.8134	2.1	0.1764	2.0	0.95	1047.0	19.7	1050.3	14.0	1057.2	13.3	1057.2	13.3
28	18329	1.2	12.5702	3.3	2.2057	3.7	0.2011	1.7	0.47	1181.1	18.6	1182.8	25.9	1186.0	64.8	1186.0	64.8
14	8692	1.5	12.4673	7.1	2.1906	7.4	0.1981	2.0	0.27	1165.0	21.6	1178.1	51.6	1202.2	140.3	1202.2	140.3
15	12162	0.9	12.2778	7.2	2.2212	7.7	0.1978	2.9	0.37	1163.5	30.7	1187.8	54.1	1232.3	140.5	1232.3	140.5
131	55090	0.7	11.4381	0.5	2.4014	1.6	0.1992	1.5	0.95	1171.1	16.5	1243.0	11.7	1369.9	10.2	1369.9	10.2
115	89653	0.6	11.2552	0.8	2.5203	1.4	0.2057	1.1	0.81	1206.1	12.4	1277.9	10.1	1400.9	15.5	1400.9	15.5
104	58013	0.5	11.2142	0.7	2.7629	2.4	0.2247	2.3	0.96	1306.8	26.9	1345.6	17.7	1407.9	13.3	1407.9	13.3
53	52497	0.3	11.1289	0.9	3.0746	4.1	0.2482	4.0	0.98	1429.0	51.3	1426.4	31.3	1422.4	16.3	1422.4	16.3
792	793828	19.4	11.0151	1.1	2.8290	2.7	0.2260	2.5	0.92	1313.5	29.5	1363.3	20.3	1442.1	20.8	1442.1	20.8
91	170816	1.7	10.8995	1.2	2.8943	2.5	0.2288	2.2	0.88	1328.2	26.4	1380.4	18.8	1462.1	22.5	1462.1	22.5
59	24717	0.4	10.7312	7.4	2.9500	10.9	0.2296	8.0	0.73	1332.4	96.3	1394.8	82.9	1491.6	140.6	1491.6	140.6
66	119580	1.8	10.4700	0.6	2.9576	2.8	0.2246	2.8	0.98	1306.1	32.7	1396.8	21.4	1538.1	10.7	1538.1	10.7
245	199995	5.3	10.3857	0.6	3.5956	4.2	0.2708	4.1	0.99	1545.0	56.6	1548.6	33.1	1553.3	11.0	1553.3	11.0
110	328130	2.2	10.1006	0.6	3.6978	2.1	0.2709	2.0	0.96	1545.3	27.4	1570.9	16.5	1605.4	10.4	1605.4	10.4
1199	612116	4.8	9.9563	0.8	3.4675	1.8	0.2504	1.6	0.89	1440.5	20.7	1519.9	14.1	1632.2	15.1	1632.2	15.1
81	103391	1.4	9.7901	1.0	3.7613	2.5	0.2671	2.3	0.92	1525.9	31.3	1584.5	20.1	1663.4	18.4	1663.4	18.4
528	323773	1.8	9.7416	0.2	3.7868	1.7	0.2675	1.7	0.99	1528.3	22.6	1589.9	13.5	1672.6	4.0	1672.6	4.0
352	347945	3.1	9.7174	0.4	3.7247	1.5	0.2625	1.5	0.97	1502.6	19.8	1576.7	12.2	1677.2	6.7	1677.2	6.7
381	296692	1.4	9.7101	0.3	3.9123	2.0	0.2755	2.0	0.99	1568.8	27.7	1616.2	16.2	1678.6	4.7	1678.6	4.7
452	788063	2.2	9.6970	0.2	4.0798	1.7	0.2869	1.7	0.99	1626.1	24.7	1650.3	14.1	1681.1	4.4	1681.1	4.4
200	407436	1.5	9.6741	0.3	3.9413	1.9	0.2765	1.9	0.99	1573.9	25.8	1622.2	15.2	1685.5	5.7	1685.5	5.7
852	249871	6.6	9.6554	1.3	3.4912	3.4	0.2445	3.2	0.93	1409.9	40.4	1525.2	27.0	1689.0	23.1	1689.0	23.1
471	373876	3.2	9.6415	0.2	4.0067	4.0	0.2802	4.0	1.00	1592.2	55.8	1635.6	32.2	1691.7	3.2	1691.7	3.2
248	474924	1.5	9.6294	0.2	4.2960	0.9	0.3000	0.9	0.97	1691.4	13.6	1692.6	7.8	1694.0	4.0	1694.0	4.0
161	123946	2.1	9.5688	0.3	4.4251	3.2	0.3071	3.1	1.00	1726.4	47.6	1717.0	26.1	1705.6	4.9	1705.6	4.9
163	338688	1.9	9.5432	0.3	4.2567	1.8	0.2946	1.7	0.98	1664.6	25.2	1685.0	14.4	1710.6	6.3	1710.6	6.3
210	316035	0.7	9.5293	0.6	4.3798	1.9	0.3027	1.8	0.96	1704.7	27.1	1708.5	15.7	1713.2	10.3	1713.2	10.3
620	115513	17.8	9.4971	0.3	4.2855	1.6	0.2952	1.6	0.98	1667.4	23.5	1690.6	13.5	1719.5	6.4	1719.5	6.4
275	389155	3.9	9.4135	0.4	4.7079	1.8	0.3214	1.8	0.98	1796.7	27.9	1768.7	15.2	1735.7	6.8	1735.7	6.8
361	369289	1.7	9.4114	0.1	4.6465	4.2	0.3172	4.2	1.00	1775.9	64.9	1757.7	35.0	1736.1	2.0	1736.1	2.0
229	295267	2.3	9.4065	0.3	4.3906	1.7	0.2995	1.7	0.98	1689.0	24.7	1710.6	14.0	1737.1	5.8	1737.1	5.8
395	739816	2.3	9.3872	0.5	4.3954	5.4	0.2992	5.4	1.00	1687.6	80.3	1711.5	44.9	1740.8	8.6	1740.8	8.6
220	343269	7.5	9.3610	2.2	4.1585	8.3	0.2823	8.0	0.97	1603.1	113.2	1665.9	67.7	1745.9	39.6	1745.9	39.6
104	154782	3.1	9.3346	2.8	3.9501	9.8	0.2674	9.4	0.96	1527.7	127.8	1624.0	79.7	1751.1	51.8	1751.1	51.8
129	86497	1.9	9.2793	0.8	3.9567	1.8	0.2663	1.6	0.90	1521.9	22.3	1625.4	14.8	1762.0	14.4	1762.0	14.4

Sample KTC-14-dz9 n = 92

U (ppm)	^{206}Pb/^{204}Pb	U/Th	^{206}Pb*/^{207}Pb* (%)	± (1σ)	^{207}Pb*/^{235}U* (%)	± (1σ)	^{206}Pb*/^{238}U* (%)	± (1σ)	error corr.	Age (Ma) ^{206}Pb*/^{238}U*	± (1σ)	Age (Ma) ^{207}Pb*/^{235}U*	± (1σ)	Age (Ma) ^{207}Pb*/^{206}Pb*	± (1σ)	Preferred age (Ma)	± (1σ)
168	7283	0.5	25.5216	26.5	0.0625	26.8	0.0116	3.9	0.15	74.1	2.9	61.5	16.0	b.d.	b.d.	74.1	2.9
280	6752	1.3	22.3375	14.3	0.0721	14.5	0.0117	2.2	0.15	74.8	1.6	70.6	9.9	b.d.	b.d.	74.8	1.6
163	8102	2.8	24.1196	12.3	0.0670	12.4	0.0117	1.8	0.15	75.1	1.4	65.8	7.9	b.d.	b.d.	75.1	1.4
216	8516	1.5	21.2483	14.7	0.0766	15.0	0.0118	2.9	0.19	75.6	2.2	74.9	10.8	52.4	352.0	75.6	2.2
138	1970	42.1	21.9848	22.1	0.0748	22.2	0.0119	2.1	0.10	76.4	1.6	73.2	15.7	b.d.	b.d.	76.4	1.6
217	6290	2.7	23.9424	24.1	0.0693	24.2	0.0120	2.0	0.08	77.1	1.6	68.1	15.9	b.d.	b.d.	77.1	1.6
139	4830	2.2	24.0033	20.4	0.0704	21.3	0.0123	6.3	0.30	78.5	4.9	69.1	14.3	b.d.	b.d.	78.5	4.9
187	10743	1.5	20.2285	10.5	0.0872	10.7	0.0128	2.1	0.20	82.0	1.7	84.9	8.7	168.5	245.3	82.0	1.7
211	16661	3.2	19.7231	17.8	0.0902	18.0	0.0129	2.1	0.12	82.7	1.7	87.7	15.1	227.3	414.9	82.7	1.7
86	3162	0.5	37.7934	36.2	0.0472	36.6	0.0129	5.3	0.15	82.8	4.4	46.8	16.7	b.d.	b.d.	82.8	4.4
687	24487	12.5	20.2808	4.3	0.0885	4.4	0.0130	0.9	0.22	83.3	0.8	86.1	3.6	162.5	99.7	83.3	0.8
1891	18846	2.3	20.9192	1.9	0.0869	2.0	0.0132	0.6	0.30	84.4	0.5	84.6	1.6	89.5	44.5	84.4	0.5
376	16386	0.6	20.6372	9.4	0.0889	10.8	0.0133	5.3	0.49	85.2	4.5	86.5	9.0	121.6	222.9	85.2	4.5
691	30559	6.0	20.8662	3.5	0.0901	3.7	0.0136	1.1	0.31	87.3	1.0	87.6	3.1	95.6	82.5	87.3	1.0
1034	62887	5.7	20.9035	2.9	0.0915	2.9	0.0139	0.5	0.18	88.8	0.5	88.9	2.5	91.3	68.6	88.8	0.5
513	31423	3.4	21.0187	4.8	0.0928	4.9	0.0141	1.2	0.24	90.5	1.1	90.1	4.3	78.3	113.8	90.5	1.1
919	54424	1.8	20.7328	2.9	0.0956	3.0	0.0144	0.7	0.24	92.0	0.6	92.7	2.6	110.7	68.0	92.0	0.6
1254	10977	0.8	20.8748	1.7	0.0963	2.0	0.0146	1.1	0.54	93.3	1.0	93.4	1.8	94.6	39.7	93.3	1.0
113	10089	1.1	23.9550	26.6	0.0844	27.1	0.0147	5.4	0.20	93.9	5.1	82.3	21.4	b.d.	b.d.	93.9	5.1
186	7378	0.5	19.5319	10.8	0.1046	10.9	0.0148	1.5	0.14	94.8	1.4	101.0	10.4	249.8	248.1	94.8	1.4
81	2510	1.0	21.3057	26.9	0.0965	27.4	0.0149	5.0	0.18	95.4	4.7	93.5	24.5	45.9	653.4	95.4	4.7
76	4291	1.1	16.8234	19.5	0.1228	20.5	0.0150	6.1	0.30	95.9	5.8	117.6	22.7	583.3	427.8	95.9	5.8
94	7349	1.0	21.8731	29.3	0.0950	29.5	0.0151	3.6	0.12	96.4	3.4	92.1	26.0	b.d.	b.d.	96.4	3.4
142	13203	0.9	21.7409	15.5	0.0961	15.6	0.0151	2.0	0.13	96.9	1.9	93.1	13.9	b.d.	b.d.	96.9	1.9
137	4983	1.0	23.0962	13.8	0.0910	14.4	0.0152	4.2	0.29	97.5	4.1	88.4	12.2	b.d.	b.d.	97.5	4.1
81	10683	1.3	24.2463	23.0	0.0888	23.7	0.0156	5.6	0.24	99.9	5.5	86.4	19.6	b.d.	b.d.	99.9	5.5
58	12543	0.9	19.4785	23.5	0.1581	23.8	0.0223	3.8	0.16	142.4	5.3	149.1	33.0	256.0	547.3	142.4	5.3
63	3599	1.3	19.6864	14.6	0.1636	15.7	0.0234	5.8	0.37	148.8	8.5	153.8	22.4	231.6	337.9	148.8	8.5
94	5101	3.5	17.5046	19.1	0.1878	20.1	0.0238	6.2	0.31	151.9	9.3	174.7	32.3	496.5	424.9	151.9	9.3
68	6879	0.9	17.2258	30.4	0.1910	30.6	0.0239	3.4	0.11	152.0	5.2	177.5	49.9	531.8	681.4	152.0	5.2
66	18351	1.4	25.2666	28.5	0.1310	28.8	0.0240	3.7	0.13	153.0	5.7	125.0	33.8	b.d.	b.d.	153.0	5.7
403	24892	0.7	19.8917	2.8	0.1676	3.2	0.0242	1.5	0.48	154.0	2.3	157.3	4.6	207.6	64.6	154.0	2.3
259	8059	0.5	20.2522	4.2	0.1658	4.7	0.0244	2.1	0.44	155.1	3.2	155.8	6.8	165.8	98.8	155.1	3.2
194	6580	6.6	19.2697	5.9	0.1925	7.3	0.0269	4.2	0.58	171.1	7.1	178.7	11.9	280.8	136.2	171.1	7.1
49	5160	0.8	19.9745	18.7	0.2088	19.4	0.0303	4.8	0.25	192.1	9.1	192.6	34.0	198.0	438.9	192.1	9.1
32	3426	1.2	22.8811	36.6	0.1949	37.4	0.0323	7.8	0.21	205.2	15.8	180.8	62.0	b.d.	b.d.	205.2	15.8
61	7479	1.1	19.5333	13.1	0.2313	15.2	0.0328	7.8	0.51	207.9	16.0	211.3	29.1	249.6	302.2	207.9	16.0
64	1946	0.7	25.5819	18.2	0.1798	18.6	0.0334	3.8	0.20	211.5	7.8	167.9	28.8	b.d.	b.d.	211.5	7.8
47	691	0.6	19.1379	28.7	0.2419	29.4	0.0336	6.4	0.22	212.9	13.5	220.0	58.2	296.5	666.7	212.9	13.5
55	3348	1.1	20.6376	17.1	0.2306	17.2	0.0345	1.7	0.10	218.8	3.6	210.7	32.7	121.6	405.6	218.8	3.6
70	11319	1.0	18.8306	13.5	0.2565	14.0	0.0350	3.8	0.27	221.9	8.3	231.8	29.1	333.3	307.3	221.9	8.3
49	3249	1.0	18.7545	20.9	0.2659	21.1	0.0362	3.3	0.16	229.1	7.4	239.4	45.1	342.5	477.5	229.1	7.4
37	4199	1.0	14.9293	15.2	0.3398	15.7	0.0368	3.9	0.25	232.9	8.8	297.0	40.3	837.2	317.7	232.9	8.8
448	50778	5.7	19.5152	2.0	0.2602	2.2	0.0368	1.1	0.49	233.1	2.5	234.8	4.7	251.8	45.1	233.1	2.5

32	4819	0.9	21.1011	20.6	0.2426	20.9	0.0371	4.0	0.19	235.0	9.3	220.6	41.6	68.9	493.5	235.0	9.3
45	4996	0.8	16.5120	18.9	0.3153	20.5	0.0378	7.9	0.39	238.9	18.6	278.3	50.0	623.7	411.9	238.9	18.6
45	3272	0.6	17.7325	15.7	0.2999	16.4	0.0386	4.8	0.29	244.0	11.5	266.3	38.5	467.9	350.3	244.0	11.5
60	6364	0.6	20.8373	13.9	0.2553	14.2	0.0386	2.9	0.20	244.0	6.9	230.9	29.3	98.8	329.6	244.0	6.9
51	4307	0.8	23.1366	21.8	0.2304	22.6	0.0387	6.1	0.27	244.5	14.5	210.5	43.1	b.d.	b.d.	244.5	14.5
49	5871	0.4	22.8266	15.7	0.2341	16.1	0.0387	3.5	0.22	245.1	8.4	213.5	30.9	b.d.	b.d.	245.1	8.4
46	9022	0.8	22.7107	24.4	0.2355	24.8	0.0388	4.4	0.18	245.3	10.5	214.7	48.0	b.d.	b.d.	245.3	10.5
189	33147	1.6	20.1916	5.5	0.2651	5.6	0.0388	1.3	0.22	245.6	3.0	238.8	11.9	172.8	127.8	245.6	3.0
65	9221	0.9	21.5111	12.8	0.2509	13.4	0.0391	4.0	0.30	247.5	9.7	227.3	27.3	23.0	308.0	247.5	9.7
322	37617	5.0	19.5516	2.0	0.2766	3.8	0.0392	3.2	0.85	248.0	7.8	248.0	8.3	247.4	46.1	248.0	7.8
54	6297	0.7	21.5977	31.1	0.2504	31.4	0.0392	4.9	0.15	248.0	11.8	226.9	64.0	13.3	762.6	248.0	11.8
71	19770	1.0	20.9365	11.2	0.2583	11.8	0.0392	3.7	0.31	248.0	9.0	233.3	24.6	87.6	266.4	248.0	9.0
54	3542	1.0	21.2905	15.0	0.2557	15.3	0.0395	2.7	0.18	249.7	6.6	231.2	31.6	47.7	360.8	249.7	6.6
34	6181	0.9	19.9400	26.4	0.2743	27.4	0.0397	7.3	0.27	250.8	18.1	246.2	60.1	202.0	623.3	250.8	18.1
53	7033	0.8	22.7808	15.3	0.2404	15.4	0.0397	1.9	0.12	251.1	4.7	218.8	30.4	b.d.	b.d.	251.1	4.7
59	8545	0.6	19.1857	11.6	0.2892	12.5	0.0402	4.6	0.37	254.3	11.4	257.9	28.5	290.7	266.5	254.3	11.4
29	35612	0.4	11.4142	3.2	2.9144	3.6	0.2413	1.5	0.43	1393.3	19.4	1385.6	27.0	1373.9	61.8	1373.9	61.8
287	122911	9.0	11.3179	0.5	2.8332	1.5	0.2326	1.5	0.95	1347.9	17.7	1364.4	11.5	1390.2	9.2	1390.2	9.2
104	80057	32.6	11.2930	1.2	2.4796	3.4	0.2031	3.2	0.94	1191.9	34.3	1266.1	24.4	1394.4	22.7	1394.4	22.7
179	214236	0.4	11.2806	0.9	2.9466	3.5	0.2411	3.4	0.97	1392.3	42.0	1394.0	26.3	1396.5	17.3	1396.5	17.3
130	204767	0.5	11.2737	0.9	2.6624	1.7	0.2177	1.4	0.83	1269.7	16.0	1318.1	12.4	1397.7	18.1	1397.7	18.1
128	95153	0.7	11.2235	0.8	2.6860	1.2	0.2186	0.9	0.75	1274.7	10.2	1324.6	8.7	1406.3	14.8	1406.3	14.8
127	95323	0.3	11.2195	0.6	2.8178	1.1	0.2293	1.0	0.87	1330.8	11.9	1360.3	8.5	1407.0	10.7	1407.0	10.7
~~64~~	~~16501~~	~~0.6~~	~~11.2150~~	~~7.8~~	~~0.8605~~	~~8.9~~	~~0.0700~~	~~4.2~~	~~0.47~~	~~436.1~~	~~17.6~~	~~630.4~~	~~41.6~~	~~1407.7~~	~~149.9~~	~~1407.7~~	~~149.9~~
188	151387	1.8	10.4719	0.5	3.1951	1.7	0.2427	1.6	0.95	1400.5	20.1	1456.0	13.0	1537.8	9.8	1537.8	9.8
472	530844	11.6	10.3138	0.4	3.0953	2.9	0.2315	2.8	0.99	1342.6	34.3	1431.5	21.9	1566.4	7.4	1566.4	7.4
167	248955	1.7	10.2934	0.4	3.0084	1.6	0.2246	1.5	0.97	1306.1	18.1	1409.7	12.0	1570.1	6.6	1570.1	6.6
128	132396	0.6	10.2490	0.6	3.2406	2.6	0.2409	2.5	0.97	1391.3	31.0	1466.9	19.8	1578.2	11.6	1578.2	11.6
90	109098	2.8	10.1860	0.8	3.4888	5.6	0.2577	5.6	0.99	1478.3	73.5	1524.7	44.4	1589.7	15.1	1589.7	15.1
50	37046	1.1	10.1585	1.5	3.3038	3.5	0.2434	3.2	0.90	1404.4	40.3	1482.0	27.5	1594.8	28.0	1594.8	28.0
278	274834	6.1	10.0822	0.3	3.7077	1.8	0.2711	1.8	0.98	1546.5	24.9	1573.0	14.8	1608.8	6.4	1608.8	6.4
153	584616	1.4	9.9535	0.6	3.7570	4.3	0.2712	4.2	0.99	1547.0	58.4	1583.6	34.4	1632.7	11.8	1632.7	11.8
15	13005	1.1	9.8960	2.1	4.1393	2.7	0.2971	1.7	0.62	1676.9	24.6	1662.1	22.1	1643.5	39.6	1643.5	39.6
92	109022	1.4	9.8668	0.5	4.0597	1.5	0.2905	1.5	0.95	1644.1	21.3	1646.2	12.5	1649.0	8.6	1649.0	8.6
67	123602	0.6	9.7600	0.6	4.2266	0.8	0.2992	0.5	0.62	1687.3	7.6	1679.2	6.7	1669.1	11.8	1669.1	11.8
457	846191	2.7	9.7188	0.2	4.0846	1.1	0.2879	1.1	0.99	1631.1	15.2	1651.2	8.7	1677.0	3.0	1677.0	3.0
572	459060	5.8	9.7122	0.2	3.5200	1.8	0.2479	1.8	0.99	1427.9	22.9	1531.7	14.2	1678.2	3.4	1678.2	3.4
338	280499	1.2	9.5529	0.5	3.9306	6.4	0.2723	6.4	1.00	1552.6	88.7	1620.0	52.2	1708.7	9.4	1708.7	9.4
501	450726	9.5	9.5524	1.1	4.3414	4.5	0.3008	4.3	0.97	1695.1	64.5	1701.3	36.8	1708.8	19.8	1708.8	19.8
559	216106	2.4	9.5423	0.2	4.4464	1.8	0.3077	1.7	0.99	1729.5	26.4	1721.0	14.5	1710.7	3.7	1710.7	3.7
200	87050	1.6	9.4980	0.8	4.3819	2.2	0.3019	2.1	0.93	1700.5	30.7	1708.9	18.2	1719.3	14.3	1719.3	14.3
723	480004	13.0	9.4888	0.2	3.7937	1.0	0.2611	1.0	0.97	1495.3	13.4	1591.4	8.3	1721.1	4.4	1721.1	4.4
234	516109	2.3	9.4608	0.2	4.4612	0.7	0.3061	0.7	0.97	1721.5	10.6	1723.8	6.0	1726.5	3.0	1726.5	3.0
187	292363	1.8	9.3788	0.4	3.6125	2.5	0.2457	2.4	0.99	1416.4	31.0	1552.3	19.6	1742.5	7.1	1742.5	7.1
131	167780	1.4	9.3557	0.2	4.5266	1.7	0.3071	1.7	0.99	1726.6	25.3	1735.9	14.0	1747.0	3.6	1747.0	3.6
338	284747	1.3	9.2787	0.2	4.3127	1.9	0.2902	1.9	0.99	1642.7	27.7	1695.8	15.9	1762.1	4.3	1762.1	4.3
117	49718	1.7	9.2755	0.5	4.6735	0.8	0.3144	0.7	0.85	1762.3	11.1	1762.5	7.1	1762.7	8.2	1762.7	8.2
230	406868	1.4	6.8137	0.3	6.9192	1.5	0.3419	1.5	0.97	1895.9	24.3	2101.1	13.5	2308.5	5.8	2308.5	5.8
705	846589	3.3	6.3804	0.4	9.2513	0.9	0.4281	0.9	0.91	2297.2	16.6	2363.2	8.7	2420.7	6.8	2420.7	6.8

1 age manually rejected due to discordance.

Summary statistics for the 7 youngest ages:
Final age: 75.7 ± 0.8 Ma 1σ
MSWD = 0.36
Probability = 0.90

Sample KTC-14-dz10 n = 33

U (ppm)	$^{206}Pb/^{204}Pb$	U/Th	(%) $^{206}Pb^*/^{207}Pb^*$	± (1σ)	(%) $^{207}Pb^*/^{235}U^*$	± (1σ)	(%) $^{206}Pb^*/^{238}U^*$	± (1σ)	error corr.	Age (Ma) $^{206}Pb^*/^{238}U^*$	± (1σ)	Age (Ma) $^{207}Pb^*/^{235}U^*$	± (1σ)	Age (Ma) $^{207}Pb^*/^{206}Pb^*$	± (1σ)	Preferred age (Ma)	± (1σ)
325	10286	0.6	19.9344	12.8	0.0814	13.0	0.0118	2.6	0.20	75.4	1.9	79.4	9.9	202.6	297.1	75.4	1.9
216	11610	0.9	20.4381	18.3	0.0825	18.6	0.0122	3.4	0.18	78.4	2.6	80.5	14.4	144.4	433.3	78.4	2.6
85	3327	0.9	16.9823	25.7	0.1032	26.1	0.0127	4.9	0.19	81.4	4.0	99.7	24.8	562.8	567.5	81.4	4.0
116	4358	2.2	21.5959	20.5	0.0819	21.3	0.0128	5.7	0.27	82.2	4.7	80.0	16.4	13.5	498.4	82.2	4.7
97	4719	0.3	24.2473	34.5	0.0736	34.8	0.0129	4.2	0.12	82.9	3.4	72.1	24.2	b.d.	b.d.	82.9	3.4
349	36242	0.9	22.1899	12.3	0.0809	12.5	0.0130	2.3	0.19	83.4	1.9	79.0	9.5	b.d.	b.d.	83.4	1.9
128	24839	0.5	22.9691	9.1	0.1385	9.7	0.0231	3.5	0.36	147.1	5.1	131.7	12.0	b.d.	b.d.	147.1	5.1
218	17036	1.3	21.6196	6.8	0.1494	7.2	0.0234	2.4	0.33	149.3	3.5	141.4	9.5	10.9	162.9	149.3	3.5
34	3427	0.9	23.1014	37.1	0.1405	37.7	0.0235	6.7	0.18	150.0	9.9	133.5	47.2	b.d.	b.d.	150.0	9.9
191	13218	0.7	21.6287	6.1	0.1506	6.9	0.0236	3.2	0.47	150.5	4.8	142.4	9.1	9.9	146.4	150.5	4.8
213	17138	1.0	21.2063	6.5	0.1545	6.7	0.0238	1.5	0.22	151.4	2.2	145.8	9.1	57.1	155.4	151.4	2.2
274	83315	1.1	21.2957	7.1	0.1546	7.2	0.0239	1.4	0.20	152.2	2.1	146.0	9.8	47.1	169.3	152.2	2.1
339	28275	1.1	19.9954	4.6	0.1789	4.8	0.0260	1.1	0.22	165.2	1.7	167.1	7.3	195.6	107.8	165.2	1.7
1026	238621	1.6	20.3200	1.5	0.1839	1.9	0.0271	1.2	0.63	172.4	2.1	171.4	3.0	158.0	35.0	172.4	2.1
442	191132	1.5	19.5494	3.1	0.2581	3.3	0.0366	1.2	0.37	231.7	2.8	233.1	6.9	247.7	71.0	231.7	2.8
240	33049	0.9	19.6633	5.7	0.2582	5.8	0.0368	1.3	0.22	233.1	2.9	233.2	12.1	234.3	131.0	233.1	2.9
832	104648	4.9	19.7747	1.2	0.2583	2.4	0.0370	2.0	0.85	234.5	4.6	233.3	4.9	221.2	28.3	234.5	4.6
833	81555	1.2	19.7294	1.1	0.2594	1.5	0.0371	1.0	0.71	235.0	2.4	234.2	3.1	226.6	24.3	235.0	2.4
317	195420	4.0	11.1384	0.2	2.9569	1.7	0.2389	1.6	0.99	1380.8	20.5	1396.6	12.6	1420.8	4.7	1420.8	4.7
46	33983	0.5	11.0960	1.4	2.9789	2.0	0.2397	1.4	0.70	1385.3	17.4	1402.3	15.1	1428.1	27.1	1428.1	27.1
205	220859	1.7	9.8515	0.7	4.0666	2.2	0.2906	2.1	0.95	1644.3	30.8	1647.6	18.2	1651.8	12.6	1651.8	12.6
51	15351	1.0	9.8149	2.2	4.0729	3.6	0.2899	2.9	0.81	1641.2	42.6	1648.9	29.8	1658.7	40.0	1658.7	40.0
111	280484	1.5	9.6808	0.3	4.3325	1.1	0.3042	1.0	0.96	1712.1	15.7	1699.6	8.9	1684.2	5.3	1684.2	5.3
118	125493	1.2	9.6305	0.7	4.2319	3.9	0.2956	3.8	0.98	1669.4	56.0	1680.2	31.8	1693.8	13.0	1693.8	13.0
368	483938	3.2	9.5651	0.2	4.3708	0.6	0.3032	0.6	0.96	1707.2	8.7	1706.8	4.9	1706.3	2.9	1706.3	2.9
489	500248	13.1	9.5494	0.2	4.3682	1.4	0.3025	1.3	0.98	1703.9	20.1	1706.3	11.3	1709.4	4.4	1709.4	4.4
161	242223	1.9	9.5391	0.5	4.4027	0.9	0.3046	0.8	0.87	1714.1	11.9	1712.9	7.5	1711.3	8.3	1711.3	8.3
962	148649	7.4	9.5162	0.1	4.4332	1.1	0.3060	1.1	0.99	1720.9	16.2	1718.6	8.9	1715.8	2.0	1715.8	2.0
94	144238	2.1	9.4807	0.9	4.4010	1.3	0.3026	1.0	0.72	1704.3	14.3	1712.5	11.0	1722.6	17.1	1722.6	17.1
757	969641	25.6	9.4574	0.8	4.5509	1.4	0.3122	1.2	0.83	1751.3	18.2	1740.3	12.0	1727.1	14.9	1727.1	14.9
244	168408	1.0	9.4269	0.4	4.4267	1.4	0.3027	1.4	0.97	1704.5	20.5	1717.4	11.7	1733.1	6.7	1733.1	6.7
156	147546	1.9	9.3940	0.4	4.5913	1.6	0.3128	1.6	0.97	1754.5	24.3	1747.7	13.6	1739.5	7.6	1739.5	7.6
414	332187	2.4	9.1748	0.3	4.7772	2.1	0.3179	2.0	0.99	1779.4	31.7	1780.9	17.3	1782.6	4.9	1782.6	4.9

decay constants and composition used: $\lambda_{235} = 9.8485 \cdot 10^{-10}$ a^{-1}, λ_{238}: $1.55125 \cdot 10^{-10}$ a^{-1}, $^{238}U/^{235}U = 137.88$.

Analyses with >10% uncertainty (1σ) in $^{206}Pb/^{238}U$ age are not included.

Analyses with >10% uncertainty (1σ) in $^{207}Pb/^{206}Pb$ age are not included, unless $^{206}Pb/^{238}U$ age is <500 Ma.

Preferred age is $^{206}Pb/^{238}U$ age for analyses with $^{206}Pb/^{238}U$ age <1000 Ma and $^{207}Pb/^{206}Pb$ age for analyses with $^{206}Pb/^{238}U$age > 1000 Ma.

Analyses with $^{206}Pb/^{238}U$ age > 600 Ma and with >20% discordance (<80% concordance) are not included.

Analyses with $^{206}Pb/^{238}U$ age > 600 Ma and with >5% reverse discordance (>105% concordance) are not included.

All uncertainties are reported at the 1σ level, and include only measurement errors.

Systematic errors are as follows (at 1σ level): [1.3% ($^{206}Pb/^{238}U$) & 0.7% ($^{207}Pb/^{206}Pb$)]

Analyses conducted by LA-MC-ICPMS, as described by Gehrels et al. (2008).

U concentration and U/Th are calibrated relative to Sri Lanka zircon reference and are accurate to ~20%.

Common Pb correction is from measured ^{204}Pb with common Pb composition interpreted from Stacey and Kramers (1975).

Common Pb composition assigned uncertainties of 1.5 for $^{206}Pb/^{204}Pb$, 0.3 for $^{207}Pb/^{204}Pb$, and 2.0 for $^{208}Pb/^{204}Pb$.

U/Pb and $^{207}Pb/^{206}Pb$ fractionation is calibrated relative to fragments of a large Sri Lanka zircon of 563.5 ± 1.6 Ma (1σ).

b.d. = below detection: Pb levels insufficient to determine $^{207}Pb/^{206}Pb$ age

*Data of J.F. Hoyt, part of dataset published in Ingersoll et al., 2013. Sample preparation and analysis performed in same manner as in this study.

APPENDIX C: IGNEOUS-ZIRCON DATA

Analysis Number	UO^+/ U^+	$^{94}Zr_2O^+$ (cps)	U (ppm)	Th (ppm)	(%) Radiogenic ^{206}Pb	$^{206}Pb^*/^{238}U$	± (1σ)	$^{207}Pb^*/^{235}U$	± (1σ)	$^{207}Pb^*/^{206}Pb^*$	± (1σ)	correlation of concordia ellipses
2014_08_08Aug\ and3_IZM@10.ais	8.82	1930	273	88.4	100	0.00372	0.000224	0.0304	0.00234	0.0594	0.00360	0.633
2014_08_08Aug\ and3_IZM@2.ais	8.59	1870	155	64.6	99.7	0.0352	0.00248	0.250	0.0241	0.0515	0.00247	0.882
2014_08_08Aug\ and3_IZM@3.ais	8.60	1780	35.8	26.6	99.9	0.194	0.0190	2.17	0.243	0.0812	0.00308	0.944
2014_08_08Aug\ and3_IZM@4.ais	8.58	1740	98.6	53.3	99.8	0.196	0.0183	2.12	0.207	0.0784	0.00155	0.980
2014_08_08Aug\ and3_IZM@5.ais	8.82	2030	189	113	99.9	0.0336	0.00174	0.233	0.0142	0.0503	0.00161	0.853
2014_08_08Aug\ and3_IZM@6.ais	8.85	2040	270	93.8	99.0	0.00372	0.000228	0.0225	0.00420	0.0438	0.00726	0.490
2014_08_08Aug\ and3_IZM@7.ais	8.49	1920	30.5	18.6	99.8	0.220	0.0227	2.45	0.270	0.0806	0.00235	0.965
2014_08_08Aug\ and3_IZM@8.ais	8.74	1910	91.6	107	99.8	0.187	0.0136	2.07	0.147	0.0803	0.000967	0.986
2014_08_08Aug\ and3_IZM@9.ais	8.73	1950	23.8	10.2	99.8	0.190	0.0189	2.12	0.194	0.0809	0.00230	0.959
2014_08_08Aug\ and4_IZM@1.ais	8.82	2060	861	382	99.9	0.276	0.0127	3.91	0.179	0.103	0.000403	0.996
2014_08_08Aug\ and4_IZM@10.ais	8.79	1960	199	88.8	99.7	0.263	0.0182	3.66	0.256	0.101	0.000765	0.994
2014_08_08Aug\ and4_IZM@11.ais	8.92	2070	257	86.9	99.9	0.237	0.0110	3.22	0.149	0.0985	0.000836	0.983
2014_08_08Aug\ and4_IZM@12.ais	8.66	2020	159	184	99.7	0.0253	0.00165	0.163	0.0142	0.0466	0.00257	0.775
2014_08_08Aug\ and4_IZM@13.ais	9.02	2080	93.6	43.0	99.6	0.169	0.00892	1.83	0.104	0.0786	0.00148	0.943
2014_08_08Aug\ and4_IZM@14.ais	8.95	2010	32.6	17.2	100	0.170	0.0147	1.82	0.174	0.0777	0.00198	0.966
2014_08_08Aug\ and4_IZM@15.ais	8.73	2050	94.7	75.5	99.8	0.192	0.0136	2.15	0.155	0.0810	0.00117	0.980
2014_08_08Aug\ and4_IZM@16.ais	8.71	2010	106	67.9	99.8	0.203	0.0131	2.21	0.150	0.0791	0.00116	0.977
2014_08_08Aug\ and4_IZM@17.ais*	9.21	1970	111	29.5	99.4	0.144	0.0102	1.52	0.0992	0.0765	0.00148	0.963
2014_08_08Aug\ and4_IZM@18.ais	8.70	2060	53.3	29.2	99.9	0.197	0.0173	2.15	0.234	0.0790	0.00229	0.980
2014_08_08Aug\ and4_IZM@19.ais	8.85	1980	218	90.1	99.6	0.266	0.0143	3.67	0.197	0.100	0.000786	0.989
2014_08_08Aug\ and4_IZM@2.ais	8.46	1870	164	96.5	99.8	0.221	0.0149	2.48	0.172	0.0813	0.00118	0.978
2014_08_08Aug\ and4_IZM@20.ais	8.59	2050	21.1	12.0	100	0.209	0.0249	2.46	0.287	0.0852	0.00264	0.966
2014_08_08Aug\ and4_IZM@22.ais*	9.39	1590	552	165	99.2	0.00278	0.000112	0.0160	0.00211	0.0417	0.00505	0.406
2014_08_08Aug\ and4_IZM@3.ais	8.60	1940	891	20.4	99.9	0.301	0.0170	4.27	0.245	0.103	0.000516	0.996
2014_08_08Aug\ and4_IZM@4.ais	8.73	2010	613	1160	99.9	0.0231	0.00124	0.156	0.0101	0.0491	0.00140	0.900
2014_08_08Aug\ and4_IZM@5.ais	8.64	2020	575	198	99.8	0.0371	0.00211	0.249	0.0156	0.0487	0.00132	0.902
2014_08_08Aug\ and4_IZM@6.ais	8.70	2030	509	164	99.9	0.299	0.0159	4.39	0.230	0.107	0.000402	0.998
2014_08_08Aug\ and4_IZM@7.ais	8.70	2070	108	35.5	97.2	0.00415	0.000347	0.0263	0.0111	0.0460	0.0182	0.399
2014_08_08Aug\ and4_IZM@8.ais	8.79	2070	239	193	99.9	0.279	0.0168	4.02	0.236	0.104	0.000868	0.990
2014_08_08Aug\ and4_IZM@9.ais	8.70	2030	183	102	99.8	0.199	0.0131	2.17	0.144	0.0794	0.000911	0.985
2014_08_08Aug\ gd7_IZM@1.ais	8.81	1970	199	61.7	99.3	0.01000	0.000587	0.0682	0.00893	0.0495	0.00490	0.700
2014_08_08Aug\ gd7_IZM@10.ais	8.73	2110	333	166	99.9	0.0247	0.00141	0.165	0.0102	0.0484	0.00171	0.826
2014_08_08Aug\ gd7_IZM@11.ais	8.75	2090	382	75.0	99.4	0.0104	0.000555	0.0683	0.00585	0.0476	0.00312	0.646
2014_08_08Aug\ gd7_IZM@12.ais	8.62	2030	76.0	43.2	96.8	0.0114	0.000769	0.0604	0.0251	0.0383	0.0151	0.368
2014_08_08Aug\ gd7_IZM@13.ais	8.74	2050	580	565	99.9	0.0295	0.00153	0.208	0.0116	0.0510	0.00108	0.925
2014_08_08Aug\ gd7_IZM@14.ais	8.61	2000	1360	1450	99.9	0.0245	0.00129	0.170	0.00958	0.0504	0.000792	0.961

2014_08_08Aug\ gd7_IZM@15.ais	8.69	2080	657	314	99.8	0.0254	0.00136	0.174	0.0104	0.0498	0.00128	0.901
2014_08_08Aug\ gd7_IZM@2.ais	8.68	2010	653	328	99.9	0.0252	0.00151	0.168	0.0101	0.0482	0.00101	0.939
2014_08_08Aug\ gd7_IZM@3.ais	8.37	1960	121	101	98.9	0.0139	0.00133	0.0947	0.0172	0.0494	0.00708	0.619
2014_08_08Aug\ gd7_IZM@4.ais	8.70	1920	1680	503	99.8	0.0243	0.00118	0.164	0.00860	0.0490	0.000777	0.954
2014_08_08Aug\ gd7_IZM@5.ais*	9.35	1910	1690	669	99.8	0.00834	0.000272	0.0538	0.00247	0.0468	0.00134	0.785
2014_08_08Aug\ gd7_IZM@6.ais	8.64	1920	2690	1200	99.9	0.0125	0.000627	0.0820	0.00429	0.0475	0.000817	0.945
2014_08_08Aug\ gd7_IZM@7.ais	8.70	2050	750	38.1	99.5	0.0105	0.000557	0.0644	0.00467	0.0444	0.00224	0.718
2014_08_08Aug\ gd7_IZM@8.ais	8.69	2050	229	140	99.5	0.0108	0.000744	0.0704	0.00828	0.0473	0.00395	0.716
2014_08_08Aug\ gd7_IZM@9.ais	8.67	2110	961	73.2	100.0	0.293	0.0149	4.26	0.222	0.105	0.000431	0.997
2014_08_08Aug\ gr_big_IZM@1.ais	8.73	2000	247	473	99.9	0.0222	0.00116	0.153	0.00995	0.0499	0.00189	0.815
2014_08_08Aug\ gr_big_IZM@10.ais	8.64	2090	372	85.3	100.0	0.240	0.0165	2.95	0.202	0.0891	0.000727	0.993
2014_08_08Aug\ gr_big_IZM@11.ais	8.93	2090	81.9	116	100	0.0205	0.00175	0.149	0.0182	0.0527	0.00250	0.957
2014_08_08Aug\ gr_big_IZM@12.ais	8.61	2010	2510	351	100.0	0.308	0.0167	4.37	0.238	0.103	0.000241	0.999
2014_08_08Aug\ gr_big_IZM@13.ais	8.80	1970	262	113	100.0	0.274	0.0152	4.06	0.224	0.107	0.000551	0.996
2014_08_08Aug\ gr_big_IZM@14.ais	8.63	2110	906	63.4	100.0	0.301	0.0160	4.38	0.231	0.106	0.000396	0.998
2014_08_08Aug\ gr_big_IZM@15.ais	8.64	2020	1290	34.9	100.0	0.265	0.0140	3.69	0.197	0.101	0.000362	0.998
2014_08_08Aug\ gr_big_IZM@2.ais	8.75	1990	366	116	100.0	0.268	0.0134	3.85	0.188	0.104	0.000698	0.991
2014_08_08Aug\ gr_big_IZM@3.ais	8.77	2090	320	695	99.9	0.0225	0.00116	0.152	0.00814	0.0492	0.00180	0.759
2014_08_08Aug\ gr_big_IZM@4.ais	8.90	1990	4530	581	99.5	0.130	0.00560	1.70	0.0727	0.0950	0.000357	0.996
2014_08_08Aug\ gr_big_IZM@5.ais	8.60	2040	309	749	99.3	0.0243	0.00151	0.168	0.0124	0.0503	0.00277	0.684
2014_08_08Aug\ gr_big_IZM@6.ais	8.75	2090	893	725	99.9	0.0233	0.00118	0.158	0.00831	0.0490	0.000883	0.940
2014_08_08Aug\ gr_big_IZM@7.ais	8.96	2100	142	149	100.0	0.201	0.0117	2.44	0.146	0.0882	0.000763	0.990
2014_08_08Aug\ gr_big_IZM@8.ais	8.53	2030	183	71.9	99.4	0.0254	0.00173	0.164	0.0163	0.0468	0.00315	0.740
2014_08_08Aug\ gr_big_IZM@9.ais	8.59	2130	325	33.8	100.0	0.194	0.0118	2.47	0.151	0.0924	0.000805	0.990

Analysis Number	Age (Ma) $^{206}Pb/^{238}U$	± (1σ)	Age (Ma) $^{207}Pb/^{235}U$	± (1σ)	Age (Ma) $^{207}Pb/^{206}Pb$	± (1σ)	Preferred age (Ma)	± (1σ)
2014_08_08Aug\ and3_IZM@10.ais	23.9	1.44	30.5	2.30	582	132	23.9	1.44
2014_08_08Aug\ and3_IZM@2.ais	223	15.4	226	19.6	263	110	223	15.4
2014_08_08Aug\ and3_IZM@3.ais	1140	103	1170	77.9	1230	74.4	1230	74.4
2014_08_08Aug\ and3_IZM@4.ais	1150	98.7	1150	67.4	1160	39.1	1160	39.1
2014_08_08Aug\ and3_IZM@5.ais	213	10.9	212	11.7	208	74.1	213	10.9
2014_08_08Aug\ and3_IZM@6.ais	23.9	1.46	22.5	4.17	b.d.	b.d.	23.9	1.46
2014_08_08Aug\ and3_IZM@7.ais	1280	120	1260	79.6	1210	57.4	1210	57.4
2014_08_08Aug\ and3_IZM@8.ais	1100	73.6	1140	48.8	1200	23.7	1200	23.7
2014_08_08Aug\ and3_IZM@9.ais	1120	102	1160	63.2	1220	55.8	1220	55.8
2014_08_08Aug\ and4_IZM@1.ais	1570	64.3	1620	37.0	1680	7.24	1680	7.24
2014_08_08Aug\ and4_IZM@10.ais	1510	92.9	1560	55.8	1640	14.1	1640	14.1
2014_08_08Aug\ and4_IZM@11.ais	1370	57.3	1460	35.8	1600	15.8	1600	15.8
2014_08_08Aug\ and4_IZM@12.ais	161	10.4	153	12.4	29.2	132	161	10.4
2014_08_08Aug\ and4_IZM@13.ais	1010	49.2	1060	37.2	1160	37.4	1160	37.4
2014_08_08Aug\ and4_IZM@14.ais	1010	81.0	1050	62.6	1140	50.6	1140	50.6
2014_08_08Aug\ and4_IZM@15.ais	1130	73.5	1160	49.9	1220	28.4	1220	28.4
2014_08_08Aug\ and4_IZM@16.ais	1190	70.4	1190	47.6	1170	28.9	1170	28.9
2014_08_08Aug\ and4_IZM@17.ais*	867	57.5	937	40.0	1110	38.6	867	57.5
2014_08_08Aug\ and4_IZM@18.ais	1160	93.0	1170	75.4	1170	57.4	1170	57.4
2014_08_08Aug\ and4_IZM@19.ais	1520	73.0	1570	42.9	1630	14.6	1630	14.6
2014_08_08Aug\ and4_IZM@2.ais	1290	78.4	1270	50.1	1230	28.6	1230	28.6
2014_08_08Aug\ and4_IZM@20.ais	1230	133	1260	84.3	1320	60.1	1320	60.1
2014_08_08Aug\ and4_IZM@22.ais*	17.9	0.722	16.1	2.11	b.d.	b.d.	17.9	0.722
2014_08_08Aug\ and4_IZM@3.ais	1700	84.0	1690	47.3	1680	9.26	1680	9.26
2014_08_08Aug\ and4_IZM@4.ais	147	7.83	147	8.86	154	66.7	147	7.83
2014_08_08Aug\ and4_IZM@5.ais	235	13.1	226	12.7	132	63.6	235	13.1
2014_08_08Aug\ and4_IZM@6.ais	1690	78.9	1710	43.4	1740	6.92	1740	6.92
2014_08_08Aug\ and4_IZM@7.ais	26.7	2.23	26.3	11.0	b.d.	b.d.	26.7	2.23
2014_08_08Aug\ and4_IZM@8.ais	1590	84.5	1640	47.7	1700	15.3	1700	15.3
2014_08_08Aug\ and4_IZM@9.ais	1170	70.7	1170	46.2	1180	22.7	1180	22.7
2014_08_08Aug\ gd7_IZM@1.ais	64.1	3.75	67.0	8.49	170	231	64.1	3.75
2014_08_08Aug\ gd7_IZM@10.ais	157	8.88	155	8.89	121	83.4	157	8.88
2014_08_08Aug\ gd7_IZM@11.ais	66.7	3.54	67.0	5.56	80.2	155	66.7	3.54
2014_08_08Aug\ gd7_IZM@12.ais	73.4	4.90	59.6	24.0	b.d.	b.d.	73.4	4.90
2014_08_08Aug\ gd7_IZM@13.ais	187	9.56	192	9.78	243	48.9	187	9.56
2014_08_08Aug\ gd7_IZM@14.ais	156	8.13	159	8.31	211	36.5	156	8.13

2014_08_08Aug\ gd7_IZM@15.ais	162	8.56	163	8.98	184	60.1	162	8.56
2014_08_08Aug\ gd7_IZM@2.ais	161	9.47	157	8.80	108	49.4	161	9.47
2014_08_08Aug\ gd7_IZM@3.ais	89.1	8.45	91.9	15.9	165	335	89.1	8.45
2014_08_08Aug\ gd7_IZM@4.ais	155	7.41	154	7.50	148	37.2	155	7.41
2014_08_08Aug\ gd7_IZM@5.ais*	53.5	1.74	53.2	2.38	37.7	68.8	53.5	1.74
2014_08_08Aug\ gd7_IZM@6.ais	80.1	3.99	80.0	4.03	76.7	40.9	80.1	3.99
2014_08_08Aug\ gd7_IZM@7.ais	67.4	3.55	63.4	4.45	b.d.	b.d.	67.4	3.55
2014_08_08Aug\ gd7_IZM@8.ais	69.3	4.75	69.1	7.86	63.7	199	69.3	4.75
2014_08_08Aug\ gd7_IZM@9.ais	1660	74.4	1690	42.9	1720	7.51	1720	7.51
2014_08_08Aug\ gr_big_IZM@1.ais	141	7.34	144	8.76	192	88.0	141	7.34
2014_08_08Aug\ gr_big_IZM@10.ais	1390	85.8	1400	52.0	1410	15.6	1410	15.6
2014_08_08Aug\ gr_big_IZM@11.ais	131	11.0	141	16.0	315	108	131	11.0
2014_08_08Aug\ gr_big_IZM@12.ais	1730	82.5	1710	45.0	1680	4.31	1680	4.31
2014_08_08Aug\ gr_big_IZM@13.ais	1560	77.0	1650	45.0	1760	9.39	1760	9.39
2014_08_08Aug\ gr_big_IZM@14.ais	1690	79.4	1710	43.7	1730	6.87	1730	6.87
2014_08_08Aug\ gr_big_IZM@15.ais	1520	71.3	1570	42.7	1640	6.65	1640	6.65
2014_08_08Aug\ gr_big_IZM@2.ais	1530	68.2	1600	39.4	1700	12.3	1700	12.3
2014_08_08Aug\ gr_big_IZM@3.ais	143	7.31	144	7.17	157	85.4	143	7.31
2014_08_08Aug\ gr_big_IZM@4.ais	788	31.9	1010	27.3	1530	7.08	788	31.9
2014_08_08Aug\ gr_big_IZM@5.ais	155	9.49	158	10.8	209	128	155	9.49
2014_08_08Aug\ gr_big_IZM@6.ais	149	7.46	149	7.29	145	42.3	149	7.46
2014_08_08Aug\ gr_big_IZM@7.ais	1180	62.6	1260	43.1	1390	16.6	1390	16.6
2014_08_08Aug\ gr_big_IZM@8.ais	162	10.9	154	14.3	40.2	161	162	10.9
2014_08_08Aug\ gr_big_IZM@9.ais	1140	63.6	1260	44.1	1480	16.5	1480	16.5

Summary statistics for the youngest ages of each sample:

Samples KTC-13-and3 and KTC-14-and4 combined (n = 3); interpreted as magmatic age:
Final age: 24.4 ± 0.9 Ma 1σ
MSWD = 0.65
Probability = 0.52

Sample KTC-14-gr-big (n = 6); interpreted as magmatic age:
Final age: 146 ± 3 Ma 1σ
MSWD = 1.14
Probability = 0.34

Sample KTC-14-gd7 (n = 5); interpreted as a xenocrystic population (magmatic age established as ~26 Ma by prior studies; see text for discussion and references):
Final age: 67.5 ± 1.8 Ma 1σ
MSWD = 0.62
Probability = 0.65

decay constants used: λ_{232}: $4.9475 \cdot 10^{-11}$ a^{-1}; λ_{238}: $1.55125 \cdot 10^{-10}$ a^{-1}

Preferred age is $^{206}Pb/^{238}U$ age for analyses with $^{206}Pb/^{238}U$ age <1000 Ma and $^{207}Pb/^{206}Pb$ age for analyses with $^{206}Pb/^{238}U$age > 1000 Ma.

all analyses against zircon reference 91500 ($^{206}Pb/^{238}U$ age = 1065 Ma) and AS3 ($^{206}Pb/^{238}U$ age = 1099 Ma)

U calculated from $UO^+/^{94}Zr_2O^+$ relative sensitivity determined on zircon reference 91500 (81.2 ppm U)

common Pb composition: $^{206}Pb/^{204}Pb = 18.86$, $^{207}Pb/^{204}Pb = 15.62$

U/Zr relative sensitivity factor: $5.73 \cdot 10^{-3}$

Th/U relative sensitivity factor: 0.907

Pb/U Calibration: Slope: 0.2115947; Intercept: 7.297308

analyses typically 10 cycles

17 analyses of zircon reference AS3 performed; relative error 0.013 1σ (n = 17)

b.d. = below detection: Pb levels insufficient to determine $^{207}Pb/^{206}Pb$ age

*UO^+/U^+ value well outside calibration range; analysis excluded from Fig. 10 and summary statistics.

APPENDIX D: RAW AND CORRECTED PALEOCURRENT DATA

Location: KTC-12-Tpc1
Mean paleocurrent direction: 172.0 ± 75.7 1σ
n = 10
Regional bedding: 144, 34W

Imbrications:	**Imbrication (uncorrected)**			**Imbrication (corrected)**			**Paleocurrent**
Measurement #	Strike	Dip	Dip Quad	Strike	Dip	Dip Quad	Trend
1	219	42	W	256.8	44.5	N	166.8
2	205	55	W	233.3	45.8	N	143.3
3	218	61	W	238.8	57.5	N	148.8
4	221	44	W	255.9	46.9	N	165.9
5	213	29	W	271.3	34.7	N	181.3
6	191	52	W	224.0	35.8	W	134.0
7	334	66	E	153.3	80.5	W	63.3
8	109	2	S	326.1	32.4	E	236.1
9	39	67	E	28.9	79.0	E	298.9
10	90	34	S	31.1	29.4	E	301.1

Location: KTC-13-Tprc9
Mean paleocurrent direction: 299.6 ± 26.3 1σ
n = 10
Regional bedding: 135, 44W

Imbrications:	**Imbrication (uncorrected)**			**Imbrication (corrected)**			**Paleocurrent**
Measurement #	Strike	Dip	Dip Quad	Strike	Dip	Dip Quad	Trend
1	118	43	S	34.0	11.7	E	304.0
2	84	67	S	56.5	46.9	S	326.5
3	70	62	S	40.9	53.4	E	310.9
4	66	57	S	33.3	53.1	E	303.3
5	125	29	S	332.7	16.1	E	242.7
6	45	32	S	357.0	52.4	E	267.0
7	68	58	S	35.6	52.3	E	305.6
8	95	55	S	50.7	32.0	S	320.7
9	115	39	S	17.0	14.1	E	287.0
10	77	66	S	49.8	51.0	S	319.8

Location: KTC-13-Tprc13*
Mean paleocurrent direction: 28.9 ± 37.9 1σ
n = 10
Regional bedding: 292, 79N (overturned)

Imbrications:	**Imbrication (uncorrected)**			**Imbrication (corrected)**			**Paleocurrent**
Measurement #	Strike	Dip	Dip Quad	Strike	Dip	Dip Quad	Trend
1	22	41	E	153.5	81.7	W	63.5
2	289	53	N	106.6	26.1	S	16.6
3	4	44	E	156.8	69.6	W	66.8
4	209	52	W	58.8	77.8	S	328.8
5	21	44	E	156.6	81.4	W	66.6
6	331	24	E	129.0	61.0	S	39.0
7	13	40	E	152.9	75.8	W	62.9
8	175	23	W	91.6	89.9	S	1.6
9	204	47	W	64.3	81.1	S	334.3
10	289	38	N	109.2	41.1	S	19.2

Location: KTC-13-Tprc17
Mean paleocurrent direction: 124.1 ± 20.7 1σ
n = 10
Regional bedding: 325, 71E (overturned)

Imbrications:	**Imbrication (uncorrected)**			**Imbrication (corrected)**			**Paleocurrent**
Measurement #	Strike	Dip	Dip Quad	Strike	Dip	Dip Quad	Trend
1	344	76	E	247.5	18.9	N	157.5
2	0	54	E	198.8	35.1	W	108.8
3	28	65	E	216.8	58.2	W	126.8
4	9	54	E	201.9	42.1	W	111.9
5	351	63	E	211.7	25.2	W	121.7
6	19	65	E	217.9	50.1	W	127.9
7	4	84	E	248.7	40.1	N	158.7
8	11	54	E	202.4	43.7	W	112.4
9	354	64	E	215.0	27.6	W	125.0
10	2	42	E	182.3	41.6	W	92.3

Location: KTC-13-Tprc26
Mean paleocurrent direction: 234.4 ± 50.8 1σ
n = 10
Regional bedding: 119, 66S

Imbrications:	**Imbrication (uncorrected)**			**Imbrication (corrected)**			**Paleocurrent**
Measurement #	Strike	Dip	Dip Quad	Strike	Dip	Dip Quad	Trend
1	119	49	S	299.0	17.0	N	209.0
2	74	51	S	356.4	40.7	E	266.4
3	84	54	S	-359.0	32.4	E	269.0
4	14	16	E	315.4	71.0	E	225.4
5	149	75	W	196.9	29.6	W	106.9
6	359	35	E	328.9	85.9	E	238.9
7	195	23	W	273.7	62.6	N	183.7
8	61	52	S	358.6	50.8	E	268.6
9	109	55	S	335.0	14.0	E	245.0
10	109	56	S	337.8	13.3	E	247.8

Location: KTC-14-Np2
Mean paleocurrent direction: 86.2 ± 91.9 1σ
n = 10
Regional bedding: 96, 74S

Imbrications:	**Imbrication (uncorrected)**			**Imbrication (corrected)**			**Paleocurrent**
Measurement #	Strike	Dip	Dip Quad	Strike	Dip	Dip Quad	Trend
1	134	55	S	222.5	38.9	W	132.5
2	95	54	S	278.4	20.0	N	188.4
3	76	70	S	351.1	19.4	E	261.1
4	126	67	S	204.7	29.1	W	114.7
5	130	82	S	176.5	34.2	W	86.5
6	109	76	S	178.7	12.7	W	88.7
7	300	87	N	149.4	30.4	W	59.4
8	66	90	S	31.5	33.6	E	301.5
9	92	85	S	75.9	11.7	S	345.9
10	114	84	S	158.5	20.3	W	68.5

Location: KTC-14-Nprc47
Mean paleocurrent direction: 337.7 ± 98.4 1σ
n = 10
Regional bedding: 115, 57S

Imbrications:	**Imbrication (uncorrected)**			**Imbrication (corrected)**			**Paleocurrent**
Measurement #	Strike	Dip	Dip Quad	Strike	Dip	Dip Quad	Trend
1	100	46	S	337.4	16.0	E	337.4
2	112	64	S	93.8	7.5	S	93.8
3	156	61	W	209.7	35.2	W	209.7
4	154	36	W	254.3	34.5	N	254.3
5	355	57	E	161.7	86.8	W	161.7
6	56	27	S	327.1	47.0	E	327.1
7	38	44	E	347.6	58.5	E	347.6
8	65	37	S	340.1	40.6	E	340.1
9	29	51	E	352.3	67.2	E	352.3
10	115	64	S	115.0	7.0	S	115

Location: KTC-14-Nprc48
Mean paleocurrent direction: 159.7 ± 40.9 1σ
n = 10
Regional bedding: 120, 60S

Imbrications:	**Imbrication (uncorrected)**			**Imbrication (corrected)**			**Paleocurrent**
Measurement #	Strike	Dip	Dip Quad	Strike	Dip	Dip Quad	Trend
1	171	71	W	208.8	47.3	W	118.8
2	184	46	W	244.5	51.7	N	154.5
3	180	47	W	242.8	48.9	N	152.8
4	154	37	W	262.7	33.8	N	172.7
5	179	35	W	258.8	48.3	N	168.8
6	181	40	W	252.1	49.2	N	162.1
7	190	67	W	221.8	62.1	W	131.8
8	174	40	W	252.4	44.7	N	162.4
9	220	55	W	245.1	80.6	N	155.1
10	77	49	S	0.4	36.3	E	270.4

Location: KTC-14-Nprc51
Mean paleocurrent direction: 275.0 ± 50.0 1σ
n = 10
Regional bedding: 120, 56S

Imbrications:	**Imbrication (uncorrected)**			**Imbrication (corrected)**			**Paleocurrent**
Measurement #	Strike	Dip	Dip Quad	Strike	Dip	Dip Quad	Trend
1	60	54	S	0.7	53.5	E	270.7
2	97	53	S	347.8	24.9	E	257.8
3	204	61	W	235.5	74.6	N	145.5
4	90	54	S	355.1	29.6	E	265.1
5	55	47	S	352.1	57.2	E	262.1
6	74	62	S	12.1	41.9	E	282.1
7	100	63	S	10.6	18.8	E	280.6
8	90	79	S	46.1	30.7	S	316.1
9	75	50	S	354.0	42.0	E	264.0
10	105	78	S	62.5	17.5	S	332.5

Location: KTC-14-Nprc57*
Mean paleocurrent direction: 51.4 ± 90.0 1σ
n = 10
Regional bedding: 244, 55N

Imbrications:	**Imbrication (uncorrected)**			**Imbrication (corrected)**			**Paleocurrent**
Measurement #	Strike	Dip	Dip Quad	Strike	Dip	Dip Quad	Trend
1	222	67	W	180.2	22.6	W	90.2
2	245	67	N	248.4	12.0	N	158.4
3	255	32	N	49.7	24.1	S	319.7
4	217	34	W	96.8	27.9	S	6.8
5	235	47	N	102.4	10.6	S	12.4
6	71	52	S	249.8	73.3	N	159.8
7	250	80	N	257.8	25.6	N	167.8
8	269	51	N	352.8	20.3	E	262.8
9	147	54	W	120.2	75.1	S	30.2
10	231	51	N	129.1	11.1	S	39.1

Location: KTC-14-Nprc59
Mean paleocurrent direction: 98.7 ± 62.5 1σ
n = 10
Regional bedding: 105, 52S

Imbrications:	**Imbrication (uncorrected)**			**Imbrication (corrected)**			**Paleocurrent**
Measurement #	Strike	Dip	Dip Quad	Strike	Dip	Dip Quad	Trend
1	121	56	S	182.7	13.5	W	92.7
2	135	47	S	217.0	23.2	W	127.0
3	131	52	S	203.1	20.4	W	113.1
4	136	62	W	183.1	27.7	W	93.1
5	131	65	S	172.0	25.6	W	82.0
6	150	60	W	196.6	37.8	W	106.6
7	296	84	N	120.5	45.2	S	30.5
8	145	58	W	196.9	33.1	W	106.9
9	136	41	W	231.3	24.8	N	141.3
10	86	56	S	23.8	15.9	E	293.8

Location: KTC-14-Nprc61
Mean paleocurrent direction: 92.9 ± 30.9 1σ
n = 10
Regional bedding: 71, 80S

Imbrications:	**Imbrication (uncorrected)**			**Imbrication (corrected)**			**Paleocurrent**
Measurement #	Strike	Dip	Dip Quad	Strike	Dip	Dip Quad	Trend
1	126	83	S	162.5	54.4	W	72.5
2	124	70	S	178.6	52.0	W	88.6
3	97	59	S	205.8	32.0	W	115.8
4	149	76	W	173.1	76.1	W	83.1
5	147	82	W	166.7	74.9	W	76.7
6	131	76	S	171.4	58.7	W	81.4
7	56	41	S	266.0	41.0	N	176.0
8	133	72	S	176.1	60.4	W	86.1
9	125	78	S	168.6	53.0	W	78.6
10	118	65	S	186.0	47.0	W	96

*Imbrications at this location poorly defined; uncertainty in applicability of these measurements as accurate paleocurrent indicators noted at time of measurement.

APPENDIX E: RAW CONGLOMERATE-COUNT DATA

Sample #	Map unit (Plates 1, 2)	P.S.	Gn.	Gr.	O.I.	S.F.F.	I.V.	F.V.	R.V.F.	Unk.	n
KTC-12-Tpc1	PεNv	0%	9%	57%	0%	0%	0%	1%	24%	9%	100
KTC-13-Tprc9	PεNv	0%	7%	66%	0%	2%	0%	0%	24%	1%	100
KTC-13-Tprc13	PεNv	0%	0%	100%	0%	0%	0%	0%	0%	0%	100
KTC-13-Tprc17	PεNv	0%	0%	53%	5%	0%	30%	9%	1%	2%	100
KTC-13-Tprc23	PεNv	0%	3%	52%	8%	0%	23%	7%	5%	2%	100
KTC-13-Tprc26	PεNv	0%	0%	93%	0%	0%	0%	1%	6%	0%	100
KTC-13-Tprc32	PεNv	0%	3%	53%	6%	0%	0%	0%	34%	4%	100
KTC-14-dz5	Npss	100%	0%	0%	0%	0%	0%	0%	0%	0%	100
KTC-14-Np2	Np	0%	36%	39%	0%	20%	0%	0%	0%	5%	100
KTC-14-Nprc47	Nps	7%	3%	4%	0%	86%	0%	0%	0%	0%	100
KTC-14-Nprc48	PεNv	0%	0%	0%	0%	100%	0%	0%	0%	0%	100
KTC-14-Nprc49	PεNvg	0%	0%	100%	0%	0%	0%	0%	0%	0%	100
KTC-14-Nprc51	Nps	4%	0%	28%	10%	36%	8%	6%	0%	8%	100
KTC-14-Nprc57	PεNv	0%	3%	85%	0%	9%	0%	0%	0%	3%	100
KTC-14-Nprc59	Npb	6%	11%	75%	0%	4%	0%	0%	0%	4%	100
KTC-14-Nprc61	Nps	2%	0%	2%	0%	95%	0%	0%	0%	1%	100

Sample #	Map unit (Fig. 6)	P.S.	Gn.	Gr.	O.I.	C.B.	V.Q.	Unk.	n
KTC-15-Ntccb1	Ntccb	0%	0%	0%	0%	100%	0%	0%	100
KTC-15-Ntcsb1	Ntcsb	41%	8%	12%	16%	17%	4%	2%	100
KTC-15-PεNvlb1	PεNvlb	0%	0%	100%	0%	0%	0%	0%	100
KTC-15-PεNvlb2	PεNvlb	0%	0%	100%	0%	0%	0%	0%	100

Abbreviations of conglomerate-clast categories (categories defined in Table 1):
P.S. = Pelona Schist
Gn. = gneiss
Gr. = granitoid
O.I. = other intrusive
S.F.F. = San Francisquito Formation sandstone and fine conglomerate
I.V. = intermediate volcanics
F.V. = felsic volcanics
R.V.F. = reworked Vasquez Formation sandstone
C.B. = Chloritic breccia and associated fault-related rock
V.Q. = Vein quartz, likely associated with Pelona Schist
Unk. = unknown/unidentifiable

n = number of cobbles counted.

APPENDIX F: RAW SANDSTONE POINT-COUNT DATA

Sample #	Qm	Qp	Fk	Fp	M	D	Lma	Lmt	Lmm	Lmv	Lvm	Lvl	Lvfg	Lvfs	Lvv	Lss	Lsc	M/U	Int.	Total
JFH-11-25P	119	2	74	199	15	10	9	0	0	0	1	3	8	7	0	0	0	19	34	500
JFH-11-26P	143	0	89	186	17	8	5	0	0	0	0	0	0	0	0	0	0	19	33	500
JFH-11-27P	150	0	70	203	19	7	0	0	0	0	0	0	1	2	0	0	0	20	28	500
JFH-11-28P	207	1	72	83	8	3	10	0	4	0	0	0	2	4	0	19	0	28	59	500
KTC-12-Tpc1	111	1	53	166	8	0	21	1	0	14	0	0	1	7	0	6	0	28	83	500
KTC-12-Tps1	109	1	55	165	26	10	3	0	0	0	0	0	0	2	0	3	0	32	94	500
KTC-13-Tprc3	130	2	115	94	0	0	7	0	1	0	0	0	0	2	0	19	12	12	106	500
KTC-13-Tprc8	32	2	61	196	3	27	8	0	1	9	2	45	15	71	0	0	0	21	7	500
KTC-13-Tprc9	154	3	56	146	8	0	25	0	2	0	0	3	1	15	0	14	3	48	22	500
KTC-13-Tprc10	42	1	49	212	19	17	11	0	1	0	3	41	7	16	0	1	1	31	48	500
KTC-13-Tprc12	117	1	98	184	20	13	16	0	0	2	0	6	3	4	0	0	0	10	26	500
KTC-13-Tprc13	101	1	113	145	3	1	6	0	1	2	2	1	1	1	0	0	0	4	118	500
KTC-13-Tprc15	137	2	85	152	10	3	12	0	0	3	0	8	2	9	0	2	0	26	49	500
KTC-13-Tprc16	66	1	35	203	21	5	16	0	1	0	1	1	4	8	0	3	3	21	111	500
KTC-13-Tprc19	22	2	57	230	11	6	23	0	0	3	1	21	2	15	0	4	0	25	78	500
KTC-13-Tprc24	114	1	84	132	0	1	20	0	0	1	1	32	9	30	0	6	19	16	34	500
KTC-13-Tprc25f	137	0	45	156	2	0	10	0	0	0	0	0	6	3	0	1	1	18	121	500
KTC-13-Tprc29	198	4	59	76	8	1	16	0	0	5	1	0	4	13	0	0	0	14	101	500
KTC-13-Tprc36	145	2	114	94	9	1	11	2	0	0	0	1	0	0	0	1	1	26	93	500
KTC-14-dz5*	75	5	7	35	73	15	40	30	6	0	0	0	0	1	0	0	2	44	167	500
KTC-14-Np1	127	0	62	153	38	11	4	0	0	0	0	0	3	0	0	1	0	28	73	500
KTC-14-Np2	126	3	66	206	28	2	9	0	0	0	0	0	0	2	0	3	0	23	32	500
KTC-14-Np3	101	4	73	233	18	0	9	0	0	0	0	0	0	0	0	2	0	10	50	500
KTC-14-Npb1	107	7	74	234	11	2	2	0	1	0	0	0	0	2	0	9	0	25	26	500
KTC-14-Npb2	70	0	65	174	13	6	3	1	3	0	0	0	0	0	0	4	0	26	135	500
KTC-14-Nprc47	133	3	86	82	23	0	13	3	1	0	0	0	13	4	0	2	0	35	102	500
KTC-14-Nprc48	123	1	59	64	5	1	18	2	2	0	1	0	4	12	0	14	6	25	163	500
KTC-14-Nprc49	64	0	63	295	1	0	16	3	0	0	0	0	0	0	0	0	0	4	54	500
KTC-14-Nprc50	134	3	143	63	13	2	21	0	0	0	0	0	2	9	0	2	2	32	74	500
KTC-14-Nprc51	194	1	95	83	19	3	18	3	1	0	0	0	3	10	0	13	0	27	30	500
KTC-14-Nprc56	115	0	137	61	5	0	4	0	0	0	0	0	0	0	0	0	0	3	175	500
KTC-14-Nprc57	97	0	85	123	11	1	3	0	0	0	0	0	1	2	0	15	0	30	132	500
KTC-14-Nprc58	84	1	124	60	8	0	7	0	1	0	0	0	2	0	0	0	0	25	188	500
KTC-14-Nprc59	116	4	55	202	29	5	9	0	1	0	0	0	0	4	0	8	0	24	43	500
KTC-14-Nprc60	163	0	73	71	29	3	8	0	0	0	0	0	2	4	0	4	0	14	129	500
KTC-14-Nprc61	172	1	54	50	8	1	11	1	0	0	0	0	4	3	0	12	1	15	167	500
KTC-14-Tprc40	178	1	14	141	7	0	16	0	6	0	0	0	1	0	0	1	0	23	112	500
KTC-14-Tprc44	115	2	70	152	18	3	8	0	1	0	1	1	5	6	0	11	1	47	59	500
KTC-14-Tprc45	147	5	78	133	10	1	23	2	0	0	1	5	6	21	0	1	3	22	42	500
P2-11-06-3*	73	10	27	90	101	3	16	12	2	6	0	0	1	2	0	0	0	31	126	500
P2-11-06-5*	131	10	50	122	65	0	26	16	4	0	0	0	0	0	0	0	0	29	47	500
P2-11-06-7*	130	17	23	72	104	3	25	21	4	0	0	0	0	0	0	0	0	31	70	500
P4-08-06-2	5	0	1	56	0	2	0	0	0	0	40	88	47	76	0	0	0	33	152	500
P4-08-06-6	2	0	4	92	3	2	4	0	1	1	23	51	37	92	0	0	0	49	139	500
P7-14-06-1*	33	1	46	130	83	51	49	1	0	0	0	0	0	0	0	0	0	21	85	500

*grain mount of disaggregated sandstone; Interstitial (Int.) counts not necessarily meaningful.

Sample #	Notes
JFH-11-25P	
JFH-11-26P	
JFH-11-27P	
JFH-11-28P	Some of the interstitial calcite is likely replaced plagioclase, which would partly explain the low Fp count
KTC-12-Tpc1	
KTC-12-Tps1	Thin carbonate lamination through middle of slide, partly responsible for high number of Int. Counts
KTC-13-Tprc3	
KTC-13-Tprc8	
KTC-13-Tprc9	33 of the M/U counts are coarse carbonate grains, presumably diagenetic replacment of other minerals
KTC-13-Tprc10	
KTC-13-Tprc12	M counts are mostly chlorite; D counts are all opaques
KTC-13-Tprc13	
KTC-13-Tprc15	11 of the M/U counts are coarse carbonate grains, presumably diagenetic replacment of other minerals
KTC-13-Tprc16	Fine grained
KTC-13-Tprc19	
KTC-13-Tprc24	Lsc grains are intrabasinal, probably lacustrine
KTC-13-Tprc25f	Fine grained
KTC-13-Tprc29	Some of the interstitial calcite may be replaced plagioclase, which would explain the low Fp count
KTC-13-Tprc36	Abundant calcite cement, some of which is likely recrystallized calcite grains
KTC-14-dz5	M counts are dominantly muscovite, but with some biotite as well
KTC-14-Np1	
KTC-14-Np2	
KTC-14-Np3	Most of the Int. counts are unfilled primary pore space
KTC-14-Npb1	
KTC-14-Npb2	
KTC-14-Nprc47	
KTC-14-Nprc48	
KTC-14-Nprc49	Coarse, angular breccia of granitic rock with silty matrix rich in carbonate, and with some euhedral carbonate rhombs, presumably secondary
KTC-14-Nprc50	Epimatrix is primarily fine grained, low birefringence material, possibly zeolites, with some secondary calcite
KTC-14-Nprc51	
KTC-14-Nprc56	
KTC-14-Nprc57	Sparry calcite cement, with thin, older iron-oxide cement outlining grains; plagioclase highly altered to calcite, and difficult to tell apart from true pore-filling calcite in places
KTC-14-Nprc58	
KTC-14-Nprc59	
KTC-14-Nprc60	Fine grained
KTC-14-Nprc61	
KTC-14-Tprc40	
KTC-14-Tprc44	Fine grained
KTC-14-Tprc45	
P2-11-06-3	Disaggregated sandstone, with lots of empty space in the slide; M counts are mainly biotite, but with significant muscovite as well
P2-11-06-5	Disaggregated sandstone, with lots of empty space in the slide
P2-11-06-7	Disaggregated sandstone, with lots of empty space in the slide
P4-08-06-2	
P4-08-06-6	Lv grains are very dark with oxides, stain and alteration; together with zeolite cement, makes counting somewhat difficult
P7-14-06-1	Disaggregated sandstone, with lots of empty space in the slide

APPENDIX G: XRF MAJOR- AND TRACE-ELEMENT DATA

Sample	KTC-13-Ndva	KTC-13-Ndvb	KTC-13-and3	KTC-14-and4	KTC-14-Tv6	KTC-14-vint1
Date	1-Sep-14	1-Sep-14	1-Sep-14	1-Sep-14	1-Sep-14	1-Sep-14
Unnormalized Major Elements (Weight %):						
SiO2	74.7	47.4	74.9	74.7	52.7	61.3
TiO2	0.096	1.62	0.092	0.100	1.82	2.06
Al2O3	12.7	15.4	12.4	11.7	16.2	17.8
FeO*	1.49	7.74	1.60	1.73	7.27	3.31
MnO	0.016	0.103	0.030	0.025	0.082	0.024
MgO	0.05	2.92	0.06	0.16	1.58	1.21
CaO	0.24	9.39	0.68	1.22	4.70	1.44
Na2O	3.07	3.98	2.41	3.29	8.21	6.91
K2O	6.51	0.50	6.81	5.17	0.13	1.54
P2O5	0.031	0.311	0.031	0.024	0.357	0.372
Sum	98.9	89.3	99.0	98.2	93.0	96.0
LOI %	0.55	10.1	0.80	1.71	6.78	3.34
Normalized Major Elements (Weight %):						
SiO2	75.5	53.1	75.6	76.1	56.6	63.9
TiO2	0.097	1.82	0.093	0.102	1.96	2.14
Al2O3	12.9	17.2	12.6	11.9	17.4	18.6
FeO*	1.51	8.66	1.61	1.76	7.82	3.45
MnO	0.016	0.115	0.030	0.025	0.088	0.025
MgO	0.05	3.27	0.06	0.17	1.70	1.26
CaO	0.24	10.5	0.69	1.24	5.06	1.50
Na2O	3.11	4.46	2.43	3.36	8.83	7.20
K2O	6.58	0.56	6.88	5.27	0.14	1.61
P2O5	0.031	0.349	0.031	0.024	0.384	0.388
Total	100.0	100.0	100.0	100.0	100.0	100.0

Major elements are normalized on a volatile-free basis, with total Fe expressed as FeO.

Unnormalized Trace Elements (ppm):						
Ni	2	66	2	4	59	54
Cr	5	192	7	5	177	215
Sc	2	22	1	1	23	17
V	4	161	6	6	146	133
Ba	946	333	1646	552	39	229
Rb	168	9	225	170	3	40
Sr	109	238	135	114	78	84
Zr	143	163	139	139	191	191
Y	22	24	14	18	25	21
Nb	19.8	21.4	18.6	19.4	26.2	29.8
Ga	14	18	17	12	15	19
Cu	2	33	3	3	26	56
Zn	30	173	23	23	38	26
Pb	5	5	18	8	1	5
La	30	21	17	20	33	44
Ce	64	43	41	50	57	72
Th	29	4	30	27	4	5
Nd	33	23	22	22	27	31
U	6	1	5	6	2	0
As >/=	4	28	11	10	10	30
sum tr.	1639	1577	2380	1209	980	1303
in %	0.16	0.16	0.24	0.12	0.10	0.13
sum m+tr	99.02	89.45	99.24	98.28	93.07	96.13
M+Toxides	99.05	89.49	99.27	98.30	93.11	96.17
w/LOI	99.60	99.56	100.08	100.01	99.89	99.51

APPENDIX H: ICPMS TRACE-ELEMENT DATA

Sample	KTC-13-Ndva	KTC-13-Ndvb	KTC-13-and3	KTC-14-and4	KTC-14-Tv6	KTC-14-vint1
Unnormalized Trace Elements (ppm):						
La	30.5	21.8	19.1	19.9	28.8	40.5
Ce	72.2	45.5	41.6	49.4	56.8	76.8
Pr	9.42	5.73	5.26	6.41	6.98	8.78
Nd	35.1	23.1	20.3	24.2	28.0	32.3
Sm	8.38	5.10	4.99	5.61	6.02	5.69
Eu	0.34	1.72	0.29	0.32	2.14	1.61
Gd	6.35	5.05	3.75	4.39	5.61	4.77
Tb	0.90	0.81	0.56	0.67	0.87	0.73
Dy	4.82	4.78	3.07	3.56	5.13	4.25
Ho	0.82	0.92	0.56	0.62	0.99	0.85
Er	1.96	2.40	1.40	1.63	2.53	2.32
Tm	0.27	0.33	0.20	0.24	0.35	0.34
Yb	1.53	2.05	1.20	1.44	2.09	2.06
Lu	0.21	0.32	0.17	0.21	0.32	0.32
Ba	960	337	1690	563	36	228
Th	28.4	3.92	29.5	27.0	4.67	4.94
Nb	18.7	21.7	17.9	18.9	25.8	28.7
Y	20.8	23.2	14.0	16.6	24.2	20.4
Hf	4.84	3.91	4.90	4.82	4.40	4.69
Ta	1.77	1.38	1.72	1.72	1.63	1.79
U	5.66	1.37	5.45	6.11	1.30	1.94
Pb	6.08	5.45	17.4	7.71	1.65	4.34
Rb	164	9.3	224	170	3.1	38.5
Cs	1.36	0.82	3.78	1.08	0.11	0.58
Sr	110	241	138	117	79	83
Sc	1.6	21.1	1.7	1.6	22.2	16.8
Zr	141	161	140	140	187	190

APPENDIX I: FIELD PHOTOGRAPHS

Photograph locations and details of samples/measurements listed in Appendix A.

Map unit symbols in parentheses correspond to those of Plates 1, 2.

Photo B1: Location of samples KTC-12-Tpc1 and KTC-14-dz3; Vasquez Formation (PɛNv)

Photo B3: microfaults synthetic to the Punchbowl fault

Photo B5: Location of samples KTC-14-Nprc51 and KTC-14-dz4; Paradise Springs formation (Nps)

Photo B7: Location of sample KTC-14-dz5; schist breccia of Paradise Springs formation (Npss)

Photo B9: Location of samples KTC-14-Nprc47 and KTC-14-dz7; Paradise Springs formation (Nps)

Photo B10: Location of samples KTC-14-Nprc48 and KTC-14-dz6; Vasquez Formation (PεNv)

Photo B15: Location of samples
KTC-14-Np2 and KTC-14-dz9;
Punchbowl Formation (Np)

Photo B17: Location of sample KTC-Nprc57;
Vasquez Formation (PεNv)

Photo B19: Location of samples KTC-Nprc59 and KTC-14-dz8; basal Punchbowl Formation (Npb)

Photo B20: anticline in the San Francisquito Formation

Photo B22: crossbedding in the Punchbowl Formation

Photo B24: small faults in the Punchbowl Formation

Photo B26: the Punchbowl fault
(Np = Punchbowl Fm., Mzqdc = crystalline basement;
see Plate 1 for details)

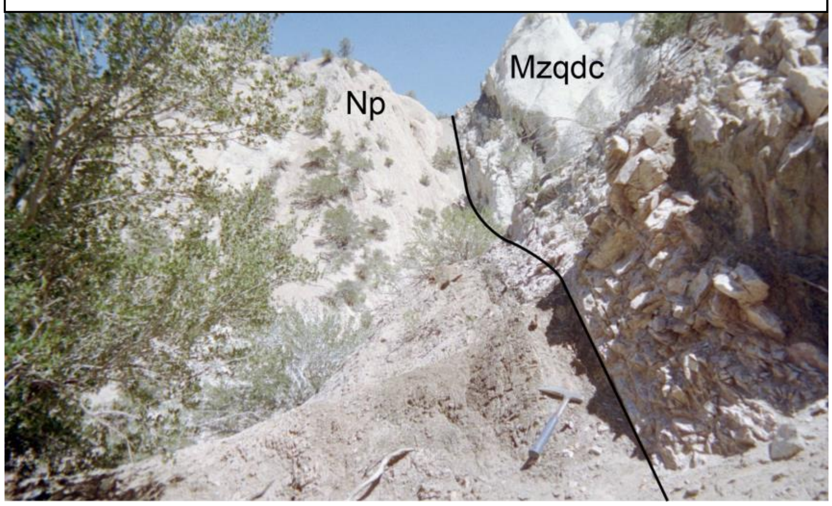

REFERENCES CITED

Advocate, D.M., Link, M.H., and Squires, R.L., 1988, Anatomy and history of an Eocene submarine canyon: the Maniobra Formation, southern California, *in* Filewicz, M.V., and Squires, R.L., eds., Paleogene stratigraphy, west coast of North America: Los Angeles, Pacific Section, Society of Economic Paleontologists and Mineralogists (SEPM), West Coast Paleogene Symposium, v. 58, p. 45-58.

Allmendinger, R.W., Cardozo, N.C., and Fisher, D., 2012, Structural geology algorithms: vectors & tensors: Cambridge, Cambridge University Press, 289 p.

Anders, E., and Grevesse, N., 1989, Abundances of the elements: Meteoritic and solar: Geochimica et Cosmochimica Acta, v. 53, p. 197-214.

Arnold, R., 1906, The Tertiary and Quaternary pectens of California: U.S. Geological Survey Professional Paper 47, 264 p.

Atwater, T., 1970, Implications of plate tectonics for the Cenozoic tectonic evolution of western North America: Geological Society of America Bulletin, v. 81, p. 3513-3536.

Atwater, T., 1989, Plate tectonic history of the northeast Pacific and western North America, *in* Winterer, E.L., ed., The eastern Pacific Ocean and Hawaii: Boulder, Colorado, Geological Society of America, Geology of North America, v. N, p. 21-72.

Barth, A.P., 1989, Mesozoic rock units in the upper plate of the Vincent thrust fault, San Gabriel Mountains, southern California [Ph.D. thesis]: Los Angeles, University of Southern California, 379 p.

Barth, A.P., Tosdal, R.M., and Wooden, J.L., 1990, A petrologic comparison of Triassic plutonism in the San Gabriel and Mule Mountains, southern California: Journal of Geophysical Research, v. 95, p. 20075-20096.

Barth, A.P., Wooden, J.L., Tosdal, R.M., Morrison, J., Dawson, D.L., and Hernly, B.M., 1995, Origin of gneisses in the aureole of the San Gabriel anorthosite complex and implications for Proterozoic crustal evolution of southern California: Tectonics, v. 14, p. 736-752.

Barth, A.P., Tosdal, R.M., Wooden, J.L., and Howard, K.A., 1997, Triassic plutonism in southern California: Southward younging of arc initiation along a truncated continental margin: Tectonics, v. 16, p. 290-304.

Barth, A.P., Wooden, J.L., Coleman, D.S., 2001, SHRIMP-RG U-Pb zircon geochronology of Mesoproterozoic metamorphism and plutonism in the southwesternmost United States: Journal of Geology, v. 109, p. 319-327.

Barth, A.P., Wooden, J.L., Howard, K.A., and Richards, J.L., 2008, Late Jurassic plutonism in the southwest U.S. Cordillera: Geological Society of America Special Paper 438, p. 379-396.

Bird, P., 1984, Laramide crustal thickening event in the Rocky Mountain Foreland and Great Plains: Tectonics, v. 3, p. 741-758.

Bird, P., 1988, Formation of the Rocky Mountains, western United States: a continuum computer model: Science, v. 239, p. 1501-1507.

Bishop, K.M., and Ehlig, P.L., 1990, The Pelona fault, central Transverse Ranges, southern California: an extensional detachment fault?: Geological Society of America Abstracts with Programs, v. 22, no. 3, p. 8.

Black, L., Kamo, S., Allen, C., Davis, D., Aleinikoff, J., Valley, J., Mundil, R., Campbell, I., Korsch, R., Williams, I., and Foudoulis, C., 2004, Improved $^{206}Pb/^{238}U$ microprobe geochronology by the monitoring of a trace-element-related matrix effect; SHRIMP, ID-

TIMS, ELA-ICP-MS and oxygen isotope documentation for a series of zircon standards: Chemical Geology, v. 205, p. 115-140.

Bohannon, R.G., 1975, Mid-Tertiary conglomerates and their bearing on Transverse Range tectonics, southern California, *in* Crowell, J.C., The San Andreas fault in southern California: A guide to the San Andreas fault from Mexico to Carrizo Plain: California Division of Mines and Geology Special Report, v. 118, p. 75-82.

Bohannon, R.G., 1976, Mid-Tertiary nonmarine rocks along the San Andreas fault in southern California [Ph.D. thesis]: Santa Barbara, University of California, 311 p.

Buesch, D.C., and Ehlig, P.L., 1982, Structural and lower Miocene volcanic rock correlation between Soledad Pass and Salton Wash along the San Andreas fault: Geological Society of America Abstracts with Programs, v. 14, p. 153.

Cardozo, N., and Allmendinger, R.W., 2013, Spherical projections with OSXStereonet: Computers & Geosciences, v. 51, p. 193-205.

Carman, M.F., Jr., 1954, Geology of the Lockwood Valley area, Kern and Ventura Counties, California [Ph.D. thesis]: Los Angeles, University of California, 194 p.

Carman, M.F., Jr., 1964, Geology of the Lockwood Valley area, Kern and Ventura Counties, California: California Division of Mines and Geology Special Report 81, 62 p.

Carter, B., and Silver, L.T., 1971, Post-emplacement structural history of the San Gabriel anorthosite complex: Geological Society of America Abstracts with Programs, v. 3, p. 92-93.

Carter, J.N., Luyendyk, B.P., and Terres, R.R., 1987, Neogene clockwise tectonic rotation of the eastern Transverse Ranges, California, suggested by paleomagnetic vectors: Geological Society of America Bulletin, v. 98, p. 199-206.

Colasanti, C.V., and Ingersoll, R.V., 2006, Unroofing of the Pelona-Orocopia Schist and palinspastic reconstruction of southern California: Geological Society of America Abstracts with Programs, v. 38, no. 5, p. 19.

Cole, R.B., and Basu, A.R., 1995, Nd-Sr isotopic geochemistry and tectonics of ridge subduction and middle Cenozoic volcanism in western California: Geological Society of America Bulletin, v. 107, p. 167-179.

Cole, R.B., and Stanley, R.G., 1995, Middle Tertiary extension recorded by lacustrine fan-delta deposits, Plush Ranch basin, Western Transverse Ranges, California: Journal of Sedimentary Research, v. 65B, p. 455-468.

Compston, W., Williams, I.S., and Meyer, C., 1984, U-Pb geochronology of zircons from lunar breccia 73217 using a sensitive high mass-resolution ion microprobe: Journal of Geophysical Research Supplement, v. 89, p. B525-B534.

Crouch, J.K., and Suppe, J., 1993, Late Cenozoic tectonic evolution of the Los Angeles basin and inner California borderland: A model for core complex-like crustal extension: Geological Society of America Bulletin, v. 105, p. 1415-1434.

Crowell, J.C., 1954, Geology of the Ridge basin area, Los Angeles and Ventura Counties: California Division of Mines Bulletin 170, Map Sheet 7, ~1:95000.

Crowell, J.C., 1962, Displacement along the San Andreas fault, California: Geological Society of America Special Paper 71, 61 p.

Crowell, J.C., 1973, Problems concerning the San Andreas fault system in southern California: Stanford University Publications in Geological Science, v. 13, p. 125-135.

Crowell, J.C., 1975a, The San Andreas fault in southern California, *in* Crowell, J.C., ed., San Andreas fault in southern California: A guide to the San Andreas fault from Mexico to Carrizo Plain: California Division of Mines and Geology Special Report, v. 118, p. 7-27.

Crowell, J.C., 1975b, Geologic sketch of the Orocopia Mountains, southeastern California, *in* Crowell, J.C., ed., San Andreas fault in southern California: A guide to the San Andreas fault from Mexico to Carrizo Plain: California Division of Mines and Geology Special Report, v. 118, p. 99–110.

Crowell, J.C., 1982, The tectonics of Ridge basin, southern California *in* Crowell, J.C., and Link., M. H., eds., Geologic history of Ridge basin, southern California: Los Angeles, Pacific Section, Society of Economic Paleontologists and Mineralogists, p. 25-41.

Crowell, J.C., 2003, Tectonics of Ridge Basin region, southern California, *in* Crowell, J.C., ed., Evolution of Ridge Basin, southern California: An interplay of sedimentation and tectonics: Geological Society of America Special Paper 367, p. 157-203.

Crowell, J.C., and Susuki, T., 1959, Eocene stratigraphy and paleontology, Orocopia Mountains, southeastern California: Geological Society of America Bulletin, v. 70, p. 581-592.

Crowell, J.C., and Walker, J.W.R., 1962, Anorthosite and related rocks along the San Andreas fault, Southern California: University of California Publications in Geological Science, v. 40, p. 219-283.

Dalrymple, G.G., 1979, Critical tables for conversion of K-Ar ages from old to new constants: Geology, v. 7, p. 558-560.

Davis, G.A., Lister, G.S., and Reynolds, S.J., 1986, Structural evolution of the Whipple and South mountains shear zones, southwestern United States: Geology, v. 14, p. 7-10.

Dibblee, T.W., Jr., 1967, Areal geology of the western Mojave Desert, California: U.S. Geological Survey Professional Paper, v. 522, 153 p., 2 plates, 1:125000.

Dibblee, T.W., Jr., 1968, Displacements on the San Andreas fault system in the San Gabriel, San Bernardino, and San Jacinto Mountains, Southern California *in* Dickinson, W.R., and Grantz, A., eds., Proceedings of conference on geological problems of San Andreas fault system: Stanford University Publications in Geological Sciences, v. 11, p. 260-278.

Dibblee, T.W., Jr., 1987, Geology of the Devil's Punchbowl, Los Angeles County, California, *in*, Hill, M.L., ed., Cordilleran Section of the Geological Society of America Centennial Field Guide: Geological Society of America Centennial Field Guide, v. 1: p. 207-210.

Dibblee, T.W., Jr., 1996a, Geologic Map of the Mint Canyon quadrangle, Los Angeles County, California: Dibblee Geological Foundation, Map DF-57, 1:24000.

Dibblee, T.W., Jr., 1996b, Geologic Map of the Agua Dulce quadrangle, Los Angeles County, California: Dibblee Geological Foundation, Map DF-58, 1:24000.

Dibblee, T.W., Jr., 1997a, Geologic Map of the Warm Springs Mountain quadrangle, Los Angeles County, California: Dibblee Geological Foundation, Map DF-64, 1:24000.

Dibblee, T.W., Jr., 1997b, Geologic Map of the Green Valley quadrangle, Los Angeles County, California: Dibblee Geological Foundation, Map DF-65, 1:24000.

Dibblee, T.W., Jr., 1997c, Geologic Map of the Sleepy Valley & Ritter Ridge quadrangles, Los Angeles County, California: Dibblee Geological Foundation, Map DF-66, 1:24000.

Dibblee, T.W., Jr., 2001, Geologic Map of the Pacifico Mountain and Palmdale quadrangles, Los Angeles County, California: Dibblee Geological Foundation, Map DF-76, 1:24000.

Dibblee, T.W., Jr., 2002a, Geologic Map of the Valyermo quadrangle, Los Angeles County, California: Dibblee Geological Foundation, Map DF-80, 1:24000.

Dibblee, T.W., Jr., 2002b, Geologic Map of the Mescal Creek quadrangle, Los Angeles and San Bernardino Counties, California: Dibblee Geological Foundation, Map DF-81, 1:24000.

Dibblee, T.W., Jr., 2002c, Geologic Map of the Crystal Lake quadrangle, Los Angeles County, California: Dibblee Geological Foundation, Map DF-87, 1:24000.

Dibblee, T.W., Jr., 2002d, Geologic Map of the Mount San Antonio quadrangle, Los Angeles and San Bernardino Counties, California: Dibblee Geological Foundation, Map DF-88, 1:24000.

Dibblee, T.W., Jr., 2003, Geologic Map of the Telegraph Peak and Phelan quadrangles, San Bernardino County, California: Dibblee Geological Foundation, Map DF-107, 1:24000.

Dibblee, T.W., Jr., 2005a, Geologic Map of the Ballinger Canyon quadrangle, San Luis Obispo, Santa Barbara, Ventura and Kern Counties, California: Dibblee Geological Foundation, Map DF-170, 1:24000.

Dibblee, T.W., Jr., 2005b, Geologic Map of the Santiago Creek quadrangle, Kern and Ventura Counties, California: Dibblee Geological Foundation, Map DF-171, 1:24000.

Dibblee, T.W., Jr., 2006a, Geologic Map of the Cuddy Valley quadrangle, Ventura and Kern Counties, California: Dibblee Geological Foundation, Map DF-199, 1:24000.

Dibblee, T.W., Jr., 2006b, Geologic Map of the Apache Canyon quadrangle, Ventura and Kern Counties, California: Dibblee Geological Foundation, Map DF-201, 1:24000.

Dickerson, R.E., 1914, The Martinez Eocene and associated formations of Rock Creek on the western border of the Mojave Desert area: California University Department of Geology Bulletin, v. 8, p. 289-298.

Dickinson, W.R., 1970, Interpreting detrital modes of graywacke and arkose: Journal of Sedimentary Petrology, v. 40, p. 695-707.

Dickinson, W.R., 1981, Plate tectonics and the continental margin of California, *in* Ernst, W.G., ed., The Geotectonic Development of California (Rubey Volume I): Englewood Cliffs, New Jersey, Prentice-Hall, p. 1-28.

Dickinson, W.R., 1996, Kinematics of transrotational tectonism in the California Transverse Ranges and its contribution to cumulative slip along the San Andreas transform fault system: Geological Society of America Special Paper 305, 46 p.

Dickinson, W.R., 1997, Tectonic implications of Cenozoic volcanism in coastal California: Geological Society of America Bulletin, v. 109, p. 936-954.

Dickinson, W.R., 2004, Evolution of the North American Cordillera: Annual Review of Earth and Planetary Sciences, v. 32, p. 13-45.

Dickinson, W.R., and Snyder, W. S., 1978, Plate tectonics of the Laramide orogeny, *in* Matthews, V., III, ed., Laramide folding associated with basement block faulting in the western United States: Geological Society of America Memoir 151, p. 355-366.

Dickinson, W.R., and Snyder, W. S., 1979, Geometry of triple junctions related to San Andreas transform: Journal of Geophysical Research, v. 84, p. 561-572.

Doherty, W., 1989, An internal standardization procedure for the determination of yttrium and the rare earth elements in geological materials by inductively coupled plasma-mass spectrometry: Spectrochimica Acta, v. 44B, p. 263-280.

Ehlert, K.W., 1982, Basin analysis of the Miocene Mint Canyon Formation, southern California, *in* Ingersoll, R.V., and Woodburne, M.O., eds., Cenozoic nonmarine deposits of California and Arizona: Los Angeles, Pacific Section, Society of Economic Paleontologists and Mineralogists (SEPM), p. 51-64.

Ehlert, K.W., 2003, Tectonic significance of the middle Miocene Mint Canyon and Caliente Formations, southern California, *in* Crowell, J.C., ed., Evolution of Ridge Basin, southern California: An interplay of sedimentation and tectonics: Geological Society of America Special Paper 367, p. 113-130.

Ehlert, K.W., and Ehlig, P.L., 1977, The "Polka-dot" granite and the rate of displacement of the San Andreas fault in southern California: Geological Society of America Abstracts with Programs, v. 9, p. 415-416.

Ehlig, P.L., 1968, Causes of distribution of Pelona, Rand, and Orocopia Schists along the San Andreas and Garlock faults, *in* Dickinson, W.R., and Grantz, A., eds., Proceedings of conference on geological problems of San Andreas fault system: Stanford University Publications in Geological Sciences, v. 11, p. 294-305.

Ehlig, P.L., 1981, Origin and tectonic history of the basement terrane of the San Gabriel Mountains, central Transverse Ranges, *in* Ernst, W.G., ed., The Geotectonic Development of California (Rubey Volume I): Englewood Cliffs, New Jersey, Prentice-Hall, p. 253-283.

Ehlig, P.L., and Ehlert, K.W., 1972, Offset of Miocene Mint Canyon Formation from volcanic source along San Andreas fault, Southern California: Geological Society of America Abstracts with Programs, v. 4, p. 154.

Ehlig, P.L., and Joseph, S.E., 1977, Polka dot granite and correlation of La Panza quartz monzonite with Cretaceous batholithic rocks north of Salton Trough, *in* Howell, D.G., Vedder, J.C., and McDougal, K.A., eds., Cretaceous geology of the California Coast Ranges west of the San Andreas fault: Pacific Section, Society of Economic Paleontologists and Mineralogists (SEPM) Field Guide 2, p. 91-96.

Ellis, A.J., 1919, Geology, *in* Ellis, A.J., and Lee, C.H., eds., Geology and ground waters of the western part of San Diego County, California, USGS Water-Supply Paper 446, p. 50-76.

Frizzell, V.A., Jr., and Weigand, P.W., 1993, Whole-rock K-Ar ages and geochemical data from middle Cenozoic volcanic rocks, southern California: A test of correlations across the San Andreas fault, *in* Powell, R.E., Weldon, R.J., II, and Matti, J.C., eds., The San Andreas fault system: displacement, palinspastic reconstruction, and geologic evolution: Geological Society of America Memoir 178, p. 273-288.

Gabb, W.M., 1869, Cretaceous and Tertiary fossils: Geological Survey of California, Palaeontology, v. 2, 299 p.

Gabriel, A., and Cox, E.P., 1929, A staining method for the quantitative determination of certain rock minerals: American Mineralogist, v. 14, p. 290-292.

Gazzi, P., 1966, Le arenarie del flysch sopracretaceo dell'Appennino modenese: correlazioni con il flysch di Monghidoro: Mineralogica e Petrografia Acta, v. 12, p. 69-97.

Gehrels, G.E., Valencia, V., and Pullen, A., 2006, Detrital zircon geochronology by Laser-Ablation Multicollector ICPMS at the Arizona LaserChron Center, *in* Olszewski, T., ed., Geochronology: Emerging Opportunities, Paleontological Society Short Course: Paleontological Society Papers, v. 12, p. 67-76.

Gehrels, G.E., Valencia, V., and Ruiz, J., 2008, Enhanced precision, accuracy, efficiency, and spatial resolution of U-Pb ages by laser ablation-multicollector-inductively coupled plasma-mass spectrometry: Geochemistry, Geophysics, Geosystems, v. 9, Q03017.

Goodmacher, J., Barnett, L., Buckner, G., Ouachrif, L., Vidigal, A., and Frost, E., 1989, The Clemens Well fault in the Orocopia Mountains of southern California: a strike-slip or normal fault structure?: Geological Society of America Abstracts with Programs, v. 21, no. 5, p. 85.

Govindaraju, K., 1994, 1994 compilation of working values and sample description for 383 geostandards: Geostandards Newsletter, v. 18, p. 1-158.

Grove, M., and Lovera, O.M., 1996, Slip-history of the Vincent thrust: role of denudation during shallow subduction, *in* Bebout, G.E., Scholl, D.W., Kirby, S.H., and Platt, J.P., eds., Subduction top to bottom: Washington, American Geophysical Union, p. 163-170.

Grove, M., Jacobson, C.E., Barth, A.P., and Vućić, A., 2003, Temporal and spatial trends of Late Cretaceous-early Tertiary underplating of Pelona and related schist beneath southern California and southwestern Arizona, *in* Johnson, S.E., et al., eds., Tectonic evolution of northwestern Mexico and southwestern USA: Geological Society of America Special Paper 374, p. 381-406.

Haxel, G., and Dillon, J., 1978, The Pelona-Orocopia Schist and Vincent-Chocolate Mountain thrust system, southern California, *in* Howell, D.G., and McDougall, K.A., eds., Mesozoic paleogeography of the western United States: Pacific Section, Society of Economic Paleontologists and Mineralogists (SEPM) Pacific Coast Paleogeography Symposium 2, p. 453-469.

Hendrix, E.D., 1993, Soledad Basin, Central Transverse Ranges, California: U.S. Geological Survey Bulletin 2053, p. 243-350.

Hendrix, E.D., and Ingersoll, R.V., 1987, Tectonics and alluvial sedimentation of the upper Oligocene/lower Miocene Vasquez Formation, Soledad Basin, southern California: Geological Society of America Bulletin, v. 98, p. 647-663.

Hendrix, E.D., Cole, R.B., and Ingersoll, R.V., 2010, Soledad and Plush Ranch basins: mid-Tertiary extensional terrane dismembered by the San Andreas fault system, *in* Clifton, H.E., and Ingersoll, R.V., eds., Geologic excursions in California and Nevada: tectonics, stratigraphy and hydrogeology: Pacific Section, SEPM (Society for Sedimentary Geology) Book 108, p. 103-171.

Hietpas, J., Samson, S., Moecher, D., and Schmitt, A.K., 2010, Recovering tectonic events from the sedimentary record: Detrital monazite plays in high fidelity: Geology, v. 38, p. 167-170.

Hill, M.L., Carlson, S.A., and Dibblee, T.W., Jr., 1958, Stratigraphy of the Cuyama Valley-Caliente Range area, California: American Association of Petroleum Geologists Bulletin, v. 42, p. 2973-3000.

Hornafius, J.S., Luyendyk, B.P., Terres, R.R., and Kamerling, M.J., 1986, Timing and extent of Neogene tectonic rotation in the western Transverse Ranges, California: Geological Society of America Bulletin, v. 97, p. 1476-1487

Hoskin, P.W.O., and Schaltegger, U., 2003, The composition of zircon and igneous and metamorphic petrogenesis: Reviews in Mineralogy and Geochemistry, v. 53, p. 27-62.

Hoyt, J.F., 2012, Provenance and detrital-zircon studies of the Mint Canyon Formation and its correlation to the Caliente Formation, southern California [M.S. thesis]: Los Angeles, University of California, 78 p.

Hsu, K.J., Edwards, G., and McLaughlin, W.A., 1963, Age of the intrusive rocks of the southeastern San Gabriel Mountains, California: Geological Society of America Bulletin, v. 74, p. 507-512.

Ingersoll, R.V., 1982, Triple-junction instability as cause for late Cenozoic extension and fragmentation of the western United States: Geology, v. 10, p. 621-624.

Ingersoll, R.V., 1990, Actualistic sandstone petrofacies: Discriminating modern and ancient source rocks: Geology, v. 18, p. 733-736.

Ingersoll, R.V., 1997, Phanerozoic tectonic evolution of central California and environs: International Geology Review, v. 39, p. 957-972.

Ingersoll, R.V., 2008a, Subduction-related sedimentary basins of the U.S.A. Cordillera, *in* Miall, A.D., ed., Sedimentary Basins of the World, Vol. 5: The sedimentary basins of the United States and Canada: Amsterdam, Elsevier, p. 395-428.

Ingersoll, R.V., 2008b, Reconstructing southern California, in Spencer, J.E., and Titley, S.R., eds., Ores and orogenesis: Circum-Pacific tectonics, geologic evolution, and ore deposits: Arizona Geological Society Digest, v. 22, p. 409-417.

Ingersoll, R.V., and Cavazza, W., 1991, Reconstruction of Oligo-Miocene volcaniclastic dispersal patterns in north-central New Mexico using sandstone petrofacies, *in* Fisher, R.V., and Smith, G.A., eds., Sedimentation in volcanic settings: SEPM (Society for Sedimentary Geology) Special Publication 45, p. 227-236.

Ingersoll, R.V., and Colasanti, C.V., 2004, Unroofing of the Pelona Schist, as documented by sedimentologic evidence along the San Andreas and Punchbowl faults: Programs and Abstracts, 2004 Annual Meeting, Pacific Sections, AAPG, SEPM and SEG, Bakersfield, p. A13-A14.

Ingersoll, R.V., and Rumelhart, P.E., 1999, Three-stage evolution of the Los Angeles basin, southern California: Geology, v. 27, p. 593-596.

Ingersoll, R.V., Bullard, T.F., Ford, R.L., Grimm, J.P., Pickle, J.D., and Sares, S.W., 1984, The effect of grain size on detrital modes: a test of the Gazzi-Dickinson point-counting method: Journal of Sedimentary Research, v. 54, p. 103-116.

Ingersoll, R.V., Grove, M., Jacobson, C.E., Kimbrough, D.L., and Hoyt, J.F., 2013, Detrital zircons indicate no drainage link between southern California rivers and the Colorado Plateau from mid-Cretaceous through Pliocene: Geology, v. 41, p. 311-314.

Ingersoll, R.V., Pratt, M.J., Davis, P.M., Caracciolo, L., Day, P.P., Hayne, P.O., Petrizzo, D.A., Gingrich, D.A., Cavazza, W., Critelli, S., Diamond, D.S., Coffey, K.T., Stang, D.M., Hoyt, J.F., Reith, R.C., and Hendrix, E.D., 2014, Paleotectonics of a complex Miocene half graben formed above a detachment fault: the Diligencia basin, Orocopia Mountains, southern California: Lithosphere, v. 6, p. 157-176.

Jacobson, C.E., Barth, A.P., and Grove, M., 2000, Late Cretaceous protolith age and provenance of the Pelona and Orocopia Schists, southern California: Implications for evolution of the Cordilleran margin: Geology, v. 28, p. 219-222.

Jacobson, C.E., Grove, M., Vućić, A., Pedrick, J.N., and Ebert, K.A., 2007, Exhumation of the Orocopia Schist and associated rocks of southeastern California: Relative rates of erosion, synsubduction tectonic denudation, and middle Cenozoic extension: Geological Society of America Special Paper 419, p. 1-37.

Jacobson, C.E., Grove, M., Pedrick, J.N., Barth, A.P., Marsaglia, K.M., Gehrels, G.E., and Nourse, J.A., 2011, Late Cretaceous-early Cenozoic tectonic evolution of the southern California margin inferred from provenance of trench and forearc sediments: Geological Society of America Bulletin, v. 123, p. 485-506.

Jahns, R.H., 1939, Miocene stratigraphy of the easternmost Ventura Basin, California: a preliminary statement: American Journal of Science, v. 237, p. 818-825.

Jahns, R.H., 1940, Stratigraphy of the easternmost Ventura Basin, California, with a description of a new lower Miocene mammalian fauna from the Tick Canyon Formation, *in* Henshaw, P.C., Wilson, R.W., Howard, H., Miller, A.H., Dougherty, J.F., and Jahns, R.H., eds., Studies of Cenozoic vertebrates and stratigraphy of western North America: Washington, D.C., Carnegie Institute of Washington Publication No. 514, p. 147-194.

Jahns, R.H., and Muehlberger, W.P., 1954, Geology of the Soledad Basin, Los Angeles County: California Division of Mines Bulletin 170, v. 2, Map Sheet 6, 1:85000.

Johnson, D.M., Hooper, P.R., and Conrey, R.M., 1999, XRF analysis of rocks and minerals for major and trace elements on a single low dilution Li-tetraborate fused bead: Advances in X-ray Analysis, v. 41, p. 843-867.

Joseph, S.E., and Davis, T.E., 1977, $^{87}Sr/^{86}Sr$ correlation of rapakivi-textured porphyry to measure offset on the San Andreas fault: Geological Society of America Abstracts with Programs, v. 9, p. 443.

Joseph, S.E., Criscione, J.J., and Davis, T.E., 1978, Rb/Sr geochronology and geochemistry of the Lowe Granodiorite, central San Gabriel Mountains, California: Geological Society of America Abstracts with Programs, v. 10, p. 111.

Kellogg, K.S., 2003, Geologic map of the Cuddy Valley quadrangle, Kern and Ventura Counties, California: U.S. Geological Survey Open-File Report 03-153, 1:24000.

Kellogg, K.S., and Miggins, D.P., 2002, Geologic map of the Sawmill Mountain quadrangle, Kern and Ventura Counties, California: U.S. Geological Survey Open-File Report 02-406, 1:24000.

Kellogg, K.S., Minor, S.A., and Cossette, P.M., 2008, Geologic map of the eastern three-quarters of the Cuyama 30'x60' quadrangle, California: U.S. Geological Survey Scientific Investigations Map 3002, 1:100000.

Kew, W.S.W., 1923, Geologic formations of a part of southern California, and their correlation: American Association of Petroleum Geologists Bulletin, v. 7, p. 411-420.

Kew, W.S.W., 1924, Geology and oil resources of a part of Los Angeles and Ventura Counties, California: U.S. Geological Survey Bulletin 753, 202 p.

Kooser, M., 1982, Stratigraphy and sedimentology of the type San Francisquito Formation, southern California, *in* Crowell, J.C., and Link, M.H., eds., Geologic history of Ridge basin, southern California: Los Angeles, Pacific Section, Society of Economic Paleontologists and Mineralogists (SEPM), p. 53-61.

Korotev, R.L., 1996, A self-consistent compilation of elemental concentration data for 93 geochemical reference samples: Geostandards Newsletter, v. 20, p. 217-245.

Lander, E.B., 1985, Early and middle Miocene continental vertebrate assemblages, central Mojave desert, San Bernardino County, California, *in* Reynolds, R.E., compiler, Geological investigations along Interstate 15, Cajon Pass to Manix Lake, California: Redlands, San Bernardino County Museum, p. 127-144.

Law, R.D., Eriksson, K., and Davisson, C., 2001, Formation, evolution, and inversion of the middle Tertiary Diligencia basin, Orocopia Mountains, southern California: Geological Society of America Bulletin, v. 113, p. 196-221.

LeBas, M.J., Lemaitre, R.W., Streckeisen, A., and Zanettin, B., 1986, A chemical classification of volcanic rocks based on the total alkali silica diagram: Journal of Petrology, v. 27, p. 745-750.

Liu, W., 1990, Paleomagnetism of Miocene sedimentary rocks in the Transverse Ranges: the implications for tectonic history [Ph.D. thesis]: Pasadena, California Institute of Technology, 233 p.

Lonsdale, 1991, Structural patterns of the Pacific floor offshore of peninsular California, *in* Dauphin, J.P., and Simoneit, B.R.T., eds., The Gulf and Peninsular Province of the Californias: American Association of Petroleum Geologists Memoir 47, p. 87-125.

Matti, J.C., and Morton, D.M., 1993, Paleogeographic evolution of the San Andreas fault in southern California: A reconstruction based on a new cross-fault correlation, *in* Powell, R.E., Weldon, R.J., II, and Matti, J.C., eds., The San Andreas fault system: displacement, palinspastic reconstruction, and geologic evolution: Geological Society of America Memoir 178, p. 107-159.

May, D.J., and Walker, N.W., 1989, Late Cretaceous juxtaposition of metamorphic terranes in the southeastern San Gabriel Mountains, California: Geological Society of America Bulletin, v. 101, p. 1246-1267.

McLean, 1976, H., Howell, D.G., and Vedder, J.G., 1976, Miocene strata on Santa Cruz and Santa Rosa Islands: a reflection of tectonic events in the southern California borderland, *in* Howell, D.G., ed., Aspects of the geologic history of the California continental borderland: Pacific Section, American Association of Petroleum Geologists, Miscellaneous Publication 24, p. 241-254.

Miller, F.K., and Morton, D.M., 1977, Comparison of granitic intrusions in the Pelona and Orocopia schists, southern California: Journal of Research of the U.S. Geological Survey, v. 5, p. 643-649.

Miller, W.S., 1934, Geology of the Western San Gabriel Mountains of California: University of California, Los Angeles, Publications in Math and Physical Sciences, v. 1, p. 1-114, 1:84480.

Muehlberger, W.R., 1958, Geology of northern Soledad basin, Los Angeles County, California: American Association of Petroleum Geologists Bulletin, v. 42, p. 1812-1844.

Nicholson, C., Sorlien, C.C., Atwater, T., Crowell, J.C., and Luyendyk, B.P., 1994, Microplate capture, rotation of the western Transverse Ranges, and initiation of the San Andreas transform as a low-angle fault system: Geology, v. 22, p. 491-495.

Noble, L.F., 1953, Geology of the Pearland quadrangle, California: U.S. Geological Survey Geologic Quadrangle Map GQ-24, 1:24000.

Noble, L.F., 1954, Geologic map of the Valyermo quadrangle and vicinity, California: U.S. Geological Survey Geologic Quadrangle Map GQ-50, 1:24000.

Nourse, J.A., 2002, Middle Miocene reconstruction of the central and eastern San Gabriel Mountains, southern California, with implications for evolution of the San Gabriel fault and Los Angeles basin: Geological Society of America Special Paper 365, p. 161-185.

Oakeshott, G.B., 1958, Geology and mineral deposits of the San Fernando quadrangle, Los Angeles County, California: California Division of Mines Bulletin 172, 147 p.

Onderdonk, N.W., 2005, Structures that accommodated differential vertical axis rotation of the western Transverse Ranges, California: Tectonics, v. 24, TC4018, 15 p.

Onderdonk, N.W., Minor, S.A., and Kellogg, K.S., 2005, Taking apart the Big Pine fault: Redefining a major structural feature in southern California: Tectonics, v. 24, TC6002, 11 p.

Paces, J.B., and Miller, J.D., 1993, Precise U-Pb ages of Duluth Complex and related mafic intrusions, northeastern Minnesota: geochronological insights to physical, petrogenetic, paleomagnetic, and tectonomagmatic processes associated with the 1.1 Ga Midcontinent Rift System: Journal of Geophysical Research, v. 98, p. 13997-14013.

Powell, R.E., 1993, Balanced palinspastic reconstruction of pre-late Cenozoic paleogeology, southern California: geologic and kinematic constraints on evolution of the San Andreas fault system, *in* Powell, R.E., Weldon, R.J., II, and Matti, J.C., eds., The San Andreas fault system: displacement, palinspastic reconstruction, and geologic evolution: Geological Society of America Memoir 178, p. 1-106.

Prothero, D.R., and Schwab, F., 2003, Sedimentary geology: an introduction to sedimentary rocks and stratigraphy (2nd ed.): New York, W. H. Freeman and Company, 557 p.

Reeder, S.W., and McAllister, A.L., 1957, A staining method for the quantitative determination of feldspars in rocks and sands from soils: Canadian Journal of Soil Science, v. 37, p. 57-59.

Robinson, K.L., and Frost, E.G., 1996, Orocopia Mountains detachment system: progressive development of a tilted crustal slab and half-graben sedimentary basin during regional extension, *in* Abbott, P.L., and Cooper, J.D., eds., Field Conference Guide 1996: Pacific Section, AAPG GS 73 and Pacific Section, SEPM Book 80, p. 277-284.

Sams, R.H., 1964, Geology of the Charlie Canyon area, northwest Los Angeles County, California [M.A. thesis]: Los Angeles, University of California, 101 p.

Sañudo-Wilhelmy, S.A., and Flegal, A.R., 1994, Temporal variations in lead concentrations and isotopic composition in the Southern California Bight: Geochimica et Cosmochimica Acta, v. 58, p. 3315-3320.

Schmitt, A.K., Grove, M., Harrison, T.M., Lovera, O., Hulen, J., and Walters, M., 2003, The Geysers – Cobb Mountain Magma System, California (Part 1): U-Pb zircon ages of volcanic rocks, conditions of zircon crystallization and magma residence times: Geochmica et Cosmochimica Acta, v. 67, p. 3423-3442.

Scholl, D.W., 1959, Exposures of San Onofre Breccia on Anacapa Island, California: American Association of Petroleum Geologists Bulletin, v. 43, p. 222-223.

Schwade, I.T., 1954, Geology of Cuyama Valley and adjacent ranges, San Luis Obispo, Santa Barbara, Kern and Ventura Counties: California Division of Mines Bulletin 170, Map Sheet 1, ~1:194000.

Sharp, R.P., 1935, Geology of the Ravenna quadrangle, Los Angeles County, California [Ph.D. thesis]: Pasadena, California Institute of Technology, 81 p.

Silver, L.T., 1966, Preliminary history of the crystalline complex of the central Transverse Ranges, Los Angeles County, California, *in* Abstracts of papers submitted for six meetings with which the Society was associated: Geological Society of America Special Paper 101, p. 201-202.

Silver, L.T., 1971, Problems of crystalline rocks of the Transverse Ranges: Geological Society of America Abstracts with Programs, v. 3, p. 193-194.

Silver, L.T., and Nourse, J.A., 2001, Comparison of timing of low angle faulting in the Rand Mountains and southern Sierra Nevada relative to the classic Vincent thrust of the eastern San Gabriel Mountains: Geological Society of America Abstracts with Programs, v. 33, no. 3, p. 72.

Silver, L.T., McKinney, C.R., Deutsch, S., and Bolinger, J., 1963, Precambrian age determination in the western San Gabriel Mountains, California: Journal of Geology, v. 71, p. 196-214.

Spencer, J.E., and Normark, W.R., 1979, Tosco-Abreojos fault zone: A Neogene transform plate boundary within the Pacific margin of southern Baja California, Mexico: Geology, v. 7, p. 554-557.

Spittler, T.E., 1974, Volcanic petrology and stratigraphy of non-marine strata, Orocopia Mountains: their bearing on Neogene slip on the San Andreas fault, southern California [M.S. thesis]: Riverside, University of California, 115 p.

Spittler, T.E., and Arthur, M.A., 1982, The lower Miocene Diligencia Formation of the Orocopia Mountains, southern California: Stratigraphy, petrology, sedimentology, and structure, *in* Ingersoll, R.V., and Woodburne, M.O., eds., Cenozoic nonmarine deposits of California and Arizona: Los Angeles, Pacific Section, Society of Economic Paleontologists and Mineralogists (SEPM), p. 83-89.

Staatz, M., 1940, Geology of Mount Pinos area, Ventura County [B.S. thesis]: Pasadena, California Institute of Technology, 47 p.

Stacey, J.S., and Kramers, J.D., 1975, Approximation of terrestrial lead isotope evolution by a two-stage model: Earth and Planetary Science Letters, v. 26, p. 207-211.

Stang, D.M., 2013, Provenance, offset equivalent and palinspastic reconstruction of the Miocene Cajon Valley Formation, southern California [M.S. thesis]: Los Angeles, University of California, 76 p.

Stanley, R.G., Stone, P., Vedder, J.G., McDougall, K., Kellogg, K.S., Minor, S.A., and Premo, W.R., 1998, New 1:24,000-scale geologic mapping in the Cuyama 30 x 60 min. sheet, southern Coast Ranges and western Transverse Ranges, Calif.: Geological Society of America Abstracts with Programs, v. 30, no. 5, p. 65-66.

Steiger, R.H., and Jäger, E., 1977, Subcommission on geochronology: convention on the use of decay constants in geo- and cosmochronology: Earth and Planetary Science Letters, v. 36, p. 359-362.

Stirton, R.A., 1933, Critical review of the Mint Canyon mammalian fauna and its correlative significance: American Journal of Science, v. 26, p. 569.

Stock, C., 1947, A peculiar new carnivore from the Cuyama Miocene, California: Southern California Academy of Science Bulletin, v. 46, p. 84-89.

Streckeisen, A., 1974, Classification and nomenclature of plutonic rocks: recommendations of the IUGS subcommission on the systematics of igneous rocks: Geologische Rundschau, v. 63, p. 773-786.

Stuart, C.J., 1979, Middle Miocene paleogeography of coastal southern California and the California Borderland: evidence from schist-bearing sedimentary rocks, *in* Armentrout, J.M., Cole, M.R., and Terbest, H., Jr., eds., Cenozoic paleogeography of the western United States: Pacific Section, Society of Economic Paleontologists and Mineralogists (SEPM) Pacific Coast Paleogeography Symposium 3, p. 29-44.

Tedford, R.H., and Downs, T., 1965, Age of the Punchbowl Formation, Los Angeles and San Bernardino Counties, California: Geological Society of America Special Paper 87, p. 234.

Tennyson, M.E., 1989, Pre-transform early Miocene extension in western California: Geology, v. 17, p. 792-796.

Terres, R.R., and Luyendyk, B.P., 1985, Neogene tectonic rotation of the San Gabriel region, California, suggested by paleomagnetic vectors: Journal of Geophysical Research, v. 90, p. 12467-12484.

Vedder, J.G., Howell, P.G., and Forman, J.A., 1979, Miocene strata and their relation to other rocks, Santa Catalina Island, California, *in* Armentrout, J.M., Cole, M.R., and Terbest, H., Jr., eds., Cenozoic paleogeography of the western United States: Pacific Section, Society of Economic Paleontologists and Mineralogists (SEPM) Pacific Coast Paleogeography Symposium 3, p. 239-256.

Weber, F.H., Jr., 1994, Geologic map of southeast-central Warm Springs Mountain 7.5-minute quadrangle, Los Angeles County, California: California Department of Conservation, Division of Mines and Geology, Open File Report 93-04, 23 p., 1:12000.

Weigand, P.W., 1982, Middle Cenozoic volcanism of the Western Transverse Ranges, *in* Fife, D.L., and Minch, J.A., eds., Geology and mineral wealth of the California Transverse Ranges: Santa Ana, South Coast Geological Society Annual Symposium and Guidebook 10, p. 170-188.

Weldon, R.J., II, Meisling, K.E., and Alexander, J., 1993, A speculative history of the San Andreas fault in the central Transverse Ranges, California, *in* Powell, R.E., Weldon, R.J., II, and Matti, J.C., eds., The San Andreas fault system: displacement, palinspastic reconstruction, and geologic evolution: Geological Society of America Memoir 178, p. 161-198.

Wiedenbeck, M., Roddick, J.C., and Spiegel, W., 1995, Three natural zircon standards for U-Th-Pb, Lu-Hf, trace element and REE analyses: Geostandards Newsletter, v. 91, p. 1-23.

Winterer, E.L., and Durham, D.L., 1962, Geology of the southeastern Ventura Basin, Los Angeles County, California: U.S. Geological Survey Professional Paper 334-H, p. 275-360.

Woodburne, M.O., 1975, Cenozoic stratigraphy of the Transverse Ranges and adjacent areas, southern California: Geological Society of America Special Paper162, 91 p.

Woodburne, M.O., and Golz, D.J., 1972, Stratigraphy of the Punchbowl Formation, Cajon Valley, Southern California: University of California Publications in Geological Sciences, v. 92, 73 p.

Woodburne, M.O., and Whistler, D.P., 1973, An early Miocene oreodont (Merychyinae, Mammalia) from the Orocopia Mountains, Southern California: Journal of Paleontology, v. 47, p. 908-912.

Woodford, A.O., 1925, The San Onofre Breccia, its nature and origin: University of California Publications in Geological Sciences, v. 15, p. 159-280.

Yarnold, J.C., 1993, Rock-avalanche characteristics in dry climates and the effect of flow into lakes: Insights from mid-Tertiary sedimentary breccias near Artillery Peak, Arizona: Geological Society of America Bulletin, v. 105, p. 345-360.

Yarnold, J.C., and Lombard, J.P., 1989, Facies model for large rock-avalanche deposits formed in dry climates, *in* Colburn, I.P., Abbott, P.L., and Minch, J., eds., Conglomerates in basin analysis: a symposium dedicated to A.O. Woodford: Bakersfield, Pacific Section, Society of Economic Paleontologists and Mineralogists (SEPM), p. 9-31.

Yin, A., 2002, Passive-roof thrust model for the emplacement of the Pelona-Orocopia Schist in southern California, United States: Geology, v. 30, p. 183-186.